Spatially Resolved Measurements of Kinematics and Flow-Induced Birefringence in Worm-like Micellar Solutions undergoing High Rate Deformations

by

Thomas J. Ober

B.S., Chemical Engineering, 2008, Cornell University (Ithaca, NY)
Minor Mechanical Engineering

Submitted to the Department of Mechanical Engineering
in partial fulfillment of the requirements for the degree of

Master of Science in Mechanical Engineering

at the

MASSACHUSETTS INSTITUTE OF TECHNOLOGY

June 2010

Author .....
Department of Mechanical Engineering
May 21, 2010

Certified by .....
Gareth H. McKinley
Professor, Mechanical Engineering
Thesis Supervisor

Accepted by .....
David E. Hardt
Graduate Officer, Department Committee on Graduate Students

Spatially Resolved Measurements of Kinematics and Flow-Induced Birefringence in Worm-like Micellar Solutions undergoing High Rate Deformations

by

Thomas J. Ober

Submitted to the Department of Mechanical Engineering
on May 21, 2010, in partial fulfillment of the
requirements for the degree of
Master of Science in Mechanical Engineering

Abstract

Worm-like micellar solutions are model non-Newtonian systems on account of their well understood linear viscoelastic behavior. Their high deformation rate, non-linear rheological response, however, remains inadequately characterized and poorly understood.

In this study, two worm-like micellar systems composed of either cetylpyridinium chloride (CPyCl) with sodium salicylate (NaSal) or cetyltrimethylammonium bromide (CTAB) with NaSal have been characterized across several orders of magnitude of deformation rate ($10^{-2} \leq \dot{\varepsilon}_{ij} \leq 10^{4}$ s^{-1}). This range enables us to span both the linear and non-linear regimes of rheological behavior for both systems. The low deformation rate rheology was characterized using conventional rheometer fixtures. The high deformation rate rheology was determined using microfluidic rheometric devices, which may be exploited to observe the response of a fluid undergoing very large deformation rates at moderate volumetric throughputs, on account of the small lengthscales associated with microfluidic devices. In these experiments, micro-particle image velocimetry (μ-PIV) was used to measure the flow kinematics and a commercial birefringence microscopy instrument (ABRIO^{TM} System, CRi., Inc.) was adapted for making full-field measurements of flow-induced birefringence (FIB) in order to obtain high-resolution measurements of the evolution of the average stress and molecular conformation in the fluids undergoing strong deformations.

First, the shear banding response of the CPyCl:NaSal system and shear thinning response of the CTAB:NaSal system were observed in Poiseuille flow through a rectilinear microchannel. Then the corresponding behavior in an extension-dominated flow through a converging microchannel was characterized. Qualitative as well as quantitative features of the flow kinematics and conformation were assessed in order to understand how the linear rheological properties of these systems effect their

respective constitutive responses in high rate extensional flows.

Thesis Supervisor: Gareth H. McKinley
Title: Professor, Mechanical Engineering

Acknowledgments

I wish to dedicate this work principally to my parents. To my mother, who made sure I maintained my focus on my studies, and to my father whose scientific legacy I will surely not surpass.

I also wish to acknowledge my fourth grade teacher, Mr. Thomas Demmo, who taught me that there are things in life more important than baseball cards.

Much thanks is also owed to my advisor, Prof. Gareth McKinley and to my mentor here at MIT, Dr. Johannes Soulages.

Contents

Chapter 1

Introduction

"The river flows
It flows to the sea
Wherever that river goes
That's where I want to be..."
– **Ballad of Easy Rider**

A viscoelastic material is one which may exhibit fluid-like (*i.e.* viscous) behavior as well as solid-like (*i.e.* elastic) behavior. These materials are some of the most commonly encountered materials in daily life. Many food products, (*e.g.* peanut butter and jelly), and consumer products, (*e.g.* shampoos and cosmetics), may be classified as viscoelastic. In addition to these examples, other viscoelastic materials are found in many areas of industry, from polymer processing, to paints and adhesives, to biological and biomedical devices, and considerably more.

One particular class of viscoelastic materials are surfactant systems, described by Rehage & Hoffmann (1991) and also Larson (1998). Surfactants are amphiphilic[1], rheological modifiers, which may be used to tune the viscosity and elasticity of a fluid. Surfactant molecules are composed of both hydrophobic and hydrophilic constituent groups, and as a consequence, under the proper conditions of temperature, salinity

and concentration, they may associate to form large molecular aggregates, known as micelles. The size and shape (*e.g.* spherical, bilayer, worm-like) of the micelles which form in solution, significantly influence the rheological properties of the surrounding medium, and as such, micellar solutions are of great industrial and practical interest. Micellar solutions are found in soaps, detergents and shampoos, and are also utilized in inkjet printing, turbulent drag reduction, as reported by Rothstein (2009), and even enhanced oil recovery, as discussed by Kefi *et al.* (2005).

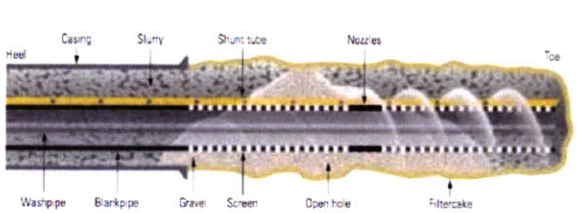

^ Gravel placement with VES fluids. Placing gravel in extended-reach highly deviated wellbores is always difficult. Using VES fluids for proppant transport along with Alternate Path technology, engineers can minimize the risk of an incomplete openhole gravel pack. Shunt tubes attached to the outside of the screen (*top right*) provide a path for the gravel-packing slurry to flow in the event of a premature screenout, or plugging.

(a) Enhanced oil recovery. See Kefi *et al.* (2005).

(b) House-hold products.

(c) Inkjet printer.

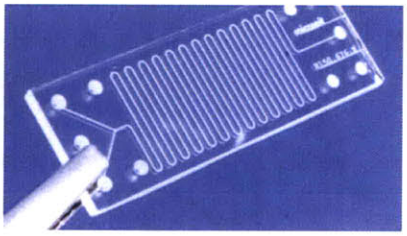

(d) Lab-on-a-chip experiments.

Figure 1.0.1: Common applications of micellar and surfactant solutions.

The primary focus of this study is in the development and refinement of rheometric techniques for measuring the rheological behavior of complex fluids undergoing high rate, or *strong* deformations, for which the elasticity of a material plays an important role in its stress response to the imposed deformation. High rate deformations in complex fluids are commonly achieved even for moderate velocities when the characteristic lengthscale of the flow is small. For example, in the case of the nozzle of an

[1]Literally *having two loves.*

inkjet printer, where the length, l, of the smallest printable feature may be on the order of tens of microns and ejection velocities, v, are on the order of meters per second, characteristic deformation rates, $\dot{\gamma}_c = v/l$, may easily be on the order of 10^4 s^{-1} or greater. In this thesis, we focus on the rheology of worm-like micellar solutions. The experimental techniques used here, however, are amenable to the study of other transparent, complex fluids.

The strain rates associated with the flow of micellar solutions in microscale geometries are evaluated with micro-particle image velocity (μ-PIV) measurements using standard equipment. The corresponding stresses associated with the flow are inferred from optically, non-invasive measurements of flow-induced birefringence (FIB) using the ABRIO^{TM} System (CRi, Inc.). The measurements of stress and strain rate may ultimately be coupled to the predictions of select constitutive models to test the performance of those models in predicting the high rate rheology of worm-like micellar solutions.

This thesis is partitioned into six core chapters, including this introductory section, Chapter 1. In Chapter 2, an overview of the scientific literature for worm-like micellar solutions and additional relevant information is presented; some focus is also given to microscale flows and flow-induced birefringence in micellar solutions. The experimental methods used in this study are described in Chapter 3 including a thorough description of current rheometric techniques for classifying the rheological behavior of surfactant solutions. Additional attention is given to the fabrication techniques used to construct the microscale test geometries.

Of concern in Chapter 4, is the calibration of the ABRIO^{TM} System, in order to demonstrate the suitability of the device for optical, microfluidic rheometry. In Chapter 4, the rheological behavior of the studied micellar solutions under shear deformations is also presented. In the penultimate Chapter 5, the rheological behavior of the studied micellar solutions under extensional deformations is discussed. In the final section, Chapter 6, concluding remarks are made and perspectives for future work are considered.

In addition to the core chapters, this thesis includes multiple appendices in which mathematical derivations of many of the results used in this work along with other useful reference material may be found.

Chapter 2

Literature Overview and Background

"Everything should be made as simple as possible, but no simpler."
– **Albert Einstein**

Micelles and their constituent surfactant molecules are the subject of a substantial body of literature. Reviews of these systems have been written by Cates (1990), Rehage & Hoffmann (1991), Cates & Fielding (2006) and Rothstein (2009) among others. Additionally, both Israelachvili (2007) and Larson (1998) have written texts which address the rheology of such systems at length. Accordingly, the purpose of this section is not to describe the known molecular structure and rheological behavior of micellar solutions in excessive detail, but to provide adequate information so that the context of this study may be appreciated.

[0]The reader unfamiliar with non-Newtonian fluid mechanics or rheology may find it instructive to read Chapter 3 prior to reading this literature overview.

2.1 Surfactant Molecules

The surfactant molecules considered in this study are amphiphiles, being composed of a hydrophilic head group and a hydrophobic tail group. The molecular structures of two such common surfactants are depicted in Figure 2.1.1 (a) and (b). The head group of such a molecule is generally polar or ionic while the tail group is an organic, covalently bonded, non-polar molecular chain. In a polar medium such as water, the polar head group will be considerably more soluble than the non-polar tail group and consequently, if sufficient in number, the molecules will exhibit a tendency to aggregate in order to maximize exposure of the hydrophilic heads to the surrounding water and simultaneously isolate the hydrophobic tails from the polar environment.

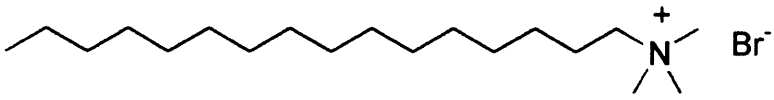

(a) Cetyl Trimethyl Ammonium Bromide Molecule ($C_{19}H_{42}BrN$)

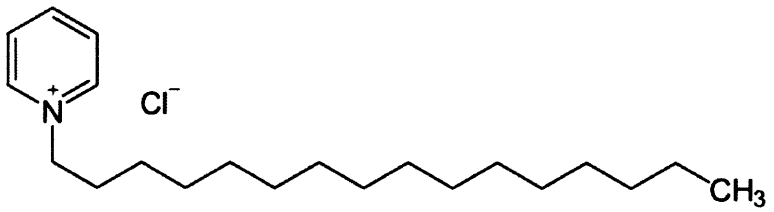

(b) Cetylpyridinium Chloride Molecule ($C_{21}H_{38}ClN$)

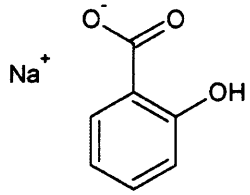

(c) Sodium Salicylate Molecule ($C_7H_5NaO_3$)

Figure 2.1.1: Molecular structures of the surfactant molecules and counterion considered in this study. In (a) and (b) the positively charged nitrogen, is a constituent of the hydrophilic, polar head group, while the flexible hydrocarbon backbone forms the hydrophobic, non-polar tail group.

2.2 Micellar Solutions

A micelle is an aggregate of surfactant molecules, which typically forms spontaneously in a solvent medium given proper conditions of surfactant concentration and salinity. For a particular temperature, the lowest concentration at which the formation of micelles is energetically favorable is known as the *critical micelle concentration*, or alternatively, for a particular concentration the minimum temperature at which micelles form is called the *Krafft temperature* as defined in IUPAC (1997). A micellar solution is a system that contains these self-assembling molecular aggregates, which themselves may vary in size and shape, such that the bulk rheological behavior of the system may be substantially different from that of the pure solvent.

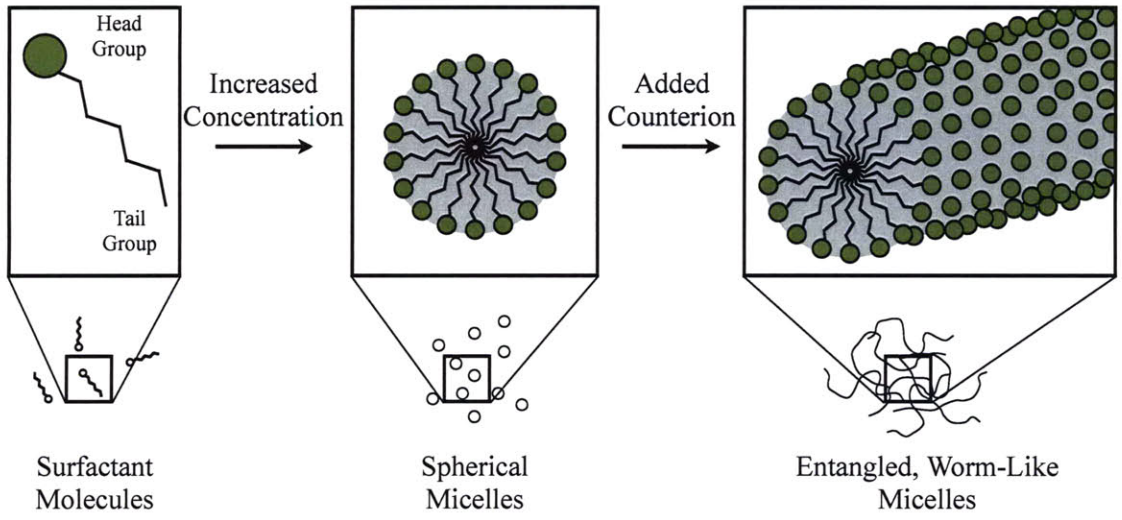

Figure 2.2.1: Schematic diagram of various surfactant aggregate morphologies. Increased concentration and salinity facilitate the formation of entangled, worm-like micelles which are responsible for the viscoelastic response of such systems.

Micelles taking the form of worm-like, flexible cylinders are often known as *living polymers*, on account of their ability to associate reversibly and dynamically and their entangled structure that is topologically similar to that of many entangled polymeric solutions. Aside from their applications as rheological modifiers, entangled, worm-like micellar solutions, depicted in Figure 2.2.1, constitute model systems for

rheological studies, because these systems exhibit ideal linear viscoelastic behavior, which can be described by the Maxwell model in the limit of small deformations and deformation rates. Furthermore, as pointed out by Rehage & Hoffmann (1991) and later Cates & Fielding (2006), these systems mimic the rheological behavior of other polymeric systems, yet their ability to self-assemble dynamically makes them suitable also for the study of non-linear rheological behavior, since, in contrast to a typical polymeric system which may degrade from high deformation rates, micellar systems can self-reassemble even after having undergone deformations significant enough to have broken the aggregates. On account of these attributes, and for reasons that are described in what follows, entangled, worm-like micellar solutions were selected for study in this thesis.

2.2.1 Molecular Structure

The morphology and size of the molecular aggregates are dictated by the surfactant concentration, prevailing ionic activity, law of mass action, and the relative size of head and tail groups. A schematic depiction of the dependency of the micellar morphology on concentration and salinity is shown in Figure 2.2.2. Possible conformations include, but are not limited to single molecules, spheres, multilayered spheres, vesicles, bilayers, and rigid or flexible cylindrical chains.

Although the physics governing micellar conformations is complex, much insight may be gained if one considers the geometric packing argument outlined by Israelachvili (2007). According to this argument, a single surfactant molecule, depicted in Figure 2.2.3, is supposed to occupy an effective volume, v, its tail group extends to some critical length, l_c, and its head group has a surface area, a_0, which has been optimized according to the prevailing ionic activity in the surrounding medium and ionic character of the head group. In general, increased counterion concentration tends to increase ionic screening, which lessens the repulsive forces between adjacent

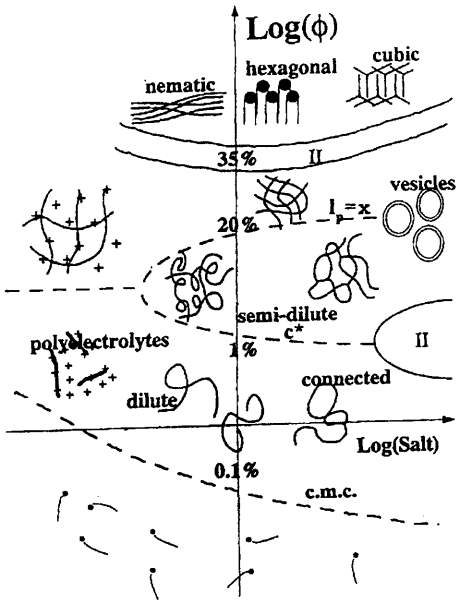

Figure 2.2.2: Schematic diagram of micelle structures for surfactant concentration, ϕ, and salinity. Image taken from Figure 12.13 in Larson (1998).

head groups, facilitating closer packing and a corresponding reduction in a_0.

The packing parameter, $v/a_0 l_c$, may be introduced, which is clearly defined as the ratio of the actual volume occupied by the molecule to a hypothetical volume that the molecule would occupy if it were perfectly cylindrical. The value of this parameter governs the realized morphology of the micellar aggregates[1]. For packing parameters smaller than unity, the surfactant molecules take the shape of a cone. In the case where $v/a_0 l_c < \frac{1}{3}$ spherical micelles depicted in Figure 2.2.1 are preferred, for $\frac{1}{3} < v/a_0 l_c < \frac{1}{2}$ cylindrical micelles form, while for $\frac{1}{2} < v/a_0 l_c$, vesicles, bilayers and other conformations are observed.

For the case of cylindrical micelles (*i.e.* $\frac{1}{3} < v/a_0 l_c < \frac{1}{2}$), which are of primary interest in this thesis, the energetically preferred configuration for an individual surfactant molecule is to reside along the length of the cylinder and away from it ends. The radius of the cylinder is thus roughly equal to the length of a constituent surfactant molecule. As cylindrical micelles cannot be infinite in length, however, hemispherical

[0]Refer to Figure 17.2 in Israelachvili (2007) or Figure 12.1 in Larson (1998).

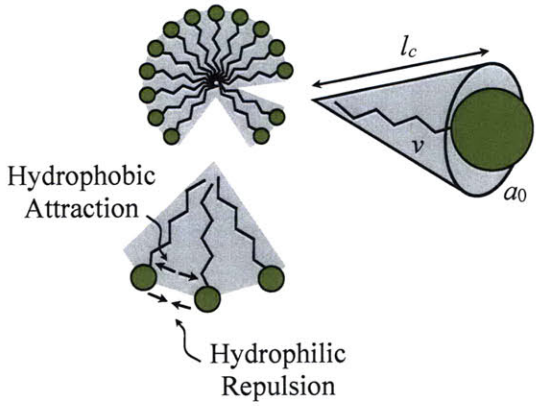

Figure 2.2.3: Schematic diagram of a micelle and its constituent surfactant molecules. Attractive and repulsive forces between adjacent surfactant molecules are depicted. The effective volume, v, occupied by a single surfactant molecule is shown in gray, for which the effective area of the head group is a_0, and the critical length of the molecule is l_c. Figure adapted from Figure 17.1 in Israelachvili (2007).

groups (for which $v/a_0 l_c < \frac{1}{3}$) must cap the cylinder. Accordingly, there is an energy penalty associated with the end-caps due to their necessary deviation from the preferred cylindrical configuration. Therefore, if conditions are such that the formation of cylindrical micelles is favorable, there will be a tendency to form lengthy cylindrical micelles in order to minimize the number of higher energy end-caps in the system. If the length of the cylinder should be substantially greater than the persistence length[2] of the micelle, a flexible or even entangled network of micelles can be expected. It is this entangled network that gives rise to the viscoelastic behavior of giant, worm-like micellar solutions.

Among many surfactant molecules that can be used to obtain worm-like structures, erucyl bis(2-hydroxyethyl) methyl ammonium chloride (EHAC) was used by Yesilata *et al.* (2006), cetyltrimethylammonium tosylate (CTAT) by Berret *et al.* (2002), cetylpyridinium chloride (CPyCl) by Rehage & Hoffmann (1991) and in this study, and cetyltrimethylammonium bromide (CTAB) by Shikata *et al.* (1994) and again

[2]Persistence lengths are commonly on the order of 10-20 nm, as reported in Cates & Fielding (2006), but may be as large as 40 nm for neutral worm-like micelles as reported in Berret (2006).

here. Commonly used counterions are sodium salicylate (NaSal), seen in Figure 2.1.1 (c), and sodium ($NaNO_3$), which may be combined with a sodium chloride (NaCl) brine.

2.2.2 Rheology of Entangled, Worm-like Micelles

Worm-like micellar solutions have become attractive systems for study due in no small part to their remarkably predictable linear rheological behavior. A comprehensive characterization of their non-linear rheological response, however, remains incomplete. Accordingly, the purpose of this subsection is to outline the most well-established rheological attributes of these systems, while also presenting areas of research that are not so well understood and remain open to further inquiry.

Linear Viscoelastic Response

Viscosity is a measure of the internal friction of a material undergoing deformations, indicating its resistance to flow and its tendency to dissipate the energy of deformation as heat. Conversely, elasticity is a measure of internal resilience of a material, indicating its ability to return to its initial shape after having been deformed and thus its ability to store the energy associated with a deformation. A viscoelastic material exhibits both viscous and elastic responses to an imposed deformation. In general, if the timescale of the deformation applied and then removed is short compared to some characteristic time, a viscoelastic material will respond as an elastic solid and resume its initial configuration, whereas if the deformation timescale is long, the material will behave as a viscous fluid and the deformation will be permanent. The characteristic timescale for comparison is a property of the material and is called the *relaxation time*, denoted by the symbol λ_M. The relaxation time is the timescale on which a stress decays or grows in a viscoelastic material and its magnitude may be taken as inversely proportional to the rate at which a material can adapt to an applied deformation.

Although relaxation processes of many polymeric systems can only be accurately described by a spectrum of relaxation times, the relaxation process of many worm-like micellar systems is of particular interest because it can often be characterized experimentally by a single relaxation time. This unique timescale, however, may be the result of a combination of timescales associated with different stress relaxation mechanisms in the system.

- *Reptation.* According to the theory of de Gennes (1979), the path of movement of an unbranched polymer chain in a sufficiently entangled polymeric network may be supposed to be constrained by its neighboring polymer chains to a tube which encompasses the molecule. If the equilibrium network is perturbed, say by the application or removal of a stress or a strain, the system will respond to the change in stress or strain on the same timescale that it takes for its individual, constituent polymer chains to adapt to that change. In response to the change, a single chain must alter its configuration in the network by diffusing along the confining tube to some new preferred configuration. Accordingly, the timescale on which such an entangled network relaxes is proportional to the time required for a single chain to move, or *reptate*[3] along the entire length of its confining tube. The reptation time is denoted λ_{rep}.

- *Breaking.* Since surfactant molecules in a micelle are held together by relatively weak van der Waals forces, the micelles are capable of breaking and reforming dynamically. Therefore an entangled system of so called *living polymers* is capable of adjusting to a change in stress or strain by breaking and reforming in order to attain the preferred configuration in response to a stress perturbation. The lifespan of a typical micelle, being the timescale between consecutive scission and fusion reactions is the breakage time, λ_{break}, as first described by Cates (1987).

- *Breathing and Rouse Modes.* Other non-reptative relaxation processes pertinent

[3]From the Latin word *reptare*, meaning to creep or slither.

to micelles are described by Larson (1998), but the notion of a confining tube is still useful. Although a chain will relax as a whole via migration through a confining tube, the constituent elements of the chain are also free to relax independently of the entire chain. For instance, the extremities of the chain can diffuse on a timescale, $\lambda_{breathe}$, that is different from that of the whole chain, λ_M. In this manner, the ends of the chain can retract into their confining tube such that the effective length of the tube is reduced. When the ends of the chain advance out of the tube again, the confining effects of the lost extremities of the tube are forgotten. These relaxation events cause the length of the tube to fluctuate in time and are known as primitive-path fluctuations or *breathing* modes. A chain may also relax via *Rouse* modes in which only a particular portion of the chain relaxes on a timescale, λ_{Rouse}, by reconfiguring itself within the tube to a more entropically favorable orientation. Both of these relaxation mechanisms typically occur on very short timescales compared to λ_M, such that high rate or high frequency deformations are necessary to observe their effects on the rheological behavior of a worm-like micellar solution, as considered by Granek & Cates (1992).

The notion of a relaxation process can be further illustrated if one considers a micellar solution initially unstrained and unstressed for all times $t < 0$. If a step strain of magnitude γ_0 were applied to the solution at $t = 0$, the solution would initially behave elastically having modulus G_0, such that the initial stress in the system would be $\tau_0 = G_0\gamma_0$. If the applied strain were to be kept constant for all subsequent times, Cates (1987) showed that the stress in the material, $\tau(t)$, would decay according to the equation

$$\frac{\tau(t)}{\tau_0} = e^{-(t/\lambda_M)^\alpha} \tag{2.2.1}$$

In the case where $\lambda_{break} \gg \lambda_{rep}$, it can be shown that Eq. 2.2.1 becomes a stretched exponential, with $\alpha = 1/4$ and $\lambda_M = \lambda_{rep}$. In this limit, breaking occurs so infre-

quently that the micelles relax entirely through a reptative process.

In worm-like micellar solutions for which salt concentration is substantial, the increased ionic screening facilitates faster breaking and accordingly a reduction in λ_{break}. With increased salinity, Rehage & Hoffmann (1991) have found experimentally that α approaches unity[4]. In the case that $\lambda_{break} \leq \lambda_{rep}$, Cates (1987) found that

$$\lambda_M = \sqrt{\lambda_{break}\lambda_{rep}} \tag{2.2.2}$$

and accordingly

$$\frac{\tau(t)}{\tau_0} = e^{-t/\lambda_M} \tag{2.2.3}$$

The monoexponential stress response described by Eq. 2.2.3 has also been found experimentally by Shikata *et al.* (1987) and Cates & Candau (1990) among others. It is clear that if $\lambda_{break} \leq \lambda_{rep}$, then $\lambda_M \leq \lambda_{rep}$ and the relaxation process is expedited by breaking. A physical explanation for this resultant geometric mean of the two timescales has been presented by Larson (1998). Since a micelle can only relax once it has fully escaped its hypothetical confining tube, a micelle of average length, $\langle L \rangle$, must traverse that same distance with respect to the confining tube, in order to completely relax. As reptation is a diffusive process, occurring on a timescale λ_{rep}, the diffusion coefficient for a reptative process is $D_{rep} = \langle L \rangle^2/\lambda_{rep}$. If $\lambda_{break} \leq \lambda_{rep}$, then the micelle will diffuse a distance $l \approx \sqrt{D\lambda_{break}}$, between each breaking process. After each breaking process, however, the length of the confining tube, through which no end of the micelle will have yet passed, will be reduced by a fractional amount $l/\langle L \rangle$, and any confining effects of the previous tube will be removed so the diffusion process will then start anew. In order to escape the tube entirely, this process must occur $n = \langle L \rangle/l$ times, so the total relaxation time of the whole process is $\lambda_M = n\lambda_{break}$. Substitution of the relevant quantities reveals $\lambda_M = \sqrt{\lambda_{break}\lambda_{rep}}$ as expected. A graphical depiction of both diffusion processes may be seen in Figure 2.2.4.

[4]Refer to Figure 14 in Rehage & Hoffmann (1991).

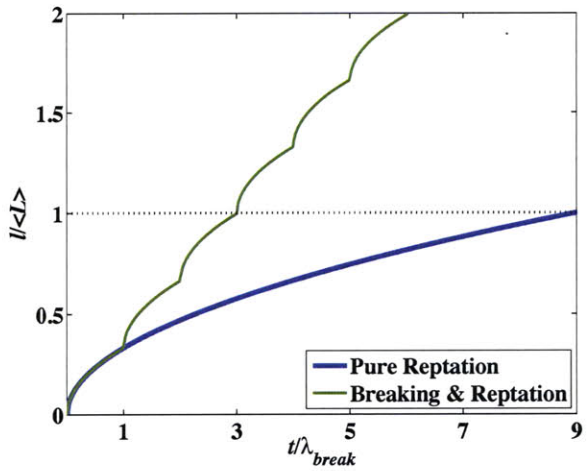

Figure 2.2.4: Fraction of average micelle length, $\langle L \rangle$, traversed by diffusion and breaking for a purely reptative process and a combined breaking and reptative process in the fast breaking limit $\lambda_{break} \ll \lambda_{rep}$. The system is completely relaxed once $l/\langle L \rangle = 1$. Here, $\lambda_{rep}/\lambda_{break} = 9$, and $\lambda_M/\lambda_{break} = \sqrt{\lambda_{rep}/\lambda_{break}} = 3$. After each breaking process, a shortened confining tube remains and the diffusive process begins anew resulting in a reduced total relaxation time.

In addition to determining the relaxation time of a material from its stress response to a step strain given by Eq. 2.2.1, the relaxation time may be measured experimentally by imposing oscillatory shear deformations at different frequencies on the material, see Section 3.1.2. If the sample exhibits a single predominant relaxation time, (*e.g.* a worm-like micellar solution), then the inverse of the frequency at which the observed elastic response of the material is equal to its viscous response is roughly equal to its relaxation time, λ_M, (Bird *et al.* (1987)). Knowledge of λ_M is clearly not sufficient to determine either λ_{break} or λ_{rep}, and to that end methods for determining these quantities from experimental measurements have been described in the work of Turner & Cates (1991), Turner & Cates (1992) and Turner *et al.* (1993). These methods have been used to determine λ_{break} and λ_{rep} for the systems in this study, which are described in Chapter 3.

Behavior in Shear

Like virtually all materials, in the limit of sufficiently small shear deformation rates, $\dot{\gamma} \ll \lambda_M^{-1}$, worm-like micellar solutions exhibit Newtonian behavior, in which the shear stress, τ, is linearly proportional to shear rate, such that $\tau = \eta_0 \dot{\gamma}$, where η_0 is the *zero-shear-rate viscosity.* Simple fluid theory shows in this slow flow limit that elastic stresses are of negligible importance and accordingly the material response is essentially entirely viscous.

For shear deformations that occur on timescales that are roughly equal to or shorter than the relaxation time of the solution, $\dot{\gamma} \geq \lambda_M^{-1}$, a deviation from Newtonian behavior, typically accompanied by the growth of elastic stresses, is observed. An appropriate dimensionless group for comparing the two timescales is the *Weissenberg* number, Wi, which is defined as the ratio of a relaxation time to a characteristic time of deformation, or alternatively $Wi = \lambda_M \dot{\gamma}_c$, where $\dot{\gamma}_c$ is a characteristic deformation rate. For $Wi \geq 1$, strong deviation from Newtonian behavior can be expected.

In low concentration worm-like micellar systems, such as those studied by Hu *et al.* (1998) and Berret *et al.* (2002), shear thickening has been observed, and the steady viscosity may evolve over thousands of shear strain units. Rehage & Hoffmann (1982) and Berret *et al.* (2002) have proposed that this dilatant behavior results from a shear induced structure (SIS) described, for example, in Lerouge & Berret (2009) that effectively thickens the system. At higher shear rates, the viscosity of these semi-dilute systems is observed to obtain a maximum value and then decrease with increasing shear rate. For the tallowalkyl ammonium acetate (TTAA) and NaSal system studied by Hu *et al.* (1998), this shear thinning was accompanied by a constant stress with increasing shear rate, which the authors attributed to a mechanical break down in the form of fracturing of the bulk fluid causing elastically driven flow instabilities.

For concentrated systems, a shear thinning viscometric behavior is generally observed. Indeed, many concentrated micellar solutions exhibit a particularly remarkable pseudoplastic behavior, in that over a range of shear rates, $\dot{\gamma}_1 < \dot{\gamma} < \dot{\gamma}_2$, (which

can often span multiple orders of magnitude) their effective viscosity may be inversely proportional to shear rate such that a constant shear stress can be applied to deform the material over that range of shear rates. Typically $\dot{\gamma}_1 \approx \lambda_M^{-1}$. The constant stress is called a *stress plateau*, and it is a striking example of the non-linear rheological behavior of worm-like micellar solutions, caused by a non-monotonicity in the underlying flow curve of the material, depicted in Figure 2.2.5. A non-montonicity results in a range of shear rates on the flow curve for which shear stress decreases with increasing shear rate. Such rheological behavior is unstable, since any perturbation in stress or shear rate about an equilibrium point in this region of the flow curve would cause the system to jump to one of the neighboring stable branches of the curve.

For average imposed shear rates, $\dot{\gamma}_1 < \langle\dot{\gamma}\rangle < \dot{\gamma}_2$, depicted in Figure 2.2.6, it is not possible for a system both to lie simultaneously on a single stable branch of the flow curve and to satisfy the average shear rate, $\langle\dot{\gamma}\rangle$. Consequently, the system must partition itself into adjacent layers of material, each undergoing different deformation rates, nominally $\dot{\gamma}_1$ and $\dot{\gamma}_2$ as depicted in Figure 2.2.6, yet coexisting at the same applied shear stress, τ_c. This phenomenon is known as *shear banding* and has formed the basis of much experimental studies, theoretical and modeling work by Lu *et al.* (2000), Vasquez *et al.* (2007) and Zhou *et al.* (2008) for example, and review articles, discussions and texts including those by Berret (2006), Cates & Fielding (2006), Fielding (2007) and Olmsted (2008).

One constitutive model that can predict a non-monotonic flow curve in steady shear is that of Johnson & Segalman (1977). For a solution having a Newtonian viscosity, μ, a "polymeric" viscosity, η, relaxation time, λ_M and elastic modulus, $G_0 = \eta/\lambda_M$, the flow curve of this model has been given by Olmsted (2008), and in non-dimensionalized form is

$$\frac{\tau_{xy}}{G_0} = Wi\left[\epsilon^2 + \frac{\epsilon}{1+Wi^2}\right] \tag{2.2.4}$$

where $\epsilon = \mu/\eta$ and $Wi = \lambda_M\dot{\gamma}$ as before. For $\epsilon \leq \frac{1}{8}$ the model may be used to predict

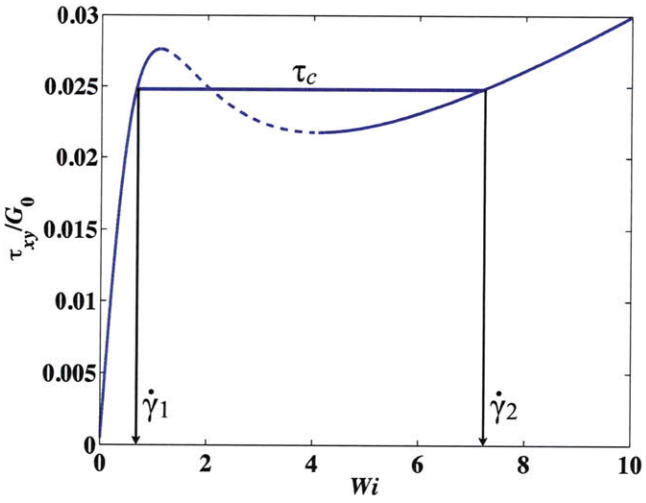

Figure 2.2.5: Flow curve for the Johnson-Selagman model for flow in steady shear given by Eq. 2.2.4 with $\epsilon = 0.05$. The dashed line indicates the unstable regime and the solid horizontal line indicates an example value of the stress plateau, τ_c.

an unstable regime of decreasing shear stress with increasing shear rate. In order to specify a unique, non-hysteretic value for the stress plateau, τ_c, stress or strain rate diffusion terms must be incorporated into the model as outlined in Olmsted *et al.* (2000).

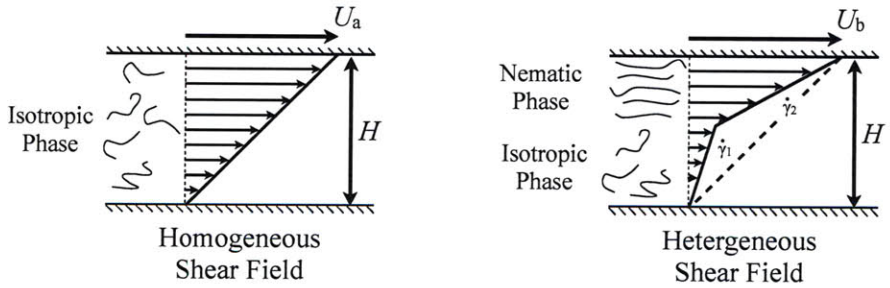

Figure 2.2.6: Schematic diagrams of a homogeneous shear field and a heterogeneous, shear banded shear field in Couette flow. For the homogeneous case, the average shear rate $\langle\dot{\gamma}\rangle_a = U_a/H \ll \dot{\gamma}_1 \approx \lambda_M^{-1}$, where λ_M is the fluid relaxation time. For the heterogeneous flow, $\dot{\gamma}_1 < \langle\dot{\gamma}\rangle_b = U_b/H < \dot{\gamma}_2$.

To first order, the fraction of the gap height, H, occupied by the low shear rate band, β_1, and the high shear rate band, β_2, may be determined by the lever rule such

that the average shear rate $\langle\dot{\gamma}\rangle$ is equal to the imposed shear rate, namely

$$\frac{U_b}{H} = \langle\dot{\gamma}\rangle = \beta_1\dot{\gamma}_1 + \beta_2\dot{\gamma}_2 \tag{2.2.5}$$

where $\beta_1+\beta_2 = 1$ (Lerouge *et al.* (2008)). This lever rule was observed experimentally by Salmon *et al.* (2003). The coexistence of more than two bands is also possible as observed by Lerouge *et al.* (2004) and Miller & Rothstein (2007). Consequently, Eq. 2.2.5 should be taken only as a simplistic generalization of the shear banding phenomenon.

For average shear rates on the order of the lower critical shear rate, $\dot{\gamma}_1$, the formation of steady state shear bands has been found to develop progressively over extended periods of time. Decruppe *et al.* (2001) observed a two phase response in a CTAB:$NaNO_3$ system to a step strain rate in the shear banding regime. They observed an initial stress overshoot and a rapid monoexponential decay in stress, followed by a slower sigmoidal decay to steady state, which often occurred on timescales equal to tens of relaxation times or longer. Similar transient behavior was also observed by Berret *et al.* (1994), Lerouge *et al.* (2000) and Becu *et al.* (2004) among others. The duration of the transient period is typically reduced as the average shear rate is increased well above $\dot{\gamma}_1$.

Cates & Fielding (2006) acknowledged that a universally accepted explanation for the molecular mechanism behind the shear banding phenomenon has not yet been found. Berret *et al.* (1994) and Berret *et al.* (1997) suggested that the shear bands may result from a flow-induced transition from a roughly isotropic to a nematic phase. In two studies of CTAB in deuterium oxide (D_2O) at 32 ^oC by Helgeson *et al.* (2009a) and Helgeson *et al.* (2009b), measurements of velocity profiles, birefringence and small angle neutron scattering (SANS) were combined to observe the microstructural features of the shear banding fluid. The authors found that shear banding in their system was coupled to a flow-induced isotropic-to-nematic transition which could be modeled by anisotropic drag on the chains which led to segment-level flow alignment

of the micelles. In their study, the nematic phase was found to coincide with the high shear rate band, seen in Figure 2.2.7 (a) and (b). This result seemed to contradict the earlier work of Fischer & Callaghan (2000) and again Fischer & Callaghan (2001), however, who also studied the same CTAB:D_2O system between 39 and 41 ^oC and found that the highly birefringence bands (indicating high molecular alignment) in a Couette geometry coincided with a region of low shear rate, seen in Figure 2.2.7 (c). Fischer & Callaghan (2001) hypothesized that the flow-induced nematic phase had a higher viscosity than that of the nematic phase in thermal equilibrium and a slip layer contributed to the bulk rheological measurements. Hu & Lips (2005) have argued that the steady state interface between the low and high shear rate bands was governed by chain disentanglement and reentanglement, having found that adjacent layers of high and low birefringence did not have large difference in shear rate indicating that an isotropic-to-nematic transition was not exclusively responsible for the shear banding in their CPyCl:NaSal system.

Hu *et al.* (2008) also investigated the difference between shear thinning and shear banding worm-like micellar solutions using 2:1 molar CPyCl:NaSal systems of varying concentrations in 0.5 M NaCl. They observed two major differences between shear banding and shear thinning systems: an underlying non-monotonic flow curve was necessary in order to see shear banding, and that shear bands set in only after an induction period for applied stresses near the stress plateau. By contrast for the shear thinning fluid no induction period to obtain steady state was observed nor were shear bands observed. They proposed that shear bands may occur due to a combination of stress relaxation by micellar breakage, molecular entanglements, steric and electrostatic interactions, and local concentration variations across the banding interface.

First normal stress differences, N_1, that were considerably larger in magnitude than the stress plateau, τ_c, have been observed for shear rates at which the stress plateau occurred. In certain systems, Larson (1998) reported that N_1 increased linearly with shear rate. As seen in Figure 2.2.8, the previously mentioned CTAB and

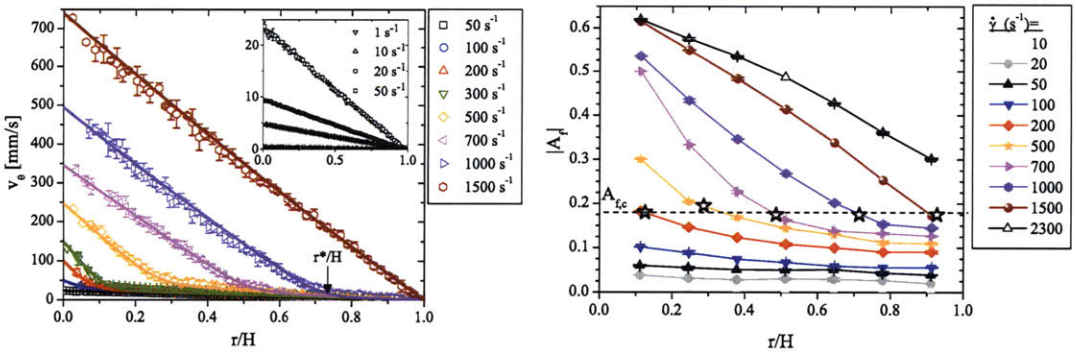

(a)

(b)

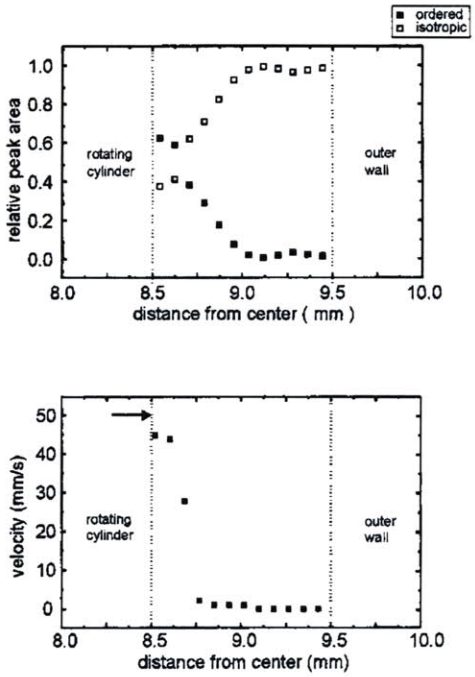

(c)

Figure 2.2.7: (a) From Helgeson *et al.* (2009b). Velocity proles against normalized gap position in steady shear for 16.7 wt% CTAB in D_2O at 32 °C for $\dot{\gamma}_1 < \dot{\gamma} < \dot{\gamma}_2$. Inset graph for data at shear rates less than $\dot{\gamma}_1$. (b) From Helgeson *et al.* (2009b). Alignment factor (defined in Helgeson *et al.* (2009b), $A_f = 0$ is no alignment, $A_f = 1$ is full alignment) versus normalized gap position measured using $1 - 2$ plan flow-SANS. Star symbols indicate the location of banding interface at the corresponding applied shear rate. (c) From Fischer & Callaghan (2001). Order and velocity profiles across a Couette cell gap, for a 20% w/v CTAB and D_2O sample with an average gap shear rate of 51 s^{-1} at 40 °C. The nematic phase exists at low shear rate near the inner wall.

D_2O system of Helgeson *et al.* (2009b), N_1 increased quadratically with $\dot{\gamma}$, for $\dot{\gamma} < \dot{\gamma}_1$, but for $\dot{\gamma} > \dot{\gamma}_1$, N_1 scaled sublinearly with $\dot{\gamma}$. As shown in Chapter 3, in the systems studies in this thesis N_1 increased superlinearly with shear rate.

Behavior in Extension

The extensional rheology of worm-like micellar solutions has been studied using the capillary breakup extensional rheometer (CaBER) by Chen & Rothstein (2004), Yesilata *et al.* (2006) and Bhardwaj *et al.* (2007) and most recently Kim *et al.* (2010). This instrument applies a near step extensional strain on a fluid sample and the subsequent reduction of the sample midpoint diameter driven by capillary forces is recorded. In the experiments with worm-like micelles, the filament incurred increasingly higher extension rates, $\dot{\varepsilon}$, as the thinning process proceeded, and the elastic stresses associated with the stretching of the micelles became significant enough to resist the thinning. Dramatic extensional thickening was observed. Additionally, solvent evaporation likely contributed to the observed increased extensional viscosity. Ultimately, the samples were observed to break through elastocapillary thinning.

In the work of Kim *et al.* (2010), the effect of initial filament diameter and applied strain in CaBER experiments on the rheological behavior of a 100:50:100 mM CPyCl:NaSal:NaCl solution was studied. A dependency on the initial configuration of the material response was observed for small strains, but for strains greater than $\varepsilon = 5$, extensional thickening was observed regardless of the initial configuration in agreement with the studies of Yesilata *et al.* (2006) and Bhardwaj *et al.* (2007). The relaxation time at large strains was found to be only weakly dependent on initial configuration, which the authors attributed to the ability of the micelles to break and reform as a means by which the influence of the initial microstructural configuration could be rapidly forgotten.

A filament stretching extensional rheometer (FiSER) was also used by Rothstein (2003) and Bhardwaj *et al.* (2007). This instrument applies a constant extension rate to the fluid sample and the subsequent evolution of the applied force and the sample

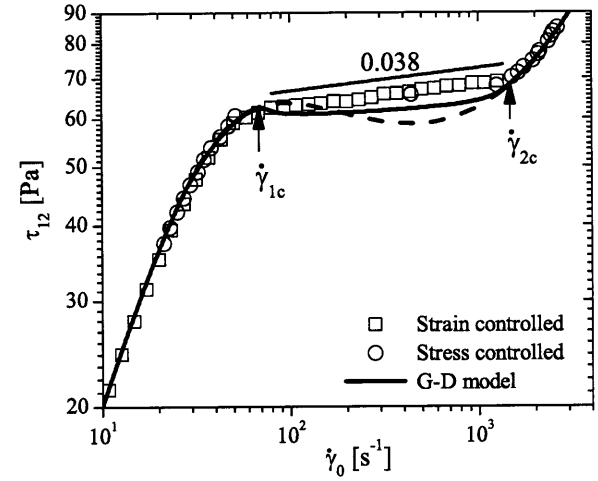

(a)

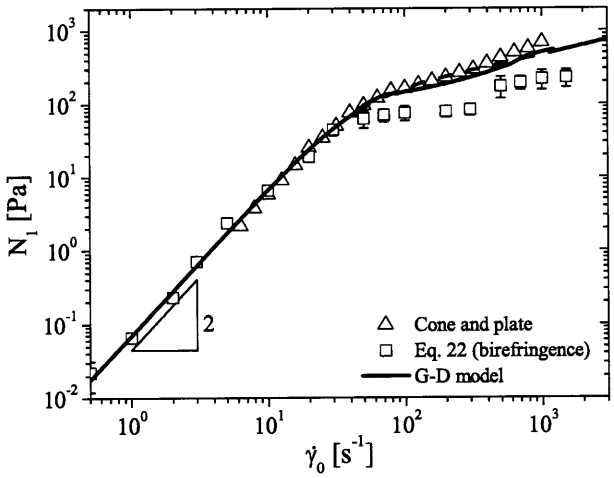

(b)

Figure 2.2.8: From Helgeson *et al.* (2009b). (a) Shear stress under steady shear for 16.7 wt % CTAB in D_2O at 32 °C. (b) First normal stress difference. Closed and open symbols represent measurements made on a cone and plate rheometer and predictions based birefringence measurements. Lines give corresponding predictions from the Giesekus-diffusion model under viscometric (dashed) and inhomogeneous (solid) flow.

midpoint diameter are measured simultaneously. In these experiments, the authors observed an extensional strain hardening behavior. Above a critical extension rate, all samples were observed to rupture *en masse* once a particular stress had been reached. This rupturing of the material was attributed to the scission of its constituent micelles, which occurred so violently on account of the flow kinematics and the elastic recoil of the micelles, that reforming reactions on the timescale of the flow were prevented. The extensional viscosity measured with CaBER and FiSER were so substantially different that Bhardwaj *et al.* (2007) also questioned the viability of using capillary breakup experiments to measure the extensional rheology of worm-like micellar systems.

Prud'homme & Warr (1994) used a Rheometrics RFX opposed nozzle extensional rheometer to measure the extensional rheology of worm-like micelles. They found extensional thickening in the system up to a critical extension rate, above which they observed strong molecular alignment with the flow accompanied by flow instabilities. At these high extension rates, extensional thinning attributed to flow-induced scission of the micelles was observed. This hypothesis was supported by the measurements of Chen & Warr (1997), who found a decrease in the radius of gyration of the micelles accompanying the onset of extensional thinning.

2.2.3 Summary of Macroscale Flows

In this section, the rheological behavior of many worm-like micellar solutions has been discussed. A typical worm-like micellar system exhibits linear viscoelastic behavior that can be characterized by a single relaxation time. In shear, deviation from Newtonian behavior typically occurs for $\dot{\gamma} \geq \lambda_M^{-1}$. For entangled systems, shear thinning accompanied by normal stress differences, which may be much larger than shear stresses at a particular $\dot{\gamma}$, is typically observed. In certain systems, a shear stress plateau over a range of shear rates, $\dot{\gamma}_1 \leq \dot{\gamma} \leq \dot{\gamma}_2$, indicative of shear banding may be observed. In extension, extensional thickening and strain hardening are commonly observed in addition to flow-induced scission of the micelles which may lead to large

scale rupture in the fluid sample or flow instabilities.

Macroscale rheometry is typically confounded by the onset of flow instabilities which place a limit on the value of the maximum deformation rates which can be attained using macroscale devices. Hence, an alternative approach is necessary to impose deformation rates beyond this limit.

2.3 Microfluidic Rheometry

Microfluidic rheometry is a rheometric technique in which the stresses and strain rates associated with the flow of a fluid in a microscale geometry are recorded. This approach may be used to determine the high deformation rate ($10^4 < \dot{\gamma} < 10^6$ s^{-1}) rheology of many fluids and requires relatively small amounts of fluid when compared to other rheometric techniques, as described in Pipe *et al.* (2008).

2.3.1 Shear Flows

Typically studies in microfluidic shear rheometry have been in regard to flow in a straight, high aspect ratio rectangular duct of width, W, height, H and length, L, for which $W \ll H \ll L$. For such flows, the shear stress at any position along the width of the channel is known from first principles (see Appendix B) and the shear rate can be calculated from the velocity profile which is often measured with micro-particle image velocimetry (μ-PIV). Knowledge of the local shear rate and stress is then used to determine the steady shear viscosity. For shear thinning or shear banding solutions in pressure driven flow, a transition from a Newtonian, parabolic profile at low flow rates to a banded profile depicted in Figure 2.3.1, occurs when $Wi = \lambda_M \langle U \rangle / W \approx 1$.

Shear thinning polyethylene oxide solutions were studied by Degre *et al.* (2006) in a rectangular, polydimethylsiloxane (PDMS) microchannel. They demonstrated the viability of their system, having found good agreement between their measurements of viscosity from the flow in the microchannel and that measured with a conventional Couette rheometer. They also commented on the need for a more rigid

geometry to test highly viscous fluids. Guillot *et al.* (2006) also studied a worm-like CPyCl:NaSal:NaCl system flowing in glass and PDMS channels. They found good agreement between their viscosity measurements in the glass microchannel and from the rheometer for all shear rates examined. Good agreement for results obtained with PDMS channel were only obtained at high shear rates. Deviation in the low shear rate results were attributed to slip.

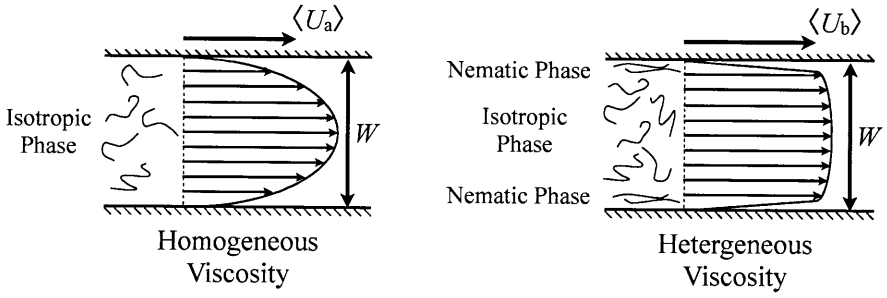

Figure 2.3.1: Schematics of a the velocity profile of a system with homogeneous viscosity field and that of shear banding system in Poiseuille flow. For the homogeneous case, the characteristic shear rate $\langle\dot{\gamma}\rangle_a = \langle U_a\rangle/W \ll \dot{\gamma}_1$, where $\langle U\rangle$ is the average velocity in the channel, W its width and λ_M is the fluid relaxation time. For the shear banding flow, $\dot{\gamma}_1 < \langle\dot{\gamma}\rangle_b = \langle U_b\rangle/W < \dot{\gamma}_2$.

Microfluidic rheometry is also unique in the study of complex fluids in that it may be exploited to probe the behavior of a system when the lengthscale of the flow geometry approaches the typical lengthscale (*e.g.* contour length, entanglement length) of the polymeric or micellar network. Flow in smallscale geometries also results in very steep stress gradients across devices, for which diffusion of stress may be important. In this regard, Masselon *et al.* (2008) studied systems of worm-like CPyCl:NaSal:NaCl and CTAB:$NaNO_3$ in a 1 mm x 200 μm glass channel and observed that the numerical value of the stress plateau varied with flow rate and was therefore dependent on more than just the local shear rate. They suggested that non-local (*i.e.* diffusive) effects were important in their systems. Conversely, Nghe *et al.* (2008), examined the same CTAB:$NaNO_3$ solution as that used by Masselon *et al.* (2008) in a 1 mm x 67 μm glass channel and observed a constant value for the stress

plateau, independent of flow rate. The measured plateau was in good agreement with that measured with a conventional rheometer and so they explicitly stated that there was no evidence for the importance of diffusion in their system. Nghe *et al.* (2008) acknowledged that their results were in contradiction to those of Masselon *et al.* (2008), but offered no explanation for the discrepancy. These disparate results may have been caused by the different aspect ratios of the channels, whose influence of the flow of worm-like micelles has been investigated by Nghe *et al.* (2009). They found that even for a channel with aspect ratio 16:1, the velocity field varied across the entire width and height of the channel, voiding the assumption of two dimensional flow necessary for the analyses of Masselon *et al.* (2008) and Nghe *et al.* (2008).

2.3.2 Extensional Flows

An introduction to microfluidic extensional rheometry is given in Pipe & McKinley (2008). For an internal extensional flow, the test fluid typically travels through a contraction or expansion such that the mean velocity of the fluid changes as it travels through the microfluidic device. Careful consideration must be given to the shape of the contraction in order to effect the desired extensional deformation. Much effort into studying flows of dilute flexible-chain solutions (*e.g.* polyethylene oxide (PEO) solutions in water) in planar-contractions has been undertaken by Rodd *et al.* (2005) and Rodd *et al.* (2007). These contractions were used to explore elastically-induced secondary flows and other instabilities. Additional work on entrance effects in flows of PEO solutions in microfluidic devices has been completed by Kang *et al.* (2005) and Kang *et al.* (2006). In these studies, large pressure drops in the entrance region were observed and attributed to large shear stresses at the walls of the channels. Additionally, the shape of the contraction, (*i.e.* planar, angled) was observed not to influence this pressure drop. Groisman & Quake (2004) studied the flow of a low weight percent polymer solution through a microfluidic rectifier, noting that elastic stresses induced by extensional and compressive deformations were responsible for a

high degree of anisotropy in the pressure drop due to the flow in the rectifier. The flow in a cross-slot geometry of the same worm-like CPyCl:NaSal and CTAB:NaSal solutions considered in this thesis was studied by Pathak & Hudson (2006) in one of the few papers on the extensional rheology of micellar systems in a microfluidic device. Their study focused primarily on flow-induced birefringence and is discussed in Section 2.4.

2.3.3 Summary of Microscale Flows

Microfluidic devices have been used to investigate the influence of non-local effects (*e.g.* stress diffusion) on the flow of micellar solutions and to observe the high deformation rate rheology of these system. To date, the body of scientific literature regarding flows of micellar solutions at the microscale is considerably smaller than that of macroscale flows and much experimental work in this area is warranted in order to gain greater insight into the non-linear rheology of these materials.

2.4 Flow-Induced Birefringence

Flow-induced birefringence is formally introduced in Chapter 3 and Appendix D. Birefringence measurements may be used to observe the degree of molecular alignment and stretching in a material (*i.e.* its conformation) and in certain cases these measurements may be related to the stress in the material with the semi-empirical *stress optical rule*, see Fuller (1995). According to this rule, the optical anisotropy in a material, Δn, is linearly proportional to its principal stress difference, $\Delta\sigma$, such that $\Delta n = C\Delta\sigma$, where C is the stress optical coefficient. Scientific papers in which birefringence measurements have been used to probe the molecular structure of surfactant systems and to test the validity of the stress optical rule for these systems are now plentiful in the literature.

Wunderlich *et al.* (1987) performed one of the earliest studies on the flow-induced birefringence of surfactant solutions using a tetradecyltrimethylammoniumsalicylate

(TTAS) system. They observed the dependence of birefringence on concentration, deformation rate and temperature. This study was followed by the work of Rehage & Hoffmann (1991) who studied the same 100:60 mM CPyCl:NaSal system that is considered in this thesis.

Shikata *et al.* (1994) studied CTAB:NaSal systems of various concentration ratios, obtaining, for weak (low) deformation rates, a single value of C that was independent of the concentration ratio. For strong (high) deformation rates, the stress optical rule was found to be invalid. Later, Decruppe *et al.* (1997) tested another CTAB system, with and without potassium bromide (KBr), finding agreement with the stress optical rule, independent of temperature, for the data points they considered.

Lerouge *et al.* (2000) studied a CTAB:$NaNO_3$ system for which the stress optical rule was found to hold at shear rates below that corresponding to the onset of the stress plateau at $\dot{\gamma}_1$, shown in Figure 2.4.1 (a). At higher rates, the authors observed a deviation from the predictions of the stress optical rule and experimental results, which they attributed to a deviation from Gaussian chain statistics for large deformation rates. A shear banding CTAB:KBr:D_2O system was also studied by Lerouge *et al.* (2004), who observed striations in the birefringence across the gap for lower shear rates coinciding with the stress plateau. At the higher shear rates but still coinciding with the stress plateau, three distinct birefringent bands shown in Figure 2.4.1 (b) were observed. This result was rationalized by the existence of a third band separating the highly aligned phase from the isotropic phase.

Decruppe & Ponton (2003) studied four solutions of 100 mM cetyltrimethylammonium chloride (CTAC) at varying NaSal concentrations, two of which exhibited a stress plateau, while the other two were shear thinning. A non-montonic variation in C with increasing NaSal concentration was observed. The authors also found that the stress optical rule failed at stresses on the order of the stress plateau for the shear banding fluids, and for stresses near the onset of shear thinning for the shear thinning fluids.

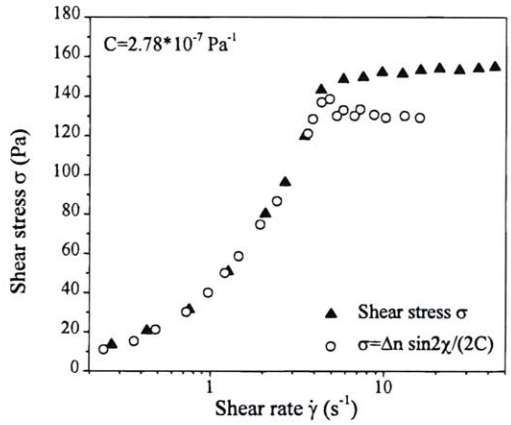

(a)

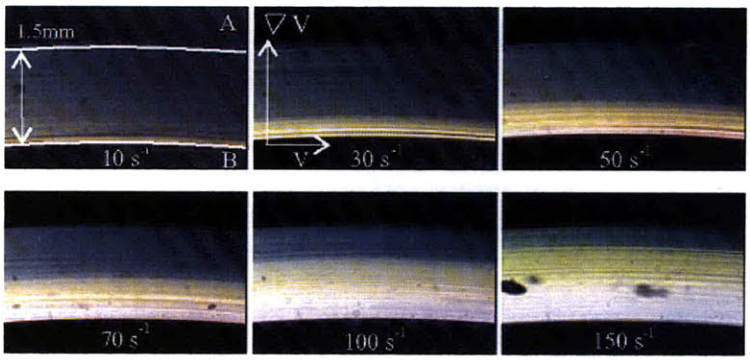

(b)

Figure 2.4.1: From Lerouge *et al.* (2000). (a) Comparison between measured shear stress and predictions from the stress optical rule. (b) From Lerouge *et al.* (2004). Birefringence of banded structure at increasing shear rates. The Couette cell is illuminated by with white light and placed between crossed polarizers. Stationary, outer wall labelled A and inner rotating wall labeled B.

Lee *et al.* (2005) examined a semidilute solution of 100:60 mM CPyCl:NaSal, claiming to have obtained the first point-wise measurements of birefringence of a shear banding worm-like micellar system across the width of a gap in a Couette cell geometry. The authors claimed that their observations of a change in sign of the birefringence between the low and high shear rate bands indicated the existence of two phases, suggesting that a shear-induced phase separation was an underlying cause of the banding behavior.

One of the few studies of birefringence of a worm-like micellar solution flowing in a microchannel is that of Pathak & Hudson (2006). In this work, measurements of flow-induced birefringence were coupled with velocimetry measurements to test the stress optical rule for extensional and shear flows in a 100:60 mM CPyCl:NaSal system and a 30:240 mM CTAB:NaSal system. For the extensional flows, the authors observed that the stress optical rule failed at flow rates for which a sharp birefringence band appeared, indicating high or nearly saturated molecular alignment with the flow. It was also found that the stress optical rule failed at a lower extensional Weissenberg number than corresponding shear Weissenberg number.

2.4.1 Summary of Flow-Induced Birefringence

In general, the flow-induced birefringence in micellar solutions has been observed to obey the stress optical rule, provided the fluid exhibited linear rheological behavior. For deformation rates above a certain value (*e.g.* $\dot{\gamma} \geq \dot{\gamma}_1$) the validity of the stress optical rule is not universal. Additionally, complex structures have been observed in banded flows revealing that the assumption that a birefringent band coincides with a high deformation rate band is also not universally valid.

In summary, measurements of birefringence may be used to gain insight into the state of conformation of a micellar system, but considerable care must be taken when attempting to relate material stresses to its optical anisotropy especially for shear banded flows or flows with considerable extensional characteristics.

Chapter 3

Experimental Methods

"In theory it works in practice."

– **Anon**

The development and refinement of reliable rheometric techniques for use in the measurement of the rheological properties of non-Newtonian fluids undergoing high-rate deformations is the main focus of this text. Nevertheless, it is fitting that suitable attention be given here, first, to the commonly employed experimental techniques for determining the rheological properties of complex fluids. To that end, the first portion of this chapter addresses the test fluids used in this study along with the conventional rheometric techniques for the characterization of the rheological characteristics of these fluids. The second portion of this chapter describes the materials, equipment and experimental techniques used to observe the high-rate deformation rheology of the test fluids, which is of primary interest in this work.

3.1 Rheological Characterization of Test Fluids

In this section, many of the most common types of rheological tests are described. Furthermore, two worm-like micellar solutions and their rheological behavior are considered.

3.1.1 Rheology and Rheometry

Rheology is the study of anything that flows or can be deformed, (Larson (1998)). Rheometry is act of quantifying the deformation of a material in order to determine the material properties of that material, (Macosko (1994)).

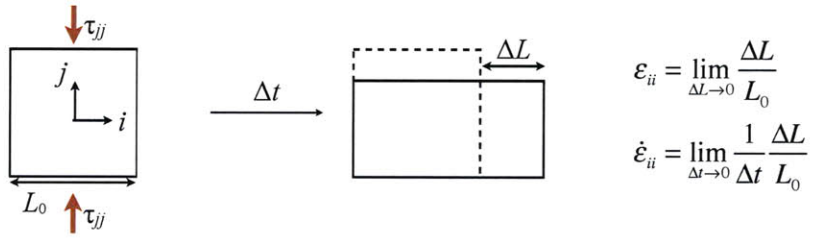

(a) Extensional Deformation.

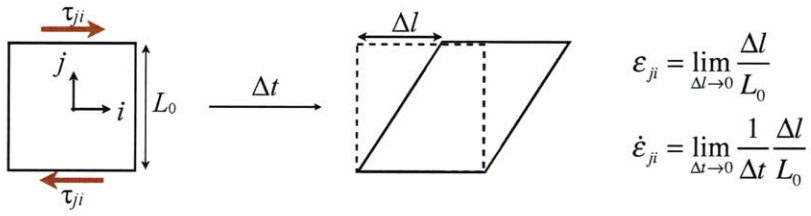

(b) Shear Deformation.

Figure 3.1.1: (a) A material undergoing an extensional deformation, ε_{ii} in time Δt. (b) A material undergoing a shear deformation, ε_{ji} in time Δt.

As such, the purpose of most any rheological test is to determine the material response of a sample of interest to an imposed deformation, deformation rate or stress, or a combination of these three. A deformation or strain, is a *dimensionless* quantity and is equal to the ratio of a change in length to an initial or reference length. A deformation is commonly denoted by the symbol ε_{ij} defined in Figure 3.1.1. A deformation or strain rate, is typically a quantity, having units of *inverse time* or *frequency*, and it is equal to the ratio of a rate of change in length to an initial or reference length. A deformation rate is commonly denoted by the symbol $\dot{\varepsilon}_{ij}$ again defined in Figure 3.1.1. A stress is a quantity having units of *force per unit area* and is commonly denoted by the symbol τ_{ij} depicted in Figure 3.1.1. The

symbols for all three quantities include the subscript ij since in all cases there is an associated directionality of the imposed deformation, deformation rate and force, and a directionality of the surface normal vector over which the imposed quantity acts. In this case, i designates the axis coincident with the outward surface normal vector and j designates the direction along which the deformation or stress is imposed. If $i = j$, the material undergoes an *extensional* deformation with an imposed *normal* stress. Conversely, if $i \neq j$, the material undergoes a *shear* deformation with an imposed *shear* stress.

3.1.2 Rheological Tests

The rheometer[1] is the quintessential rheometric device which may be used to measure both the viscous as well as elastic properties of a test sample. Common types of rheometers and tests are described below.

Rotational Rheometer

A rotational, or torsional rheometer is a device which may be used to determine the rheological behavior of a test sample undergoing a shear deformation[2], $\dot{\gamma}_{ij}$. Shear deformations are commonly encountered in flows in a pipe or in coating processes. The archetypal rotational rheometer consists of a stationary plate and an axially symmetric fixture, illustrated in Figure 3.1.2, separated by some distance, H, which may vary with radial position. The test material is then positioned between the fixture and the plate, and the fixture is rotated at either a constant angular velocity Ω or with a constant imposed torque, such that the shear rate and any r and z is $\dot{\gamma}_{z\theta} \equiv \frac{dv_\theta}{dz}$, and the resultant torque or angular velocity, respectively, is recorded. Any axial loads exerted by the material on the fixture and plate may also be recorded. These measured quantities are then related to the material functions of the test sample

[1] A viscometer is also a device which may be used to measure material properties, however, strictly speaking, a viscometer is only capable of measuring viscosity and typically only under a single shear rate.

(*e.g.* viscosity) through appropriate mathematical relations presented, for example, in Bird *et al.* (1987) and Macosko (1994).

The two most commonly employed fixtures to measure material properties with a rotational viscometer are the cone-and-plate and the plate-plate geometries, portrayed in Figure 3.1.2, (see Macosko (1994) for additional details). A cone-and-plate geometry, depicted in Figure 3.1.2 (a), consists of a flat bottom plate and an upper cone, whose angle with respect to the flat bottom plate is ϑ. For small ϑ, the gap height may be shown to increase linearly with radial position, such that $H = r\tan\vartheta \approx r\vartheta$, where H is the gap height at some radial position r. The shear rate imposed by a cone-and-plate is $\dot{\gamma}_{z\theta} = \Omega/\vartheta$ and it is therefore invariant to radial position. A plate-plate fixture consists of two parallel plates separated by some user-selected gap height, H, which is constant for all radial positions. The shear rate for a plate-plate fixture is defined $\dot{\gamma}_{z\theta} = r\Omega/H$, and it varies linearly with radial position.

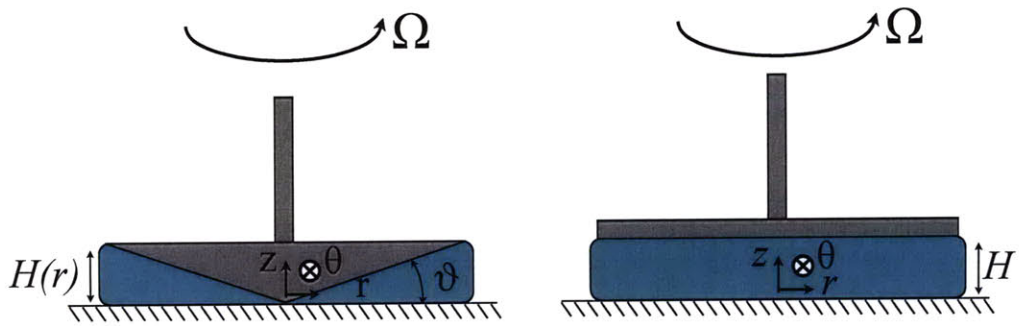

(a) Cone-and-Plate Geometry. (b) Plate-Plate Geometry.

Figure 3.1.2: Two commonly used geometries to measure viscosity on a rheometer.

Small Amplitude Oscillatory Shear

A small amplitude oscillatory shear (SAOS)[3] test may be used to determine the linear viscoelastic properties of a material of interest. In this test, a sinusoidally, time-varying shear strain or shear stress is imposed on a material, such that the

[2]For describing a shear strain and shear strain rate, is it convention to use the notations γ_{ij} and $\dot{\gamma}_{ij}$, respectively, instead of ε_{ij} and $\dot{\varepsilon}_{ij}$.

shear strain of the material, γ, follows the relation $\gamma(t) = \gamma_0 \sin \omega t$, where γ_0 is the applied shear strain amplitude, ω is the frequency of the deformation and t is time. The anticipated shear stress, τ, of the material associated with the imposed deformation is also sinusoidal and time-varying, and it obeys the relation $\tau(t) = G'(\omega)\gamma_0 \sin(\omega t) + G''(\omega)\gamma_0 \cos(\omega t)$. G' and G'' are defined, respectively, as the storage modulus and loss modulus, and evidently they may depend on the frequency of the applied deformation. For a particular frequency, ω, G' characterizes the elasticity of the material, or alternatively, G' may be thought to characterize the ability of the material to *store* the energy required to deform it. Conversely, G'' characterizes the amount of energy *loss* associated with the deformation through viscous dissipation.

Arguably the simplest model for linear viscoelastic behavior is the Maxwell model (see Appendix A). A mechanical analogue consists of a linear spring having modulus G_0, and a linear dashpot having damping coefficient $\eta_0 = G_0 \lambda_M$, where λ_M is the relaxation time of the material and is the characteristic time-scale over which a stress in the material grows or decays. For a material which may be described by the Maxwell model, the storage and loss moduli are

$$G'(\omega) = G_0 \left(\frac{(\lambda_M \omega)^2}{1 + (\lambda_M \omega)^2} \right) \tag{3.1.1}$$

$$G''(\omega) = G_0 \left(\frac{\lambda_M \omega}{1 + (\lambda_M \omega)^2} \right) \tag{3.1.2}$$

Clearly, when $\lambda_M \omega = 1$, $G' = G''$ and at this frequency of the applied deformation, the elastic and viscous properties of the material are of equal relative importance. For such materials that exhibit Maxwellian behavior, this cross-over frequency, where $\omega = \lambda_M^{-1}$, may be readily identified from measurements with a rheometer and exploited to determine the relaxation time of the material.

[3]The use of the phrase *small amplitude*, as opposed to *large amplitude*, indicates that the imposed shear strain amplitude, γ_0, is small enough such that the test sample exhibits linear behavior and all of its material functions are independent of γ_0. For an introduction to non-linear viscoelasticity see Dealy & Wissbrun (1990).

Steady Shear: Wall Driven

A steady shear test may be used to measure the viscosity of a material as well as the shear-induced normal stress difference the material may exhibit. In making any such measurement with a rotational rheometer, one aims to relate a measured or imposed stress, $\tau_{z\theta}$, to a measured or imposed shear rate $\dot{\gamma}_{z\theta}$. The coefficient of proportionality is the aforementioned viscosity, η, which may itself depend on shear rate, such that $\tau_{z\theta} = \eta(\dot{\gamma}_{z\theta})\dot{\gamma}_{z\theta}$. In rheology, the resultant plot of the measured shear viscosity against shear rate is called a *flow curve.*

In the case of a rotational rheometer, a linear velocity profile in the material is assumed based on the kinematics of the geometry, such that $v_\theta = r\Omega z/H(r)$. This kinematically driven flow is called *Couette* flow. In order to determine applied stress, $\tau_{z\theta}$, it is necessary to relate the measured torque, Γ, applied on the sample by the rheometer to the applied stress. The measured torque is the integral of the product of the applied force, $2\pi\eta(\dot{\gamma}_{z\theta})\dot{\gamma}_{z\theta}rdr$, and radial position, r, from $r = 0$ to $r = R$, where R is the radius of the fixture.

$$\Gamma = 2\pi \int_0^R \eta(\dot{\gamma}_{z\theta})\dot{\gamma}_{z\theta}r^2 dr \tag{3.1.3}$$

In the limit of small shear rates, all fluids exhibit a constant viscosity known as the *zero-shear-rate viscosity*, η_0. It is only at deformation rates which are roughly equal to or greater than the inverse of the longest relaxation time of the fluid that the viscosity may deviate from the zero-shear-rate value, corresponding to a *non-Newtonian* response. In addition to a viscosity, most non-Newtonian fluids also exhibit a non-zero first normal stress difference, $N_1 \equiv \tau_{\theta\theta} - \tau_{zz}$, and possibly a second normal stress difference, $N_2 \equiv \tau_{zz} - \tau_{rr}$. These stress difference are manifestations of shear-induced tension in the molecules as described in Bird *et al.* (1987). These elastic stresses are characterized by material functions called the first and second normal stress coefficients, Ψ_1 and Ψ_2 respectively, such that $N_1 = \Psi_1(\dot{\gamma}_{z\theta})\dot{\gamma}_{z\theta}^2$ and $N_2 = \Psi_2(\dot{\gamma}_{z\theta})\dot{\gamma}_{z\theta}^2$. As with viscosity, both Ψ_1 and Ψ_2 may depend on imposed shear rate. The first normal

stress coefficient may be measured for a cone and plate if the rheometer is equipped with an axial force transducer. Measurement of the second normal stress coefficient is considered in Macosko (1994).

Steady Shear: Pressure Driven

A capillary rheometer is another device which may be used to determine the viscosity of a material. This device consists of either a cylindrical or high aspect ratio, rectangular duct. The test material is forced through the capillary at either a constant volumetric flow rate, Q, or a constant imposed pressure gradient, dP/dx. Such a pressure driven flow is called *Poiseuille* flow, or *Hagen-Poiseuille* flow if the flow is in a cylindrical duct.

One might consider the use of a capillary rheometer to determine the inertia-free, rheological behavior of a material, especially at high deformation rates as discussed in Pipe *et al.* (2008), which would be unattainable with a rotational rheometer due to the onset of turbulence, flow instabilities caused by the large centrifugal acceleration associated with high rotation rates or elastic instabilities in the fluid at high shear rates.

As in the case of the rotational rheometer, the viscosity of a material may be measured with a capillary rheometer if the applied stress at the wall of the capillary duct, τ_{wall}, can be suitably related to the imposed deformation rate of the material at the wall, $\dot{\gamma}_{wall}$. The derivation of this relationship, known as the Weissenberg-Rabinowitsch-Mooney Correction, for flow in a high aspect ratio capillary duct is given in Appendix B, and it can be written in the form

$$\dot{\gamma}_{wall} = \frac{\dot{\gamma}_N}{3}\left(2 + \frac{d\ln Q}{d\ln \tau_{wall}}\right) \tag{3.1.4}$$

where $\dot{\gamma}_N$ is the wall shear rate of a Newtonian fluid corresponding to the volumetric flow rate, Q, of the fluid through the capillary. It is shown in Appendix B, that $\dot{\gamma}_N = 6Q/HW^2$, with H and W being the height and width of the channel, respectively,

and ($H \gg W$). Furthermore, the imposed or measured pressure drop, ΔP, across the capillary duct of length, L, may be related to the wall shear stress by the relation $\tau_{wall} = \Delta PW/2L$. This result is true in the limit of $H \gg W$, and in that case it is independent of the material.

Eq. 3.1.4 may be used to determine the viscosity of a material as long as the no-slip condition is experimentally realized. In order to apply Eq. 3.1.4, one must measure the wall shear stress, τ_{wall}, at multiple flow rates, Q, to evaluate a discretized form of the differential logarithmic term in Eq. 3.1.4. Evidently, for a Newtonian fluid, this logarithmic term is unity for all flow rates.

The high shear rate rheological behavior of the fluids tested in this study was measured with the Viscometer/Rheometer-on-a-Chip © (VROC), (RheoSense Inc.). VROC is a high aspect ratio, rectangular capillary rheometer containing four pressure transducers positioned along the length of the capillary. The device may be used to measure the transient as well as steady rheological behavior of Newtonian and many non-Newtonian fluids in shear. The dimensions and features of VROC are listed in Table 3.1.1. A description of this system is offered in Pipe *et al.* (2008). The channel is fitted with four inline, 800 x 800 μm^2 microelectromechanical systems (MEMS) along its centerline which measure the local pressure. The MEMS sensor are positioned at distances from the entrance of the channel given in Figure 3.1.3. Previous measurements of the channel roughness and profile obtained with a mechanical surface profilometer are reported in Pipe *et al.* (2008), who found variations in channel depth of less than 1% the total depth. Additional measurements of surface asperities were obtained using a Zygo optical interferometer, in which the surface asperities in 180 μm x 130 μm sample areas at varying postions in the channel were found to be on the order of 10 nm. A sample profile is given in Figure 3.1.4.

Extensional Rheometry

An extensional rheometer is a device which may be used to determine the rheological behavior of a test sample undergoing an extensional deformation, $\dot{\varepsilon}_{ii}$. Extensional

Table 3.1.1: Dimensions and properties of VROC MEMS-based devices used in this study.

Channel ID	Width W [μm]	Height H [mm]	Length L [mm]	Maximum P [kPa]
6V10C5100016	50.7	2.83	12.65	40
8VC05100072	51.2	3.308	8.8	125
9VD04100059	40.2	3.2	11	1000

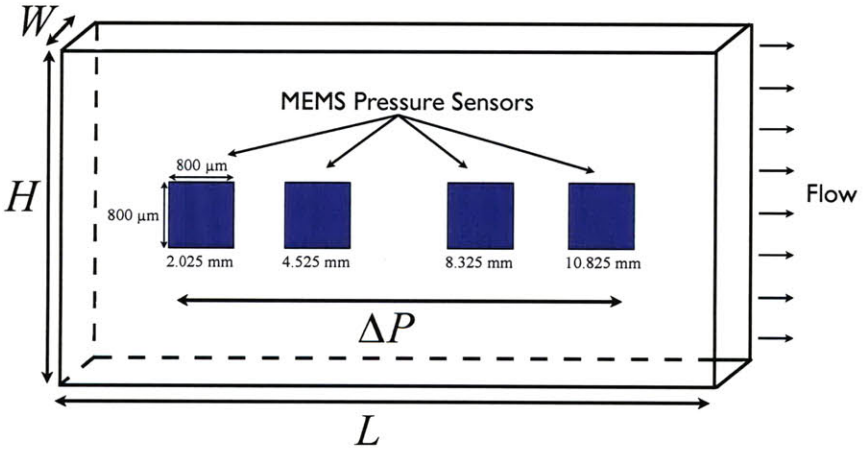

Figure 3.1.3: Schematic diagram of the VROC rectangular channel. Four MEMS pressure sensors are flush mounted along the centerline of the channel with positions given with respect to the channel entrance.

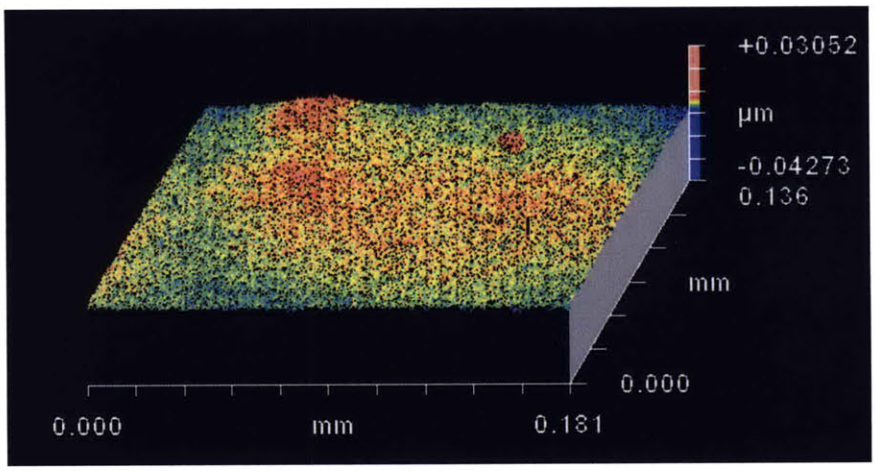

Figure 3.1.4: Surface asperity plot of a 180 μm x 130 μm sampling area along the side wall of the VROC rectangular chip obtained with a Zygo optical interferometer, 20x objective.

deformations are commonly encountered in flows through a nozzle contraction and in extrusion processes. The measurement of extensional properties of a material is generally a non-trivial task, because it is very difficult to design a device which can maintain a constant and homogeneous extension rate, while imposing deformations in the material for which, at all times, the influence of gravity and fluid inertia are small compared to the action of viscosity and elasticity.

The extensional viscosity, η_E, is the coefficient of proportionality between an imposed extensional strain rate, $\dot{\varepsilon}_{ii}$, and a imposed normal stress difference, $\tau_{ii} - \tau_{jj}$, where the extensional viscosity is defined $\eta_E = (\tau_{ii} - \tau_{jj})/\dot{\varepsilon}_{ii}$. The ratio of the extensional viscosity to the shear viscosity is called the Trouton ratio. For a Newtonian fluid in a uniaxial, extensional deformation Trouton (1906) showed that this ratio is equal to three. Because of the different kinematics, the Trouton ratio of a Newtonian fluid undergoing a planar, extensional deformation is four.

Transient Extensional Rheometry using Capillary Thinning

The Capillary Breakup Extensional Rheometer (CaBER) is a device which may be used to apply a near step-extensional strain to a test sample such that the resulting

extensional thinning of the sample due to capillary action can be recorded. In this test, a fluid sample is loaded between two concentric, circular plates having diameter a_0, as depicted in Figure 3.1.5. A rapid step-extensional strain is then applied to the sample, occurring on the order of 50 ms. The subsequent transient evolution of the filament diameter is measured by a laser micrometer.

In general, at times only shortly after the application of the step strain, the thinning process is governed by an interplay between fluid inertia, viscosity and capillarity. At longer times, when the aspect ratio of the filament length to diameter has become large, for a Newtonian fluid, the thinning process is governed by a balance between viscosity and capillarity. For a non-Newtonian fluid, however, elasticity may also be important as the filament thins, as discussed by McKinley (2005).

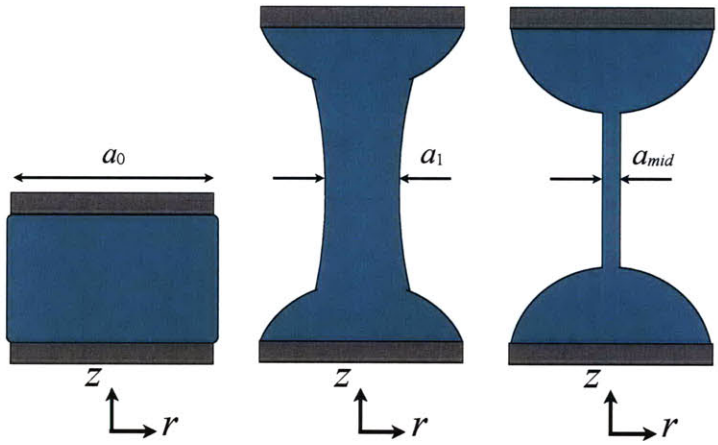

Figure 3.1.5: Three stages of a typical CaBER test. (Left) Unstrained fluid sample of diameter, a_0. (Center) Fluid sample of diameter, a_1, immediately after cessation of applied extensional strain. (Right) High aspect ratio, thinning filament having time varying diameter, a_{mid}.

Once the filament is of a high aspect ratio, the lubrication approximation may be applied to relate the experimentally measured thinning rate of the filament diameter at its mid-section to the instantaneous extension rate of the filament. In the absence of azimuthal velocity, the continuity equation for solenoidal flow in cylindrical coordinates is

$$\frac{1}{r}\frac{\partial}{\partial r}(rv_r) + \frac{\partial}{\partial z}v_z = 0 \tag{3.1.5}$$

Evidently, $\frac{\partial}{\partial z}v_z \equiv \dot{\varepsilon}_{zz}$ and if the magnitude of the radial velocity may be assumed to increase linearly with radial position then $v_r = \frac{da_{mid}}{dt}\frac{r}{a_{mid}}$ where a_{mid} is the diameter of the filament at an instant in time, then Eq. 3.1.5 reduces to

$$\dot{\varepsilon}_{zz} = -\frac{2}{a_{mid}}\frac{da_{mid}}{dt} \tag{3.1.6}$$

This result may also be obtained, by noting that, as pointed out by Anna & McKinley (2001), $\varepsilon_{zz} = 2\ln(a_0/a_{mid})$, which, when differentiated with respect to time yields Eq. 3.1.6.

The normal stress difference, $\tau_{zz} - \tau_{rr}$, in the filament may be determined by noting that because the radius of curvature of the filament is small compared to the radius of curvature of the fluid reservoirs above and below the filament depicted in Figure 3.1.5, the Laplace pressure in the reservoirs is negligible compared to that in the filament, and as such

$$\tau_{zz} - \tau_{rr} = \frac{2\sigma}{a_{mid}} \tag{3.1.7}$$

where σ is the surface tension of the fluid. Clearly the influence of hydrostatic pressure is eliminated in this analysis.

The extensional viscosity, η_E, of the test fluid is simply the quotient of Eq. 3.1.7 and Eq. 3.1.6, whereby

$$\eta_E = -\frac{\sigma}{\frac{da_{mid}}{dt}} \tag{3.1.8}$$

For a Newtonian fluid, η_E is constant and accordingly the filament diameter, a_{mid} decreases linearly with time, such that

$$\frac{a_{mid}}{a_0} = 1 - \frac{t}{t_{vc}} \tag{3.1.9}$$

where t_{vc} is the characteristic visco-capillary time and is given by Papageorgiou (1995) to be $t_{vc} = 12(1+\beta)a_0\eta_0/\sigma$, where η_0 is the Newtonian shear viscosity of the fluid. β is a constant which determines the particular similarity solution of the thinning behavior, and may be taken to be $\beta = 0.175$ for CaBER. The analysis for a non-Newtonian fluid, however, is not necessarily as simple, since the extensional viscosity may depend on extension rate. In the case where viscous effects are negligible and the thinning process is governed by elasticity and capillarity, Entov & Hinch (1997) determined an expression for the time evolution of the filament diameter using a multi-mode FENE model.

$$\frac{a_{mid}}{a_1} = \left(\frac{\eta_p a_1}{2\lambda_{ext}\sigma}\right)^{1/3} e^{-t/3\lambda_{ext}} \tag{3.1.10}$$

Where a_1 is the midpoint diameter of the filament immediately after the application of the step strain is complete, $\eta_p = \eta_0 - \eta_s$ is the effective polymeric viscosity, and λ_{ext} is the longest characteristic relaxation time of the fluid for this extensional flow. Accordingly, a highly elastic filament thins exponentially in time with a time constant, λ_{ext}, which may be identified experimentally with the CaBER instrument.

Extensional Deformations: Pressure Driven

In the same way that the shear viscosity of a material can be measured with a capillary rheometer, so too can the extensional viscosity of a material, in principle, be measured with an analogous device. This experimental approach lends itself well to obtaining large extension rates, which would be difficult to obtain using other macroscale devices. This form of extensional rheometry, however, is still in its developmental stages, and due to the complex interplay between viscosity and elasticity for such flows, experimental results obtained with this approach are generally not as amenable to simple analysis as are the results of other approaches. In recent work by Wang *et al.* (2010), however, an attempt has been made to decouple the viscous and elastic stresses for flow of a foaming-grade polystyrene fluid in a hyperbolic

contraction.

In this study, the flow in hyperbolic contractions is considered, building on the work of Oliveira *et al.* (2007). The use of a hyperbolic geometry, depicted in Figure 3.1.6, to study extensional deformations was proposed by James (1991). For an antisymmetric contraction depicted in Figure 3.1.6 (b), having length, l_c, height, h_c, upstream width, w_u, width at the contraction exit, w_c, the width, w, at any x obeys the relation

$$w(x) = \frac{K}{s+x} \tag{3.1.11}$$

where $s = l_c w_c/(w_u - w_c)$ and $K = s w_u$. For a given volumetric flow rate, Q, the extension rate along the centerline of the contraction, $\dot{\varepsilon}$, may be approximated as the difference between the average velocity at the outlet of the contraction and the average velocity at its inlet divided by the length, l_c, over which the change in velocity occurs.

$$\dot{\varepsilon} = \frac{Q}{l_c h_c}\left(\frac{1}{w_c} - \frac{1}{w_u}\right) \tag{3.1.12}$$

The maximum Hencky strain, ε_H, of a material element flowing through the contraction occurs at its exit and is

$$\varepsilon_H = \ln\left(\frac{w_u}{w_c}\right) \tag{3.1.13}$$

Finally, if the extra pressure drop, ΔP, across the contraction can be measured, the extensional viscosity, η_E, of the fluid may be determined with the result derived in Appendix C.

$$\eta_E = \frac{Q\Delta P}{V_c \dot{\varepsilon}^2} \tag{3.1.14}$$

where V_c is the volume of the contraction, given by $V_c = K h_c \ln[(s+l_c)/s]$. For the EVROC contractions, $\varepsilon_H = 1.9$.

Table 3.1.2: Dimensions and properties of EVROC used in this study. For the antisymmetric configuration, $s = 140.4$ μm, $K = 4.072$ x 10^5 μm^2, and $V_c = 1.549$ x 10^8 μm^3.

Channel ID	Height h_c [μm]	Width w_u [μm]	Width w_c [μm]	Length l_c [μm]	Maximum P [kPa]	Misc.
7VBE1000036	200	2900	433	800	40	Symmetric
7VBE1000044	200	2900	433	800	40	Antisymmetric

The high extension rate rheological behavior of the fluids tested in this study was measured with the Extensional Viscometer/Rheometer-on-a-Chip © (EVROC), (RheoSense Inc.). The EVROC is a microfluidic device, which is fitted with MEMS pressure transducers that are positioned in the same locations as those in the VROC device. The symmetric contraction is positioned between the middle two transducers, such that the transducers are approximately 1 mm upstream and downstream of the contraction inlet and outlet. For the antisymmetric contraction, the upstream transducer lies roughly 1 mm before the contraction inlet, and the downstream transducer 1.8 mm beyond the outlet. The device may be used to measure the rheological behavior of Newtonian and many non-Newtonian fluids in extension. The dimensions and features of EVROC are listed in Table 3.1.1.

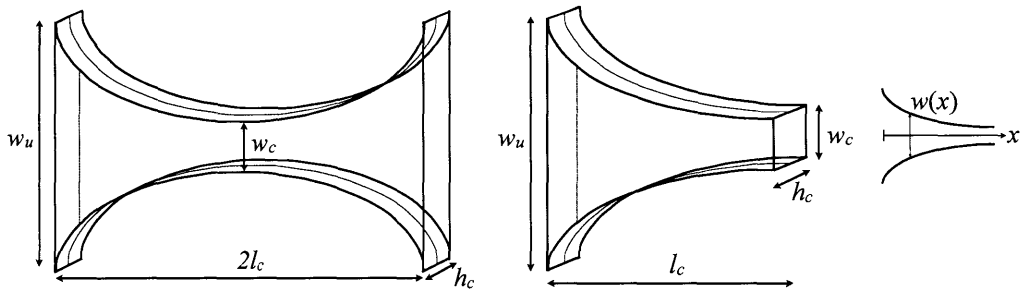

(a) EVROC Symmetric Channel (b) EVROC Antisymmetric Channel

Figure 3.1.6: Schematics of the EVROC contraction channels.

3.1.3 Test Fluid Formulations and Rheological Properties

Two surfactant solutions have been examined in the experiments addressed in this thesis. The first solution consists of 100 mM cetylpyridinium chloride (CPyCl) (Alfa Aesar) and 60 mM sodium salicylate (NaSal) (Alfa Aesar) in de-ionized water. A solution with this composition was discussed at length by Rehage & Hoffmann (1991). The second solution consists of 30 mM cetyltrimethylammonium bromide (CTAB) (Sigma Aldrich) and 240 mM NaSal (Alfa Aesar) in de-ionized water. Similar solutions were studied by Shikata *et al.* (1994). The surfactant and counter ion concentration ratios were selected because it is known that for these ratios the molecules form worm-like micelles.

The solutions were allowed to equilibrate at room temperature, in a cool, dry and unlighted environment for many weeks from the time of their preparation before any experiments were conducted. These two systems exhibit distinctly different rheological behavior under shear. Both solutions are strongly shear thinning, but the CPyCl system exhibits shear banding, a phenomenon which has been described elsewhere in this thesis, across many decades of shear rates. Furthermore, these micellar solutions possess large stress optical coefficients, C, which made them ideal for the birefringence measurements explained below. In this study, the literature values of the stress optical coefficient for each solution were assumed valid. Rehage & Hoffmann (1991) have reported the stress optical coefficient for the CPyCl system as -2.3 x 10^{-7} Pa^{-1} at 20 ^{o}C. Shikata *et al.* (1994) listed the stress optical coefficient of the CTAB system as -3.1 x 10^{-7} Pa^{-1} at room temperature (~25 ^{o}C). Both of these solutions were also studied by Pathak & Hudson (2006), who considered experiments similar to those described in this theses.

Linear Viscoelasticity

The linear viscoelastic response of both micellar solutions at 22 ^{o}C was measured with an AR-G2 stress-controlled rheometer (TA Instruments). The resulting data from the

SAOS test have been fitted with a single mode Maxwell model, following the method of Turner & Cates (1991), according to which, a least squares fit of a single mode Maxwell model was fitted only to the moduli at frequencies equal to or less than the frequency at which G'' reaches its maximum. From this fit, values of λ_M, η_0 and G_0 in Table 3.1.3 were determined. Both fluids may be seen to have Maxwell relaxation times given in Eq. 3.1.1 and Eq. 3.1.2, on the order of one second. In addition to being the respective Maxwell relaxation time for these micellar solutions, this value of λ_M corresponds also to the value in Eq. 2.2.2.

From the work of Turner & Cates (1991), it was also possible to estimate the breaking time, λ_{break} for each system. On the Cole-Cole plots in Figure 3.1.8, a line of slope -1 was fit to the storage and loss moduli for which the slope between adjacent points was -1 ± 0.5. The intersection of this line with the abscissa corresponds to an asymptotic plateau modulus, $G_{plateau}$. The storage and loss moduli were then non-dimensionalized by $G_{plateau}$, whereby $\mu'(\omega) = G'(\omega)/G_{plateau}$ and $\mu''(\omega) = G''(\omega)/G_{plateau}$. The diameter of the of the fitted semi-circle in the non-dimensionalized Cole-Cole plots were then related to the breaking time, λ_{break} according to the theory of Turner & Cates (1991). The reptation time, λ_{rep} was then obtained from Eq. 2.2.2. These timescales are listed in Table 3.1.3.

At high frequencies, $\omega \gg \lambda_M^{-1}$, both fluids exhibit a minimum in G'', indicating the importance of the breathing and Rouse relaxation modes discussed in Section 2.2.2.

Estimates of the microstructural features may be made using the theory found in Doi & Edwards (1986). The correlation distance, ξ, being the absolute distance between entanglement points, in an entangled network follows the relation

$$\xi \simeq \left(\frac{k_B T}{G_0}\right)^{\frac{1}{3}} \tag{3.1.15}$$

where k_B is the Boltzmann constant[4], T is absolute temperature and G_0 is the plateau modulus. Values of ξ for both micellar systems in this study are listed in Table 3.1.3. Furthermore, the entanglement strand length, l_e, being the arc length along the mi-

celle between two adjacent entanglement points may be estimated as

$$l_e \simeq \xi^{5/3}/l_{persist}^{2/3} \tag{3.1.16}$$

where $l_{persist}$ is the persistent length, which may interpreted as the lengthscale on which the micelle acts as a rigid rod. This quantity can be determined from measurements of optical anisotropy in a material as outlined by Shikata *et al.* (1994).

An estimate of the average contour length, $\langle l \rangle$, being the arc length of a fully extended micelle, may be determined according to the work of Granek & Cates (1992). In the case of $\lambda_{break} \gg \lambda_{Rouse}$, where λ_{Rouse} is the Rouse relaxation time of the micelle, a lower bound for $\frac{l_e}{\langle l \rangle}$ is

$$\frac{l_e}{\langle l \rangle} \simeq \frac{G''_{min}}{G_0} \tag{3.1.17}$$

Here, l_e and $\langle l \rangle$ have been determined based on reasonable assumptions for $l_{persist}$, all of which are presented in Table 3.1.3.

Shear Rheology

The steady shear rheology of these systems at low to moderate shear rates was measured on an advanced rheometric expansion system (ARES) strain-controlled rheometer (TA Instruments, New Castle DE, USA). All tests were conducted at 22 °C. Multiple tests of each solution were conducted to ensure the reliability of the rheological measurements. The rheological properties of these solutions have been summarized in Table 3.1.3.

The steady shear data is presented in Figure 3.1.9. In the limit of low shear rates, both fluids exhibit Newtonian behavior, with zero-shear-rate viscosities listed in Table 3.1.3. For shear rates of the order $\dot{\gamma} \simeq \lambda_M^{-1}$ or greater, evidently both systems exhibit a pronounced deviation from Newtonian behavior. The dependence of the viscosity of both fluids on shear stress, in the shear thinning regime, may be

[4] $k_B = 1.3806503 \times 10^{-23}$ J/K

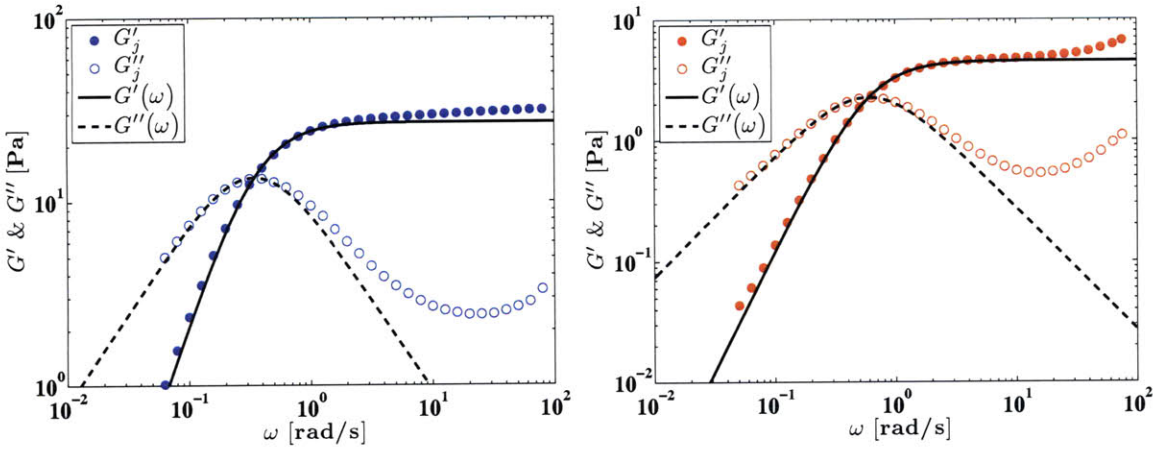

(a) CPyCl:NaSal 100:60 mM.

(b) CTAB:NaSal 30:240 mM.

Figure 3.1.7: Storage and loss moduli of 100:60 mM CPyCl:NaSal and 30:240 mM CTAB:NaSal solutions in SAOS at 22 ^{o}C. The notations G'_j and G''_j denote the discretely measured moduli at ω_j, following the notation in Bird *et al.* (1987). The solid and dashed lines are the resultant fit of a single mode Maxwell model with λ_M, η_0 and G_0 given in Table 3.1.3.

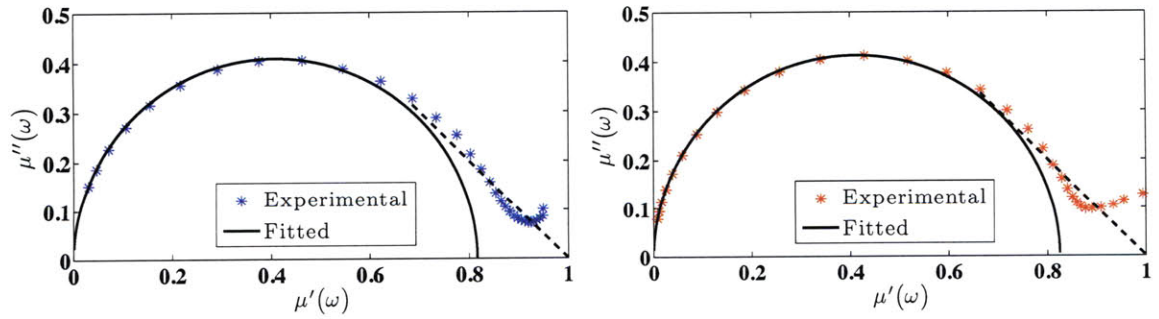

(a) CPyCl:NaSal 100:60 mM.

(b) CTAB:NaSal 30:240 mM.

Figure 3.1.8: Non-dimensionalized Cole-Cole plots of 100:60 mM CPyCl:NaSal and 30:240 mM CTAB:NaSal solutions in SAOS at 22 ^{o}C. $\mu'(\omega) = G'(\omega)/G_{plateau}$ and $\mu''(\omega) = G''(\omega)/G_{plateau}$. As prescribed by Turner & Cates (1991), the dashed line of slope -1 denotes the asymptotic behavior of G' and G'' as $\omega \to \infty$, provided only reptative processes are prevalent at high frequency.

fit with the Ellis model, given in Bird *et al.* (1987), of the form

$$\eta = \frac{\eta_0}{1 + \left(\frac{\tau}{\tau_{1/2}}\right)^{\alpha-1}} \tag{3.1.18}$$

where η_0 is the zero-shear-rate viscosity as usual, $\tau_{1/2}$ is the value of the shear stress at which the viscosity is equal to half its zero-shear-rate value, and α is a fitting coefficient[5]as listed for both fluids in Table 3.1.3. Fits of this model to the flow curve of each fluid are shown in Figure 3.1.10. It is also apparent from Figure 3.1.9, that in the regime of rate dependent viscosity, a constant shear stress may be applied to deform the CPyCl system across nearly two orders of magnitude of shear rates. Such a *stress plateau* is the hallmark of a shear banding solution as discussed in Cates & Fielding (2006) and Rothstein (2009). In this regime, the viscosity of the CPyCl system is also essentially inversely proportional to shear rate. For the CPyCl system, shear banding occurs at shear rates above approximately $\dot{\gamma} \approx \lambda_M^{-1} \approx 0.25$ s^{-1}. These results for the CPyCl system are very similar to those of Lee *et al.* (2005). For the shear rates measured with the ARES, the CTAB system may be seen to exhibit a markedly shear thinning, $\eta \sim \dot{\gamma}^{-0.6}$, behavior for measured shear rates greater than 0.5 s^{-1}.

At shear rates greater than $\dot{\gamma} \approx 3\lambda_M^{-1} \approx 1$ s^{-1}, both fluids exhibit remarkably similar first normal stress differences, N_1, as measured by the ARES rheometer. This normal stress difference for both fluids may be seen to increase superlinearly with shear rate, and for the lowest shear rates at which N_1 was measured, $N_1 \sim \dot{\gamma}^2$, which is depicted by the black line in Figure 3.1.9 (a). The quadratic scaling is in agreement with the predictions of the upper convected Maxwell model, see Bird *et al.* (1987), for which the first normal stress coefficient, Ψ_1, is predicted to be $\Psi_1 = 2\eta_0\lambda_M$. This Ψ_1 is, however, a substantial over estimate of the actual first normal stress coefficient, since, for the shear rates at which N_1 was measured, the viscosity of neither fluid is

[5]The Ellis model reduces to the simpler Power Law model, $\eta = m\dot{\gamma}^{n-1}$, (Bird *et al.* (1987)), in the limit of $\tau \gg \tau_{1/2}$, for which $\alpha = n^{-1}$.

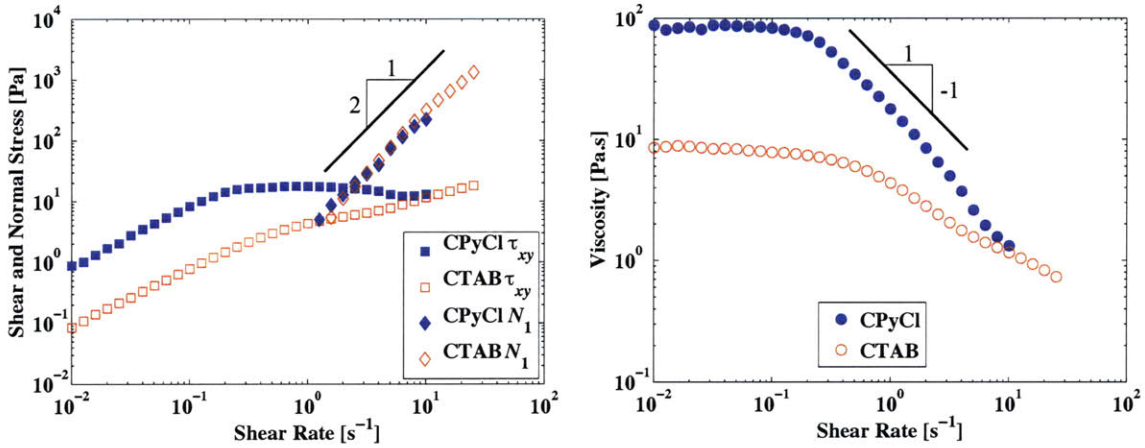

(a) Shear Stress and First Normal Stress Difference.

(b) Shear Viscosity.

Figure 3.1.9: Steady shear rheology of 100:60 mM CPyCl:NaSal and 30:240 mM CTAB:NaSal solutions at 22 ^{o}C. The solid black line of slope 2 indicates quadratic proportionality with shear rate. The solid black line of slope -1 indicates an inverse proportionality in viscosity with shear rate.

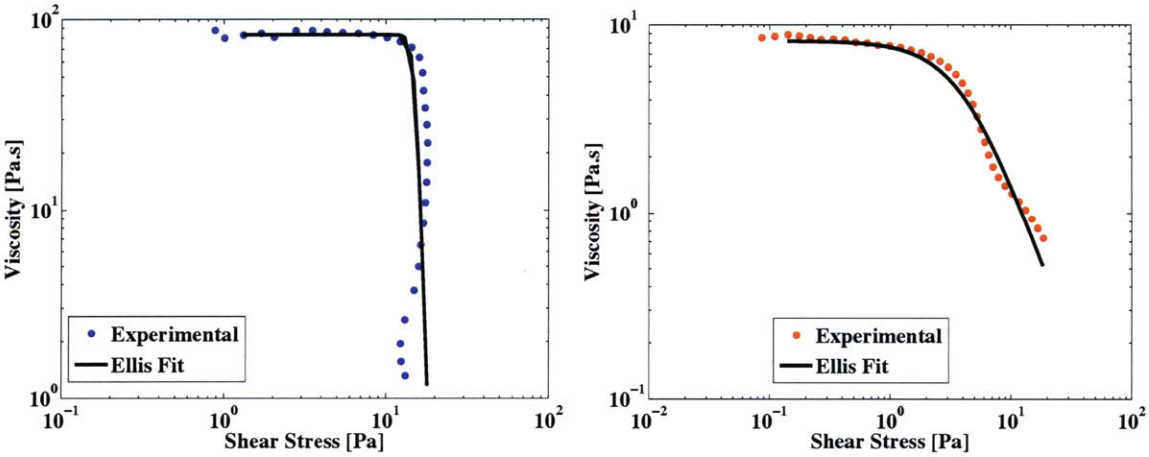

(a) CPyCl.

(b) CTAB.

Figure 3.1.10: Fits of the Ellis model to the steady shear rheology of 100:60 mM CPyCl:NaSal and 30:240 mM CTAB:NaSal solutions at 22 ^{o}C.

its respective zero-shear-rate value. In reality, for both systems, $\Psi_1 \approx 3$ Pa.s^2.

For the CPyCl system, at $\dot{\gamma} > 10$ s^{-1}, and for the CTAB system at $\dot{\gamma} > 30$ s^{-1}, the meniscus of the test fluid becomes unstable and a large fraction of the sample is ejected from the gap. This instability is not a result of the large centrifugal acceleration associated with the rotational motion of the fluid, but rather the large normal stress difference associated with the high deformation rate which overcomes the resisting Laplace pressure of the meniscus. Such edge fracture was initially noted by Hutton (1963), who proposed that the instability occurred when the first normal stress difference was

$$N_1 = \kappa \frac{\sigma}{H_{rim}} \tag{3.1.19}$$

where κ is a value inversely proportional to the fraction of elastic energy converted to surface energy, σ is surface tension and H_{rim} is the gap height at the rim of the fixture. In later work, Tanner & Keentok (1983) found that the second normal stress difference dictated the onset of the edge instability, whereby

$$N_2 = \frac{\sigma}{H_{rim}} \tag{3.1.20}$$

This proposal was supported experimentally by Lee *et al.* (1992), who have argued that N_2 is the relevant elastic stress which dictates instability, having found that edge fracture for a selection of six polymer solutions occurred at an approximately constant value of N_2, though different values of N_1 for each fluid. Tanner & Keentok (1983) also noted that inertia should only be of relevance when $\frac{3}{20}\rho R^2\omega^2 = \sigma/H_{rim}$ or, alternatively, the critical shear rate at which edge fracture should occur is

$$\dot{\gamma}_c = \sqrt{\frac{20}{3}\frac{\sigma}{\rho H_{rim}^3}} \tag{3.1.21}$$

For the systems studied here, the surface tension may be estimated as $\sigma \approx 0.032$ N/m as reported in Bhardwaj *et al.* (2007), $\rho \approx 1{,}100$ kg/m^3, and for a cone and plate

fixture, $H_{rim} = R\vartheta$, with $R = 0.025$ m and $\vartheta = 0.0402$ rad, thus $H_{rim} = 0.001$ m. Hence the onset of an edge instability due to fluid inertia should have occurred at shear rates around $\dot{\gamma}_c = 440$ s^{-1}, and accordingly inertia is not the dominant cause of edge fracture. Supposing $\kappa \approx 1$ in Eq. 3.1.19, then the onset of edge fracture due to elastic stresses would occurr when elastic stresses are of order 32 Pa. As no measure of N_2 was possible in this study, it will suffice to mention that the CPyCl solution exhibits the edge instability when $N_1 \approx 300$ Pa and the CTAB solution when $N_1 \approx 1000$ Pa, and in light of the negligible role of inertia in the instability, it seems likely that elastic stresses are responsible for the edge fracture. This instability rendered high shear rate rheometry of these fluids with a rotational rheometer impossible, and provided further motivation for pursuing microfluidic rheometry.

The high shear rate rheology of both solutions was determined with VROC (channel 8VC05100072), and the resultant flow curves are presented in Figure 3.1.11. In these tests, a constant volumetric flow rate through the channel was imposed using a Harvard PHD 4400 programmable pump (Harvard Apparatus) and a glass syringe (Hamilton Gastight). The pressure drop along the length of the channel was measured for each imposed flow rate and related to the wall shear stress. Multiple tests were conducted to ensure repeatability. The Weissenberg-Rabinowitsch-Mooney Correction in Eq. 3.1.4 was applied to determine the true wall shear rate. A third order polynomial was fit to five consecutive data points to determine numerically the local differential correction term in Eq. 3.1.4 for each data point. Due to uncertainty in fit, however, the correction was only applied to those data points for which $0 \leq \frac{d \ln Q}{d \ln \tau_{wall}} \leq 10$, all other data points were left as the apparent Newtonian shear rate.

The temperature of the test fluids were controlled with a thermal jacket system (Rheosense Inc.), coupled with an F12-ED Refrigerated/Heating Circulator (Julabo Inc.). The temperatures of the fluid samples within the test channel were recorded with a sensor in the VROC device, and they varied between 22 and 22.5^{o}C throughout the duration of the tests.

Similar measurements without the cooling system have been made and a tempera-

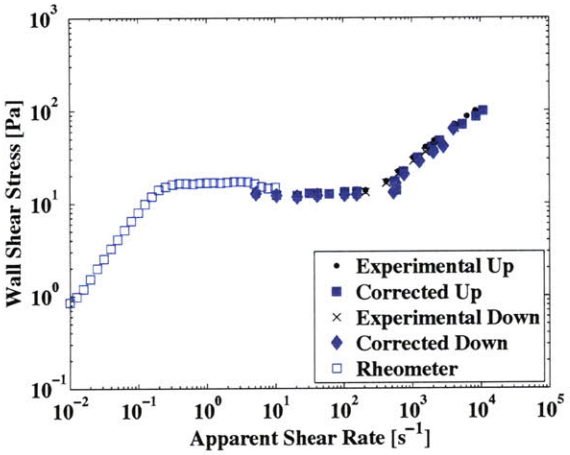

(a) Shear Stress of 100:60 mM CPyCl:NaSal.

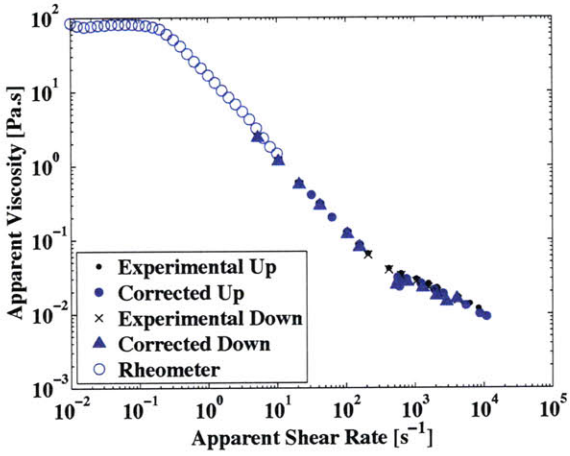

(b) Shear Viscosity of 100:60 mM CPyCl:NaSal.

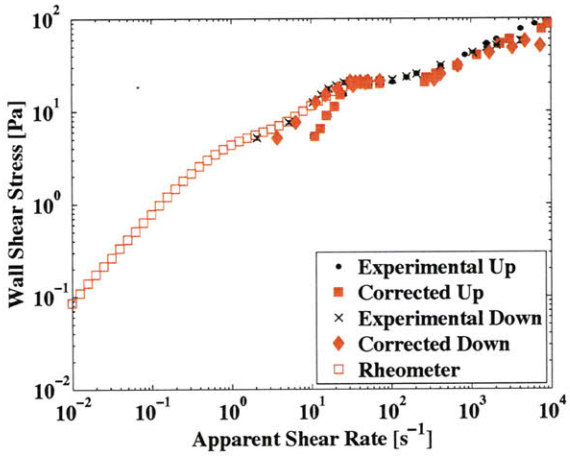

(c) Shear Stress of 30:240 mM CTAB:NaSal.

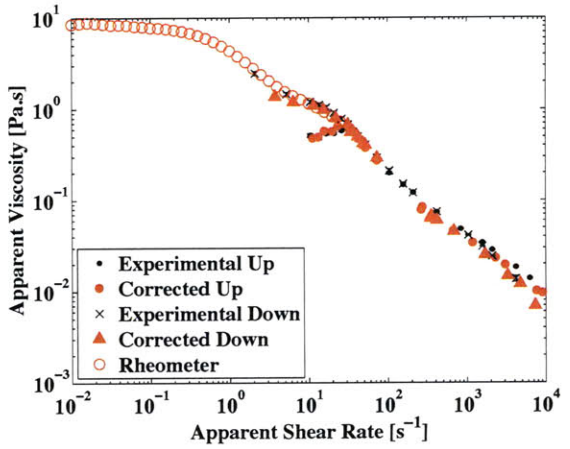

(d) Shear Viscosity of 30:240 mM CTAB:NaSal.

Figure 3.1.11: Steady shear rheology of 100:60 mM CPyCl:NaSal and 30:240 mM CTAB:NaSal solutions at 22-22.5 ^{o}C obtained with VROC, channel 8VC05100072. Experimental markers indicate raw results. Corrected markers indicate results obtained with the application of the Weissenberg-Rabinowitsch-Mooney Correction in Eq. 3.1.4. The markers denoted by 'Up' indicate those that were obtained from an increasing sweep of wall shear rates, and conversely, the markers denoted by 'Down' indicate those that were obtained from an decreasing sweep of wall shear rates. Rheometer markers indicate results obtained with the ARES rheometer.

ture rise of 2 to 3^{o}C during the test was observed. The influence of viscous heating due to the high shear rates, (Pipe *et al.* (2008)), may be considered on non-dimensional grounds if one considers the magnitude of the Brinkman number, Br, which is the ratio of viscous heating to conductive heat transfer within the fluid. This ratio is

$$Br = \frac{\eta \langle U \rangle^2}{k \Delta T} \tag{3.1.22}$$

where η is viscosity, $\langle U \rangle$ is a characteristic speed, k is the thermal conductivity of the fluid and ΔT is a characteristic temperature drop in the fluid. Evidently, for this flow, $\langle U \rangle = Q/WH$, where Q is volumetric flow rate, and W and H are the width and height of the channel, respectively. Seeking a conservatively high estimate of Br, one may assume η is the zero-shear-rate viscosity of the fluid, although in reality the true viscosity at high flow rates was substantially smaller than the zero-shear-rate value. For the CPyCl solution, then, $\eta \approx 80$ Pa.s, $Q = 10$ μL/s, being the maximum flow rate experimentally realized, W and H given in Table 3.1.1, $k \approx 0.6$ W/m^{o}C for water and $\Delta T = 0.5$ ^{o}C being representative of the temperature fluctuations during the experiment. In this case, $Br \approx 1$, and hence in the worst case viscous heating was adequately balanced by the cooling system and temperature variations in the fluid may be neglected.

Tests were completed with a sweep of increasing wall shear rate, followed by a sweep of decreasing wall shear rate in order to check for hysteretic fluid behavior.

It is clear from the flow curve in Figure 3.1.11 (a) that the CPyCl solution exhibits no hysteretic behavior for the shear rates observed with VROC. For the CPyCl solution a stress plateau at apparent shear rates spanning four order of magnitude is evidenced in Figure 3.1.11 (a). As before the viscosity at shear rates corresponding to the stress plateau is inversely proportional to shear rate. At shear rates greater than approximately $\dot{\gamma} \approx 500$ s^{-1}, the stress again increases with increasing shear rate, indicating a departure from the stress plateau. The viscosity at $\dot{\gamma} > 500$ may be seen in Figure 3.1.11 (b) to decrease further with increasing shear rate, with $\eta \sim \dot{\gamma}^{-0.5}$.

The CTAB solution exhibits a multi-valued viscosity for $3 \leq \dot{\gamma} \leq 30$ s^{-1}, as may be seen in the flow curve in Figure 3.1.11 (c), that is path dependent at the shear stresses that were minimally, but reliably detectable with VROC. For the sweep of increasing wall shear rates, the apparent viscosity measured with VROC is considerably lower than that obtained with the conventional cone-and-plate rheometer. For the sweep of decreasing wall shear rates, however, it is clear that the flow curve obtained with VROC superposes nicely with that obtained with the conventional rotational rheometer. The reason for this hysteretic behavior is not entirely clear. It is possible that in this microscale geometry, a flow instability accompanies the transition from essentially Newtonian behavior at very low wall shear rates to non-Newtonian behavior at the moderate shear rates for which the multi-valued viscosity occurs. This instability may be a low shear rate analogue of the vorticity banding instability in a CTAB:NO_3 solution at high shear rates observed by Fardin *et al.* (2009). For a small range of shear rates spanning less than an order of magnitude greater than those at which the bifurcation in the apparent viscosity occurs, the CTAB solution exhibits a stress plateau indicative of shear banding. At shear rates greater still, $\dot{\gamma} > 300$ s^{-1}, the stress increases with increasing shear rate, but the viscosity as seen in Figure 3.1.11 (d) decreases further with increasing shear rate, having a power law dependence on shear rate (*i.e.* $\eta \sim \dot{\gamma}^{n-1}$, $n \approx 0.4$) similar to that at the shear rates at the onset of shear thinning.

Extensional Rheology

The extensional rheology of the test fluids at low to moderate extension rates and to large extensional strains was measured with CaBER. The sequence of filament profiles in Figures 3.1.12 and 3.1.13 are typical of what was commonly observed as the filament thinned under the action of capillarity. In the tests of the CPyCl solution shown in Figure 3.1.12, the unstrained filament diameter was $a_0 = 6$ mm, the initial filament height was $h_0 = 2.4$ mm and the final gap was $h_f = 7.1$ mm, corresponding to a Hencky strain of $\varepsilon_H = \ln(7.1/2.4) = 1.08$. For the tests of the CTAB system

Table 3.1.3: Rheological and rheo-optical properties of the test solutions at 22 °C. ◇Persistence length for CPyCl has been assumed. *Persistence length for CTAB solution given in Shikata *et al.* (1994) has been assumed. *Here the stress optical coefficients given by Rehage & Hoffmann (1991) and Shikata *et al.* (1994) have been assumed to be valid at 22 °C.

	100:60 mM CPyCl:NaSal	30:240 mM CTAB:NaSal
Maxwell Model		
λ_M [s]	2.9	1.7
η_0 [Pa.s]	78	7.5
G_0 [Pa]	27	4.5
Ellis Model		
η_0 [Pa.s]	83	8.3
α	25	2.8
$\tau_{1/2}$ [Pa]	15	4.1
Ψ_1 [Pa.s^2]	3	3
λ_{break} [s]	1.5	0.8
λ_{rep} [s]	5.5	3.4
$G_{plateau}$ [Pa]	33	5.5
G''_{min} [Pa]	2.5	0.6
ξ [nm]	50	97
$l_{persist}$ [nm]	20◇	26*
l_e [nm]	92	230
$\langle l \rangle$ [μm]	1.2	1.7
λ_{ext} [s]	4.0	2.3
C [Pa^{-1}]	-2.3 x 10^{-7}*	-3.1 x 10^{-7}*

seen in Figure 3.1.13 the unstrained filament diameter was $a_0 = 6$ mm, the initial filament height was $h_0 = 2.1$ mm and the final gap was $h_f = 6.2$ mm, corresponding to a Hencky strain of $\varepsilon_H = \ln(6.2/2.1) = 1.08$. The top end plate was displaced to its final position at an exponential rate over a 50 ms period. The time $t = 0$ corresponds to the instant the application of the step strain was complete.

The evolution of the filament diameter for both fluids may be seen in Figure 3.1.14. In these plots, a_1 is taken as the diameter of the filament at $t = 0$, coinciding with the completion of the applied strain. The two fluids thin in qualitatively different manners. The CTAB solution, by virtue of its low viscosity initiates elasto-capillary thinning shortly after the application of the step strain. It is also clear from the images in Figure 3.1.13 that the majority of the filament remains on the lower plate during the test. The considerably more viscous CPyCl solution exhibits a prolonged period of visco-capillary thinning followed by a relatively abrupt transition to the elasto-capillary thinning preceding rupture of the filament.

The extensional relaxation time, λ_{ext}, given by Eq. 3.1.10 for both fluids was obtained from the slope of a best-fit line to the results given in Figure 3.1.14 as indicated on the plots. These values are listed in Table 3.1.3. The determined extensional relaxation times are roughly twice their respective Maxwell relaxation times, ($\lambda_{ext}/\lambda_M \approx 2$). This ratio compares well to the work of Kim *et al.* (2010), who studied a 100:50:100 mM CPyCl:NaSal:NaCl system and observed $\lambda_{ext}/\lambda_M \approx 1.3$, though it differs from the findings of Yesilata *et al.* (2006), who studied EHAC:NH_4Cl systems and found $\lambda_{ext}/\lambda_M \approx 0.3$. These variations indicate that relaxation processes in micellar systems depend on the kinematics of the imposed flow field (*e.g.* SAOS versus extension flow) as well as the constituent molecules.

For this study, tests with the EVROC were completed using only the antisymmetric configuration. No temperature control device was used during the experiments during which ambient temperature varied between 21 and 23 ^oC. No corrections for decoupling the shear and extensional contribution to the pressure drop, as discussed, for example by Wang *et al.* (2010) were applied to the results. The apparent ex-

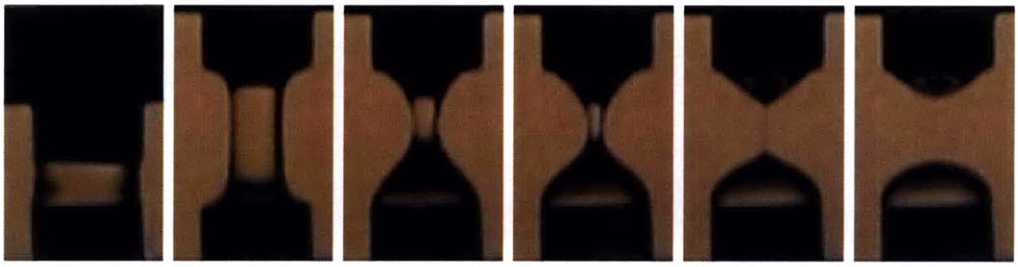

(a) $t < 0$. (b) $t = 0$. (c) $t = \frac{t_{rup}}{4}$. (d) $t = \frac{t_{rup}}{2}$. (e) $t = \frac{3t_{rup}}{4}$. (f) $t = t_{rup}$.

Figure 3.1.12: Filament profiles of a CaBER experiment with the 100:60 mM CPyCl:NaSal solution at 22-23 ^{o}C. The time t_{rup} is the time at which the filament ruptures. The applied Hencky strain is $\varepsilon_H = \ln(h_f/h_0) = 1.08$. Plate diameter was $a_0 = 6$ mm, corresponding to the width of the dark region at the bottom of each image.

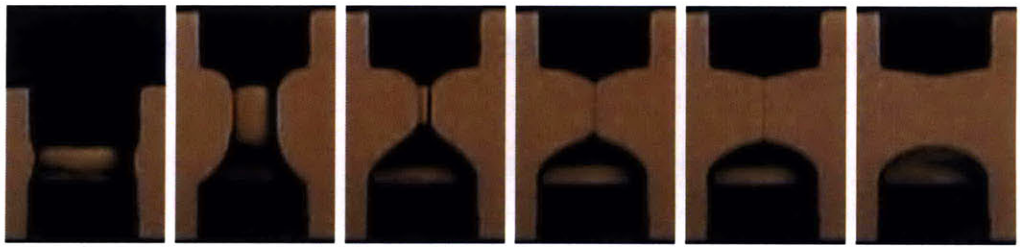

(a) $t < 0$. (b) $t = 0$. (c) $t = \frac{t_{rup}}{4}$. (d) $t = \frac{t_{rup}}{2}$. (e) $t = \frac{3t_{rup}}{4}$. (f) $t = t_{rup}$.

Figure 3.1.13: Filament profiles of a CaBER experiment with the 30:240 mM CTAB solution at 22-23 ^{o}C. The time t_{rup} is the time at which the filament ruptures. The applied Hencky strain is $\varepsilon_H = \ln(h_f/h_0) = 1.08$. Plate diameter was $a_0 = 6$ mm, corresponding to the width of the dark region at the bottom of each image.

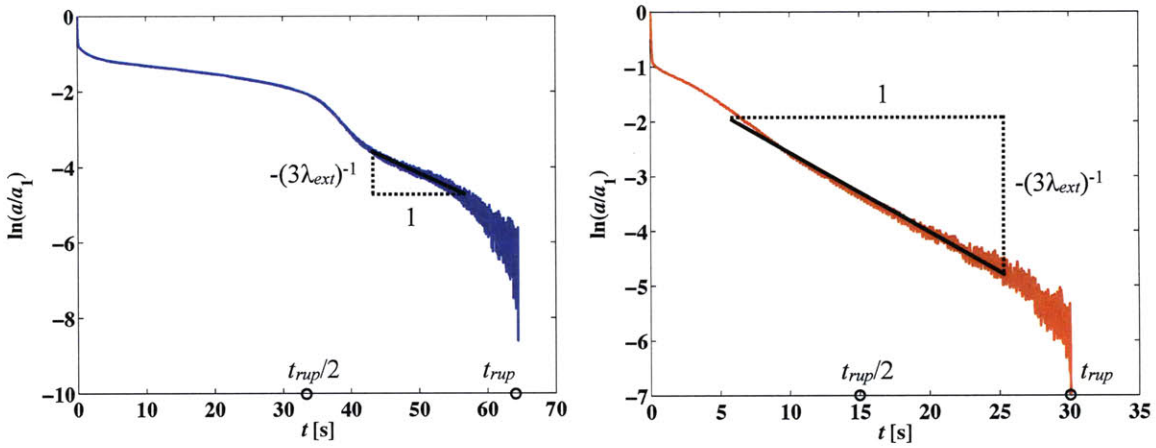

(a) 100:60 mM CPyCl:NaSal.

(b) 30:240 mM CTAB:NaSal.

Figure 3.1.14: Extensional rheology of 100:60 mM CPyCl:NaSal and 30:240 mM CTAB:NaSal solutions at 22-23 °C measured with CaBER. Applied $\varepsilon_H = 1.08$.

tensional viscosity, $\eta_E(\dot{\varepsilon})$, as given in Eq. 3.1.14 are plotted in Figure 3.1.15. The normal stress difference, N_1, obtained from the relation $N_1 = \eta_E(\dot{\varepsilon})\dot{\varepsilon}$ is also included in Figure 3.1.15. At the lowest apparent extension rates, both fluids exhibit constant extensional viscosities, having apparent plateau values approximately 100 times their respective zero-shear-rate viscosities. This considerably large apparent Trouton ratio has also been observed for a Newtonian fluid by the author of this thesis and is a result of the mixed nature of the flow leading to a superposition of pressure drops due to shear and extensional stresses as discussed in Pipe & McKinley (2008). At increasing apparent extension rates, evidently the extensional viscosity of both fluids decreases, until at extension rates $10 \leq \dot{\varepsilon} \leq 100$ s^{-1} ($20 \leq De = \lambda_M \dot{\varepsilon} \leq 200$), both fluids exhibit constant apparent elastic stresses. The plateau in stress may coincide with a critical stress, corresponding to an approximate value of N_1 in Figure 3.1.15, at which the micelles in each system break *en masse*, in a manner similar to the phenomenon described for the experiments of Bhardwaj *et al.* (2007) and in simulations of Cromer *et al.* (2009). At still higher extensional rates, $\dot{\varepsilon} \geq 100$ s^{-1}, for both systems, N_1 increases with increasing $\dot{\varepsilon}$.

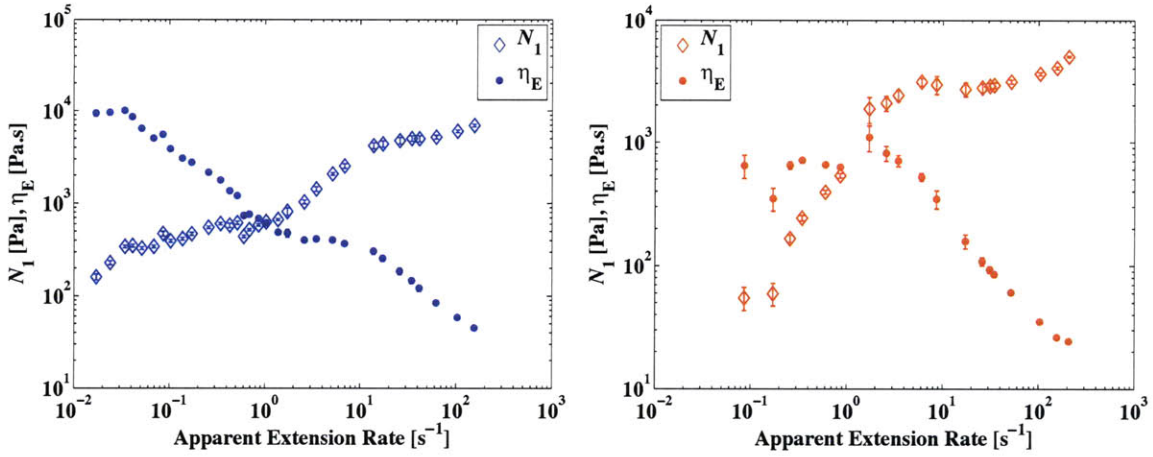

(a) 100:60 mM CPyCl:NaSal. (b) 30:240 mM CTAB:NaSal.

Figure 3.1.15: Extensional rheology of 100:60 mM CPyCl:NaSal and 30:240 mM CTAB:NaSal solutions at 21-23 ^{o}C obtained with EVROC.

Flow-Induced Birefringence

A birefringent material is one whose ordinary and extraordinary indices of refraction[6], n_1 and n_2, are not equal, (Fuller (1995)), as depicted in Figure 3.1.16 (a). This difference in refractive indices is known as optical anisotropy (*i.e.* a directional dependence), and it is defined $\Delta n \equiv n_1 - n_2$. As a consequence of this optical anisotropy, the state of polarization of a lightwave traveling through the material will change as it propagates through the material.

Certain polymeric and micellar solutions exhibit flow-induced birefringence, whereby a deformation imposed on a material induces optical anisotropy in that material as a result of changes in the molecular conformation. The reader is encouraged to refer to Fuller (1995) and Larson (1998) for comprehensive treatises on the molecular nature of the optical properties of complex fluids. The derivation of many of the following results, however, is discussed at length in Appendix D of this thesis.

In the study presented in this thesis, we are interested in determining the material stresses from measurements of flow-induced birefringence, induced by velocity

[6]Refractive index: $n_i = c/v_{p,i}$ where c is the speed of light in a vacuum, $v_{p,i}$ is the phase speed of light in a medium along the i-direction.

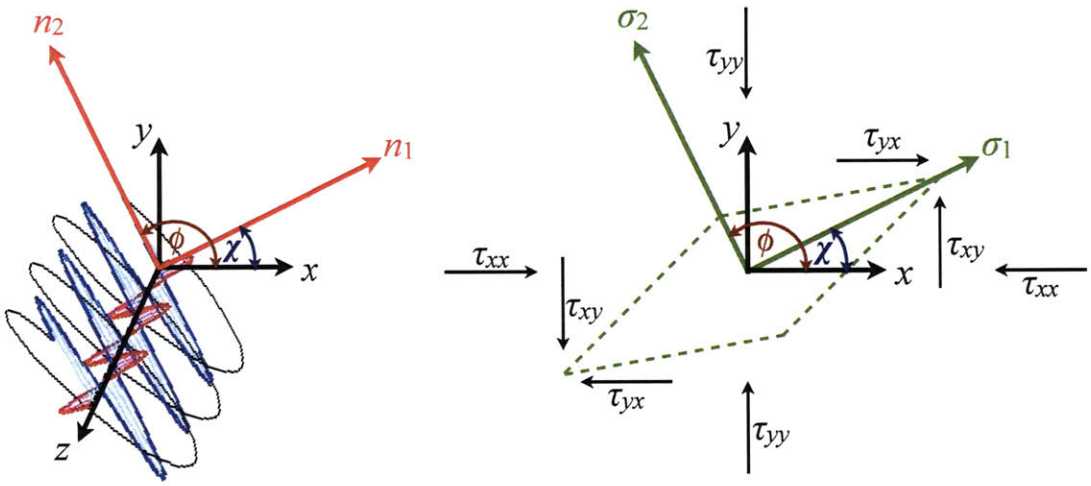

(a) (b)

Figure 3.1.16: (a) Optically anisotropic material with principal optical axes and indices of refraction, n_1 and n_2 in the xy-plane. A monochromatic, polarized lightwave propagating along the z-axis is depicted. Projections of the electromagnetic vector of the light wave onto the xz-plane (red) and yz-plane (blue) are shown. (b) Material deforming along principal stress axes and with principal stresses, σ_1 and σ_2 in the xy-plane.

gradients in a flowing complex fluid. The stress optical rule provides the link between stress in the material and its optical anisotropy. The stress optical rule states that the principal stress difference, $\Delta\sigma \equiv \sigma_1 - \sigma_2$ of a material with principal stresses σ_1 and σ_2, as depicted in Figure 3.1.16 (b), is linearly proportional to the difference between the ordinary and extraordinary indices of refraction, Δn. The coefficient of proportionality is the stress optical coefficient, C, which depends on temperature and other material properties, and is generally an empirically determined value for a particular material, as for example in the works of Rehage & Hoffmann (1991), Shikata *et al.* (1994) and Lerouge *et al.* (2000).

$$\Delta n = C\Delta\sigma \tag{3.1.23}$$

The stress optical rule follows from the assumption that, as the polymeric stress tensor and the average orientation of a polymer network both obey Gaussian statistics, the

principal optical axes of a polymer coincide with the principal stress axes, as outlined in Fuller (1995). One may note, then, from Eq. 3.1.23, that if the stress optical coefficient, C, of a material is known, and Δn can be ascertained, it is possible to make optically, non-invasive measurements of the anisotropic state of stress in a material.

The optical anisotropy of a material Δn, cannot be measured directly, but an experimentally measurable quantity, which may be related to the optical anisotropy of a material is called *retardance* and is denoted by the symbol δ, given in radians. The retardance is the phase angle between two mutually orthogonal lightwaves propagating in space, (*e.g.* the red and blue lightwaves depicted in Figure 3.1.16 (a)). A dimensional retardance, being denoted r, and having units of length, may be obtained if one considers the wavelength of the light wave, λ, by the relation

$$\frac{\delta}{2\pi} = \frac{r}{\lambda} \tag{3.1.24}$$

Retardance may be related to the optical anisotropy of a material, Δn, if Δn is known along the direction of light propagation. In this case of constant Δn, for a birefringent sample having length, L, along the direction of light propagation, (*e.g.* along the z-axis depicted in Figure 3.1.16 (a)), then the retardance and optical anisotropy are related by the expression

$$\frac{\delta}{2\pi} = \frac{\Delta n L}{\lambda} \tag{3.1.25}$$

The principal stress, σ_1 and σ_2, are the eigenvalues of the two-dimensional stress tensor which characterizes the deviatoric stresses associated with the material deformation depicted in Figure 3.1.16 (b). The principal stress difference, $\Delta\sigma \equiv \sigma_1 - \sigma_2$, may be related to the stresses in the xy-frame via Eq. 3.1.26.

$$\Delta\sigma = \sqrt{N_1^2 + 4\tau_{xy}^2} \tag{3.1.26}$$

Where τ_{xy} is the shear stress and N_1 is the first normal stress difference, as described in Section 3.1.2, such that $N_1 \equiv \tau_{xx} - \tau_{yy}$.

The second quantity of interest is called the *azimuthal angle* and is denoted by the symbol χ. The azimuthal angle is the orientation of one of the principal axes with respect to some global laboratory reference frame, and, in the case of Figure 3.1.16, χ is the angle between the first principal axis and the x-axis. The azimuthal angle is related to τ_{xy} and N_1 with Eq. 3.1.27.

$$\chi = \frac{1}{2} \arctan\left(\frac{2\tau_{xy}}{N_1}\right) \tag{3.1.27}$$

Since, in general, the stress tensor is symmetric, its eigenvectors, which coincide with the principal axes, are generally mutually orthogonal. Accordingly the second principal axis, whose orientation with respect to the x-axis in Figure 3.1.16 is denoted by ϕ, is related to χ by the simple relation $\phi \equiv \chi + \pi/2$.

Experimental evidence suggests that the stress optical rule may be assumed valid for flow of worm-like micellar systems provided the material exhibits predominantly linear behavior, as seen, for example, in the work of Shikata *et al.* (1994), Lerouge *et al.* (2000) and Decruppe & Ponton (2003). The validity of the stress optical rule, particularly, in completely describing the non-linear rheology of these solutions, however, has come in doubt in certain cases by the works of Lerouge *et al.* (2000) and Pathak & Hudson (2006) among others, as discussed in Section 2.4. In this study, the stress optical rule has been used to probe qualitatively the rheology of the systems studied, and in certain cases quantitative comparisons between experimental results and predictions of the rule are made.

3.2 Experimental Setup

In this section, the experimental equipment and techniques that were used in this study are addressed. The basic components for each experiment consisted of a

microscope, an imaging system, test geometry and fluid, glass syringe (Hamilton Gastight), syringe pump, PHD 4000 programmable pump (Harvard Apparatus) or Multi-Phaser^{TM} NE-1000 programmable pump (New Era Pump Systems, Inc.). Syringes were selected appropriately, such that for a specified volumetric flow rate, the pump functioned well within its limits of operation. Syringes were connected to test geometries using Tygon® microbore tubing (inner diameter 0.508 mm (0.020")) (Cole Parmer Instrument Co.) and metal connector joints (inner diameter 0.254 mm (0.010")) (New England Small Tube Corp.), which were bent to ensure a good seal, by reducing the bending moment on the joints due to the weight of the microbore tubing. In all tests, the length of the tubing was kept to a minimum in order to reduce compliance in the entire system, thereby shortening the duration of experimental transients. Experiments were performed in climate controlled rooms in which the temperature was recorded to have fluctuated between 22-24 ^{o}C for the duration of all experiments.

3.2.1 Channel Fabrication

The microchannel rectangular rheometer was manufactured using a technique similar to that of Guillot *et al.* (2006). Two anodized, 1 mm x 2 cm x 8 cm aluminum strips were used to construct the sidewalls of the channel. The inside walls of the channel were polished with 2000 grit sandpaper and thoroughly cleaned. The two strips were glued together with a two-part epoxy (Devcon). A spacer was placed between the strips to ensure a constant width between the strips. Once the epoxy had set, the spacer was removed and the distance between the strips was checked with an optical microscope in order to ensure that the channel walls were parallel. Thin layers of the same epoxy were spread on the top and bottom of the strips and 150 μm thick microscope cover slips were pressed onto the adhesive. Care was taken to ensure that no epoxy seeped into the channel. Luer stub adapter syringe tips were then adhered to the channel at both ends and additional epoxy was added where needed

to ensure the channel was sealed. A step-by-step procedure is given in Appendix F. The dimensions of the straight channel used in this study were width, $W = 130 \pm 5$ μm, height, $H = 1,000 \pm 10$ μm, and length, $L = 5$ cm, as depicted in Figure 3.2.1.

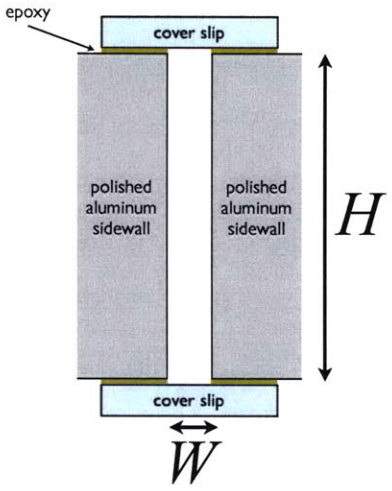

(a) Cross-section of straight channel. Schematic depiction is roughly to scale.

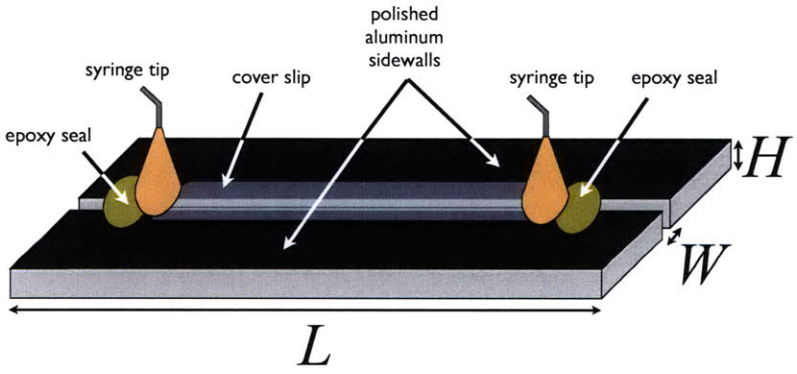

(b) Perspective view of straight channel.

Figure 3.2.1: Cross-section and perspective views of the straight, anodized aluminum rectangular rheometer.

The antisymmetric hyperbolic contraction microchannels were fabricated with polydimethylsiloxane (PDMS) (Dow Corning) using standard, soft photolithographic fabrication processes described in Xia & Whitesides (1998). Scott (2004) and Rodd *et al.* (2005) have also addressed additional relevant fabrication techniques in the

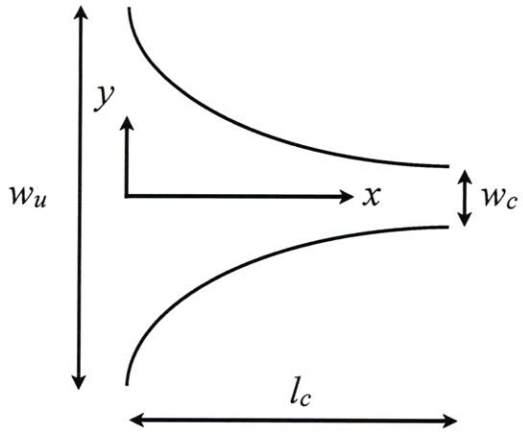

Figure 3.2.2: Schematic diagram of hyperbolic contraction.

manufacture of the PDMS microchannels used here for rheometry. Each mircochannel was replicated from a male mold consisting of a silicon substrate and cured SU-8 2050 permanent epoxy photoresist (Micro Chem), Figure 3.2.3 (1). A brief procedure outlining the replication process is given in Appendix F. Connector ports in the semi-cured PDMS were punctured with a 0.50 mm stainless steel Uni-Core punch (Harris), Figure 3.2.3 (3). Semi-cured PDMS replicates were sealed to a 150 μm thick microsope cover slip, on which PDMS had been spun coat, Figure 3.2.3 (4). In this fashion all four bounding walls of the channel where made of the same material. The surface features of the spun coat layer are shown in Figure 3.2.5, with asperities on the order of 0.5 μm. The dimensions of the contraction were length, $l_c = 1100$ μm, height, $h_c = 35$ μm, upstream width, $w_u = 1000$ μm and contraction width, $w_c = 50$ μm as depicted in Figure 3.2.2.

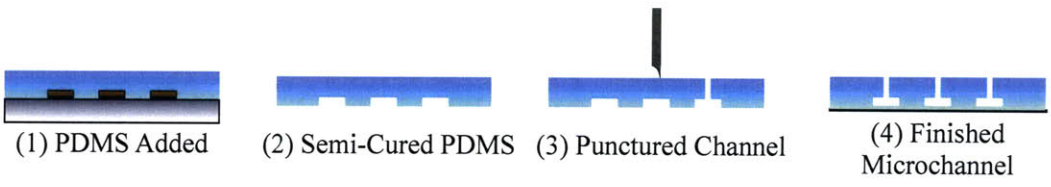

Figure 3.2.3: Simplified PDMS microchannel fabrication process.

Each mold was fabricated in a Class 100 clean room. SU-8 2050 photoresist (MicroChem) was spun coat on a bare silicon wafer to obtain a uniform film thickness on the wafer surface, Figure 3.2.4 (2). A contrast enhancer, CEM 388SS (Shin Etsu MicroSi) was also used in the fabrication of the mold, Figure 3.2.4 (4). Soulages *et al.* (2009) have demonstrated that the use of this contrast enhancer facilitated well-defined features in the microchannels and near perfectly vertical channel walls. The presence of the contrast enhancer in the mold fabrication process also necessitated the use of a BC 7.5 barrier coat (Shin Etsu MicroSi), which was added to the surface of the SU-8 2050 prior to addition of the contrast enhancer, Figure 3.2.4 (3). The barrier coat served to prevent cross-contamination of the photoresist and the contrast enhancer. A high-resolution chrome mask (Advance Reproductions), shown in Figure 3.2.6, was used in the UV exposure step, Figure 3.2.4 (5). Uncured material was removed with suitable solvents, Figure 3.2.4 (7), and the resultant mold was examined under a microscope to determine the ultimate quality of the mold. A more detailed procedure describing this process is given in Appendix F.

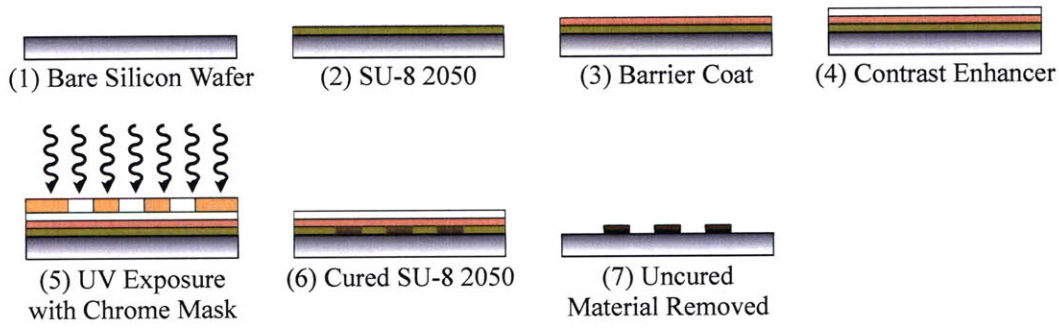

Figure 3.2.4: Simplified overview of mold fabrication process.

3.2.2 Micro-Particle Image Velocimetry

Micro-particle image velocimetry (μ-PIV) is a correlative technique, in which one images the temporal displacement of microscale markers moving in a flowing fluid

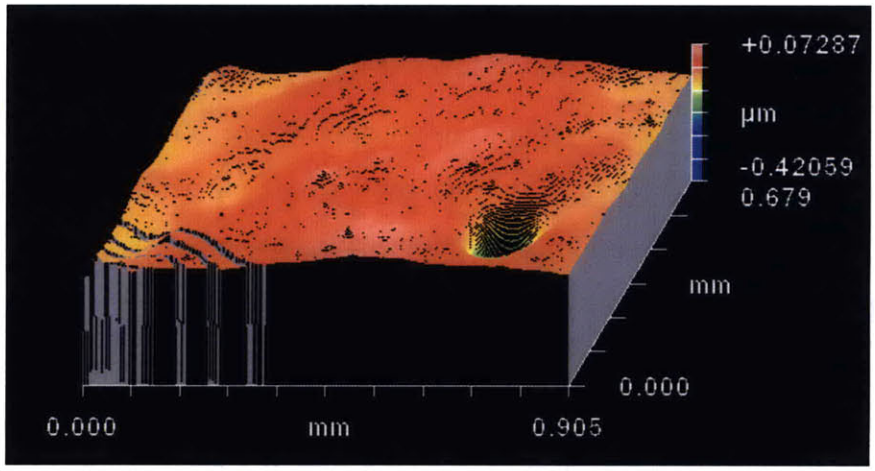

Figure 3.2.5: Surface asperity plot of a 900 x 680 μm sampling area of a cured PDMS, spun coat cover slip obtained with a Zygo interferometer, 20x objective.

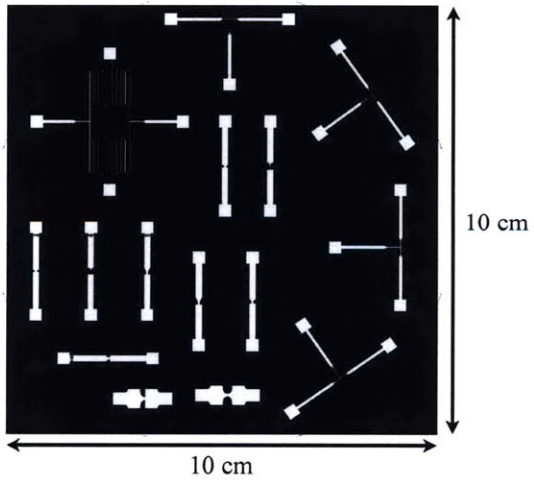

Figure 3.2.6: Depiction of chrome mask used in replication process.

in order to infer the fluid velocity field, (Raffel *et al.* (1998)). In this study, μ-PIV has been used to measure the velocity fields in the flow of the two test fluids in each microscale geometry in order to determine the corresponding strain rates for a given flow.

In the simplest case, a PIV system consists of a camera, a light source, a transparent flow geometry and a test fluid that contains tracer particles, whose position the camera can detect only when illuminated by the light source. In order to determine the trajectory of the particles, the camera must capture a sequence of image pairs, for which the elapsed time between the taking of each image is known. For a consecutive pair of images, i and $i+1$, having been taken a time Δt apart, the velocity, $\overrightarrow{v}_j$ of the j-th particle in the image pair, having position vector $\overrightarrow{r}_{j,i} = (x_{j,i}, y_{j,i})$ in the first image and position vector $\overrightarrow{r}_{j,i+1} = (x_{j,i+1}, y_{j,i+1})$ in the second image, may be found to be $\overrightarrow{v}_j = (\overrightarrow{r}_{j,i+1} - \overrightarrow{r}_{j,i})/\Delta t$. A velocity field may then be determined by compiling the velocity vectors of all the particles in the image pair as depicted in Figure 3.2.8. If the flow is steady, a time averaged velocity field may be obtained by averaging the velocity vectors measured over a sequence of image pairs.

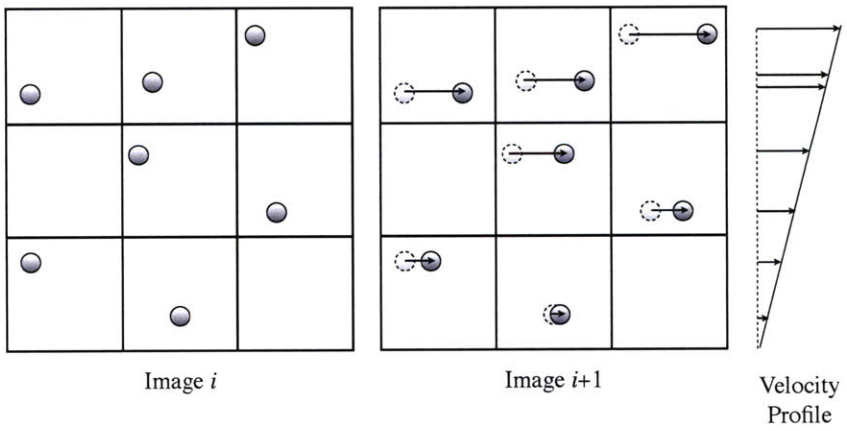

Figure 3.2.7: Qualitative depiction of the translation of particle tracers in an image pair. To aid the eye, the images are subdivided into a 3 x 3 grid, in a similar manner to the algorithms used by most PIV software.

For experiments in which the scale of the flow is amply large, it is typical to

use a laser to form a thin, focused light sheet which may be used to illuminate a particular cross-section of the flow which is of interest. In examining flows in microscale geometries, however, Meinhart *et al.* (2000) point out that optical access may be restricted or the effective thickness of the light sheet may be on the order of the dimensions of the geometry. Accordingly, an alternative approach for μ-PIV experiments is known as volume illumination, whereby the entire volume of a region of flow is illuminated and the spatial resolution of all measurements must be controlled by selecting suitable optical components (*e.g.* objective, light wavelength, camera resolution, *etc.*).

For a particular optical objective and camera, the distance over which sample features may be considered in focus is called the *depth of field.* The expression given by Meinhart *et al.* (2000) may be used to determine the depth of field, δz, for a particular system.

$$\delta z = \frac{n\lambda_0}{(NA)^2} + \frac{ne}{(NA)M} \tag{3.2.1}$$

In Eq. 3.2.1, n is the refractive index of the observed sample, λ_0 is the wavelength of imaged light (in a vacuum), NA is the numerical aperture of the objective with magnification, M. The minimum resolvable feature size is denoted by e, and for a system using a charge-coupled device (CCD) camera, e is the spacing between pixels.

Although a tracer particle may be fully in focus only in the depth of field, additional particles beyond the depth of field, though within its vicinity, may also contribute substantially to the overall signal detected by the camera. Accordingly the true depth over which measurements of the fluid velocity may be resolved is larger than the depth of field, and it is called the *depth of measurement.* The expression for the depth of measurement, δz_m, has also been given by Meinhart *et al.* (2000), whereby any particle, having an imaged light intensity greater than 10% of its fully in focus intensity, is considered to lie within the depth of measurement.

$$\delta z_m = \frac{3n\lambda_0}{(NA)^2} + \frac{2.16d_p}{\tan\theta} + d_p \tag{3.2.2}$$

For this expression, the parameters given for Eq. 3.2.1 are the same, with $\theta = \sin^{-1}(NA/n)$ and d_p is the particle diameter. Eq. 3.2.2 holds in the case where $e/M > d_p$. Typical depths of field and measurement used in this study are presented in Table 3.2.1.

Table 3.2.1: Working distance, WD, numerical aperture, NA, magnification, M, depth of field and depth of measurement for typical experiments in this thesis. PIV-Cam 14-10 and BlueFox are the two camera systems used in this study. For the μ-PIV system used here, $n = 1.33$, $\lambda_0 = 580$ nm, $e = 6.8$ μm, $d_p = 1.1$ μm.

Objective	WD [mm]	NA	M	δz_m [μm]	PIV-Cam 14-10 e/M [μm]	PIV-Cam 14-10 δz [μm]	BlueFox e/M [μm]	BlueFox δz [μm]
10x 0.25 NA Standard	7	0.25	10	47.3	0.65	15.8	0.74	12.4
10x 0.3 NA Plan Fluor	16	0.3	10	34.4	0.65	11.4	0.74	8.6
20x 0.5 NA Plan Fluor	2.1	0.5	20	14.5	0.32	3.9	0.37	3.1
40x 0.75 NA Plan Fluor	0.72	0.75	40	7.3	0.16	1.7	0.19	1.4
40x 0.9 NA Plan Fluor	0.3	0.9	40	5.1	0.16	1.2	0.19	1.0

A necessary assumption for the use of μ-PIV in flow diagnostics is that the tracer particles do not themselves influence either the rheological properties of the test sample or the kinematics of the velocity field. It is therefore important that the particles be small compared to the smallest dimension of the flow geometry and that they not alter the viscosity of the material. In the experiments studied here, both test fluids were seeded with 0.02 wt.% 1.1 μm diameter fluorescent particles (Invitrogen), having excitation and emission of 520 and 580 nm, respectively. Since the smallest dimension of any geometry considered in this thesis was 35 μm or greater, the particles have been assumed not to have influenced the flow. Furthermore, for particles having a density similar to that of the test fluid, the volume fraction of the particles may be approximated as $\Phi = 2 \times 10^{-4}$, for which the expression given by Einstein (1906) may be used to predict a minimal increase in viscosity, $\eta = \eta_0(1+2.5\Phi+O(\Phi^2)) = 1.0005\eta_0$.

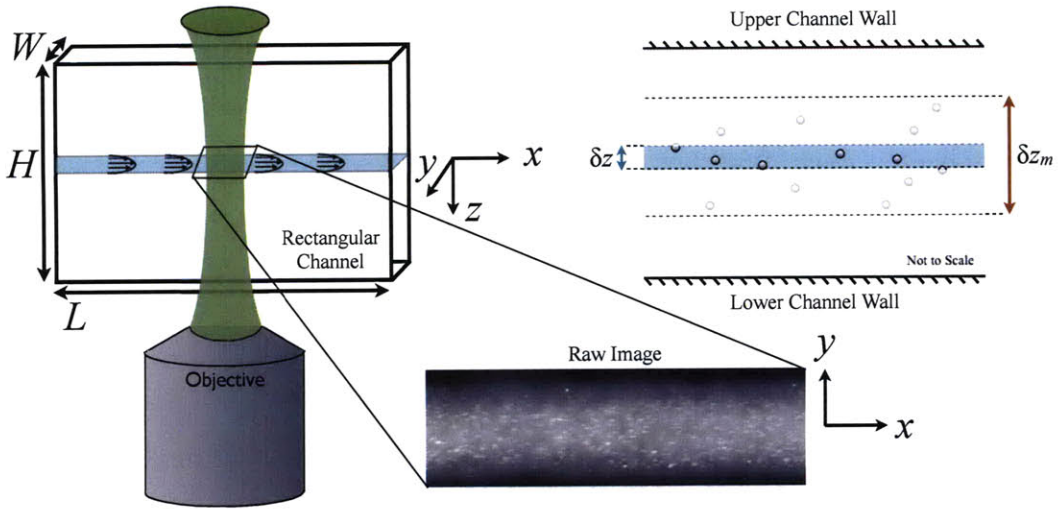

Figure 3.2.8: Schematic depiction of the depths of field and measurement. The tracer particles are fully in focus within the depth of field. The tracer particles may still be marginally resolved in the depth of measurement, though they cannot be resolved beyond this thickness. The xyz-coordinate system is centered along the centroidal axis of the channel.

Evidently, the presence of the particles increased the viscosity of the system by a negligibly small amount.

The μ-PIV system used in this study utilizes epifluorescence microscopy[7]and was discussed at length in Scott (2004) and more briefly in Rodd *et al.* (2005). This system consisted of a 1.4 megapixel (1376 x 1024 pixels) CCD PIV-Cam 14-10, exposure time camera (TSI Instruments), a double-pulsed 532 nm Nd:YAG laser with pulse width, $\delta t = 5$ ns. A G-2A filter was also used to allow only the emitted light with wavelengths, $\lambda \geq 590$ nm to impinge on the camera. For a given flow rate, the elapsed time between consecutive image pairs, Δt, $(1.2 < \Delta t < 60,000\ \mu s)$, was selected to achieve a particle displacement $(2d_p < \Delta x < 7.5d_p)$ suitable for analysis.

At least 25 consecutive images pairs for the straight channel and 75 for the hyperbolic contraction were ensemble averaged to determine full-field maps of the steady

[7]In epifluorescence microscopy, a light wave is used to excite fluorescent portions of the imaged specimen, and only the resultant emitted light wave is observed. As a result, for epifluorescence microscopy the light observed by the photodetector is not the same light that which initially impinges on the sample.

flow velocity profiles using a conventional cross-correlation PIV algorithm with the Insight 6 software (TSI Insight). Interrogation windows of 16 x 16 pixels for the straight channel and 32 x 32 for the hyperbolic contraction were used in the correlation scheme. Each quadrant of an interrogation window was overlapped by the respective quadrant of an adjacent window. Post-processing to remove spurious velocity vectors and any subsequent data analysis of the velocity profiles was completed using MATLAB with a script written by the author of this thesis.

Streakline images were obtained with BlueFOX (Matrix Vision) camera and a continuous illumination mercury lamp with peak emission at 532 nm.

All focal planes were taken with respect to the bottom of each microchannel, which was identied as the lowest plane for which a stationary fluorescent particles was in focus. The uncertainty in the vertical position of a focal plane is accordingly of the order of the uncertainty of identifying the lowest most particles, or equivalently the depth of field, δz, which is given for the each objective used in this study in Table 3.2.1. Additional uncertainty was introduced from the size of a division on the microscope focussing micrometer, which was determined to be 1.5 μm.

Measurements of velocity profiles in the straight channel were completed with a 10x 0.3 NA objective. This objective yielded a viewing area encompassing the entire width (y-axis in Figure 3.2.8) of the channel and approximately 1 mm sections along the length (x-axis) of the channel. The depth of measurement, δz_m for this system was 47.3 μm, so measurements were taken at planes above the bottom of the channel at 50, 100, 150, 200, 250, 300, 350, 400, 450, 600, 750 and 900 μm. Measurement planes above 450 μm, were found, in general, to capture an insufficient number of particles to determine velocity fields. This weakened signal was attributed to reduced light intensity at higher image planes caused by reflection and absorption of light at lower imaging planes. Interrogation windows were 16 x 16 pixels, hence uncertainty in the x and y-positions of a velocity vector were the size of the interrogation window, corresponding to the horizontal error bars in velocity profile plots in Section 4.2.

To determine the average velocity profile for the flow through the straight channel,

the x-components of the velocity profile at a particular y-position were determined by taking the ensemble average of all the measured x-velocities in the viewing area at that particular y-position. Error in the value of the x-velocity, therefore, was taken as the standard deviation of the ensemble average, corresponding to the longitudinal error bars in velocity profile plots in Section 4.2. y-components of the velocity profile were found to be negligibly small in comparison to the x-component at any position in the channel.

Flow through the hyperbolic contraction was observed using similar techniques as those used with the straight channel, but with a 20x 0.5 NA objective. Full-field velocity maps were only measured at the centerplane of the contraction. Since the average fluid velocity increased considerably along the length of the contraction, multiple images sets were acquired using appropriately adjusted time steps between laser pulses, Δt. With the 20x objective used here, only portions of the entire contraction could lie in the field of view, thus three image sequences of the contraction inlet, midsection and outlet, respectively were combined to obtain the velocity profile along the entirety of the contraction. The x-component of the centerline velocity at a particular x-position was taken as the average of the x-component of the velocity vectors in the middle third of the outlet width of the contraction (*i.e.* $y = \pm 8.3$ μm). Error bars in the velocities seen in the velocity profile plots in Section 5.2 correspond to the standard deviation of those data points.

3.2.3 ABRIO^{TM} System (CRi, Inc.)

The ABRIO^{TM} imaging system is a commercially available instrument, provided by CRi, Inc., originally designed to measure the birefringence of biological samples. The system can make pixelwise resolved measurements of birefringence, and it can measure retardance to within 0.02 nm.

With little modification this system has been used in the study described in this thesis to measure the birefringence of flowing complex fluids in microscale geometries.

The basic components of the device are the interference filter and circular polarizer, the liquid crystal compensator optic and the CCD camera. The optical train, or combination of optical elements, of this device may be viewed in Figure 3.2.9.

The white light source, interference filter and circular polarizer together provide a monochromatic ($\lambda = 546$ nm), circularly polarized light wave. This light wave then impinges on a sample with retardance, δ, and extinction angle, Θ. The wave then passes through a liquid crystal compensator containing two birefringent media with fixed extinction angles and variable, but known retardances, α and β, and a linear polarizer with a fixed orientation. The emerging light beam then impinges on a detector, which measures the intensity of the beam. The ratio of this measured final intensity, I, and the initial intensity of the beam, I_{in} depends on these parameters according to the following relation:

$$\frac{I}{I_{in}} = \frac{1}{2}\{1 + \cos(\alpha)\sin(2\Theta)\sin(\delta) + \cos(\delta)\cos(\beta)\sin(\alpha) - \cos(2\Theta)\sin(\delta)\sin(\alpha)\sin(\beta)\} \tag{3.2.3}$$

The operating premise of the ABRIO system is presented in Shribak & Oldenbourg (2003), but a simplified description of the system will be offered here. In the taking of a single birefringence measurement of a sample, the ABRIO system actually takes five images of that sample, varying the birefringence of the liquid crystal compensator according to the five frame algorithm listed in Table 3.2.2. Five separate measurements are required to apply the background correction as well as account for any absorbance of light by the sample. Here α and β are the variable retardances of the liquid crystal compensator as described above, while θ is called the swing angle, which can also be varied depending on the prevailing specimen retardance, to obtain accurate measurements, with a typical value around 0.17 radians (10^o). Once the five intensities have been measured, the parameters, A and B, may be calculated from Eq. 3.2.4, from which the sample retardance and extinction angle may be determined from Eq. 3.2.5 and 3.2.6. Algorithms that require as few as two measurements of in-

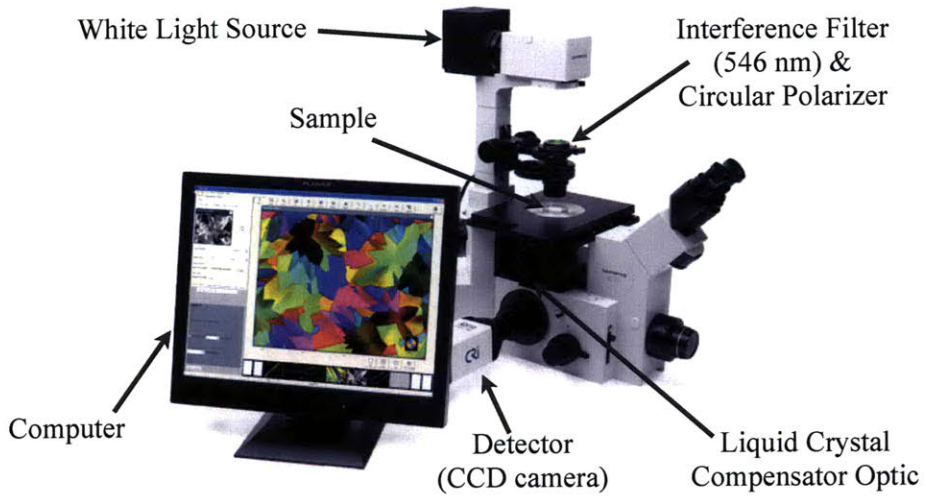

(a) ABRIO system retrofit to a standard inverted optical microsope. Image courtesy of CRi, Inc.

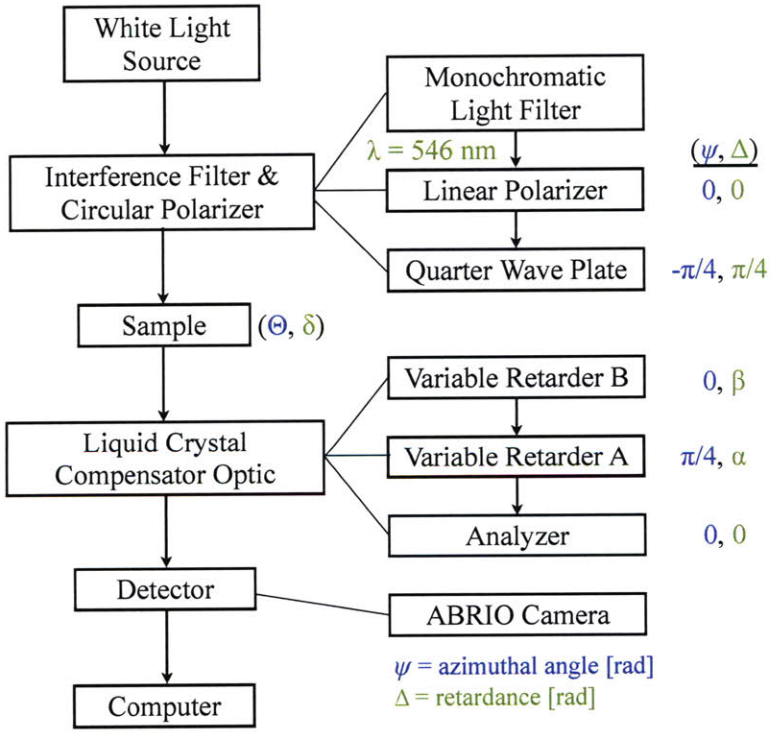

(b) Flow diagram of the optical train in the ABRIO system.

Figure 3.2.9: ABRIO Optical Train.

tensity are also described in Shribak & Oldenbourg (2003), and although they allow for faster image acquisition, they are accordingly less accurate.

Table 3.2.2: Five frame algorithm for the ABRIO system.

Measurement Number	α	β	Measured Intensity
0	$\pi/2$	π	I_0
1	$\pi/2-\theta$	π	I_1
2	$\pi/2+\theta$	π	I_2
3	$\pi/2$	$\pi-\theta$	I_3
4	$\pi/2$	$\pi+\theta$	I_4

$$\begin{aligned} A &= \frac{I_1-I_2}{I_1+I_2-2I_0}\tan\left(\frac{\theta}{2}\right) = \sin(2\Theta)\tan(\delta) \\ B &= \frac{I_4-I_3}{I_4+I_3-2I_0}\tan\left(\frac{\theta}{2}\right) = \cos(2\Theta)\tan(\delta) \end{aligned} \tag{3.2.4}$$

$$\delta = \begin{cases} \arctan(\sqrt{A^2+B^2}) & \text{if } I_1+I_2-2I_0 \geq 0 \\ \pi - \arctan(\sqrt{A^2+B^2}) & \text{if } I_1+I_2-2I_0 < 0 \end{cases} \tag{3.2.5}$$

$$\Theta = \begin{cases} \frac{1}{2}\arctan\left(\frac{A}{B}\right) & \text{for } A \geq 0 \;\&\; B \geq 0 \\ \frac{\pi}{2}+\frac{1}{2}\arctan\left(\frac{A}{B}\right) & \text{for } B < 0 \\ \pi+\frac{1}{2}\arctan\left(\frac{A}{B}\right) & \text{for } A < 0 \;\&\; B \geq 0 \end{cases} \tag{3.2.6}$$

For measurements made by the ABRIO system, Θ always coincides with the orientation of the slow optical axis.

The ABRIO system can also apply a background correction to account for any residual birefringence of the sample. This correction is made by taking some user-specified background image, determining the birefringence in this image, calculating the initial A_{bg} and B_{bg} of the image, and then subtracting the values of A_{bg} and B_{bg}, respectively, from the A_{im} and B_{im} of all subsequent images, to obtain the A and B, which ABRIO uses for Eq. 3.2.5 and 3.2.6. Although this correction may seem trivial to make, it is only applicable when the birefringence of the sample and

background are small compared to the wavelength of incident light. The justification of this background correction is presented in Shribak & Oldenbourg (2003).

For the tests with the straight channel, two sets of experiments with different background corrections were completed. To determine the evolution of the birefringence profiles along the length of the channel, a background image was taken without the channel in view, in order to remove any parasitic birefringence caused by the optical train. Accordingly, any residual birefringence of the channel was not accounted for in these images so as not to apply a background correction for a particular location of the channel to images at other locations. Therefore the results obtained for the evolution of the birefringence profiles have not been corrected for any additional birefringence caused by the channel. In a second set of experiments, a single viewing location along the length of the channel was selected and a background image was taken of the channel at that location filled with the stagnant test fluid. Accordingly, in this second set of experiments, the residual birefringence of the channel was taken into account. In order to minimize possible blurring of the measured birefringence, as discussed in Appendix E, the aperture of the incident light was reduced to the minimum amount for which the ABRIO system could obtain a strong enough signal to take measurements. For the straight channel experiments, the aperture was about $\theta_{min} \approx 2^o$ as depicted in Figure E.2.2 (a). The channel walls were also constructed of an opaque material preventing extraneous light from entering the field of view. Glycerine, a non-birefringent fluid, was pumped through the channel at a relatively high calculated wall shear stress of 30 Pa, in order to determine if stress-induced birefringence in the channel itself was significant. At this wall shear stress no change in the birefringence of the channel was observed.

For experiments with the hyperbolic contraction, a background image was taken with the contraction filled with the stagnant test fluid in view. For the hyperbolic contractions the aperture of the incident light was around 1^o.

3.3 Summary

In this chapter, the conventional experimental methods used to measure the rheological behavior in shear and extension of the two worm-like surfactant systems studied in this thesis have been addressed. Furthermore, the techniques for observing their rheological behavior in microfluidic devices have also been presented. The kinematics associated with the flow of these systems at this small scale may be determined with μ-PIV and molecular conformation as well as some indication of material stresses may be observed with measurements of flow-induced birefringence using the ABRIO system. Combining the measurements, we may begin to probe the poorly understood high deformation rate ($\dot{\gamma} \gg \lambda_M^{-1}$ and $\dot{\varepsilon} \gg \lambda_M^{-1}$) rheology of worm-like, micellar systems.

Chapter 4

Shear Deformations

In this section, the results of experiments designed to investigate the rheological behavior of the two test fluids undergoing steady shearing deformations are discussed. Fully developed and developing flow in a long, high aspect ratio rectangular duct was examined. Velocity profiles were determined from measurements with μ-PIV as described in Section 3.2.2 using fluid samples seeded with fluorescent tracer particles. In separate experiments using the same rectangular duct and fluid samples without tracer particles, indirect measurements of stress and molecular orientation in the flowing test fluids were made using measurements of flow-induced birefringence following the technique presented in Section 3.2.3.

4.1 Dimensional Analysis

Dimensional analysis is the process by which the relevant parameters for a physical phenomenon (*e.g.*, length, time, mass *etc.*) may be systematically compared in order to determine their relative significance in analyzing that phenomenon. If done properly, dimensional analysis may be used to characterize the phenomenon in a universal way. Typically, the result of dimensional analysis is a set of dimensionless numbers which are commonly ratios of lengthscales, timescales, or some other physical quantity.

Flows of complex fluids at the microscale may be characterized by the *Weissenberg* number, Wi, *Deborah* number, De, which are both ratios of a material time scale to an experiment time scale, the *Reynolds* number, Re and the *elasticity* number, El, which is the ratio Wi/Re as used by Rodd *et al.* (2005), Rodd *et al.* (2007) and Oliveira *et al.* (2007). Within the framework of this thesis, Wi and De are two distinct quantities. Wi is the ratio of a material time to a characterisitic time of deformation, while De is the ratio of a material time to the analogue of a residence time as described in McKinley *et al.* (1996). As usual, Re is the ratio of inertial stresses and viscous stresses and is less than unity for the experiments in this study. El is commonly viewed as the ratio of elastic stresses to inertial stresses, but it may also be associated with the ratio between the kinematic viscosity of the material, ν, and a representative elastic diffusivity constant taken as the square of some relevant length scale, l_{char}, divided by the relaxation time of the material, λ_M, such that $El = \nu/(l_{char}^2/\lambda_M)$, ((McKinley (2005)).

For the flow of a micellar solution in the rectangular microchannel used in this study, the relevant physical parameters are

- the height of the channel, H, [m]
- the width of the channel, W, [m]
- the distance downstream of channel entrance, where flow is observed, L_{obs}, [m]
- the imposed volumetric flow rate, Q, [m^3/s]
- the density of the fluid, ρ, [kg/m^3]
- the zero-shear rate viscosity of the fluid, η_0, [Pa.s]
- the relaxation time of the fluid, λ_M, [s]

Additional relevant parameters, that are not independent of those listed above are the hydraulic diameter, $D_h = 2HW/(H+W)$ and the average fluid velocity in the channel, $\langle U \rangle = Q/WH$.

According to the Buckingham Π-theorem given by Buckingham (1914), for N parameters described by P fundamental physical dimensions, $K = N - P$ dimensionless groups are necessary to fully specify a physical phenomenon. Therefore, for the experiment considered here with the $N = 7$ listed parameters encompassing $P = 3$ physical quantities, $K = 4$ dimensionless groups are required, three of which are the aforementioned Re, Wi and De, and the fourth is the aspect ratio of the channel, A^*.

The aspect ratio of the channel is defined as the ratio of the channel height to its width.

$$A^* = \frac{H}{W} \tag{4.1.1}$$

For the channel used in this study, $H = 1000$ μm, and $W = 130$ μm, so $A^* \approx 8$, which is large enough that the flow can be considered to be predominantly two-dimensional throughout the majority of the channel. In this limit the hydraulic diameter also reduces to $D_h \approx 2W$.

The Reynolds number is defined using the hydraulic diameter, which is the appropriate lengthscale for relating the influence of inertia and viscosity.

$$Re = \frac{\rho \langle U \rangle D_h}{\eta_0} = \frac{\rho Q D_h}{\eta_0 H W} \tag{4.1.2}$$

For all flow rates observed in this study, $Re \ll 1$, indicating that inertial turbulence was never a possibility. This ratio could also have been defined in terms of a rate dependent characteristic viscosity, (*i.e.* $\eta(\dot{\gamma}_c)$ with $\dot{\gamma}_c = \langle U \rangle / W$), in which case the characteristic viscosity could be taken from the flow curves measured with VROC in Figure 3.1.11. Even a conservative estimate of highest Re would have been of order one, which is again far from the critical Reynolds number required for the onset of turbulence (*i.e.* $Re_c \approx 2000$). This Reynolds number was also used in the correlation for small Re given in Pipe *et al.* (2008) for determining the entrance length for a Newtonian fluid, $L_e = D_h(0.6/(1+0.035Re)+0.056Re)$. According to this correlation, for all Re observed in this study $L_e \ll L_{obs}$, and accordingly, neglecting the influence of elastic stresses on the flow, the flow was taken to be kinematically fully developed.

Since the flow was visualized in two-dimensional planes, the lengthscale in the Weissenberg number was taken to be the channel width. The characteristic deformation rate was therefore considered to be $\dot{\gamma}_c = \langle U \rangle / W$.

$$Wi = \frac{\lambda_M \langle U \rangle}{W} \tag{4.1.3}$$

For $Wi \sim 1$, deformations occurred on timescales roughly equal to the relaxation time of the fluid and the onset of non-Newtonian behavior was observed. As the magnitude of the Weissenberg number was increased, strong departures from Newtonian behavior were observed, including shear thinning and considerable elastic stresses.

The Deborah number is defined as the ratio of the fluid relaxation time to what may be considered the residence time of the fluid in the channel for a particular observation distance.

$$De = \frac{\lambda_M \langle U \rangle}{L_{obs}} \tag{4.1.4}$$

The magnitude of De gave an indication for how fully the flow was expected to have developed at the point of observation. For $De \ll 1$, sufficient time had elapsed for the elastic stresses to have developed and the flow could be taken as fully developed.

An additional dimensionless ratio is the elasticity number which is defined

$$El = \frac{Wi}{Re} = \frac{\lambda_M \eta_0}{\rho W D_h} \tag{4.1.5}$$

This number is independent of the dynamics of the flow, since it depends only on the properties of the fluid and dimensions of the channel. For both fluids, $El \gg 1$, indicating that inertial stresses were negligible compared to elastic stresses for the experiments discussed in this section.

The range of magnitudes of these dimensionless groups experimentally realized in the study of flow through a straight channel are given in Table 4.1.1.

Table 4.1.1: Range of flow rates and dimensionless parameters experimentally considered for flow in a straight, high aspect ratio rectangular duct with 100:60 mM CPyCl:NaSal (El = 7.0 x 10^7) and 30:240 CTAB:NaSal (El = 2.4 x 10^6) solutions at 22-23^o C.

10 μL/hr	$\leq$	Q	$\leq$	10^4 μL/hr
10^{-8}	$\leq$	Re	$\leq$	10^{-3}
10^{-1}	$\leq$	Wi	$\leq$	10^3
10^{-3}	$\leq$	De	$\leq$	10

4.2 Flow Kinematics

In this section, the simplified governing equations for the flow of the test fluids considered in this thesis are presented and solved. Experimental results obtained from micro-particle image velocimetry are also presented and discussed. Information regarding the depth of measurement and data processing scheme may be found in Section 3.2.2. Finally, the experimental results are compared with the predictions of the Ellis model as a metric for gauging the suitability of this model in predicting the measured flow-induced birefringence of these fluids that is considered in Section 4.3.

4.2.1 Anticipated Velocity Profiles: Theoretical Formulation

For fully developed, inertialess flow along the x-axis of a rectangular duct having length, L, width, W, along the y-axis and height, H, along the z-axis and height depicted in Figure 3.2.8, the governing equation of motion is

$$0 = \frac{\partial \tau_{xx}}{\partial x} + \frac{\partial \tau_{yx}}{\partial y} + \frac{\partial \tau_{zx}}{\partial z} - \frac{\partial P}{\partial x} \tag{4.2.1}$$

where τ_{ij} is a deviatoric stress and P is pressure.

Provided the dimensions of the duct are such that $W \ll H \ll L$, which is approximately the case for the channel used in this study, Eq. 4.2.1 may be simplified to

$$\frac{\partial P}{\partial x} = \frac{\partial \tau_{yx}}{\partial y} \tag{4.2.2}$$

Eq. 4.2.2 may be solved to obtain a velocity profile if a suitable constitutive equation relating deviatoric stresses to flow kinematics is selected. For this study, the Ellis model has been used for reasons discussed earlier, but results for both a Newtonian and a Power-Law fluid, (Bird *et al.* (1987)), are also considered in Appendix B. The velocity profile, u_x, for an Ellis model fluid in a rectangular duct whose walls are at $y = \pm\frac{W}{2}$ is derived fully in Appendix B, and it is

$$u_x = \frac{\tau_{wall}}{4\eta_0} W \left[\left(1 - \frac{4y^2}{W^2} \right) + \frac{2}{\alpha + 1} \left(\frac{\tau_{wall}}{\tau_{1/2}} \right)^{\alpha - 1} \left(1 - \left| \frac{2y}{W} \right|^{\alpha + 1} \right) \right] \tag{4.2.3}$$

where η_0, $\tau_{1/2}$ and α are fitted parameters from the Ellis model, τ_{wall} is the shear stress at the walls of the channel, which is related to the pressure gradient, such that $\tau_{wall} = \frac{1}{2} W \frac{dP}{dx}$ and the no slip boundary condition at the walls is applied.

The shear rate, $\dot{\gamma}_{xy}$, at any position across the width of the channel is the derivative of Eq. 4.2.3 with respect to y

$$\dot{\gamma}_{xy} = -\frac{\tau_{wall}}{\eta_0} \frac{2y}{W} \left[1 + \left(\frac{\tau_{wall}}{\tau_{1/2}} \right)^{\alpha - 1} \left| \frac{2y}{W} \right|^{\alpha - 1} \right] \tag{4.2.4}$$

Eq. 4.2.3 can also be integrated across the width and height of the channel to obtain the total volumetric flow rate, Q, from which the average velocity in the channel, $\langle U \rangle$, may also be determined

$$\langle U \rangle = \frac{Q}{WH} = \frac{\tau_{wall}}{6\eta_0} W \left[1 + \frac{3}{\alpha + 2} \left(\frac{\tau_{wall}}{\tau_{1/2}} \right)^{\alpha - 1} \right] \tag{4.2.5}$$

In the experiments discussed in this thesis, the volumetric flow rate, Q, was prescribed, not the wall shear stress, τ_{wall}. Therefore, in order to determine the velocity profile for a given Q, the corresponding τ_{wall} must be determined by iteration of

Eq. 4.2.5. In this manner, the predicted velocity profiles in Figures 4.2.3 and 4.2.5 were obtained for comparison with the experimentally measured results.

4.2.2 CPyCl Solution

Velocity profiles for the CPyCl solution may be seen in Figures 4.2.1 (a), 4.2.2 and 4.2.3. The most general feature in these profiles is the transition from a mixed Newtonian and shear banding profile at low Wi to a very markedly shear banding, nearly perfect plug-like profile, with $u_{x,max} = \langle U \rangle$ at moderate Wi. At higher $Wi > 1$ a departure from perfect plug-like flow, for which $u_{x,max} = \langle U \rangle$, and increased thickness of the shear banding layer may be observed.

Three dimensional velocity profiles may be seen in Figure 4.2.2. At the lowest Weissenberg number, the velocity profile varied considerably along the height (z-axis) of the channel since this $Wi = 1$ coincided with the transition from a Newtonian-like flow profile to a shear banding profile seen at higher Wi. For all higher Wi, the velocity profiles were uniform, and plug-like throughout the channel height.

An additional noteworthy feature in the velocity profiles, especially at low Wi is what appears to be evidence of slip between the fluid and the channel walls. This apparent slip at the lowest Wi was likely an artifact of very thin shear banding layers, predicted by the Ellis model, which were too thin to be resolved by the μ-PIV system. The thickness of the shear banding layers can be estimated by assuming the classical picture of a shear banding fluid flowing in a channel as described in Section 2.3, whereby the shear rate within the band is assumed to be $\dot{\gamma}_2 \approx 500$ s^{-1} which lies at the end of the stress plateau of the CPyCl system seen in Figure 3.1.11 (a). To first order, this thickness of the shear banding layer is $\delta_{SB} \approx \langle U \rangle / \dot{\gamma}_2$. For $Wi = 1$ and $Wi = 5$, $\langle U \rangle = 47$ μm/s and $\langle U \rangle = 180$ μm/s, respectively, and hence $\delta_{SB} \approx 0.1$ μm and $\delta_{SB} \approx 0.4$ μm, respectively. For the μ-PIV system used for theses experiments, the minimum resolvable feature $e/M = 0.65$ μm as listed in Table 3.2.1 and accordingly the shear banding layer is too thin to be resolved at low Wi.

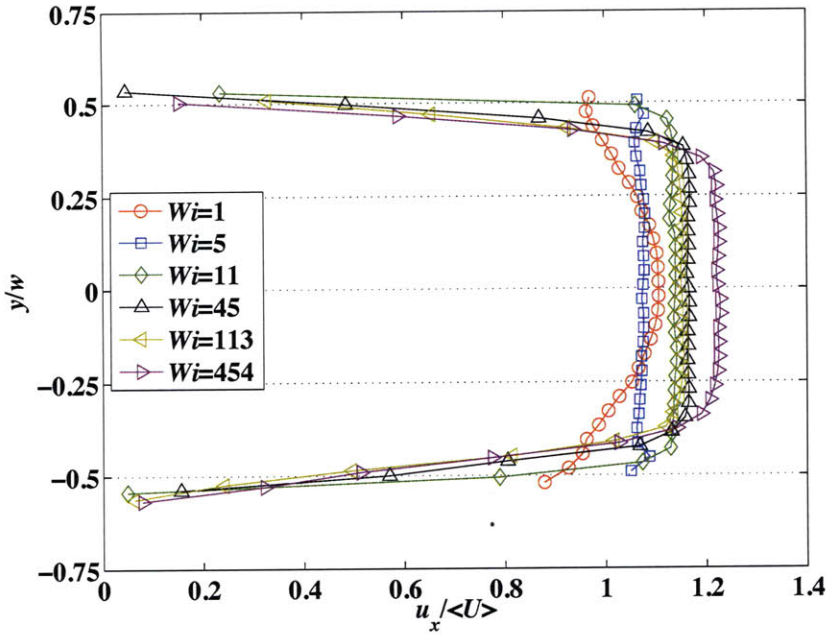

(a) 100:60 mM CPyCl:NaSal.

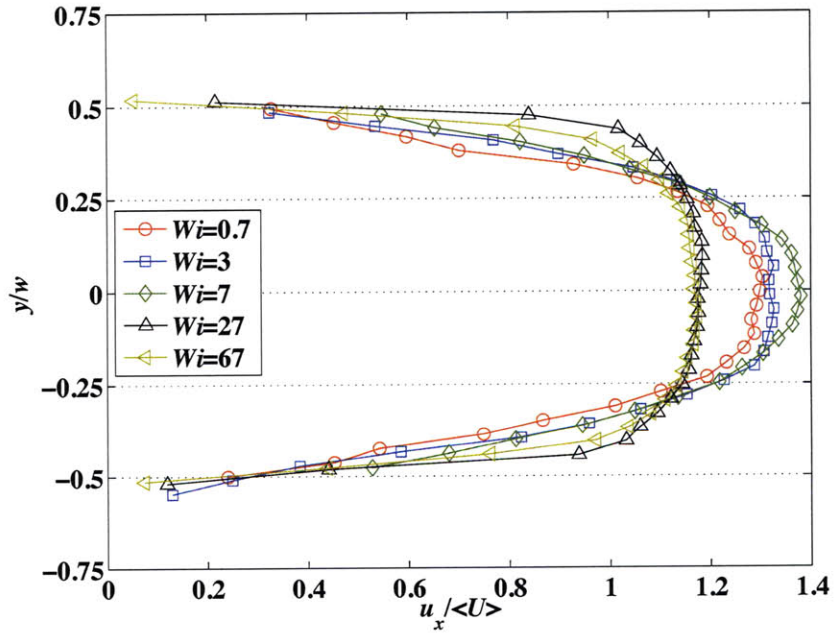

(b) 30:240 mM CTAB:NaSal.

Figure 4.2.1: Representative non-dimensionalized experimental velocity profiles at increasing Wi in the rectangular duct taken at 200 to 300 μm above the bottom of the channel. $L_{obs} = 3.5$ cm.

At high Wi estimates of a slip velocity are confounded by the uncertainty in exact position of the channel walls. This uncertainty can be attributed in part to slight variations on the order of 5 μm $(0.04W)$ in the channel width at varying heights in the channel. Further complexity in deciphering the exact position of the channel walls may have been caused by reflection and refraction of light off the channel walls leading to a slight blurring of the walls.

The Ellis model predictions may be seen in Figure 4.2.3 to capture the experimentally measured velocity profiles at low to moderate $Wi \leq 10$ to within experimentally resolvable limits. This result confirms the ability of the Ellis model to predict global changes in the velocity profile arising from the strongly rate dependent viscosity. The discrepancy between the model predictions and experimental results especially at high $Wi \gg 10$, however, is possibly due to the confining effects of the upper and lower channel walls on account of the moderate aspect ratio of the channel, and also the inability of the Ellis model to precisely capture the underlying shear banding dynamics associated with the CPyCl solution.

4.2.3 CTAB Solution

Velocity profiles of the CTAB solution may be seen in Figures 4.2.1 (b), 4.2.4 and 4.2.5. The CTAB solution exhibits a very clear transition from a parabolic-like velocity profile associated with the flow of a Newtonian fluid at low $Wi \leq 1$, to a U-like velocity profile associated with the flow of a moderately shear thinning fluid at moderate to high $Wi \gg 1$.

It is clear from the three dimensional velocity profiles in Figure 4.2.4, that only at moderate to large $Wi \geq 7$ was the velocity profile uniform along the majority of the height (z-axis) of the channel. The most extreme example of deviation from uniformity along the channel height occurred for $Wi = 0.7$ and may be seen in Figure 4.2.4 (a). The unusual velocity profiles may caused by the interfacial instability studied by Fielding & Olmsted (2006) and Fielding & Wilson (2010), although this feature is

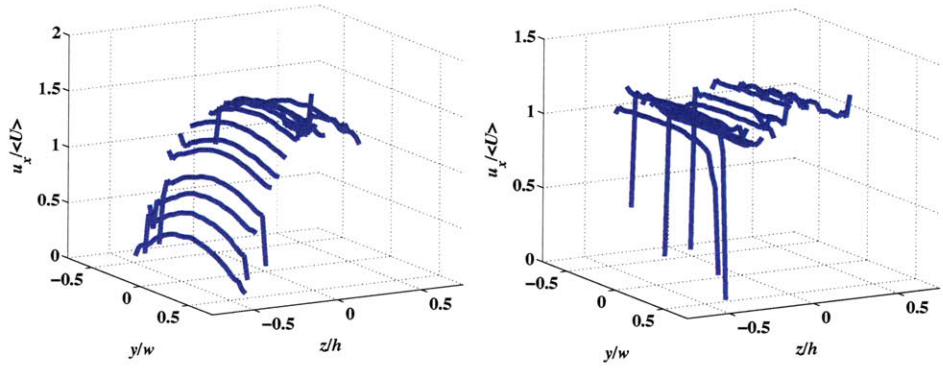

(a) $Wi = 1$, $Q = 25$ μL/hr. (b) $Wi = 5$, $Q = 100$ μL/hr.

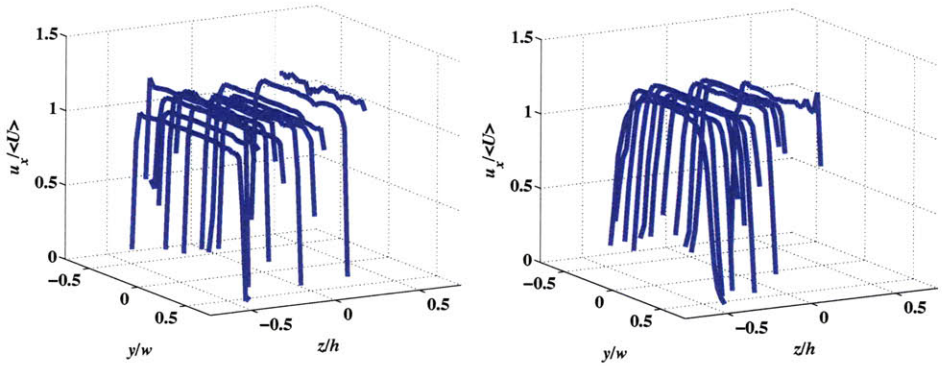

(c) $Wi = 11$, $Q = 250$ μL/hr. (d) $Wi = 45$, $Q = 1,000$ μL/hr.

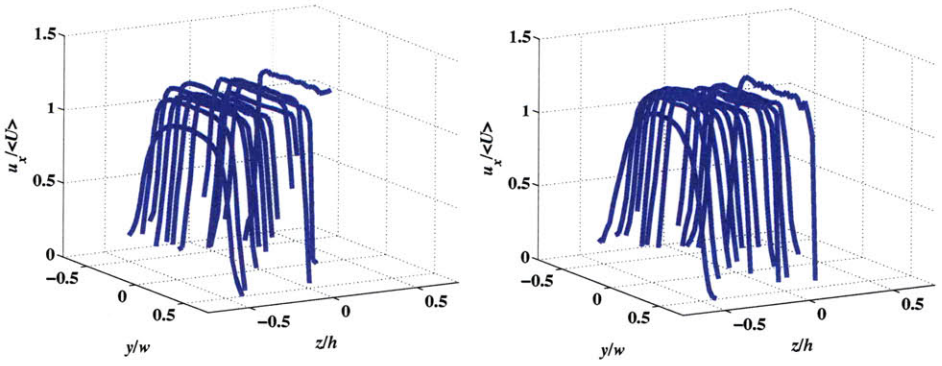

(e) $Wi = 113$, $Q = 2,500$ μL/hr. (f) $Wi = 454$, $Q = 10,000$ μL/hr.

Figure 4.2.2: Non-dimensionalized experimental velocity profiles at increasing Wi for the 100:60 mM CPyCl:NaSal solution in the rectangular duct taken at $50 \leq z \leq 900$ μm above the bottom of the channel. $L_{obs} = 3.5$ cm.

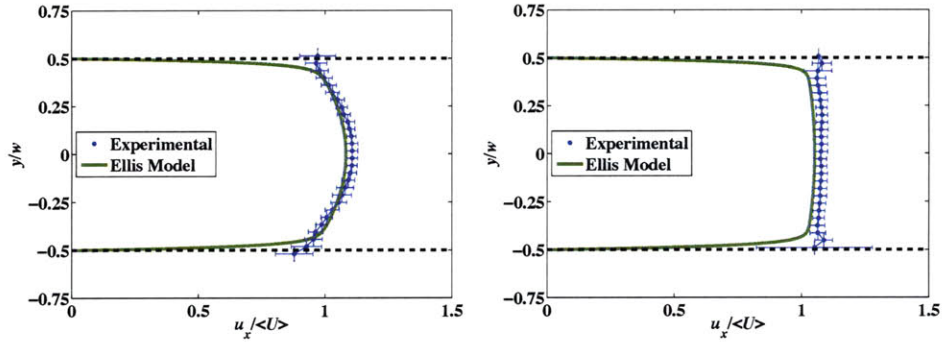

(a) $Wi = 1$, $Q = 25$ μL/hr.

(b) $Wi = 5$, $Q = 100$ μL/hr.

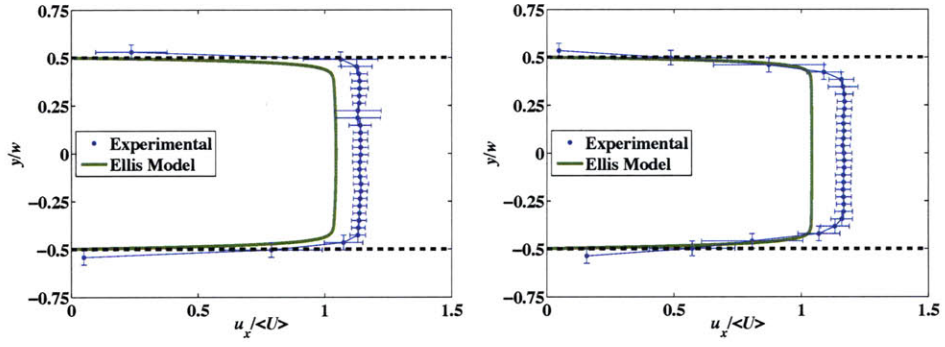

(c) $Wi = 11$, $Q = 250$ μL/hr.

(d) $Wi = 45$, $Q = 1,000$ μL/hr.

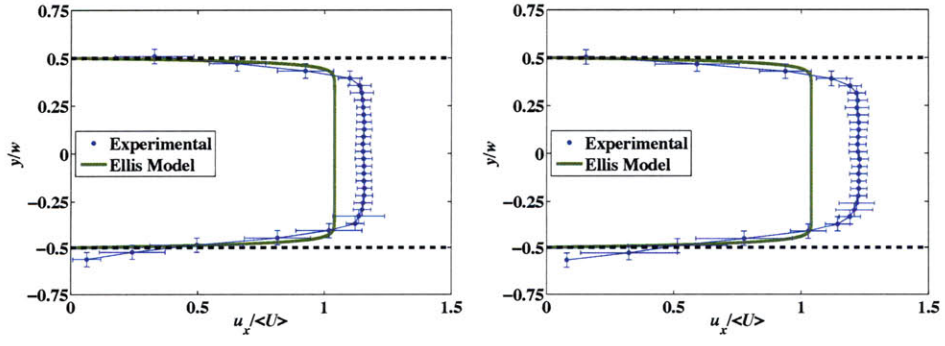

(e) $Wi = 113$, $Q = 2,500$ μL/hr.

(f) $Wi = 454$, $Q = 10,000$ μL/hr.

Figure 4.2.3: Representative non-dimensionalized experimental and predicted velocity profiles at increasing Wi for the 100:60 mM CPyCl:NaSal solution in the rectangular duct taken at 200 to 300 μm above the bottom of the channel. $L_{obs} = 3.5$ cm.

particularly perplexing because it occured in a predominantly shear thinning, but not shear banding fluid. Velocity profiles at lower Wi could not be observed in this fluid due to limitation in the maximum time step ($\Delta t_{max} = 60,000$ μs) between images that could be taken with the μ-PIV system.

Two dimensional velocity profiles are portrayed in Figure 4.2.5. The Ellis model is capable of predicting only some features of the velocity profiles observed for the CTAB solution. In its two dimensional form, it is clearly incapable of capturing the gradients along the z-axis seen in Figure 4.2.4 (a), which may be related to the hysteretic behavior for this system seen in Figure 3.1.11 (c) for $5 \leq \dot{\gamma}_{apparent} \leq 50$ s^{-1}. At intermediate Wi, the experimental and predicted model match, but at the highest $Wi \geq 27$ observed, the measured shear rate near wall is greater than the predicted value. This deviation from predicted behavior indicates a reduced viscosity than that predicted by the Ellis model at the corresponding shear rate. Estimates of the shear rate near the wall at $Wi \geq 27$ using the Ellis model are on the order of 100 s^{-1}. This high rate coincides roughly with the end of the apparent stress plateau observed for this fluid in Figure 3.1.11 (c). On account of these results, it is evident that for the Ellis model parameters for CTAB listed in Table 3.1.3, this model is capable of capturing the experimentally observed velocity profiles most faithfully for $Wi = 7$.

4.3 Stress and Birefringence

In this section, the methodology for predicting the shear stress and first normal stress difference in the fluids flowing in the channel is presented. The predicted stresses are then related to the optical anisotropy by the stress optical rule in Eq. 4.3.3, which is then compared to the measured results. The background correction discussed in Section 3.2.3 was applied to all images unless otherwise noted. Finally the suitability of the ABRIO system for measuring the flow-induced birefringence of worm-like micellar solutions in microscale flows is discussed.

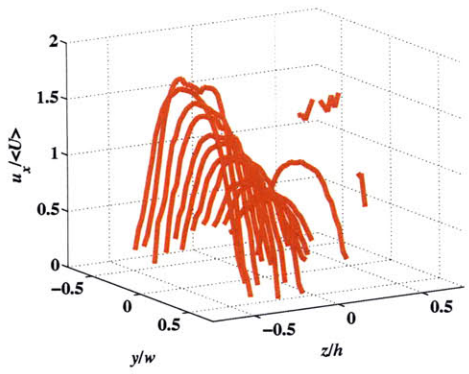

(a) $Wi = 0.7$, $Q = 25$ μL/hr.

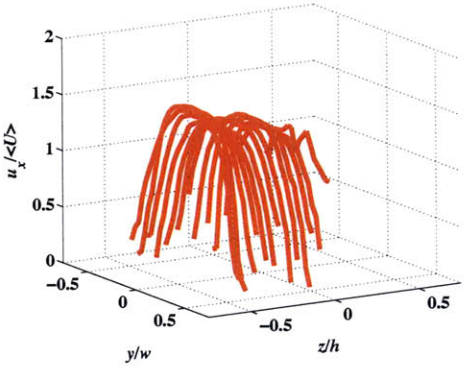

(b) $Wi = 3$, $Q = 100$ μL/hr.

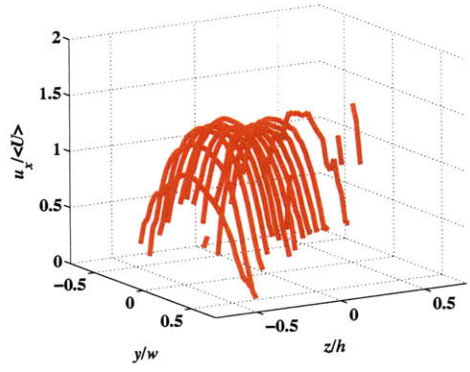

(c) $Wi = 7$, $Q = 250$ μL/hr.

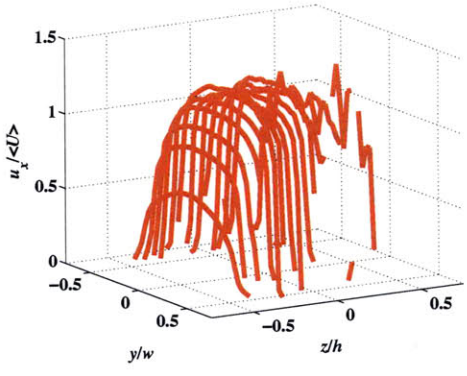

(d) $Wi = 27$, $Q = 1,000$ μL/hr.

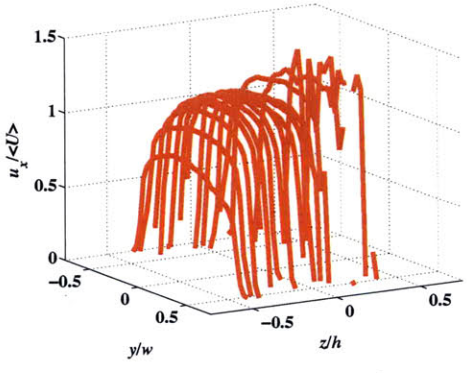

(e) $Wi = 67$, $Q = 2,500$ μL/hr.

Figure 4.2.4: Non-dimensionalized experimental velocity profiles at increasing Wi for the 30:240 mM CTAB:NaSal solution in the rectangular duct taken at $50 \leq z \leq 900$ μm above the bottom of the channel. $L_{obs} = 3.5$ cm.

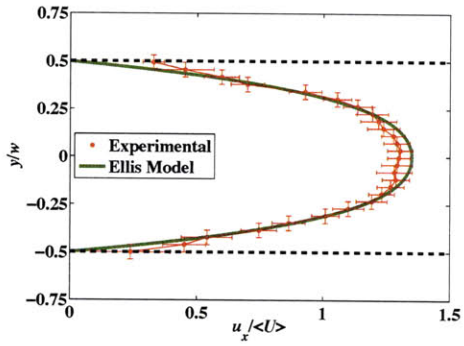

(a) $Wi = 0.7$, $Q = 25$ μL/hr.

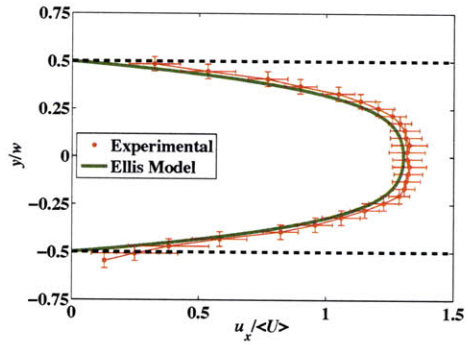

(b) $Wi = 3$, $Q = 100$ μL/hr.

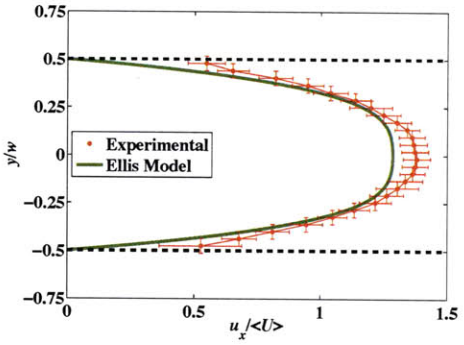

(c) $Wi = 7$, $Q = 250$ μL/hr.

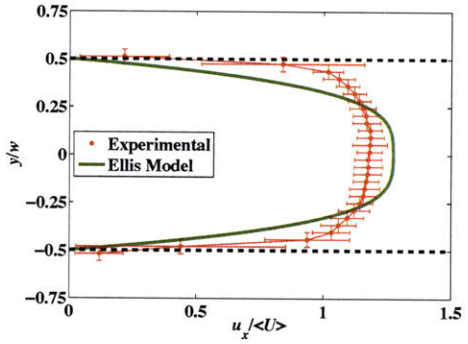

(d) $Wi = 27$, $Q = 1,000$ μL/hr.

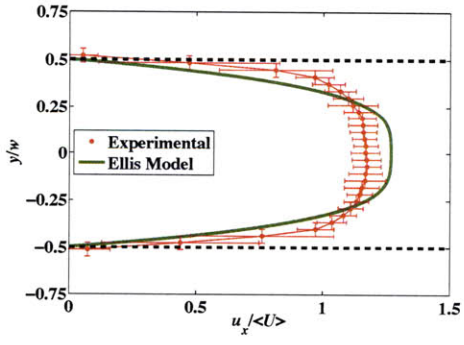

(e) $Wi = 67$, $Q = 2,500$ μL/hr.

Figure 4.2.5: Representative non-dimensionalized experimental and predicted velocity profiles at increasing Wi for the 30:240 mM CTAB:NaSal solution in the rectangular duct taken at 200 to 300 μm above the bottom of the channel. $L_{obs} = 3.5$ cm.

4.3.1 Anticipated Stress Profiles: Theoretical Formulation

In addition to being used to predict the velocity profiles in the channel, the Ellis model was used to predict the shear and normal stresses in the channel. It is shown in Appendix B that for fully developed flow of any material in a high aspect ratio duct, the magnitude of the shear stress, τ_{xy}, varies linearly with position between $-\tau_{wall}$ and τ_{wall}, and it is therefore necessarily zero at the centerline of the channel. For a given volumetric flow rate, Q, once τ_{wall} is specified for Eq. 4.2.5, the shear stress at all positions across the width of the channel is known. The shear stress follows the relation

$$\tau_{xy} = -\tau_{wall}\frac{2y}{W} \tag{4.3.1}$$

The elastic stresses in the channel were predicted by interpolation of N_1 with shear rate, as calculated from Eq. 4.2.4, from the normal stress data obtained on a rotational rheometer.

At flow rates high enough that the shear rate predicted by Eq. 4.2.4 at a particular y-value was greater than the shear rates for which data from the rotational rheometer were obtained, no estimate of shear and normal stresses were made. For this reason the predicted profiles of retardance and azimuthal angle for high Wi do not extend completely to the walls in Figures 4.3.4 and 4.3.8.

The calculated deviatoric stresses, τ_{xy} and N_1, at any position in the channel were used to calculate the principal stress difference, $\Delta\sigma$ from

$$\Delta\sigma = \sqrt{N_1 + 4\tau_{xy}^2} \tag{4.3.2}$$

This value was then used to predict the optical anisotropy, Δn, from the stress optical rule in Eq. 4.3.3, presented previously in Section 3.1.3.

$$\Delta n = C\Delta\sigma \tag{4.3.3}$$

Although this rule has been found in the literature to be valid mostly for low Wi flows of micellar solutions as discussed in Section 2.4, for the sake of obtaining a first order estimate of the flow-induced birefringence for the experiments considered here, it's applicability for all Wi in this study has been assumed.

Finally, the optical anisotropy was related to the measured retardance, δ, with the assumption that gradients in the flow along the height of the channel were negligible such that Δn was taken as approximately invariant along the the z-axis. For a lightwave with wavelength, λ, the measured retardance is

$$\delta = 2\pi\Delta n\frac{H}{\lambda} \tag{4.3.4}$$

The anticipated azimuthal angle, which indicates molecular orientation, was calculated from Eq. D.1.14. Since N_1 for these fluids is positive, the ABRIO system has been designed to detect the orientation of the slow optical axis, and the sign of the stress optical coefficient of both micellar systems is negative, the correct expression for the azimuthal angle is then

$$\Theta = \frac{\pi}{2} + \frac{1}{2}\arcsin\left(\frac{2\tau_{xy}}{\sqrt{N_1^2 + 4\tau_{xy}^2}}\right) \tag{4.3.5}$$

For the results presented here, $\Theta = 0^o$ coincides with the direction of flow (x-axis), with Θ increasing counterclockwise, such that $\Theta = 90^o$ coincides with the y-axis.

Eq. 4.3.4 and 4.3.5 have been used to obtain the predicted profiles in Figures 4.3.4 and 4.3.8.

4.3.2 CPyCl Solution

Evolution of the Birefringence Profiles

In order to observe the evolution of the optical anisotropy as the CPyCl solution flowed down the channel, birefringence profiles were measured at L_{obs} = 1.5, 2, 2.5, 3, 3.5 and 4 cm downstream from the inlet of the channel. These measurements were

made having accounted for the residual birefringence of the optical train only, as the alternative of applying a background correction for a particular L_{obs} to all other points of observation along the channel length would have been inaccurate. Accordingly, the residual birefringence caused by the channel was not corrected for in the profiles of Figure 4.3.1.

For a particular value of Wi, the Deborah number, De, is the dimensionless quantity that dictates how fully developed one can expect flow and the optical anisotropy to be.

At predominantly low $Wi < 10$, all De corresponding to the different L_{obs} were considerably less than unity such that the optical anisotropy is fully developed within the length of the channel as is evidenced by the superposition of the profiles. Minor deviations from a symmetric profile for these low Wi were attributed to the residual birefringence of the channel, whose contribution to the measured signal was not insignificant at these low flow rates, being as much as $\delta_{residual} \leq 0.05$ rad in some regions of the channel.

For moderate to high $Wi > 100$, the Deborah number was of order unity within the channel indicating that within the length of the channel a fully relaxed stress profile may not have been observable, thus spatially developing birefringence profiles were observed corresponding to a relaxation of stress within the fluid as it travelled the length of the channel. At the highest $Wi = 454$, the peak magnitude of retardance, occuring in the shear banding layer near the walls as seen in Figure 4.3.1 (f) changed little compared to the gradual decay in retardance in the bulk of the flow. This result suggests that relaxation process occur considerably more rapidly in the banded, high shear rate layer than in the unbanded, low shear rate region of the flow.

Background Corrected Profiles

Measurements of retardance and azimuthal angle, for which the residual birefringence of the channel was corrected, were taken at $L_{obs} = 3.5$ cm. Pseudocolor plots of CPyCl retardance, constructed by the ABRIO system, may be viewed in Figure 4.3.2 and

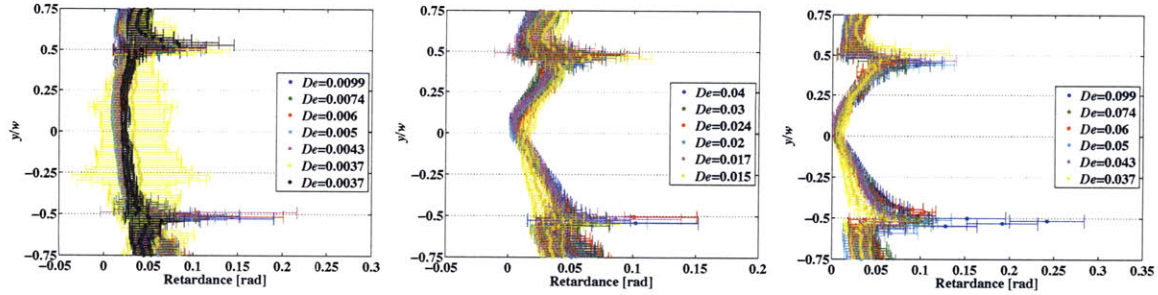

(a) $Wi = 1$, $Q = 25$ μL/hr. (b) $Wi = 5$, $Q = 100$ μL/hr. (c) $Wi = 11$, $Q = 250$ μL/hr.

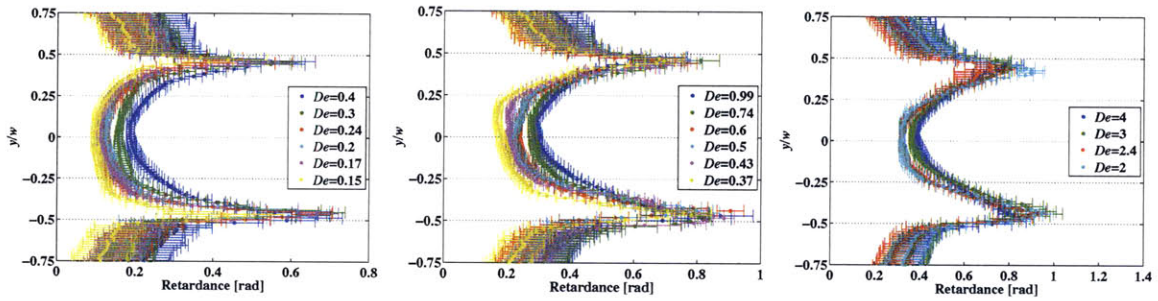

(d) $Wi = 45$, $Q = 1,000$ μL/hr. (e) $Wi = 113$, $Q = 2,500$ μL/hr. (f) $Wi = 454$, $Q = 10,000$ μL/hr.

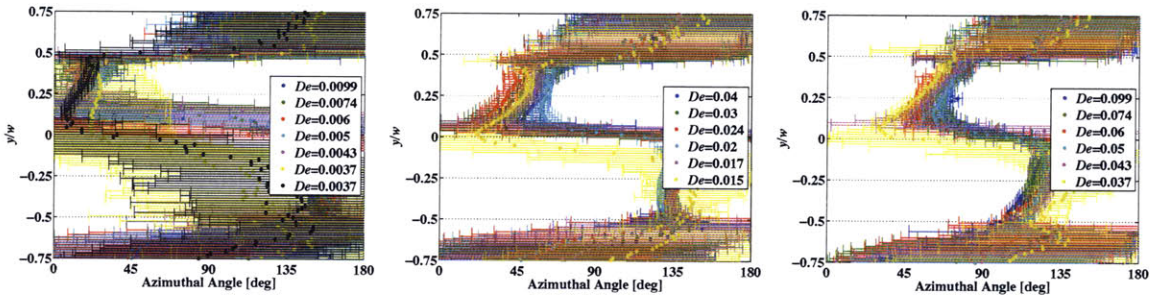

(g) $Wi = 1$, $Q = 25$ μL/hr. (h) $Wi = 5$, $Q = 100$ μL/hr. (i) $Wi = 11$, $Q = 250$ μL/hr.

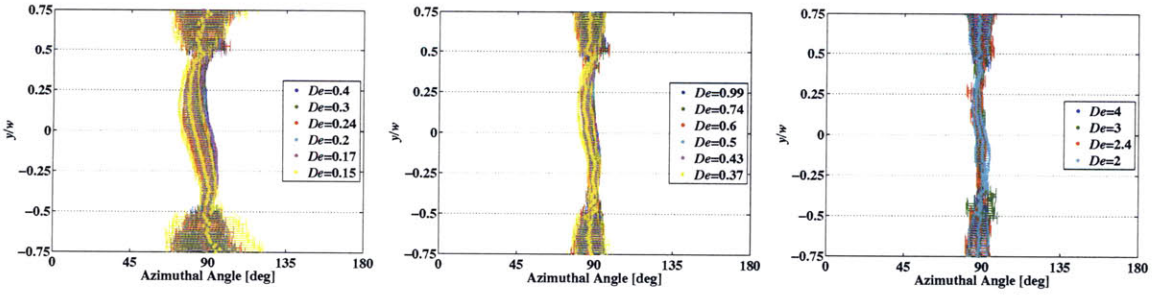

(j) $Wi = 45$, $Q = 1,000$ μL/hr. (k) $Wi = 113$, $Q = 2,500$ μL/hr. (l) $Wi = 454$, $Q = 10,000$ μL/hr.

Figure 4.3.1: Uncorrected retardance ((a)-(f)) and azimuthal angle ((g)-(l)) profiles at different De (different L_{obs}) for the 100:60 mM CPyCl:NaSal solution in the rectangular duct.

the resultant spatially-averaged retardance and azimuthal angle profiles at a selection of Wi may be viewed in Figures 4.3.3 and 4.3.4.

At low $Wi < 5$, the experimental retardance profiles increased linearly from the centerline of the channel to the wall, taking on a V-like profile. Since τ_{xy} varies linearly with position for this type of flow, this result indicates that for low Wi, only τ_{xy} was the predominant contribution to $\Delta\sigma$, given by Eq. 4.3.2, and thus the normal stress difference, N_1, were confined to a thin region near the wall and were not detectable with this measurement system. The linear increase in retardance with position was also predicted by the Ellis model, although exact quantitative agreement may have differed on account of the uncertainty in the true value of the stress optical coefficient, C for this system. A reduction in C by about 50% would have yielded more ideal agreement.

For increasing $Wi > 10$, regions of high, but localized retardance near the walls developed yielding a U-like profile, indicating the growth of high shear rate bands. The change in retardance in the middle of the channel with increasing Wi was gradual when compared to the more rapid change in the high shear rate regions. This small change is qualitatively predicted by the Ellis model and is due to the fact that for this CPyCl system the same wall shear stress is able to span a many fold increase in the average velocity $\langle U \rangle$ and thus Wi.

As seen in Figure 4.3.2, the retardance increases at all y-values with increasing Wi except for in the profile for $Wi = 1135$. This result is likely due to the large value of the Deborah number ($De \approx 5$), indicating that at this high flow rate, the birefringence may not have had substantial time to develop within the length of the channel. The model predictions are clearly least accurate at very high Wi.

The azimuthal angle profiles exhibited odd symmetry about the centerline of the channel. At low Wi, the azimuthal angle was 45^o and 135^o on opposite sides of the channel width as predicted by the Ellis model. These limiting values for Θ predicted by Eq. 4.3.5 reveal that τ_{xy} was indeed considerably greater than N_1 for this flow rate, with the change from 45^o to 135^o having arisen from the change in sign of τ_{xy}

on opposite sides of the channel.

With increasing Wi, the azimuthal angle approached 90^o at all points in the channel, indicating increased elastic stresses and high molecular alignment in the direction of flow. The increased contribution of elastic stresses even in regions of low shear rate can by rationalized by the possibility of diffusion of elastic stresses due to the importance of non-local effects seen for other systems in the work of Masselon *et al.* (2008), for example. Clearly this result was not captured by the predictions of the Ellis model, and more sophisticated models, such as those of Olmsted *et al.* (2000) or Vasquez *et al.* (2007) are needed to capture stress diffusion.

Deviations between experimental and predicted results may been also due to three dimensionality of the flow, although velocity profiles given in Figure 4.2.2 indicate that for moderate to high $5 < Wi < 100$ three dimensional effects in the kinematics at the top and bottom of the channel were confined to around only 10% of the channel height. Some blurring of the measured signal on account of the finite numerical aperture of the incident light may have also have occurred, as discussed in Appendix E.

4.3.3 CTAB Solution

Evolution of the Birefringence Profiles

For the same reasons stated before, the residual birefringence of the channel was not corrected for in the profiles of Figure 4.3.5.

For low to moderate $Wi < 10$, it is apparent that the retardance profiles for all De superpose, with the exception of a slight decay in the retardance at the mid-section of the profile ($y/w = 0$). Since comparatively little change in retardance with decreasing De is observed near the walls where shear rates are highest, the decay in retardance in the middle of the channel suggests that relaxation processes occur more gradually for this CTAB system in regions of low shear rate than in regions of high shear rate.

Only at the high $Wi > 50$ in Figure 4.3.5 (f) can appreciable decay in the retardance be observed for the whole profile, which can be attributed to De being of order

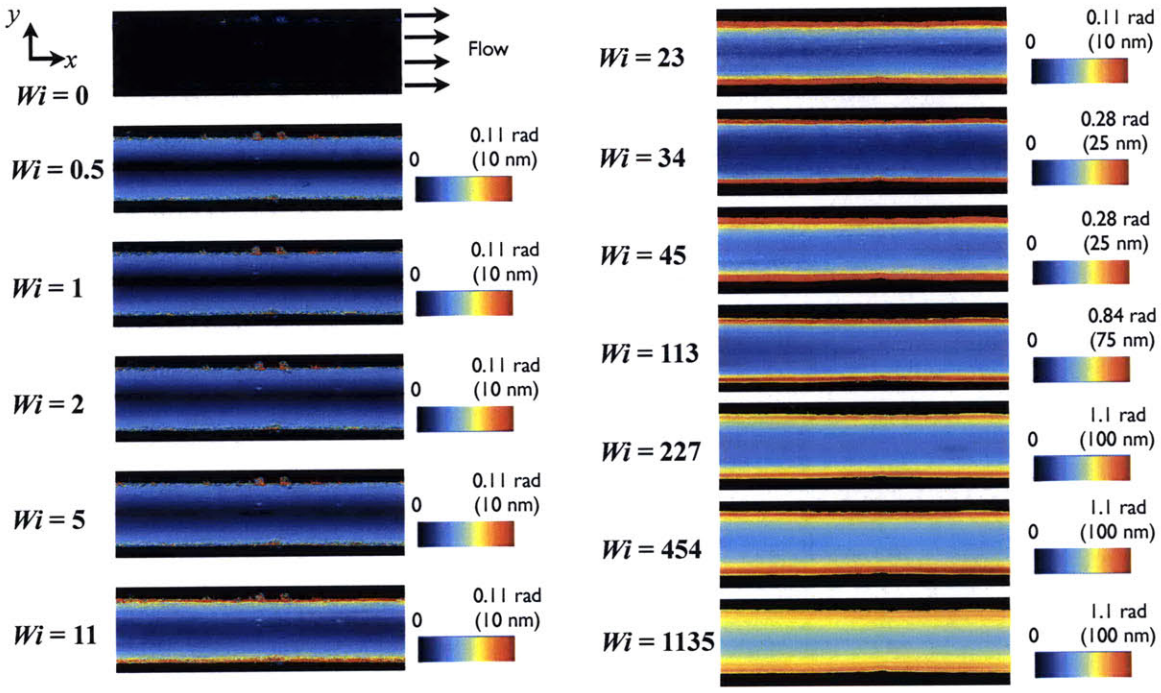

Figure 4.3.2: Pseudocolor plots of retardance for the 100:60 mM CPyCl:NaSal solution in the rectangular duct. $L_{obs} = 3.5$ cm.

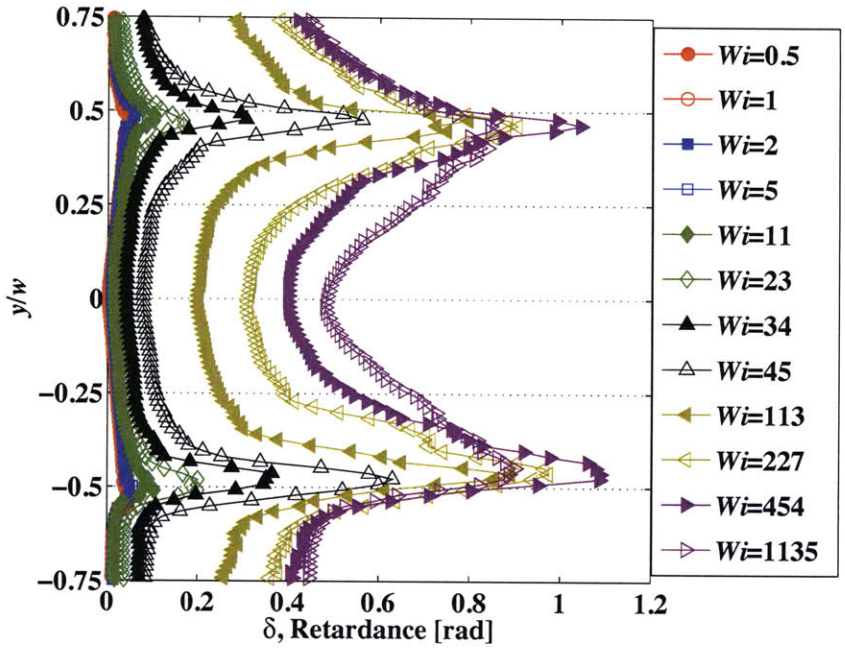

(a) Retardance Profiles.

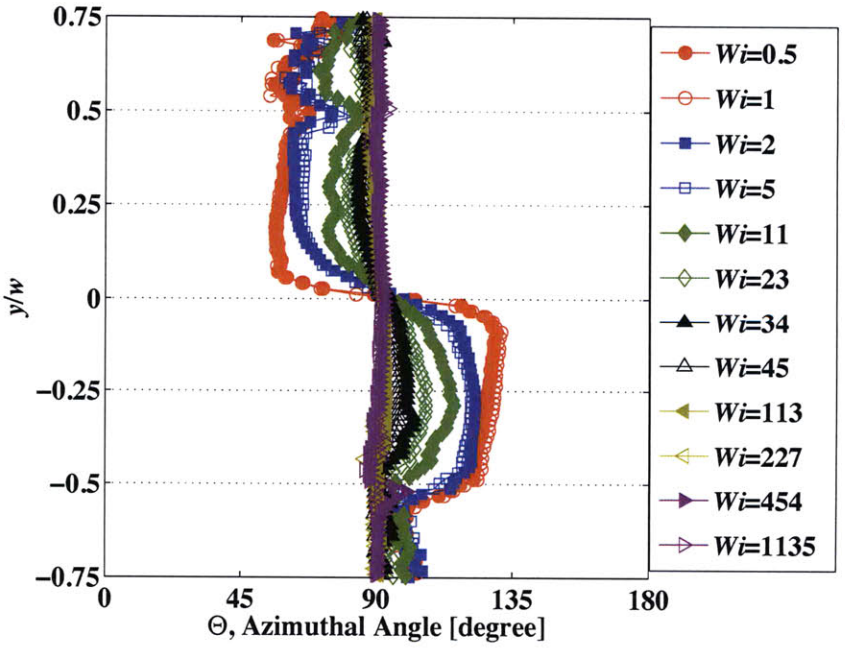

(b) Azimuthal Angle Profiles.

Figure 4.3.3: Superposed representative non-dimensionalized experimental retardance and azimuthal angle profiles at increasing Wi for the 100:60 mM CPyCl:NaSal solution in the rectangular duct. $L_{obs} = 3.5$ cm.

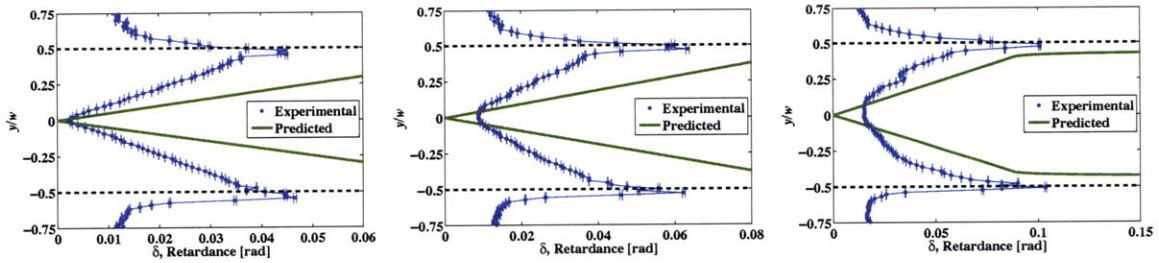

(a) $Wi = 1$, $Q = 25$ μL/hr. (b) $Wi = 5$, $Q = 100$ μL/hr. (c) $Wi = 11$, $Q = 250$ μL/hr.

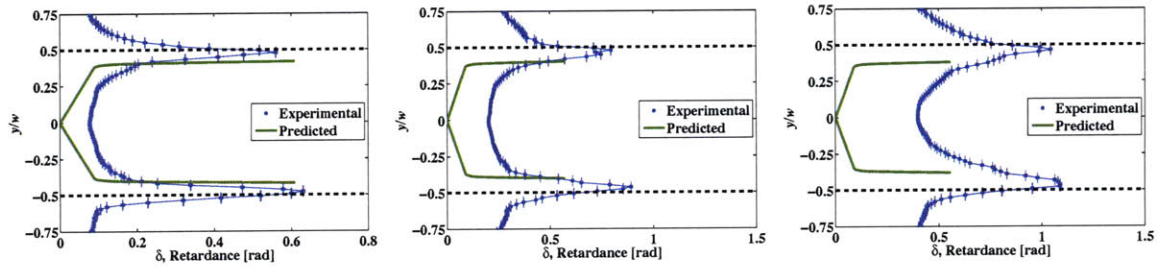

(d) $Wi = 45$, $Q = 1,000$ μL/hr. (e) $Wi = 113$, $Q = 2,500$ μL/hr. (f) $Wi = 454$, $Q = 10,000$ μL/hr.

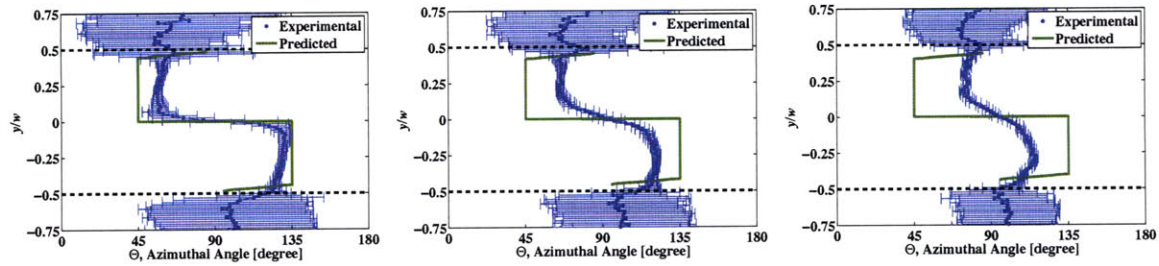

(g) $Wi = 1$, $Q = 25$ μL/hr. (h) $Wi = 5$, $Q = 100$ μL/hr. (i) $Wi = 11$, $Q = 250$ μL/hr.

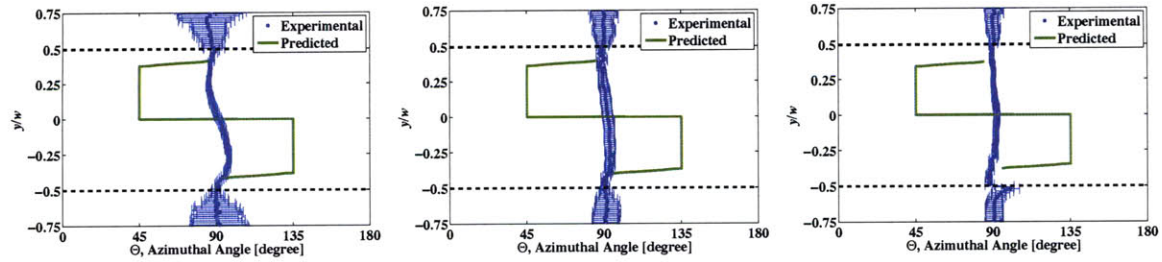

(j) $Wi = 45$, $Q = 1,000$ μL/hr. (k) $Wi = 113$, $Q = 2,500$ μL/hr. (l) $Wi = 454$, $Q = 10,000$ μL/hr.

Figure 4.3.4: Representative non-dimensionalized experimental and predicted retardance ((a)-(f)) and azimuthal angle ((g)-(l)) profiles at increasing Wi for the 100:60 mM CPyCl:NaSal solution in the rectangular duct. $L_{obs} = 3.5$ cm.

unity at all L_{obs} for this flow rate.

Background Corrected Profiles

Background corrected measurements of the flow-induced birefringence in the CTAB system were taken at $L_{obs} = 3.5$ cm. Pseudocolor plots of retardance may be seen in Figure 4.3.6 and the resultant spatially-averaged retardance and azimuthal angle profiles may be viewed in Figures 4.3.7 and 4.3.8.

In Figure 4.3.7 (a), it is apparent that for $Wi > 100$ retardance throughout the width of the channel appears to decrease with increasing Wi. This observation was likely a result of a still spatially developing flow given that $De \geq 1$ for these large Wi at the location of observation.

For all Wi, retardance profiles took on a consistently V-like shape, indicating that there were no band-like regions of localized, high shear and normal stresses that would have caused high retardance. At low $Wi < 10$, agreement between measured and predicted results is best, although this result is perplexing on account of the spatial variations in the velocity profiles along the height of the channel as seen in Figure 4.2.4 (a). For intermediate $10 \leq Wi \leq 100$, deviation between predicted and experimental profiles is most pronounced and is likely due to a break down in the stress optical rule at these high deformation rate. For $Wi > 100$, some deviation was likely the result of a still spatially developing flow.

An odd symmetry in the azimuthal angle profiles about the channel centerline may be seen for this system. For even the lowest Wi examined here seen in Figure 4.3.8 (g), the azimuthal angle did not attain the limiting values of 45^o and 135^o, indicating that even for the lowest Wi considered here, the elastic stresses were substantial enough to partially align the molecules in the flow direction across all positions in the width of the channel. For high Wi, the azimuthal angle approached 90^o across the entire channel, indicating high molecular alignment in the flow direction. Excepting narrow regions for which predicted shear rates were low enough that shear stresses were predicted by the Ellis model to dominate over normal stresses, the flattening of

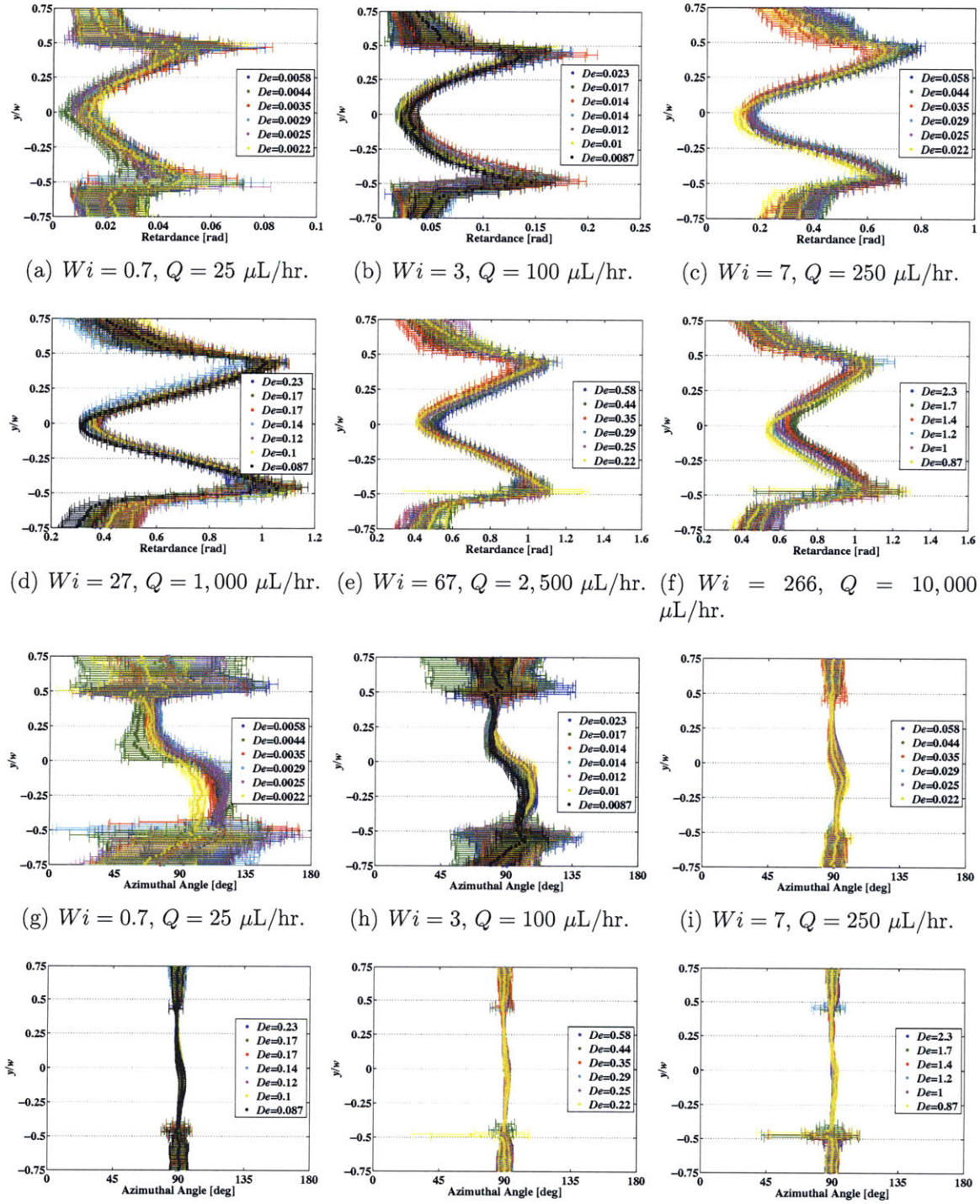

(a) $Wi = 0.7$, $Q = 25$ μL/hr. (b) $Wi = 3$, $Q = 100$ μL/hr. (c) $Wi = 7$, $Q = 250$ μL/hr.

(d) $Wi = 27$, $Q = 1,000$ μL/hr. (e) $Wi = 67$, $Q = 2,500$ μL/hr. (f) $Wi = 266$, $Q = 10,000$ μL/hr.

(g) $Wi = 0.7$, $Q = 25$ μL/hr. (h) $Wi = 3$, $Q = 100$ μL/hr. (i) $Wi = 7$, $Q = 250$ μL/hr.

(j) $Wi = 27$, $Q = 1,000$ μL/hr. (k) $Wi = 67$, $Q = 2,500$ μL/hr. (l) $Wi = 266$, $Q = 10,000$ μL/hr.

Figure 4.3.5: Uncorrected retardance ((a)-(f)) and azimuthal angle ((g)-(l)) profiles at different De (different L_{obs}) for the 30:240 mM CTAB:NaSal solution in the rectangular duct.

the azimuthal angle around 90^o was more accurately captured by the Ellis model for the CTAB system than for the CPyCl system. The inability of the measurements to resolve the thin regions for which the azimuthal angle was predicted not to be 90^o, may be attributed to slight blurring of the signal discussed in Appendix E. On account of the deviations between measured and predicted retardance for this CTAB system, however, it is difficult to comment with complete confidence on the possible influence of non-local effects in the distribution of elastic stresses within the channel width.

Deviations between experimental and predicted results for the CTAB system may be attributed to reasons similar to those given previously for the CPyCl system. Additionally, the Ellis model provides an overly simplified description of the shear rheology of the CTAB system, since it cannot capture the combined shear thinning and shear banding behavior seen in this system for $\dot{\gamma} > 30$ s^{-1} in Figure 3.1.11 (c). Clearly a more sophisticated model is necessary to predict the stress field in this fluid for $Wi \gg 10$ in order to predict the flow-induced birefringence.

4.4 Summary

Velocity and birefringence profiles of CPyCl and CTAB micellar solutions spanning multiple orders of magnitude in flow rates and resulting Wi have been presented in this section. Shear banding in the CPyCl system was observed from velocimetry measurements, evidenced by high shear rate bands localized near the walls of the channel and plug-like flow in the bulk. Shear banding was also confirmed from measurement of flow-induced birefringence, as evidenced by the narrow, localized regions of high retardance near the channel walls. In contrast to the CPyCl system, velocimetry measurements of the CTAB solution never revealed plug-like flow profiles even up to the maximum flow rate ($Wi = 67$) for which velocimetry measurement were made, although they indicated strong shear thinning behavior, as expected for this system. No regions of localized, high retardance were identified in the birefringence measure-

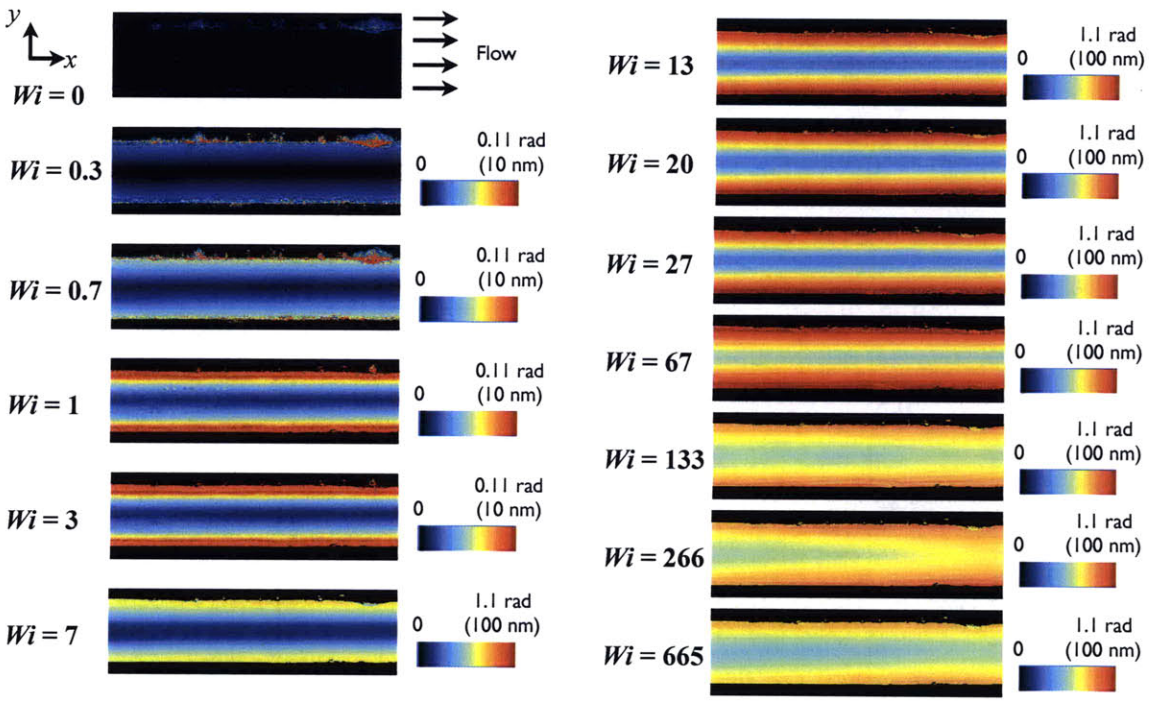

Figure 4.3.6: Pseudocolor plots of retardance for the 30:240 mM CTAB:NaSal solution in the rectangular duct. $L_{obs} = 3.5$ cm.

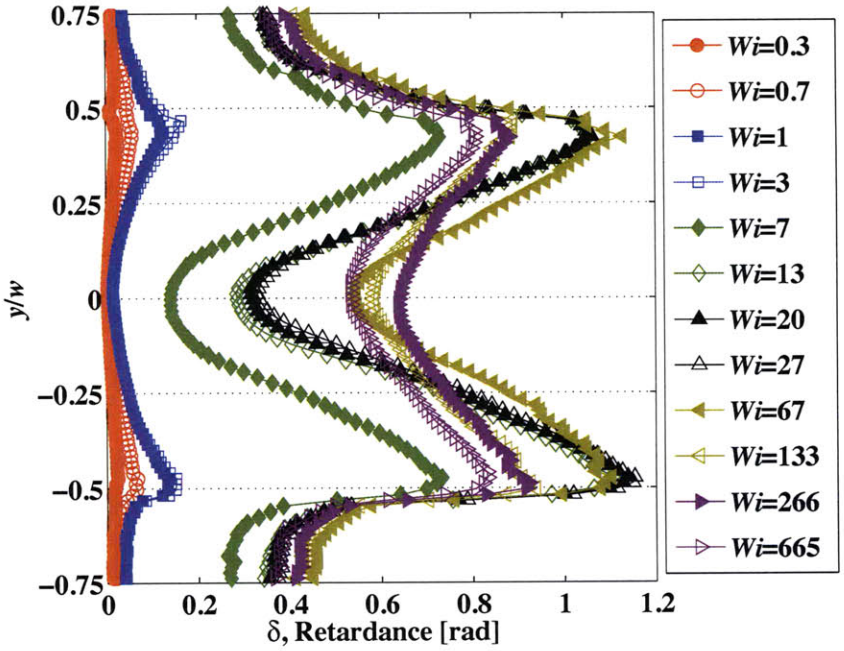

(a) Retardance Profiles.

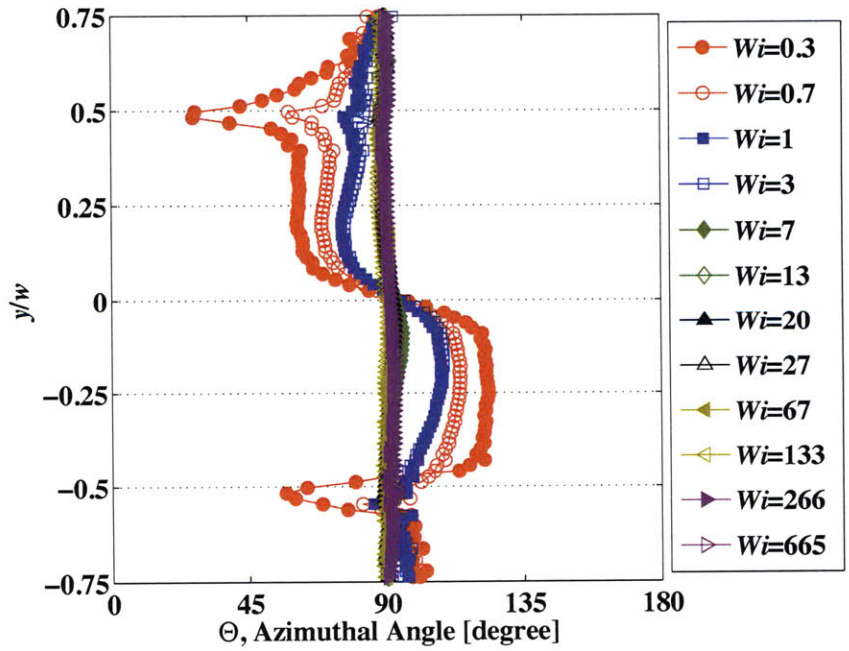

(b) Azimuthal Angle Profiles.

Figure 4.3.7: Superposed representative non-dimensionalized experimental retardance and azimuthal angle profiles at increasing Wi for the 30:240 mM CTAB:NaSal solution in the rectangular duct. $L_{obs} = 3.5$ cm.

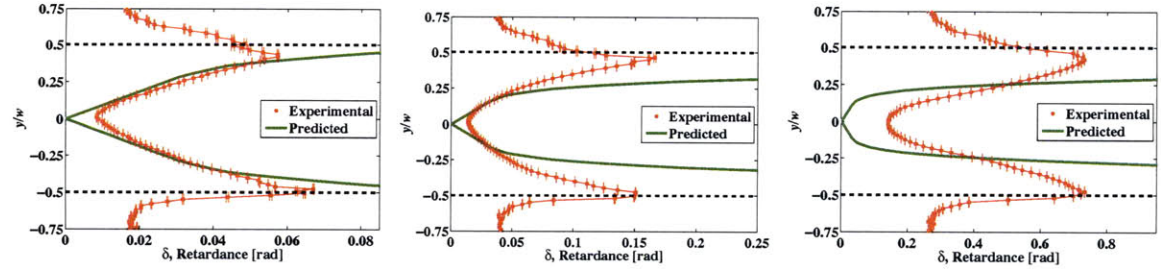

(a) $Wi = 0.7$, $Q = 25$ μL/hr. (b) $Wi = 3$, $Q = 100$ μL/hr. (c) $Wi = 7$, $Q = 250$ μL/hr.

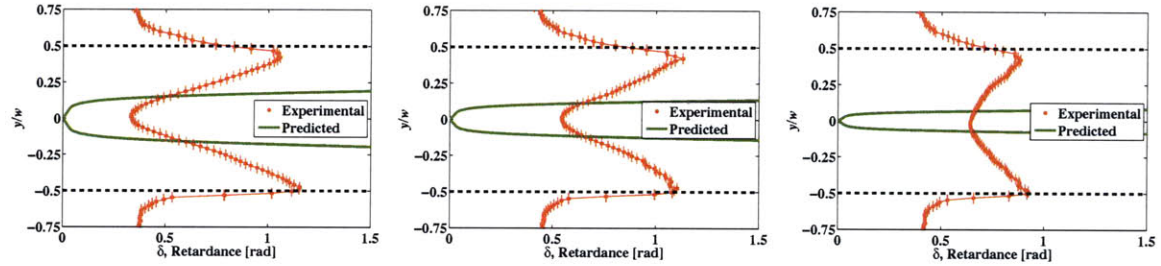

(d) $Wi = 27$, $Q = 1,000$ μL/hr. (e) $Wi = 67$, $Q = 2,500$ μL/hr. (f) $Wi = 266$, $Q = 10,000$ μL/hr.

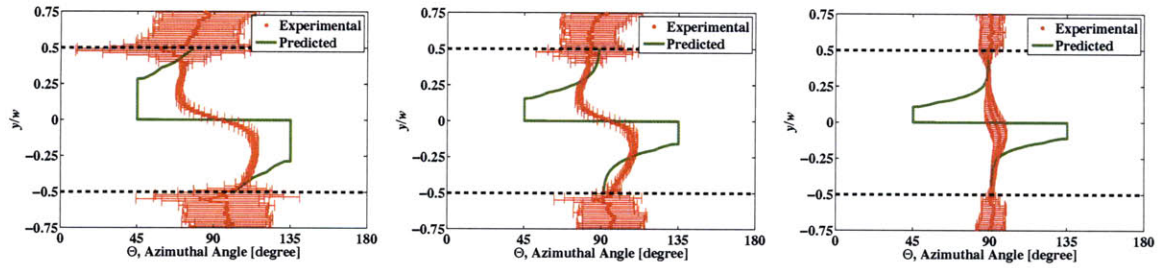

(g) $Wi = 0.7$, $Q = 25$ μL/hr. (h) $Wi = 3$, $Q = 100$ μL/hr. (i) $Wi = 7$, $Q = 250$ μL/hr.

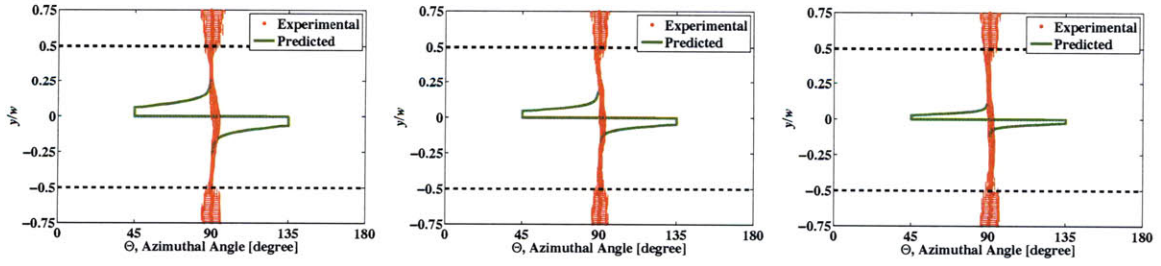

(j) $Wi = 27$, $Q = 1,000$ μL/hr. (k) $Wi = 67$, $Q = 2,500$ μL/hr. (l) $Wi = 266$, $Q = 10,000$ μL/hr.

Figure 4.3.8: Representative non-dimensionalized experimental and predicted retardance ((a)-(f)) and azimuthal angle profiles at increasing Wi for the 30:240 mM CTAB:NaSal solution in the rectangular duct. $L_{obs} = 3.5$ cm.

ments of the CTAB system. Both systems exhibited similar behavior in the azimuthal angle profiles, indicating increased molecular alignment in the direction of flow along the entire channel width with increasing Wi.

For the flow at low to moderate $Wi < 10$ and $De < 1$, at which the Ellis model was seen to predict most faithfully the measured velocity profiles of the CPyCl and CTAB systems, the predictions of retardance are also most in line with experimental measurements. Retardance profiles increased approximately linearly from the channel centerline to the walls indicating that shear stresses were predominant at the low Wi. The agreement between the model and experiment at low Wi validate the use of the ABRIO system, having been originally designed primarily to measure birefringence in biological systems, (Shribak & Oldenbourg (2003)), for use in rheo-optical measurements. Sources of error between model predictions and experimental results at $Wi > 10$ can be attributed to some uncertainty in the true value of the stress optical coefficient, C, and the likelihood of a non-affine relationship between stress and optical anisotropy for high Wi. Errors may also arise from the inability of the model to predict what may be diffusion of elastic stresses from the regions of high to low shear rate that is indicated by the high degree of molecular orientation across the whole width of the channel evidenced in the azimuthal angle profiles.

Chapter 5

Extensional Deformations

In this section, the results of experiments designed to investigate the rheological behavior of the two test fluids undergoing extensional deformations are discussed. One particular device that can impose an extensional deformation is a contraction taking the form of a hyperbola. This geometry can be used to impose a nominally constant extension rate along the its centerline for a given volumetric flow rate, as discussed in James (1991) and more recently Wang *et al.* (2010). The validity of the assumption of constant extension rate has also been previously investigated n a numerical study by Feigl *et al.* (2003) and experimentally and numerically by Oliveira *et al.* (2007)

In the experiments conducted here, the flow in a microscale, planar hyperbolic contraction was examined. Velocity profiles and thus extension rates along the centerline of the contraction were determined from measurements with μ-PIV as described earlier. Indirect measurements of stress and molecular orientation in the flowing test fluids were made using measurements of flow-induced birefringence.

5.1 Dimensional Analysis

For the flow of a micellar solution in the hyperbolic contraction used in this study, the relevant physical parameters are

- the height of the contraction, h_c, [m]
- the upstream (inlet) width of the contraction, w_u, [m]
- the downstream (outlet) width of the contraction, w_c, [m]
- the length of the contraction, l_c, [m]
- the imposed volumetric flow rate, Q, [m^3/s]
- the density of the fluid, ρ, [kg/m^3]
- the zero-shear rate viscosity of the fluid, η_0, [Pa.s]
- the relaxation time of the fluid, λ_M, [s]

For this flow some extra relevant parameters, that are not independent of those listed above are the hydraulic diameter of the channel, $d_h = 2h_c w_c/(h_c + w_c)$ and the average fluid velocity at the exit of the channel, $\langle U_c \rangle = Q/h_c w_c$.

Again, according to the Buckingham Π-theorem, for the $N = 8$ listed parameters encompassing $P = 3$ physical quantities, $K = 5$ dimensionless groups are necessary to fully specify the flow through the contraction studied here.

The first group is the aspect ratio of the channel is defined as the ratio of the channel height to its width.

$$a^* = \frac{h_c}{w_c} \tag{5.1.1}$$

For the channel used in this study, $h_c = 35$ μm and $w_c = 50$ μm, so $a^* = 0.7$.

The second quantity is the maximum Hencky strain in the channel, which is derived below in Eq. 5.2.3 and equals

$$\varepsilon_H = \ln\left(\frac{w_u}{w_c}\right) \tag{5.1.2}$$

For the channel used in this study, $w_u = 1,000$ μm and $w_c = 50$ μm, so $\varepsilon_H = 3.0$.

The Reynolds number is defined using the hydraulic diameter, which is the appropriate lengthscale for relating the influence of inertia and viscosity at the exit of the contraction.

$$Re = \frac{\rho \langle U_c \rangle d_h}{\eta_0} = \frac{\rho Q d_h}{\eta_0 h_c w_c} \tag{5.1.3}$$

An alternative definition for Re would have the characteristic speed as that at the inlet of the contraction $\langle U_u \rangle = Q/h_c w_u$ and w_u as the characteristic length. This definition would be redundant, however, since $\langle U_c \rangle w_c \approx \langle U_u \rangle w_u$, so the magnitude of Re using either definition would have been nearly the same.

The Weissenberg number is defined in terms of the characteristic shear rate at the exit of the contraction, which can be taken to be of order $\dot{\gamma}_c \approx \langle U_c \rangle / w_c$.

$$Wi = \frac{\lambda_M \langle U_c \rangle}{w_c} \tag{5.1.4}$$

The Deborah number is defined as the ratio of the fluid relaxation time to a residence time or equivalently a time of observation. For these experiments the characteristic time of observation is taken as the time required for the material to obtain one unit of strain, which is equal to $\dot{\varepsilon}^{-1}$, where $\dot{\varepsilon}$ is defined in Eq. 5.2.2. Accordingly De is defined

$$De = \lambda_M \dot{\varepsilon} \tag{5.1.5}$$

The elasticity number, which is the ratio of Wi to Re, or equivalently the ratio of elastic stresses to inertial stresses is defined

$$El = \frac{\lambda_M \eta_0}{\rho w_c d_h} \tag{5.1.6}$$

For both fluids, $El \gg 1$, indicating that in the experiments discussed below inertial stresses were not of importance.

The range of magnitudes of these dimensionless groups experimentally realized in the study of flow through a hyperbolic contraction are given in Table 5.1.1.

Table 5.1.1: Range of flow rates and dimensionless parameters experimentally considered for flow in a hyperbolic, microscale contraction ($\varepsilon_H = 3.0$) with 100:60 mM CPyCl:NaSal ($El = 1.9$ x 10^8) and 30:240 CTAB:NaSal ($El = 1.1$ x 10^7) solutions at 22-23^o C.

1 μL/hr	$\leq$	Q	$\leq$	10^3 μL/hr
10^{-7}	$\leq$	Re	$\leq$	10^{-4}
10	$\leq$	Wi	$\leq$	10^3
1	$\leq$	De	$\leq$	10^2

5.2 Flow Kinematics

For an extensional flow, a gradient in the velocity parallel to that velocity vector exists, hence the rate of deformation, $\dot{\varepsilon} = \partial u_x/\partial x$ is non-zero. For a planar hyperbolic contractions having length, l_c, height, h_c, upstream width, w_u, width at the contraction exit, w_c, the width, w, at any x takes the form

$$w(x) = \frac{K}{s + x} \tag{5.2.1}$$

where $s = l_c w_c/(w_u - w_c)$ and $K = s w_u$. For a constant volumetric flow rate, Q, the average velocity at any x-position is $u_x = Q/h_c w(x)$, therefore the extension rate, $\dot{\varepsilon}$ is

$$\dot{\varepsilon} = \frac{Q}{l_c h_c}\left(\frac{1}{w_c} - \frac{1}{w_u}\right) \tag{5.2.2}$$

and is evidently independent of x.

The Hencky strain, ε_H, is a dimensionless quantity, which is a measure of the fractional amount by which a material element is deformed as it flows through the contraction. This strain varies monotonically along the x-direction and the average

Hencky strain is equal to

$$\varepsilon_{H,x} = \int_0^t \dot{\varepsilon} dt = \int_0^t \frac{d\langle u_x \rangle}{dx} dt = \int_{\langle U_u \rangle}^{\langle U \rangle} \frac{d\langle u_x \rangle}{\langle u_x \rangle} = \ln \frac{\langle U \rangle}{\langle U_u \rangle} = \ln \left(\frac{Q/h_c w(x)}{Q/h_c w_u} \right) = \ln \left(\frac{w(x)}{w_u} \right) \tag{5.2.3}$$

The maximum Hencky strain occurs at the exit of the contraction and is therefore equal to

$$\varepsilon_H = \ln \left(\frac{w_u}{w_c} \right) \tag{5.2.4}$$

For the contraction used to study the flow kinematics and flow-induced birefringence, $\varepsilon_H = 3.0$. For comparison, the strain in the EVROC device presented in Chapter 3 is $\varepsilon_H = 1.9$.

5.2.1 CPyCl Solution

Streakline images of the flow of the CPyCl system through the hyperbolic contraction are presented in Figure 5.2.1. For the flow rates measured, at $De \leq 10$, a steady, symmetrical flow through the contraction was observed. The steady velocity profile along the centerline of the mid-plane of the contraction for $De = 4$ may be viewed in Figure 5.2.2. At this De, the corresponding nominal extension rate, calculated from Eq. 5.2.2, was $\dot{\varepsilon} = 1.4$ s^{-1}, but a more accurate fit to the measured velocity profile yielded $\dot{\varepsilon}_{true} = 1.7$ s^{-1}, which can be rationalized by the confining effects of the contraction walls, necessitating a slightly higher velocity along the contraction centerline. The axial velocity increased superlinearly with axial position near the very exit of the contraction, $1000 \leq x \leq 1100$ μm, such that $u_x(\varepsilon_H = 3.0) \approx 2\langle U_c \rangle$ as seen in Figure 5.2.2 (b). This rapid increase in velocity can be attributed to the confining effects of all four channel walls on the flow near the outlet of the contraction where the aspect ratio of the channel was nearly unity, $a^* \approx 1$. Whereas at the inlet of the contraction, the vertical walls of the contraction were far removed from the

bulk of the fluid flow, at the channel exit, for which $a^* \approx 1$, momentum diffusion was equally rapid in both the y and z-axes, necessitating an increased maximum centerline velocity.

The onset of a time-varying behavior at the inlet of the contraction occurred at a critical Deborah number of $De_c = 20$. Because of this time-varying behavior for $De \geq 20$, the assumption of constant extension rate along the centerline of the contraction could only be verified with μ-PIV at lower flow rates corresponding to $De \leq 20$ and $Q \leq 50$ μl/hr. At this onset point, the fluid was periodically partitioned into regions of rapid flow, corresponding to the upper half of Figure 5.2.1 (e) and regions of essentially stagnant flow seen in the lower half of the same image, while at other times the flow was uniform as seen at lower De. The period of fluctuations in the flow field was on the order of 10 seconds. This evident heterogeneity appeared to have arisen from the formation of long, entangled viscoelastic streaks extending many contraction-lengths upstream of the contraction exit. At $De_c = 20$ the flow at the outlet of the contraction, however, was steady. At $De = 40$ (not shown) the flow at the outlet of the contraction was observed also to be unsteady and three dimensional.

With increasing De, the frequency in the velocity fluctuations increased. For $De \geq 100$, shown in Figure 5.2.1 (g), no flow partitioning was observed, but instead fluctuations in velocity occurred uniformly in the contraction inlet and outlet with no transitions between a homogeneous and heterogeneous flow as seen for lower De. Given the low Re associated with this flow, these velocity fluctuations were likely the result of elastic turbulence discussed, for example, by Groisman & Steinberg (2000), Larson (2000) and Morozov & van Saarloos (2007).

5.2.2 CTAB Solution

Streakline images of the CTAB solution flowing through the contraction may be seen in Figure 5.2.3. At low to moderate De, the flow was steady and laminar. The axial velocity along the centerline of the contraction measured at two low De are

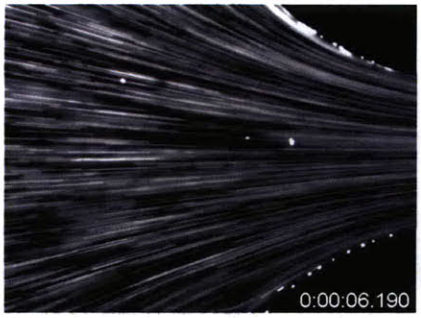

(a) $De = 4$, $Q = 10$ μL/hr.

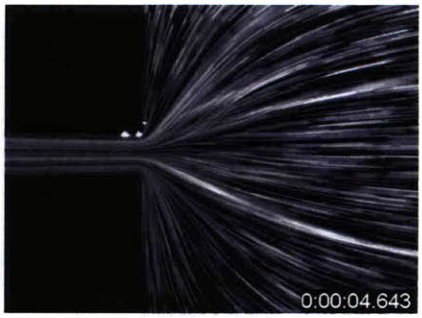

(b) $De = 4$, $Q = 10$ μL/hr.

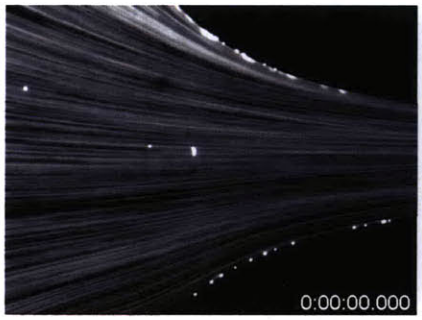

(c) $De = 10$, $Q = 25$ μL/hr.

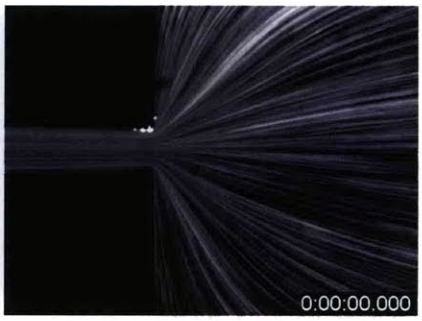

(d) $De = 10$, $Q = 25$ μL/hr.

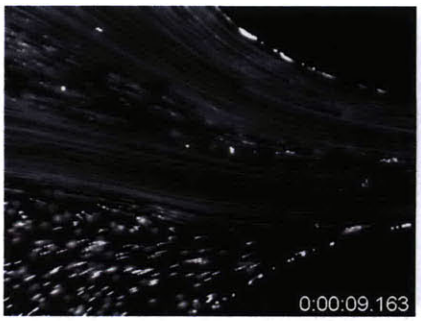

(e) $De = 20$, $Q = 50$ μL/hr.

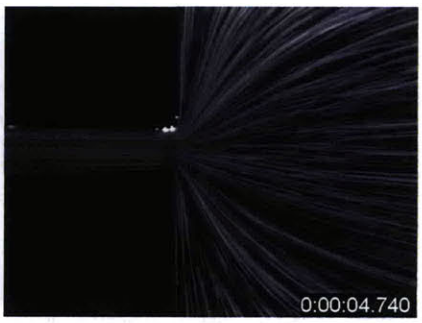

(f) $De = 20$, $Q = 50$ μL/hr.

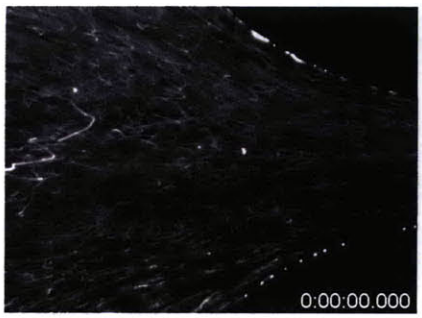

(g) $De = 199$, $Q = 500$ μL/hr.

(h) $De = 199$, $Q = 500$ μL/hr.

Figure 5.2.1: Streakline images of the flow of 100:60 mM CPyCl:NaSal solution at the entrance (left images) and exit (right images) of a hyberbolic contraction with $\varepsilon_H = 3.0$ at increasing De. Flow is from left to right.

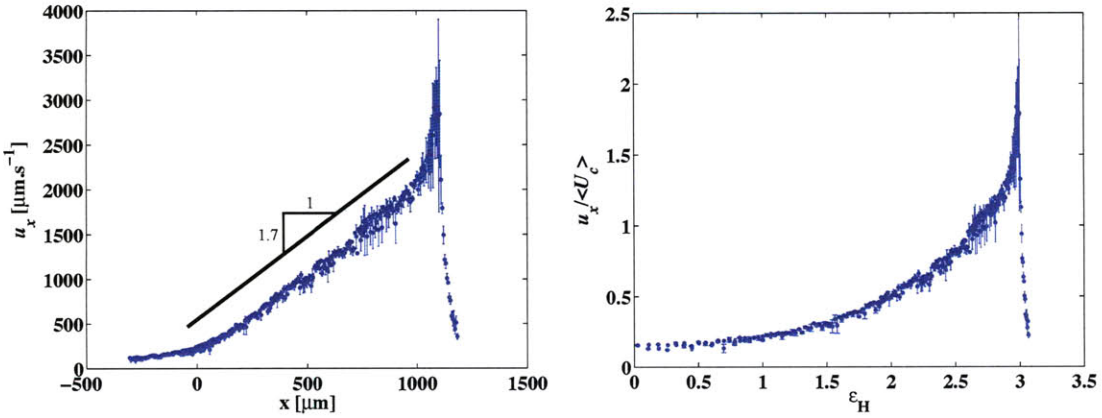

(a) $De = 4$, $Q = 10$ μL/hr.

(b) $De = 4$, $Q = 10$ μL/hr.

Figure 5.2.2: Velocity profile of the 100:60 mM CPyCl:NaSal solution along the centerline of a hyberbolic contraction with $\varepsilon_H = 3.0$. Axial velocity at each x-value averaged over the middle third of the outlet width of the contraction (*i.e.* $y = \pm 8.3$ μm). Error bars correspond to the standard deviation of those data points.

shown in Figure 5.2.4. For both flow rates, the experimentally realized extension rates were $\dot{\varepsilon}_{true} = 2.8$ s^{-1} for $De = 2$ and $\dot{\varepsilon}_{true} = 7$ s^{-1} for $De = 6$, corresponding to approximately twice the nominal extension rates of $\dot{\varepsilon} = 1.4$ s^{-1} and $\dot{\varepsilon} = 3.4$ s^{-1} for each respective flow rate calculated from Eq 5.2.2. This deviation resulted from the confining effects of the walls.

At $De \approx 10$, the flow was still laminar, but no longer symmetrical about the axis of the contraction as also seen for the CPyCl system. Representative streaklines of this partitioned flow are shown in Figure 5.2.3 (e).

With increasing De, the velocity profile became time varying and succumbed to the onset of elastically driven turbulence.

5.3 Stress and Birefringence

In this section, the flow-induced birefringence along the centerline of the contraction is measured and related to the state of stress and molecular alignment of the micellar systems as they flow and deform in the contraction. The spatially resolved measure-

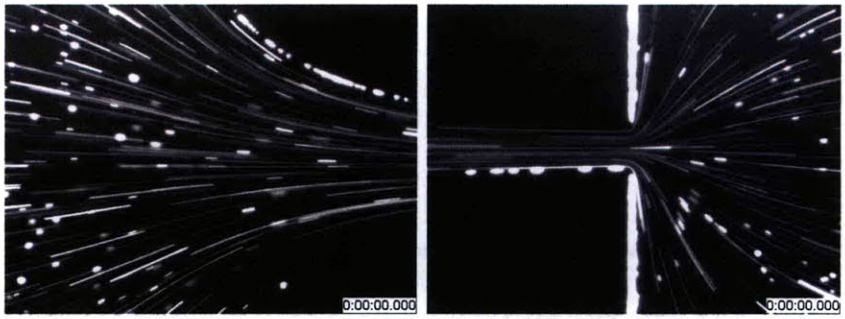

(a) $De = 2$, $Q = 10$ μL/hr. (b) $De = 2$, $Q = 10$ μL/hr.

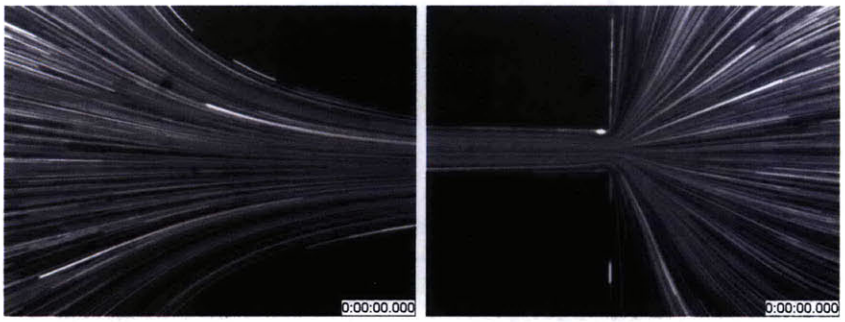

(c) $De = 6$, $Q = 25$ μL/hr. (d) $De = 6$, $Q = 25$ μL/hr.

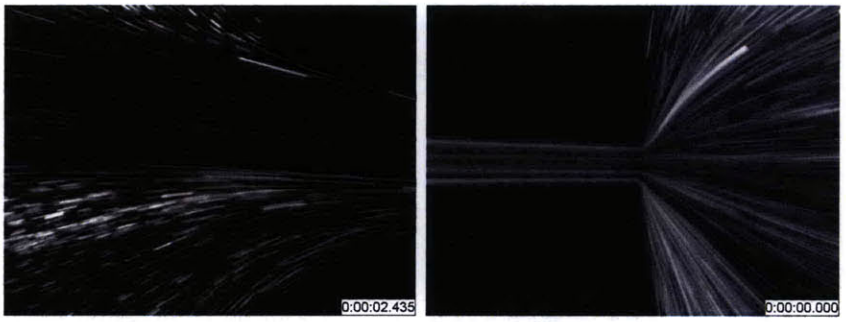

(e) $De = 12$, $Q = 50$ μL/hr. (f) $De = 12$, $Q = 50$ μL/hr.

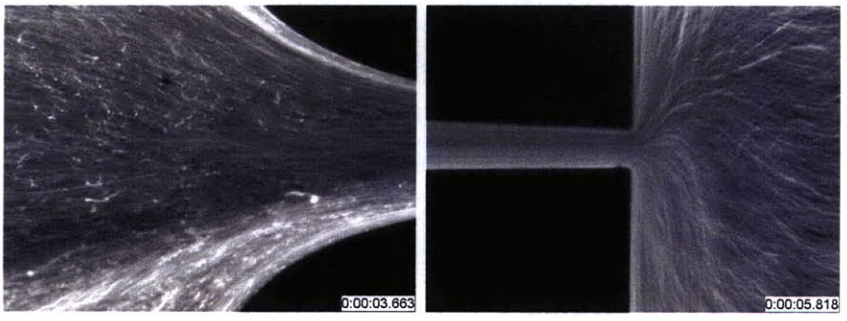

(g) $De = 58$, $Q = 250$ μL/hr. (h) $De = 58$, $Q = 250$ μL/hr.

Figure 5.2.3: Streakline images of the flow of 30:240 mM CTAB:NaSal solution at the entrance (left images) and exit (right images) of a hyberbolic contraction with $\varepsilon_H = 3.0$ at increasing De. Flow is from left to right.

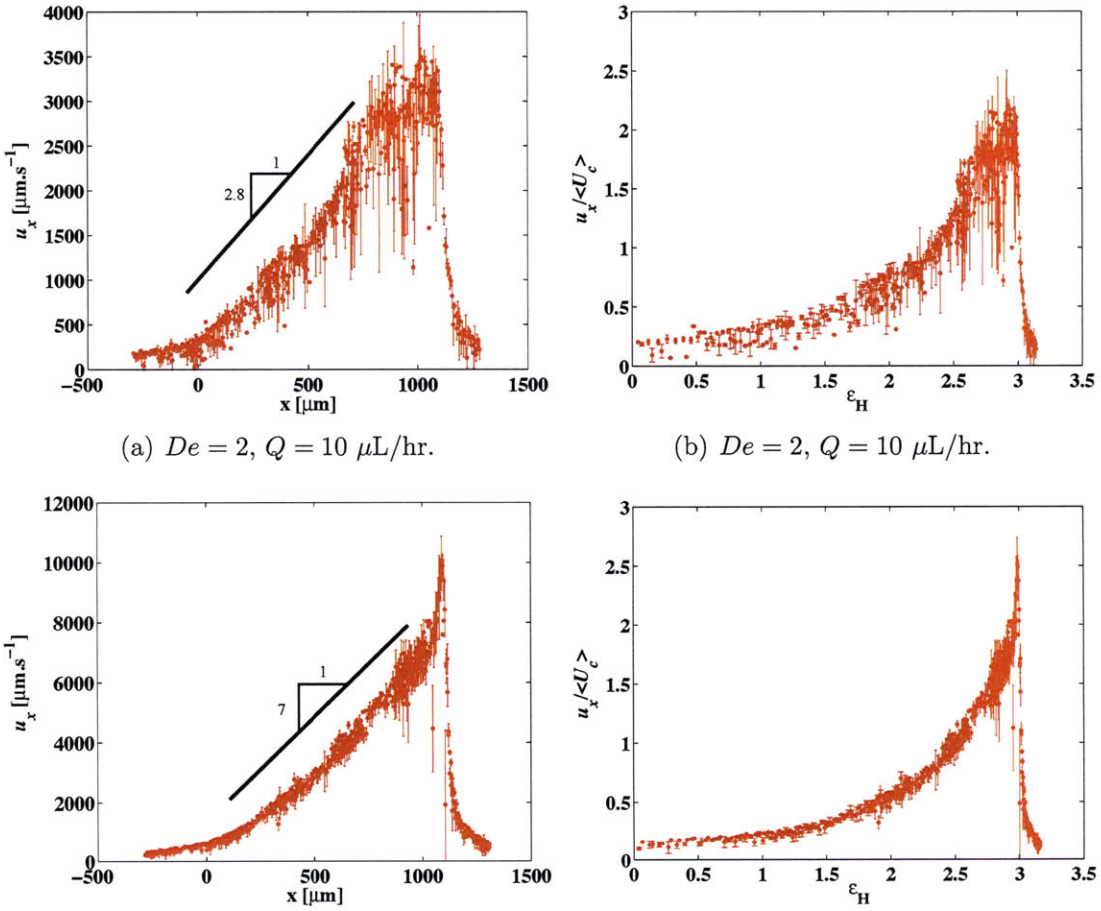

(a) $De = 2$, $Q = 10$ μL/hr.

(b) $De = 2$, $Q = 10$ μL/hr.

(c) $De = 6$, $Q = 25$ μL/hr.

(d) $De = 6$, $Q = 25$ μL/hr.

Figure 5.2.4: Velocity profile of the 30:240 mM CTAB:NaSal solution along the centerline of a hyberbolic contraction with $\varepsilon_H = 3.0$. Axial velocity at each x-value averaged over the middle third of the outlet width of the contraction (*i.e.* $y = \pm 8.3$ μm). Error bars correspond to the standard deviation of those data points.

ments of flow-induced birefringence reveal the local evolution of the material stresses as the fluid undergoes extension.

5.3.1 CPyCl Solution

Pseudocolor plots of retardance measured for the CPyCl system throughout the entire contraction are given in Figure 5.3.2. Evidently, a moderate $De = 10$ was necessary to observe any birefringence, indicating that a flow of moderate strength was required to obtain any measurable amount of molecular alignment and thus optical anisotropy. Increasing the flow rate or De was accompanied by increased retardance throughout the entire contraction.

The retardance profiles along the axis of the contraction at increasing De may be seen in Figure 5.3.1 (a), and again depicted in three dimensional form in Figure 5.3.3. For $De = 10 < De_c$, the retardance increased approximately linearly with accumulated strain, indicating that the accumulated stress, being proportional to retardance, was also proportional to strain and therefore primarily elastic in nature.

With slightly higher $De = 20 \approx De_c$, a plateau in retardance with increasing strain occurred, followed by a non-monotonicity in the average retardance profile with strain at still increasing $De > 20 \approx De_c$. The subsequent non-montonicity in retardance seen at the highest $De > De_c$ can be attributed to the relaxation of stress within the sample prior to attainment of maximum strain.

This relaxation process may be linked with a turbulent mixing of stressed and unstressed material, although other relaxation processes may also be important. Given the high rate of deformations for the large $De \gg De_c$ for which non-monotonicity is observed, it is unlikely that reptative processes alone were the predominant relaxation mechanism. Given the short flow time scales, $\dot{\varepsilon}^{-1}$, at these high De compared to the relatively long breaking times, λ_{break}, listed in Table 3.1.3, it is likely that the micelles were broken apart so strongly by the flow that they were unable to reform during their residence time in the contraction. In this way, breaking facilitated the

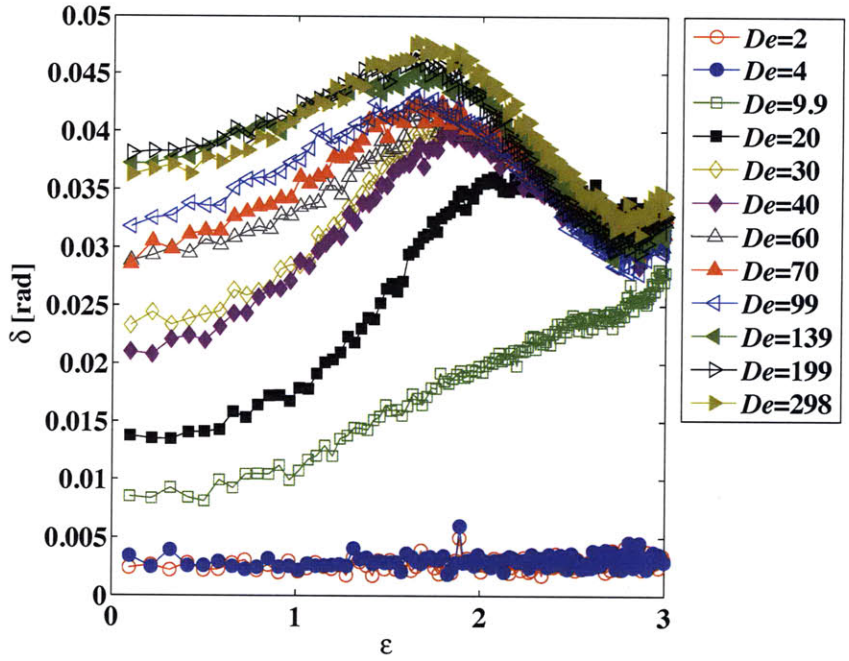

(a) 100:60 mM CPyCl:NaSal. $El = 1.9 \text{ x } 10^8$.

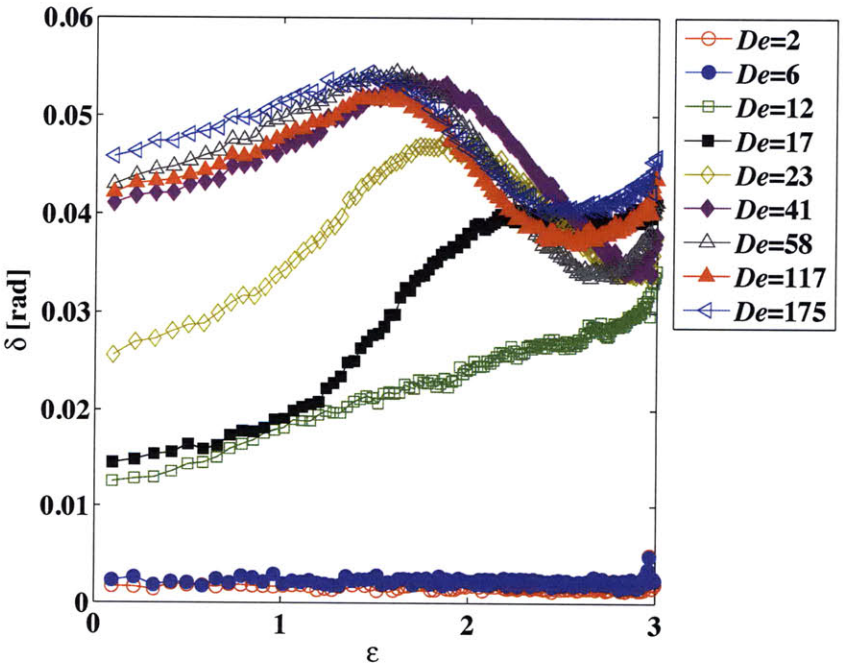

(b) 30:240 mM CTAB:NaSal. $El = 1.1 \text{ x } 10^7$.

Figure 5.3.1: Retardance profiles at different De along the centerline of the hyperbolic contraction with exit Hencky strain, $\varepsilon_H = 3.0$.

relaxation in stress and thus the retardance prior to attainment of maximum strain as reflected in the non-monotonic flow retardance profiles at high De seen in Figure 5.3.3. This plateau retardance value marking the onset of importance of breaking processes for this flow was around 0.03 rad, which can be related to the principal stress difference following the assumption of the validity[1]of Eq. 3.1.25 and 3.1.23, to obtain a corresponding $\Delta\sigma \approx 325$ Pa. From the simulations of Cromer *et al.* (2009) for the uniaxial flow of a worm-like micellar system described by the VCM model, peak principal stress differences were found to be $5G_0 \leq \Delta\sigma \leq 12G_0$ for $2 \leq De \leq 100$. These peak stresses correspond to the stresses at which rupture of the long constituent species was predicted by the VCM model and range from $135 \leq \Delta\sigma \leq 324$ Pa for the CPyCl system. These values for $\Delta\sigma$ agree well with the crude calculations from the stress optical rule, but it should be noted that the experimentally realized flow kinematics (three dimensional, turbulent at high De) were not accounted for in the model predictions. This value of $\Delta\sigma$ is an order of magnitude smaller, however, than the tensile stresses at which Bhardwaj *et al.* (2007) observed filament rupture in similar CPyCl:NaSal systems on a filament stretching extensional rheometer (FiSER). The slight increase in retardance following the dip near the contraction outlet results from the superlinear increase in axial velocity near the exit of the channel as seen in the velocimetry measurements discussed previously.

The peak retardance along the contraction and the retardance at the maximum strain are plotted against De in Figure 5.4.1 (a) and (b) respectively. Evidently, the maximum retardance increased slightly with increasing strain rate, but the retardance at the exit of the channel was nearly independent of De, indicating that the breaking stress may have varied slightly with De, but that the fluid was able to relax to a roughly constant stress, neglecting the slight dip near the channel outlet, prior to exiting the channel.

With increasing flow strength, the measured azimuthal angle along the channel

[1]This value must be taken as approximate given the three dimensionality of the flow and the possible break-down of the stress optical rule for strong flows.

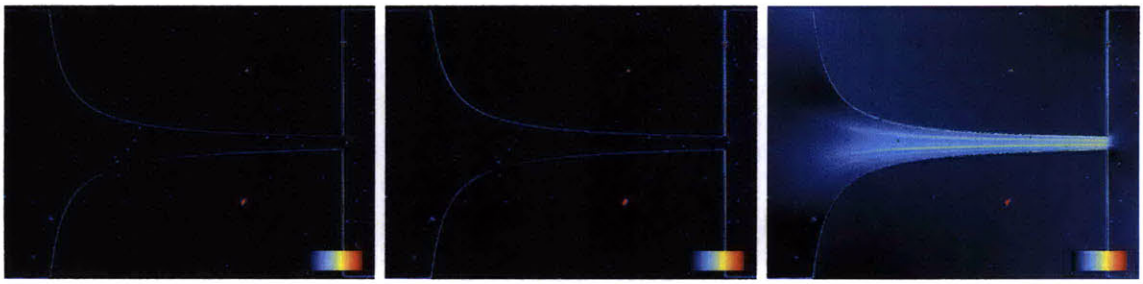

(a) $De = 2$, $Q = 5$ μL/hr. (b) $De = 4$, $Q = 10$ μL/hr. (c) $De = 10$, $Q = 25$ μL/hr.

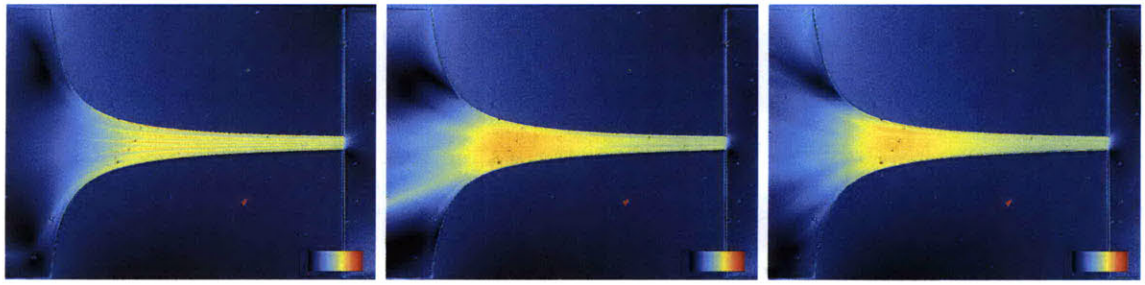

(d) $De = 20$, $Q = 50$ μL/hr. (e) $De = 30$, $Q = 75$ μL/hr. (f) $De = 40$, $Q = 100$ μL/hr.

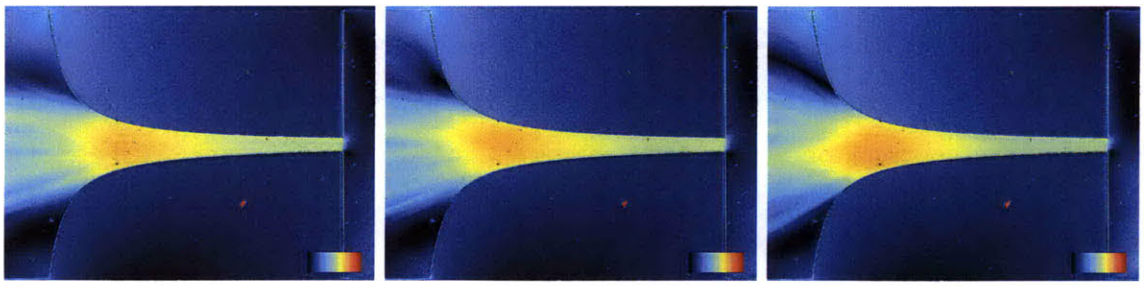

(g) $De = 60$, $Q = 150$ μL/hr. (h) $De = 70$, $Q = 175$ μL/hr. (i) $De = 99$, $Q = 250$ μL/hr.

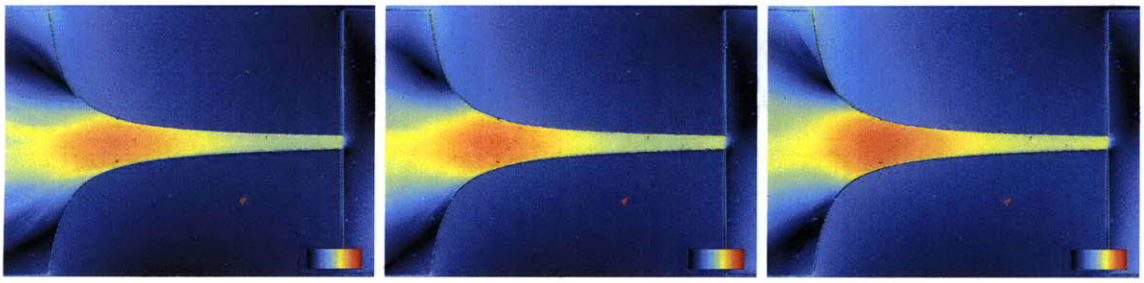

(j) $De = 139$, $Q = 350$ μL/hr. (k) $De = 199$, $Q = 500$ μL/hr. (l) $De = 298$, $Q = 750$ μL/hr.

Figure 5.3.2: Pseudocolor retarance plots for the 100:60 mM CPyCl:NaSal solution flowing in a hyperbolic contraction with exit Hencky strain, $\varepsilon_H = 3.0$. Color scale ranges from 0 to 0.06 rad (0 to 5 nm).

centerline shown in Figure 5.3.3 (b) approached 90^o, coinciding with the y-axis of the simplified channel depicted in Figure 3.2.2. This result indicates that with increasing flow strength, the slow optical axis, coinciding with one of the principal strain axes was oriented perpendicular to the flow direction, and thus the primary strain axis coincided with the x-axis as expected in for this strong extensional flow.

5.3.2 CTAB Solution

Full-field pseudocolor plots of retardance for the CTAB system may be seen in Figure 5.3.4. As before, a moderate $De = 12$ marked the onset of detectable birefringence. For large De, the region of maximum retardance intensity, indicated by red, was very clearly near the contraction entrance at $\varepsilon_H \approx 1.5$ and $x \approx 300$ μm.

The retardance profiles shown in Figure 5.3.1 (b) reveal a similar transition from a monotonic at $De < De_c$ to non-montonic behavior with a transitional $De_c \approx 17$, and plateau retardance around 0.04 rad. Again, applying Eq. 3.1.25 and 3.1.23 this plateau retardance corresponds to $\Delta\sigma \approx 320$ Pa. This value is again an order of magnitude smaller than the measured ruptured stresses of Bhardwaj *et al.* (2007), but it is far larger than the predictions of Cromer *et al.* (2009) corresponding to $22 \leq \Delta\sigma \leq 54$ Pa ($5G_0 \leq \Delta\sigma \leq 12G_0$). Clearly further investigation is necessary to understand the rupturing behavior of this shear thinning system. As before, dips in the retardance profiles just before the contraction exit were observed, arising from the superlinear increase in velocity near the contraction outlet.

The behavior of peak retardance and the retardance at the maximum strain are plotted in Figure 5.4.1 (a) and (b) respectively. The peak retardance exhibited a plateau with increasing strain rate, indicating that the breaking stress was independent of De. The retardance at the channel exit continued to increase with De, suggesting that the material could recover quickly enough, on account of its shorter λ_{break} compared to that of the CPyCl system, from the initial stress overshoot for the stress to regrow before the the fluid exited the channel.

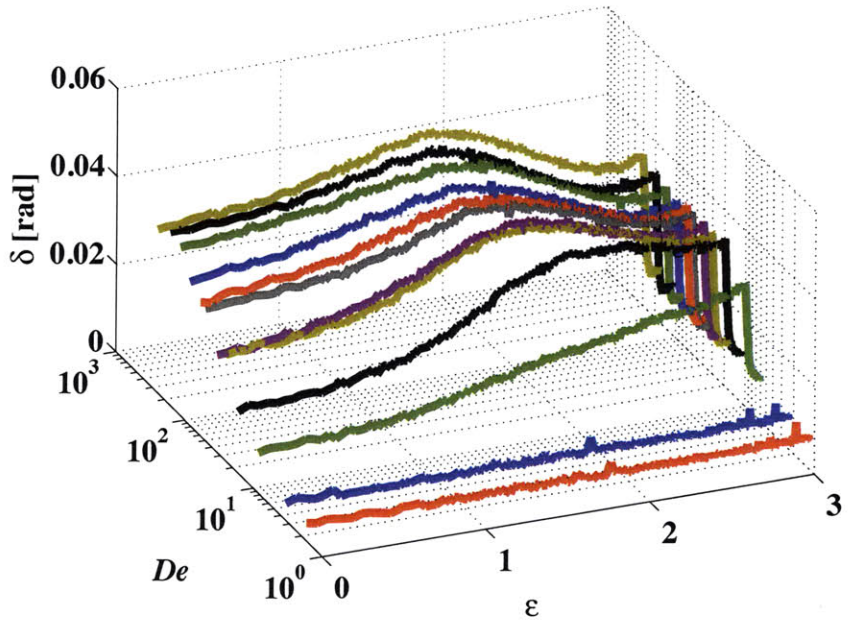

(a) Retardance profiles along the centerline of the hyperbolic contraction at different *De*.

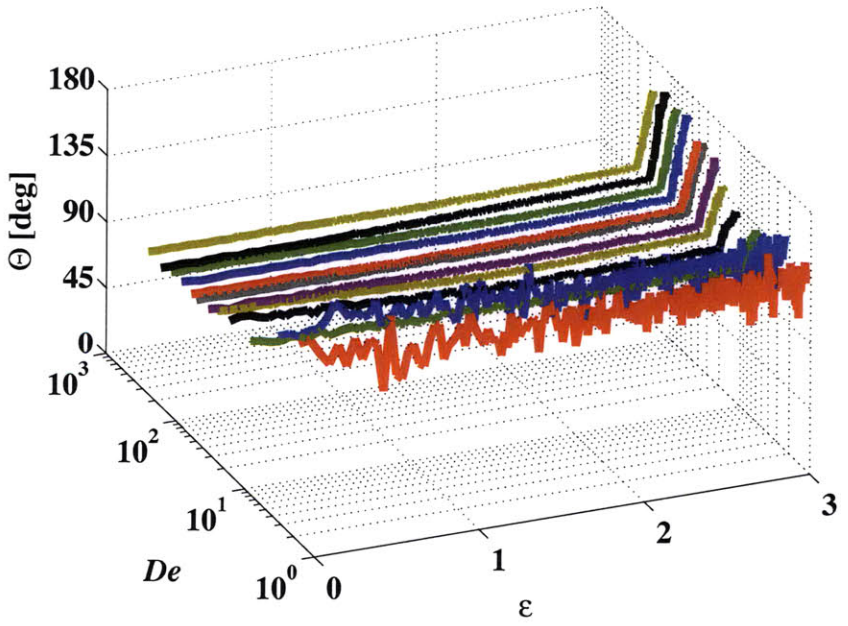

(b) Azimuthal angle profiles along the centerline of the hyperbolic contraction at different *De*.

Figure 5.3.3: Retardance and azimuthal angle profiles for the 100:60 mM CPyCl:NaSal solution flowing in a hyperbolic contraction with exit Hencky strain, $\varepsilon_H = 3.0$. Values at each x-value averaged over the middle third of the outlet width of the contraction (*i.e.* $y = \pm 8.3$ μm).

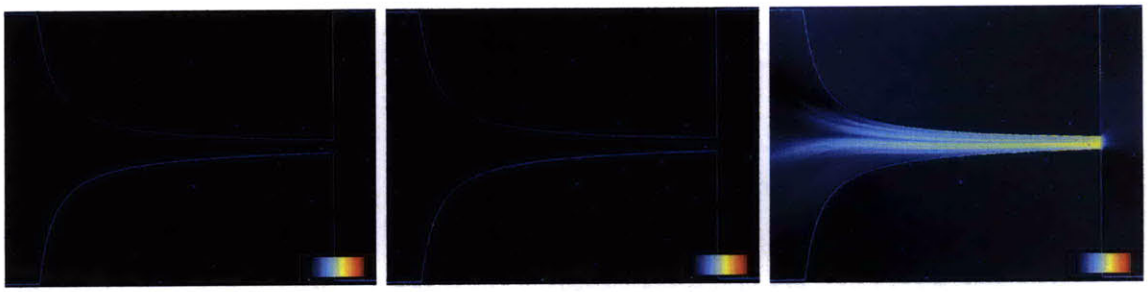

(a) $De = 2$, $Q = 10$ μL/hr. (b) $De = 6$, $Q = 25$ μL/hr. (c) $De = 12$, $Q = 50$ μL/hr.

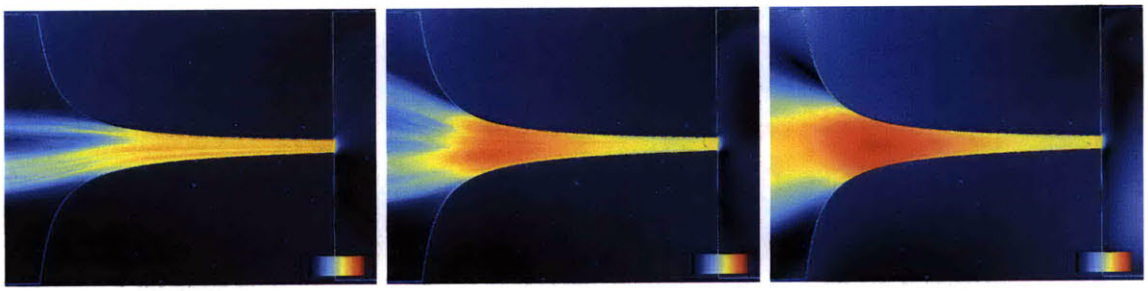

(d) $De = 17$, $Q = 75$ μL/hr. (e) $De = 23$, $Q = 100$ μL/hr. (f) $De = 41$, $Q = 175$ μL/hr.

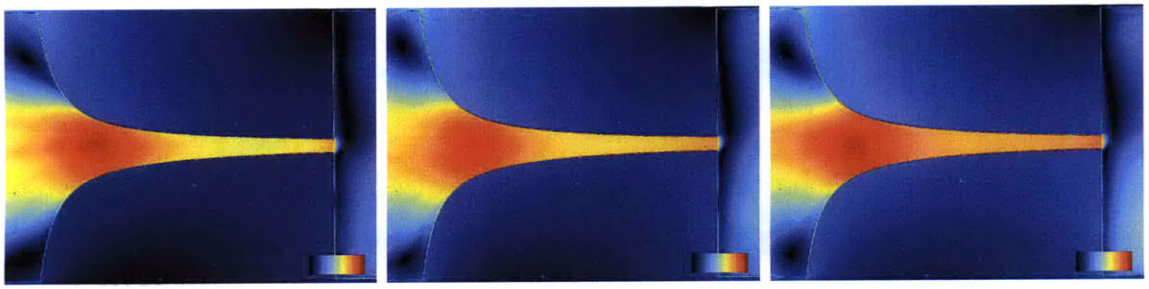

(g) $De = 58$, $Q = 250$ μL/hr. (h) $De = 117$, $Q = 500$ μL/hr. (i) $De = 175$, $Q = 750$ μL/hr.

Figure 5.3.4: Pseudocolor retarance plots for the 30:240 mM CTAB:NaSal solution flowing in a hyperbolic contraction with exit Hencky strain, $\varepsilon_H = 3.0$. Color scale ranges from 0 to 0.06 rad (0 to 5 nm).

As observed for the CPyCl system, the azimuthal angle measured for the CTAB system approached 90^o with increasing De, indicating a high degree of molecular alignment along the channel centerline.

5.4 Summary

In this section, the results of experimental measurements of velocimetry and flow-induced birefringence for the flow of CPyCl and CTAB micellar systems in a microscale hyperbolic contraction were discussed. The experiments spanned a range of flow rates corresponding to almost three orders of magnitude of De.

Measurements of axial velocity along the centerline of the contraction for both solutions revealed that at low to moderate $De < De_c$, a nearly constant extension rate was experimentally realized as desired. Experimentally measured $\dot{\varepsilon}_{true}$ were greater than the predicted $\dot{\varepsilon}$ based on the average velocity by approximately 20% for the CPyCl system and 100% for the CTAB system indicating that in this mixed shear and extensional flow the CTAB system was markedly less shear thinning than the CPyCl system. For $De \approx 10$ the flow field was observed to become unstable and time-varying, with increased frequency of fluctuations and randomness accompanying increased De.

Qualitatively and quantitatively similar trends with De were observed in the birefringence of both the CPyCl and CTAB systems in this microscale flow. A transition from a monotonic to a non-monotonic relationship between retardance and strain, coinciding with $De \approx 10$, reveals the importance of a rapid relaxation mechanism, such a breaking of the micelles, in high deformation rate extensional flows. The similarities in the behavior of these two systems in this extension dominated flow could be anticipated from their nearly identical first normal stress differences in shear, similar Maxwell relaxation times, λ_M and breakup times in CaBER, λ_{ext}, as well as their similar behavior in EVROC. This observation is remarkable on account of the highly disparate shear behavior of these systems and reveals very clearly the need to test

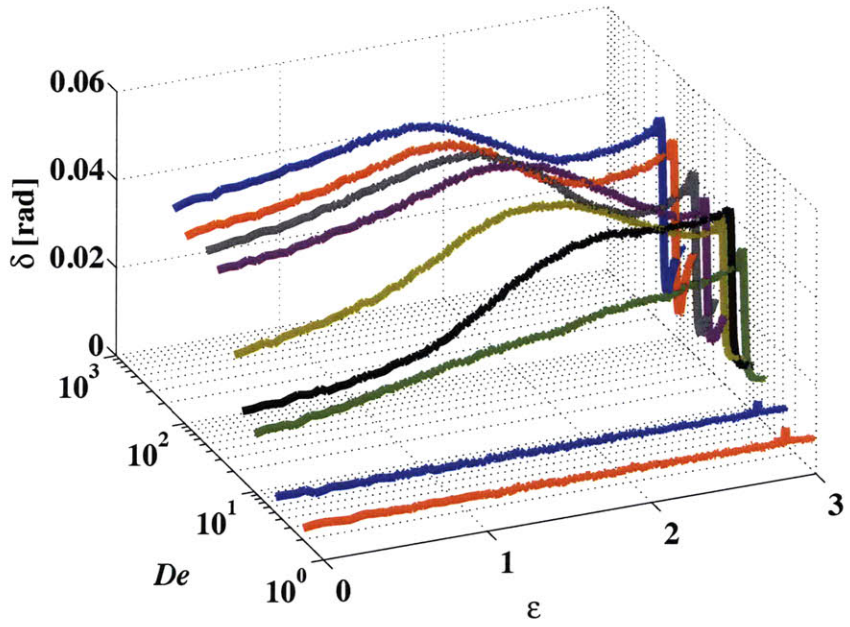

(a) Retardance profiles along the centerline of the hyperbolic contraction at different *De*.

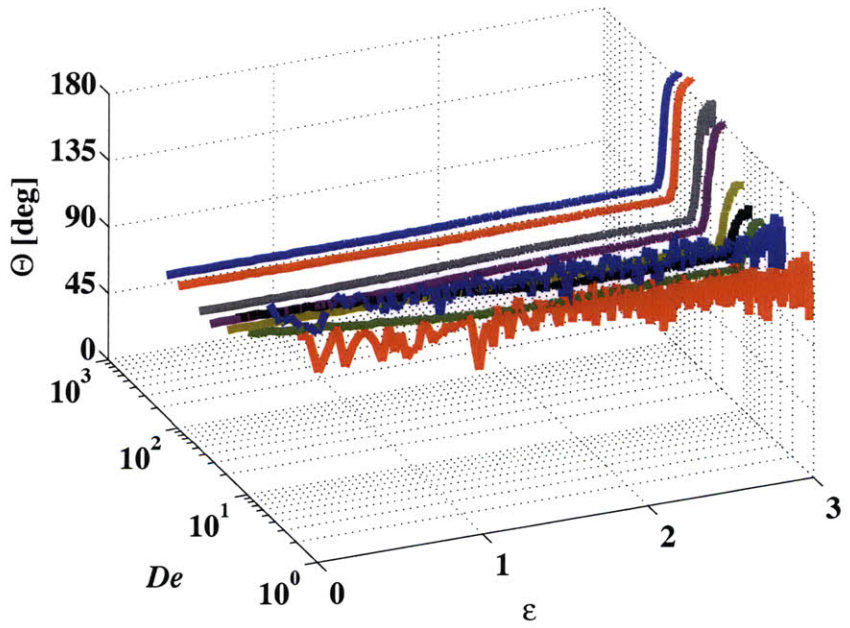

(b) Azimuthal angle profiles along the centerline of the hyperbolic contraction at different *De*.

Figure 5.3.5: Retardance and azimuthal angle profiles for the 30:240 mM CTAB:NaSal solution flowing in a hyperbolic contraction with exit Hencky strain, $\varepsilon_H = 3.0$. Values at each x-value averaged over the middle third of the outlet width of the contraction (*i.e.* $y = \pm 8.3$ μm)

such system in both shear and extensional flows in order to fully characterize them.

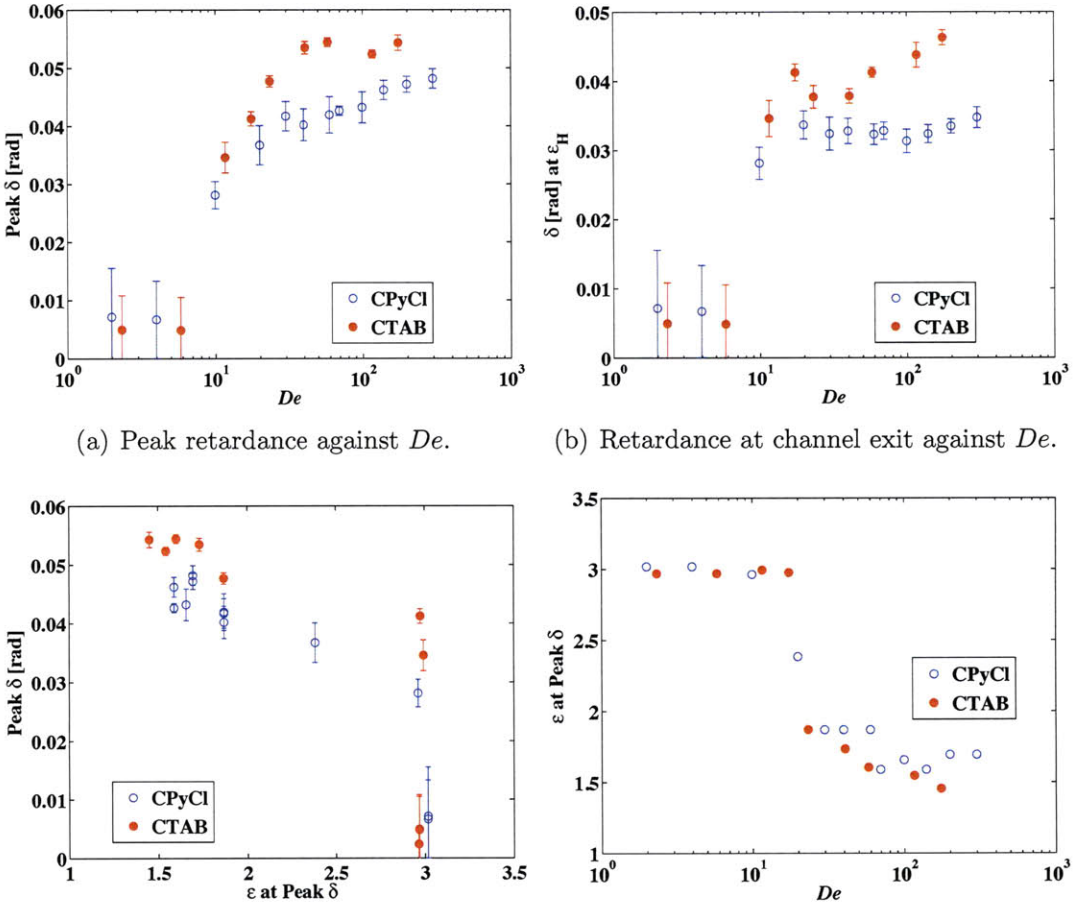

(a) Peak retardance against De.

(b) Retardance at channel exit against De.

(c) Peak retardance against strain. (Each point corresponds to a different De.)

(d) Strain corresponding to peak retardance against De.

Figure 5.4.1: Key summarized results of measured birefringence for flow through the hyperbolic contraction with exit Hencky strain, $\varepsilon_H = 3.0$.

Chapter 6

Conclusion

"Science never solves a problem without creating ten more."

– **George Bernard Shaw**

The primary goal of this thesis has been the development and refinement of rheometric techniques for measuring the rheological behavior of complex fluids undergoing high rate deformations in microscale geometries. The resulting analysis combines velocimetry measurements using μ-PIV and measurements of flow-induced birefringence (FIB) of two surfactant, worm-like micellar systems.

The two test fluids, one a 100:60 mM CPyCl:Nasal system and the other a 30:240 mM CTAB:NaSal system, were characterized using conventional macroscale as well and microscale rheometric techniques in order to determine fully their shear and extensional rheology. In small amplitude oscillatory deformations (SAOS), a single mode Maxwell model could capture the response of both systems at low to moderate frequencies, with both fluids having Maxwell relaxation times on the order of one second. In steady shear experiments using both a rotational rheometer and a microcapillary rheometer, the CPyCl system was observed to exhibit a stress plateau, indicative of shear banding, across many decades of nominal shear rate, while the CTAB system was found to be predominantly shear thinning. The behavior of both

systems undergoing planar extensional deformations in a hyperbolic converging die was very similar. The extensional relaxation times of both systems, as measured with a capillary break-up rheometer were roughly twice their respective Maxwell relaxation times. Extensional thinning was observed for both fluids flowing through a hyperbolic microscale contraction.

In the experiments combining μ-PIV and FIB, both pressure driven flow through a straight channel and through a contraction were considered, as a means of probing the rheological properties of the test fluids, respectively in shear and extension. These two fluid systems were found to exhibit qualitatively different behavior in shear deformations in both macroscale devices as well as microfluidic geometries. By contrast their observed behavior in extensional deformations was remarkably similar, with a transition from steady, laminar flow to unsteady flow for $De_c \approx 10$ and ultimately elastically driven turbulent flow for $De_c \gg De_c$. These results demonstrate that differences in the high rate, non-linear shear rheology of two worm-like micellar systems do not necessarily manifest themselves as differences in the high rate extensional response of the materials.

6.1 Use of the ABRIO^{TM} System for Rheometry

Unique to the work discussed in this thesis is the utilization of a commercially available birefringence microscopy system, originally designed to examine biological systems, for optical rheometry. The calibration experiments discussed in Chapter 4 utilized a prototypical flow in a rectilinear channel to compare the flow-induced birefringence measurements of two worm-like micellar solutions against the predictions of a relatively simple constitutive model in order to demonstrate that the ABRIO^{TM} system could be reliably used for quantitative optical rheometry. In Chapter 5, the system was used to take spatially resolved measurements of the evolution of FIB of the same two fluids in an extensional flow. The greatest strength of the ABRIO^{TM} system in probing the rheo-optical behavior of complex fluids, is its ability to achieve high

spatial resolution measurements of the the spatio-temporal dynamics of a complex fluid as it deforms in a microfluidic device.

6.2 Relevance to Constitutive Modeling

Worm-like micellar systems are ideal, model viscoelastic fluids for study since they exhibit idealized linear viscoelastic behavior for small deformations, which can be predicted by relatively simple constitutive models. The non-linear rheology of these systems is far less well understood theoretically or experimentally.

One particular model intended to describe the rheology of worm-like micellar systems is the Vasquez-Cook-McKinley (VCM) model first proposed by Vasquez *et al.* (2007). In this paper, the VCM model was used to predict the behavior of a worm-like micellar system in both SAOS and steady shear. Later Cromer *et al.* (2009) used this model to predict the rheological response of such a system in a uniaxial extensional flow.

The experimental techniques described in this thesis are well-suited to determining the high deformation rate rheology of many complex fluids, which can assist in the validation of existing constitutive models, in particular the VCM model, and in their improvement. Fitting parameters for the models are typically determined from the rheological properties measured from SAOS, steady shear and transient extension using the macroscale techniques described in Chapter 3. Based on these measurements, the models may be used to predict the high deformation behavior of micellar solutions, which may be compared against the measurements using the microscale flows described in Chapters 4 and 5. For this purpose, the experimental results presented in this thesis as well future results obtained using the experimental techniques presented here are amenable to comparison with the predictions of the VCM as well as other models.

6.3 Future Work

There are several possible paths for future work based on this study.

Firstly, since relating flow-induced birefringence to stress is of significant interest in this work, it is highly desirable to measure directly the stress optical coefficient of both test fluids studied in this thesis and the critical conditions for the onset of any non-linear behavior between stress and flow-induced optical anisotropy. Clearly, this characterization would facilitate more accurate prediction of flow-induced birefringence. Systems for making such measurements typically employ a Couette cell system like those used by Lerouge *et al.* (2000) and Lee *et al.* (2005) for example, but the author of this thesis did not have access to any such device during the experiments addressed here.

Secondly, the apparent hysteretic behavior of the CTAB solution, as seen in the micro-capillary rheometry experiments discussed in Section 3.1.3 merits further investigation. Velocimetry measurements in a channel of similar construction and dimensions of that in the VROC, would greatly provide insight into the the origin of this observed flow instability which leads to an apparent multi-valued viscosity and to explore other elastic instabilities including elastically driven turbulence.

In order to understand more fully the rheological behavior of both micellar systems in the high rate extensional deformations addressed in Chapter 5, it is necessary to characterize the flow kinematics and onset of elastic instabilities more comprehensively than has so far been completed. Additionally, channels with posts positioned far upstream of the contraction could be used to disentangle the long strands of the molecules prior to entering the contraction as a means of potentially delaying the onset of the instability to a flow rate considerably higher than the onset flow rate observed in this work.

Finally, the ultimate utility of the ABRIO system lies in its relative ease of use and its ability to obtain measurements of optical anisotropy with high spatial resolution. Having demonstrated the suitability and reliability of this system for measuring

the flow-induced birefringence of two worm-like micellar systems in a relatively simple straight channel flow, we may be confident in its ability measure flow-induced birefringence of considerably more complicated flows. Accordingly, in future work the ABRIO system should be used to examine flows though hyperbolic geometries of various contraction ratios and the stability of extension dominated complex flows.

Appendix A

Maxwell Model for Linear Viscoelastic Flows

A.1 Governing Scalar Equation

While contemplating the possibility that gases could exhibit viscoelastic behavior, (Bird *et al.* (1987)), James Clerk Maxwell proposed a scalar, constitutive equation for the shear stress, τ, in a linear viscoelastic material having relaxation time, λ and viscosity η_0.

$$\tau + \lambda \frac{d\tau}{dt} = \eta_0 \dot{\gamma} \tag{A.1.1}$$

where t is time and $\dot{\gamma}$ is an applied shear strain rate.

A.1.1 Solving the Maxwell Equation for Simple Deformations

A commonly employed test in the determination of important rheological properties of a material is small amplitude oscillatory shear (SAOS). In this test, a material sample is deformed in shear in a sinusoidally varying fashion. The applied shear

strain, γ, obeys the relation $\gamma = \gamma_0 \sin \omega t$, where γ_0 is the shear strain amplitude and ω is the oscillation frequency of the applied strain. Evidently, the shear strain rate, $\dot{\gamma}$, follows the relation $\dot{\gamma} = \gamma_0 \omega \cos \omega t$. If such a deformation is imposed on a material governed by the Maxwell equation, Eq. A.1.1 becomes

$$\tau + \lambda \frac{d\tau}{dt} = \eta_0 \gamma_0 \omega \cos \omega t \tag{A.1.2}$$

The solution to Eq. A.1.2 consists of a homogenous solution, τ_h, and a particular solution, τ_p, such that $\tau = \tau_h + \tau_p$.

First, we solve for the homogenous solution:

$$\tau_h + \lambda \frac{d\tau_h}{dt} = 0 \tag{A.1.3}$$

Clearly the τ_h obeys the relation $\tau_h = \tau_{0,h} e^{-t/\lambda}$, where $\tau_{0,h}$ is the stress applied to the material at $t = 0$, which is then completely removed for all $t > 0$. Eq. A.1.3 describes the scenario in which a material experiences a constant shear stress of magnitude $\tau_{0,h}$ for all $t < 0$, when at $t = 0$ this stress is instantly and entirely removed. In this case, for all $t > 0$, the stress in the material decays exponentially with time constant λ as shown in Figure A.1.1 (a).

For the case of small amplitude oscillatory shear, the homogeneous solution is not important since the effect of any non-zero $\tau_{0,h}$ on the material stress, τ, decays exponentially in time, such that in the limit of long times only the particular solution, τ_p will be observed. Consequently $\tau = \tau_p$, and we must solve Eq. A.1.2.

Since the imposed shear strain rate is sinusoidally varying in time, it is logical to seek a solution for the resultant material stress which takes the form $\tau = A \sin \omega t + B \cos \omega t$, where A and B are coefficients yet to be determined. Since the applied strain obeys $\gamma = \gamma_0 \sin \omega t$, the magnitude of A distinguishes the elastic or *stored* response of the material, and since the applied shear strain rate obeys $\dot{\gamma} = \gamma_0 \omega \cos \omega t$, the magnitude of B distinguishes the viscous or *lost* response of the material. In this case, Eq. A.1.2 becomes

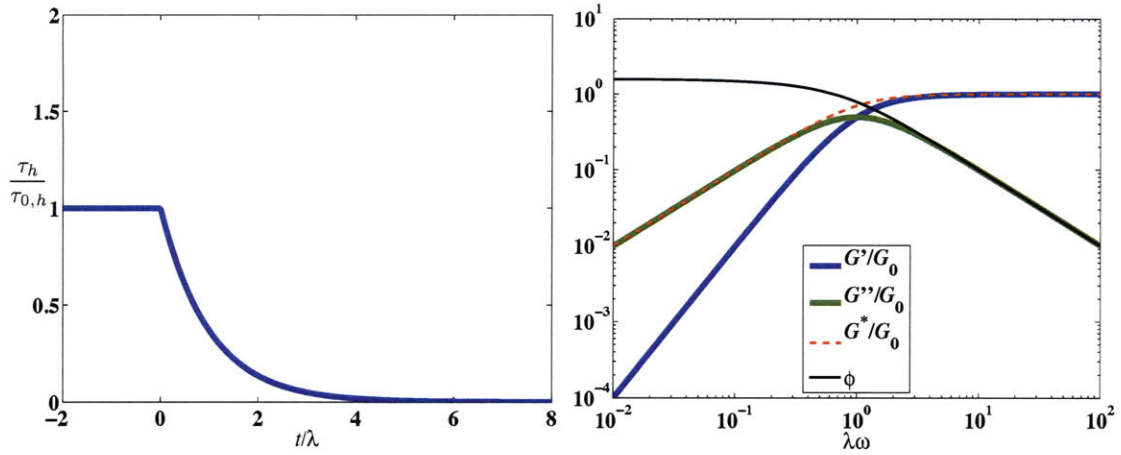

(a) (b)

Figure A.1.1: (a) Stress decay for a Maxwell fluid. (b) Normalized moduli and phase angle, in radians, for a Maxwell fluid undergoing a linear oscillatory shear deformation.

$$A\sin\omega t + B\cos\omega t + \lambda\big(A\omega\cos\omega t - B\omega\sin\omega t\big) = \eta_0\gamma_0\omega\cos\omega t \tag{A.1.4}$$

When the sine and cosine terms in Eq. A.1.4 are segregated, we obtain the following two equations which may be used to determine A and B.

$$\begin{aligned} A - \lambda\omega B &= 0 \\ B + \lambda\omega A &= \eta_0\gamma_0\omega \end{aligned} \tag{A.1.5}$$

After some algebra we obtain

$$A = G_0\gamma_0\left(\frac{(\lambda\omega)^2}{1+(\lambda\omega)^2}\right) \tag{A.1.6}$$

$$B = G_0\gamma_0\left(\frac{\lambda\omega}{1+(\lambda\omega)^2}\right) \tag{A.1.7}$$

where G_0 is called the plateau modulus and is defined $G_0 \equiv \eta_0/\lambda$. Convention dictates that A/γ_0 and B/γ_0 are the actual coefficients of interest in characterizing the linear viscoelastic response of a material to an oscillatory deformation. In this manner the

elastic modulus or *storage modulus*, G' is defined

$$G'(\omega) = G_0\left(\frac{(\lambda\omega)^2}{1+(\lambda\omega)^2}\right) \tag{A.1.8}$$

and the viscous modulus or *loss modulus*, G'' is defined

$$G''(\omega) = G_0\left(\frac{\lambda\omega}{1+(\lambda\omega)^2}\right) \tag{A.1.9}$$

Evidently, the resultant response of a Maxwell fluid to time-dependent, oscillatory deformations obeys the relation

$$\tau = G'(\omega)\gamma_0 \sin\omega t + G''(\omega)\gamma_0 \cos\omega t \tag{A.1.10}$$

or alternatively,

$$\tau = G^*\gamma_0 \sin(\omega t + \phi) \tag{A.1.11}$$

where G^* is called the *complex modulus*, such that $G^* = \sqrt{G'^2 + G''^2}$, and ϕ is the phase angle difference between imposed shear strain and the material response, such that $\phi = \arctan(G''/G')$.

In the limit of $\lambda\omega \ll 1$, the elastic response (*i.e.* G') of the material may be seen to increase quadratically with increasing ω, but the viscous response (*i.e.* G'') increases only linearly with increasing ω. In this regime, the characteristic timescale of the imposed shear strain (*i.e.* $1/\omega$) is very large compared to the relaxation time of the material, and as a consequence the material has ample time to adjust to the imposed strain and as such the work associated with imparting that deformation on the fluid is mostly lost through viscous dissipation. Hence in the limit of low ω, $G'' \gg G'$.

In the opposite limit of $\lambda\omega \gg 1$, the elastic response is invariant to ω, while the viscous response decreases linearly with increasing ω. In this regime, the characteristic timescale of the imposed shear strain is very small compared to the relaxation time of the material, and as a consequence the material is unable to adjust to the imposed

strain and as such the work associated with imparting that deformation on the fluid is mostly stored as elastic energy. Hence in the limit of high ω, $G' \gg G''$.

The magnitudes of G' and G'' are equal when $\lambda\omega = 1$. At this cross-over frequency, $1/\omega = \lambda$ and accordingly the characteristic timescale of the imposed deformation is equal to the relaxation time of the material.

Appendix B

Poiseuille Flow in a Rectangular Geometry

B.1 Geometry and Flow Fundamentals

A commonly encountered problem in fluid mechanics is that of pressure-driven flow in a rectangular geometry: a duct depicted in Figure B.1.1 having width, w, height, h and length, l, such that in a typical case $w \leq h \ll l$. In this depiction, the coordinate axes coincide with the centroidal axes of the duct. In the general case, the dominant flow is along the length of the duct.

If the flow within the duct is fully developed, then all fluid elements flowing in the duct travel at constant velocity, and thus the vectoral sum of the forces acting on any element is zero. For an applied pressure drop, ΔP, acting over the cross-sectional area of the duct wh, along a capillary duct of length l, there must be an equal and opposite frictional force acting on the fluid at its boundary. Hence the integral of the shear stress, τ_{xy}, over the surface area of the duct must equal the force due to the pressure drop. The surface area of the duct is simply the product of its length and perimeter, s, such that

$$\Delta P w h = l \oint \tau_{xy} ds \tag{B.1.1}$$

In the case where $h \gg w$, the perimeter may be approximated as $s \approx 2h$, and if the shear stress along the perimeter of the fluid may be assumed roughly constant, the integral in Eq. B.1.1 may be evaluated to obtain

$$\Delta P w h = 2 l h \tau_{xy} \tag{B.1.2}$$

or alternatively

$$\frac{\Delta P}{l} = 2\frac{\tau_{xy}}{w} \tag{B.1.3}$$

Since the width of the channel is arbitrary, it may be replaced by the coordinate $2y$, where $y = 0$ corresponds to the centerline of the duct, and the resulting expression is

$$\tau_{xy} = \frac{\Delta P}{l} y \tag{B.1.4}$$

Hence, the shear stress, τ_{xy}, within the fluid is zero at the centerline of the duct and it increases linearly with distance away from the centerline. This result is strictly only valid for ducts where $h/w = \infty$, but it is independent of the rheological properties of the test fluid and thus independent of the test fluid. It is also this independence from the test fluid which makes capillary rheometers so versatile.

B.2 Flow of a Newtonian Fluid

For flow of a Newtonian fluid in a duct, the complete equation of motion in the x-direction is

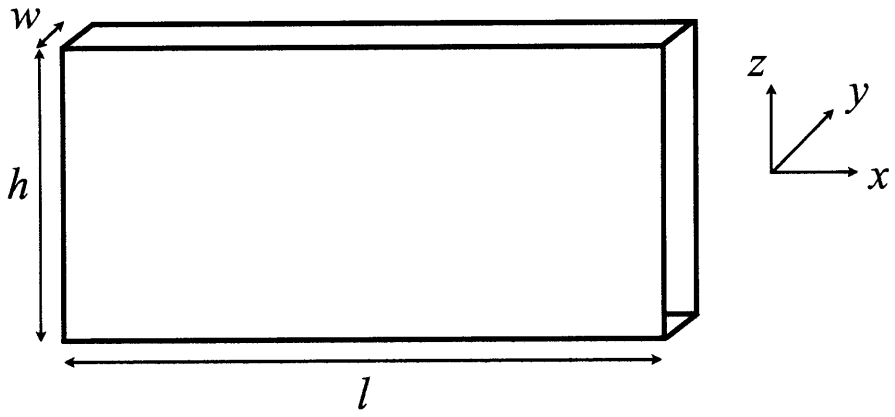

Figure B.1.1: Typical rectangular duct for fluid flow.

$$\rho\left(\frac{\partial u_x}{\partial t}+u_x\frac{\partial u_x}{\partial x}+u_y\frac{\partial u_x}{\partial y}+u_z\frac{\partial u_x}{\partial z}\right)=\mu\left(\frac{\partial^2 u_x}{\partial x^2}+\frac{\partial^2 u_x}{\partial y^2}+\frac{\partial^2 u_x}{\partial z^2}\right)-\frac{\partial P}{\partial x} \quad \text{(B.2.1)}$$

where ρ is the density of the fluid, $u_x$is the x-velocity, μ is the viscosity of the fluid and P is pressure within the duct. If the flow is fully developed and inertia-free (*i.e.* Re is small), Eq. B.2.1 reduces to

$$\frac{\partial P}{\partial x}=\mu\left(\frac{\partial^2 u_x}{\partial x^2}+\frac{\partial^2 u_x}{\partial y^2}+\frac{\partial^2 u_x}{\partial z^2}\right) \quad \text{(B.2.2)}$$

This result is the Poisson equation and it may be solved by some suitable means. Further simplifications, however, can be used to reduce the complexity of B.2.2 and they are described below.

B.2.1 Two-Dimensional Flow

For long ducts, any gradients in the velocity along the x-direction are negligibly small. Furthermore, the pressure gradient may be assumed to be approximately constant. If the duct is of a high aspect ratio, such that $w \ll h$, gradients in the z-direction are also minimal and accordingly the governing equation of motion reduces to

$$\frac{dP}{dx} = \mu \frac{d^2 u_x}{dy^2} \tag{B.2.3}$$

The general solution to Eq. B.2.3 is

$$u_x = \frac{1}{2}\frac{dP}{dx} y^2 + C_1 y + C_2 \tag{B.2.4}$$

Applying the no-slip boundary condition requires $u_x = 0$ at $y = \pm w/2$ and making appropriate substitutions, one finds

$$u_x(y) = \frac{3}{2}\langle U \rangle \left(1 - \frac{4y^2}{w^2}\right) \tag{B.2.5}$$

where the brackets $\langle\rangle$ indicate a spatially averaged quantity. It may be shown that for a given volumetric flow rate Q

$$\langle U \rangle = \frac{Q}{wh} = -\frac{w^2}{12\mu}\left(\frac{dP}{dx}\right) \tag{B.2.6}$$

Of particular importance in what follows, the shear rate, $\dot{\gamma}$, along the width of the duct varies linearly with position and obeys the relation

$$\dot{\gamma} = -12\frac{Q}{w^2 h}\frac{y}{w} \tag{B.2.7}$$

Since the shear stress, τ in a Newtonian fluid obeys the relation $\tau = \mu\dot{\gamma}$, Eq. B.2.7 reveals that the shear stress increases linearly from the one wall of the duct to the other wall and is zero at the centerline of the channel. This results confirms our observation in Eq. B.1.4 and is of importance in the discussion that follows on non-Newtonian fluids.

B.2.2 Three-Dimensional Flow

For channels whose aspect ratios are of order unity, (*i.e.* $w \approx h$), Eq. B.2.2 may only be simplified to

$$\frac{\partial P}{\partial x} = \mu\left(\frac{\partial^2 u_x}{\partial y^2} + \frac{\partial^2 u_x}{\partial z^2}\right) \tag{B.2.8}$$

with boundary conditions $u_x = 0$ at $y = \pm w/2$ and $z = \pm h/2$. Eq. B.2.8 is the Poisson equation and its solution is composed of a two dimensional Fourier series. This equation may be solved, and for the case when $w \leq h$, White (2003) gives the resultant velocity as

$$u_x(y,z) = \frac{4w^2}{\mu\pi^3}\left(-\frac{dP}{dx}\right)\sum_{j\ odd}^{\infty}(-1)^{\frac{j-1}{2}}\left[1 - \frac{\cosh(j\pi z/w)}{\cosh(j\pi h/2w)}\right]\frac{\cos(j\pi y/w)}{j^3} \tag{B.2.9}$$

with corresponding volumetric flow rate

$$Q = \frac{hw^3}{12\mu\pi^3}\left(-\frac{dP}{dx}\right)\left[1 - \frac{192w}{\pi^5 h}\sum_{j\ odd}^{\infty}\frac{\tanh(j\pi h/2w)}{j^5}\right] \tag{B.2.10}$$

Evidently, Eq. B.2.10 may be rearranged to obtain an explicit expression for the pressure gradient, which may then be substituted into Eq. B.2.9 to obtain a relationship between the velocity profile and the volumetric flow rate Q.

$$u_x(y,z) = \frac{48Q}{\pi^3 wh}\frac{\sum_{j\ odd}^{\infty}(-1)^{\frac{j-1}{2}}\left[1 - \frac{\cosh(j\pi z/w)}{\cosh(j\pi h/2w)}\right]\frac{\cos(j\pi y/w)}{j^3}}{1 - \frac{192w}{\pi^5 h}\sum_{j\ odd}^{\infty}\frac{\tanh(j\pi h/2w)}{j^5}} \tag{B.2.11}$$

In the limiting case of $w \ll h$, Eq. B.2.11 reduces to the result for two dimensional flow given by Eq. B.2.5. The three dimensional result is also useful for determining the approximate boundary layer thickness for the flow in the top and bottom of a duct where $w < h$ (*i.e.* the thickness of the region where the flow is fully three dimensional). This boundary layer thickness is of the order w for a Newtonian fluid, such that the flow may be approximated as simply two dimensional by Eq. B.2.5 in the domain $-(h-w)/2 < y < (h-w)/2$.

[0]Eq. B.2.9 and B.2.10 differ slightly from those given in White (2003), since the the respective domains also differ. Here $-w/2 \leq y \leq w/2$ and $-h/2 \leq z \leq h/2$ whereas in White (2003) $-w \leq y \leq w$ and $-h \leq y \leq h$.

B.3 Flow of a non-Newtonian Fluid

In general, the governing equations of motion for a non-Newtonian fluid in a rectangular geometry are substantially complicated that it is not possible to reduce them to simple equations which may be solved analytically. Nevertheless, there exist a few models which may be used to obtain analytically useful results.

B.3.1 Power-Law Model

The viscosity, η, of a Power-Law fluid, described in Bird *et al.* (1987), obeys the phenomenological constitutive equation

$$\eta = m|\dot{\gamma}|^{n-1} \tag{B.3.1}$$

where $\dot{\gamma}$ is an imposed shear rate, m is a positive constant called the consistency index with dimensions Pa.s^n, and n is a dimensionless positive constant. Evidently, m equals the magnitude of the viscosity of the fluid at $\dot{\gamma} = 1\ s^{-1}$. Thus the Power-Law model may be used to model the deformation rate-dependence of the viscosity of a material. For a Newtonian fluid, $n = 1$. For shear thinning fluids, whose viscosity decreases with increasing shear rate, $n < 1$, whereas for shear-thickening fluid, whose viscosity increases with increasing shear rate, $n > 1$.

Clearly this model has the weakness that for the case of $n \neq 1$, in the limit of very small or very large shear rates, the viscosity may be seen to obtain unphysically small or large quantities. Despite this drawback, the Power-Law model is a relatively simple model which provides useful analytical results.

B.3.2 Flow of a Power-Law Fluid in a Duct

For a long, high aspect ratio duct, the result of a simple linear momentum balance along the entire length of the channel found in Eq. B.1.4, may be made into a differential expression such that

$$\frac{dP}{dx} = \frac{d\tau}{dy} \tag{B.3.2}$$

It is clear from Eq. B.3.2, that regardless of the fluid type the shear stress is a linear function of position along the width of the channel. τ may be substituted with a suitable constitutive model, and in the case of the Power-Law model

$$\frac{dP}{dx} = \frac{d}{dy}\left(m\left|\frac{du_x}{dy}\right|^{n-1}\frac{du_x}{dy}\right) = \frac{d}{dy}\left(m\left|\frac{du_x}{dy}\right|^{n}\right) \tag{B.3.3}$$

This equation may be solved easily if one recognizes that the flow must be symmetrical about the x-axis and then solves for the solution in the domain $0 \leq y \leq w/2$. The appropriate boundary conditions are $u_x = 0$ at $y = w/2$ and $du_x/dy = 0$ at $y = 0$. Integrating Eq. B.3.4 once, one obtains

$$\left|\frac{du_x}{dy}\right|^{n} = \frac{1}{m}\frac{dP}{dx}y + \frac{C_1}{m} \tag{B.3.4}$$

Due to the symmetry of the problem, $C_1 = 0$ and thus

$$\left|\frac{du_x}{dy}\right| = \left(\frac{1}{m}\frac{dP}{dx}y\right)^{\frac{1}{n}} \tag{B.3.5}$$

Since $du_x/dy < 0$ for $0 \leq y \leq w/2$, Eq. B.3.5 may be simplified to

$$\frac{du_x}{dy} = -\left(\frac{1}{m}\frac{dP}{dx}y\right)^{\frac{1}{n}} \tag{B.3.6}$$

Integrating again, one obtains

$$u_x = -\left(\frac{1}{m}\frac{dP}{dx}\right)^{\frac{1}{n}}\frac{1}{1+\frac{1}{n}}y^{1+\frac{1}{n}} + C_2 \tag{B.3.7}$$

By the no slip condition at $y = 0$, $C_2 = 0$, and when suitable substitutions are made, the resultant equation may be expressed

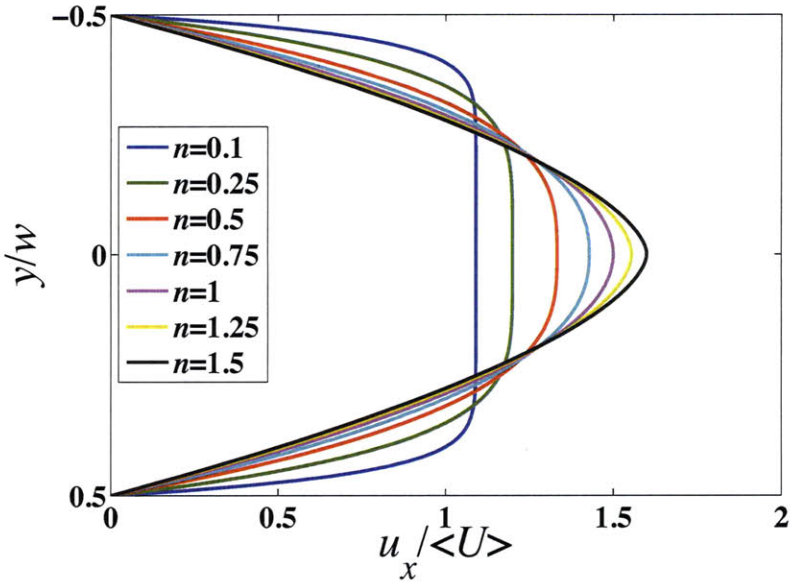

Figure B.3.1: Normalized velocity profiles of a Power-Law fluid flowing in a high aspect ratio duct.

$$u_x(y) = \frac{2n+1}{n+1}\langle U\rangle\left(1 - \left|\frac{2y}{w}\right|^{\frac{n+1}{n}}\right) \tag{B.3.8}$$

where $-w/2 \leq y \leq w/2$. It may be shown that

$$\langle U\rangle = \frac{Q}{wh} = \frac{n}{2n+1}\left(\frac{w}{2}\right)^{\frac{n+1}{n}}\left(\frac{-1}{m}\frac{dP}{dx}\right)^{\frac{1}{n}} \tag{B.3.9}$$

Eq. B.3.8 and B.3.9 reduce to Eq. B.2.5 and B.2.6 respectively when $n = 1$. For the purpose of illustration, representative normalized velocity profiles of Power-Law fluids of varying n are presented ing Figure B.3.1.

B.3.3 Ellis Model

The Ellis Model, described in Bird *et al.* (1987), is another phenomenological constitutive equation with three fitting parameters which may be used to predict both the plateau viscosity of a fluid as well as its deviation from Newtonian behavior. This

model relates the viscosity, η, to the shear stress, τ, and takes the form

$$\eta = \frac{\eta_0}{1 + \left(\frac{\tau}{\tau_{1/2}}\right)^{\alpha-1}} \tag{B.3.10}$$

where η_0 is the zero shear rate viscosity as usual, $\tau_{1/2}$ is the value of the shear stress at which the viscosity is equal to half its zero shear rate value, and α is a fitting coefficient which correlates to n in Eq. B.3.1 such that $\alpha = 1/n$. By multiplying Eq. B.3.10 by the shear rate $\dot{\gamma}$ and with suitable rearrangement, one may obtain the following relation

$$\dot{\gamma} = \frac{\tau}{\eta_0}\left[1 + \left(\frac{\tau}{\tau_{1/2}}\right)^{\alpha-1}\right] \tag{B.3.11}$$

B.3.4 Flow of a Ellis Model Fluid in a Duct

A velocity profile for the flow of an Ellis Model fluid in a rectangular geometry may be obtained from a rearrangement of the earlier result for the stress profile of Eq. B.1.4 in the channel.

$$\tau = \tau_{wall}\frac{2y}{w} \tag{B.3.12}$$

where τ_{wall} is the magnitude of the shear stress at the wall for which $y = \pm w/2$. Inserting Eq. B.3.12 into Eq. B.3.11 and recognizing that $\dot{\gamma} = \frac{du_x}{dy}$, one obtains

$$\frac{du_x}{dy} = \frac{\tau_{wall}}{\eta_0}\frac{2y}{w}\left[1 + \left|\frac{\tau_{wall}}{\eta_0}\frac{2y}{w}\right|^{\alpha-1}\right] \tag{B.3.13}$$

for which the relevant boundary condition is $u_x = 0$ at $y = w/2$. The resultant velocity profile then takes the form

$$u_x = \frac{\tau_{wall}}{4\eta_0}w\left[\left(1 - \frac{4y^2}{w^2}\right) + \frac{2}{\alpha+1}\left(\frac{\tau_{wall}}{\tau_{1/2}}\right)^{\alpha-1}\left(1 - \left|\frac{2y}{w}\right|^{\alpha+1}\right)\right] \tag{B.3.14}$$

and the average velocity is

$$\langle U \rangle = \frac{Q}{wh} = \frac{\tau_{wall}}{6\eta_0} w \left[1 + \frac{3}{\alpha + 2} \left(\frac{\tau_{wall}}{\tau_{1/2}} \right)^{\alpha - 1} \right] \tag{B.3.15}$$

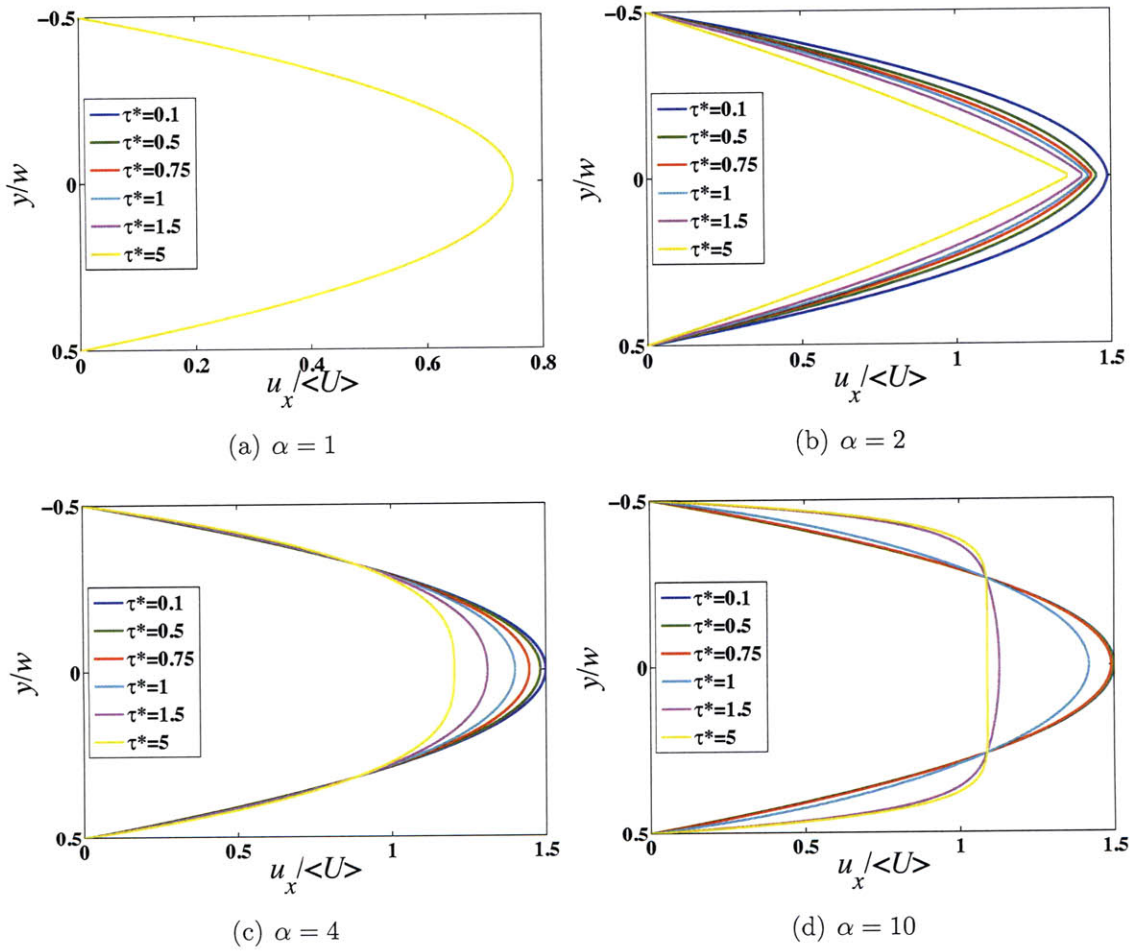

(a) $\alpha = 1$

(b) $\alpha = 2$

(c) $\alpha = 4$

(d) $\alpha = 10$

Figure B.3.2: Normalized velocity profiles of an Ellis Model fluid flowing in a high aspect ratio duct with varying α and $\tau* = \frac{\tau_{wall}}{\tau_{1/2}}$.

These results may be written in more familiar forms if the substitution $\tau_{wall} = -\frac{dP}{dx}\frac{w}{2}$ is made, such that

$$u_x = -\frac{w^2}{8\eta_0}\frac{dP}{dx}\left[\left(1-\frac{2y^2}{w^2}\right)+\frac{2^{2-\alpha}}{\alpha+1}\left|\frac{dP}{dx}\frac{1}{\tau_{1/2}}\right|^{\alpha-1}\left(1-\left|\frac{2y}{w}\right|^{\alpha+1}\right)\right] \tag{B.3.16}$$

and the average velocity is

$$\langle U\rangle = \frac{Q}{wh} = -\frac{w^2}{12\eta_0}\frac{dP}{dx}\left[1+2^{1-\alpha}\frac{3}{\alpha+2}\left|\frac{dP}{dx}\frac{1}{\tau_{1/2}}\right|^{\alpha-1}\right] \tag{B.3.17}$$

Notice that in the case where $\alpha = 1$, Eq. B.3.17 reduces to twice the Newtonian results in Eq. B.2.6. This apparent anomaly can be rationalized by noting that in the case of $\alpha = 1$, Eq. B.3.10 gives a viscosity equal to half η_0. Furthermore, it is not possible to invert Eq. B.3.14 to obtain an explicit relation for τ_{wall} in terms of Q, so iteration is necessary to determine τ_{wall} if Q is specified. For the purpose of illustration, representative normalized velocity profiles of Ellis Model fluids at varying α and $\tau* = \frac{\tau_{wall}}{\tau_{1/2}}$ are presented in Figure B.3.2.

B.3.5 Weissenberg-Rabinowitsch-Mooney Correction

Derivations of the Weissenberg-Rabinowitsch correction for flow in a circular capillary are given in Bird *et al.* (1987) and Macosko (1994), but a full derivation of the Weissenberg-Rabinowitsch-Mooney correction for flow in a high aspect ratio rectangular capillary is offered here. Proper use of this correction is dependent on the experimental realization of the *no-slip* condition at the walls of the capillary.

A rectangular capillary rheometer consists of a long, high aspect ratio tube along with a device that can measure the pressure drop, ΔP, across the capillary duct for an imposed volumetric flow rate of fluid, Q.

It is logical to suppose that, regardless of the nature of the fluid, the fully-developed velocity profile of a fluid flowing in a symmetric, planar geometry should itself be symmetrical about the centerline of the geometry. Consequently, if a velocity profile, $u_x(y)$, may be assumed across the width, w, of the capillary duct, one may

determine one half of the volumetric flow rate in the duct, $\frac{1}{2}Q$

$$\frac{1}{2}Q = h\int_0^{w/2} u_x(y)dy \tag{B.3.18}$$

which may be solved using integration by parts to obtain

$$\frac{1}{2}Q = h\left[u_x y\Big|_{y=0}^{y=w/2} - \int_{u_{x,y=0}}^{u_{x,y=w/2}} y du_x\right] \tag{B.3.19}$$

and since $U = 0$ at $y = w/2$

$$\frac{1}{2}Q = -h\int_{u_{x,y=0}}^{u_{x,y=w/2}} y du_x \tag{B.3.20}$$

Multiplying the resulting integral by unity, one obtains

$$\frac{1}{2}Q = -h\int_0^{w/2} y\left(\frac{du_x}{dy}\right)dy \tag{B.3.21}$$

Eq. B.3.2 may be integrated to find that $y = (dx/dP)\tau$, since $\tau = 0$ at $y = 0$, due to the symmetry of the velocity profile. Again, Eq. B.3.2 may be rearranged to obtain and explicit expression for dy, which may be substituted into Eq. B.3.20, and when the limits of integration are correctly adjusted, one obtains

$$\frac{Q}{2h} = -\int_0^{\tau_{y=w/2}} \frac{dx}{dP}\tau\left(\frac{du_x}{dy}\right)\frac{dx}{dP}d\tau = -\int_0^{\tau_{y=w/2}} \left(\frac{dx}{dP}\right)^2\left(\frac{du_x}{dy}\right)\tau d\tau \tag{B.3.22}$$

Evidently, for fully developed flow dP/dx is constant, and accordingly Eq. B.3.22 may be rearranged to obtain

$$\frac{Q}{2h}\left(\frac{dP}{dx}\right)^2 = -\int_0^{\tau_{y=w/2}} \frac{du_x}{dy}\tau d\tau \tag{B.3.23}$$

Assuming $dP/dx = \Delta P/l$, and considering the result obtained in Eq. B.1.4, one may rearrange Eq. B.3.23 to obtain

$$\frac{2Q}{hw^2}\tau_{wall}^2 = -\int_0^{\tau_{wall}} \frac{du_x}{dy}\tau d\tau \tag{B.3.24}$$

where $\tau_{y=w/2}$ has been replaced by τ_{wall}. Eq. B.3.25 may be differentiated with respect to τ_{wall}, to obtain

$$\frac{d}{d\tau_{wall}}\left[\frac{2Q}{hw^2}\tau_{wall}^2 = -\int_0^{\tau_{wall}} \frac{du_x}{dy}\tau d\tau\right] \tag{B.3.25}$$

According to Leibniz rule, this equation becomes

$$\frac{4Q}{hw^2}\tau_{wall} + \frac{2\tau_{wall}^2}{hw^2}\frac{dQ}{d\tau_{wall}} = -\tau\frac{du_x}{dy}\bigg|_0^{\tau_{wall}} = \tau_{wall}\dot{\gamma}_{wall} \tag{B.3.26}$$

since the velocity gradient at $y = w/2$ is negative. One may further simplify Eq. B.3.26 to

$$\frac{6Q}{hw^2}\left(2 + \frac{\tau_{wall}}{Q}\frac{dQ}{d\tau_{wall}}\right) = 3\dot{\gamma}_{wall} \tag{B.3.27}$$

having divided by τ_{wall}, factorized Q and multiplied the equation by 3. Setting $y = w/2$ in Eq. B.2.7, one obtains the wall shear rate for a Newtonian, $\dot{\gamma}_N = 6Q/hw^2$. Substituting this result in Eq. B.3.27, noting that for a quantity q, $dq/q = d\ln q$, and rearranging appropriately, one obtains the following relation for the true shear rate at the wall

$$\dot{\gamma}_{true} = \frac{\dot{\gamma}_N}{3}\left(2 + \frac{d\ln Q}{d\ln \tau_{wall}}\right) \tag{B.3.28}$$

This result may be exploited to determine the true viscosity of any material flowing in a rectangular capillary duct. It should be noted that for a Newtonian fluid $d\ln Q/d\ln\tau_{wall} = 1$, and on finds that for a Newtonian fluid $\dot{\gamma}_{true} = \dot{\gamma}_N$, as expected.

Appendix C

Flow in a Hyperbolic Contraction

C.1 Geometry and Flow Fundamentals

For the hyperbolic contraction depicted in Figure C.1.1 having length, l_c, height, h_c, upstream width, w_u, width at the contraction exit, w_c, the width, w, at any x takes the form

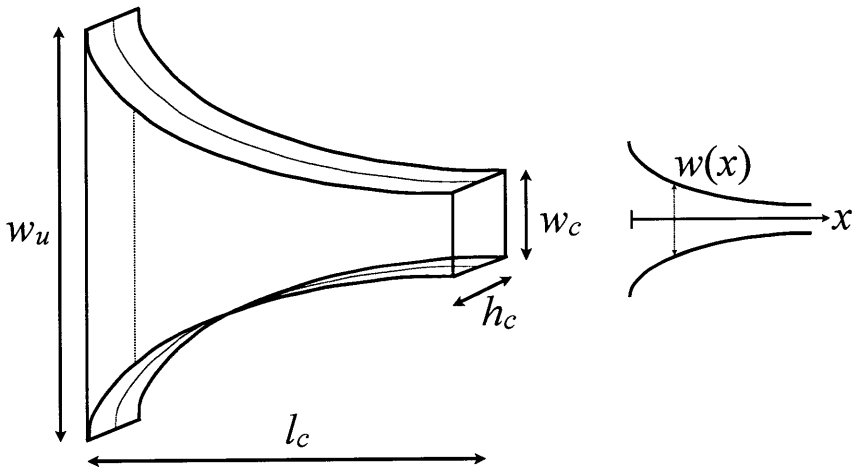

Figure C.1.1: Schematic of a hyperbolic contraction.

$$w(x) = \frac{K}{s + x} \tag{C.1.1}$$

where $s = l_c w_c/(w_u - w_c)$ and $K = s w_u$. Given a constant volumetric flow rate, Q, through the contraction, the average velocity at any x-position is $u_x = Q/h_c w(x)$, and the extension rate, $\dot{\varepsilon}_{xx}$ is

$$\dot{\varepsilon}_{xx} = \frac{Q}{l_c h_c}\left(\frac{1}{w_c} - \frac{1}{w_u}\right) \tag{C.1.2}$$

The Hencky strain, ε_H, varies monotonically along the x-direction and is equal to

$$\varepsilon_{H,x} = \int_0^t \dot{\varepsilon}_{xx} dt = \int_0^t \frac{du_x}{dx} dt = \int_{\langle U_u \rangle}^{\langle U \rangle} \frac{du_x}{u_x} = \ln \frac{\langle U \rangle}{\langle U_u \rangle} = \ln\left(\frac{Q/h_c w(x)}{Q/h_c w_u}\right) = \ln\left(\frac{w(x)}{w_u}\right) \tag{C.1.3}$$

The maximum Hencky strain occurs at the exit of the contraction and is therefore equal to

$$\varepsilon_H = \ln\left(\frac{w_u}{w_c}\right) \tag{C.1.4}$$

C.2 Determination of Extensional Viscosity

The extensional viscosity of the material may be calculated using an energy argument outlined in Pipe & McKinley (2008). Consider the control volume depicted in Figure C.2.1, having initial width, x_0, height, y_0, and unchanging length, l, into the page. If this volume incurs an infinitesimal change in width and height, Δx and Δy respectively, and the volume is incompressible, it is clear that $x_0 y_0 = (x_0 + \Delta x)(y_0 + \Delta y)$. Multiplying out this result, and noting that second order terms may be neglected in the limit of infinitesimal change in volume, one obtains

$$x_0 y_0 = x_0 y_0 + \Delta x y_0 + \Delta y x_0 \tag{C.2.1}$$

Eliminating like terms and dividing Eq. C.2.1 by the initial volume, $x_0 y_0$, one finds $0 = \Delta x/x_0 + \Delta y/y_0$. Hence the sum of extensional strains is zero. When an instantaneous

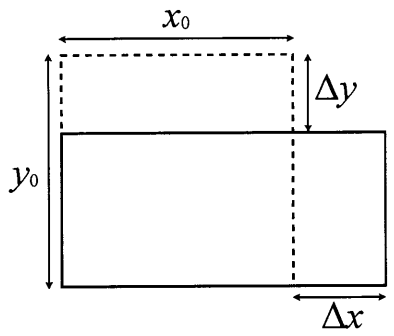

Figure C.2.1: Two dimensional deformation of a control volume.

time derivative of this result is taken, one obtains the continuity equation for a two-dimensional flow

$$0 = \frac{\partial}{\partial t}\left[\lim_{\Delta x,\Delta y\to 0}\left(\frac{\Delta x}{x_0}+\frac{\Delta y}{y_0}\right)\right] = \frac{\partial}{\partial t}\left[\varepsilon_{xx}+\varepsilon_{yy}\right] = \dot{\varepsilon}_{xx}+\dot{\varepsilon}_{yy} \tag{C.2.2}$$

Furthermore, if the stresses τ_{xx} and τ_{yy} act on the control volume as it deforms, the net work per unit length into the page for the infinitesimal volume change is

$$W' = \tau_{xx} y_0 \Delta x + \tau_{yy} x_0 \Delta y \tag{C.2.3}$$

where the prime indicates *per unit length.* Dividing Eq. C.2.3 by $x_0 y_0$, one obtains an expression for the work per unit volume.

$$W''' = \tau_{xx}\frac{\Delta x}{x_0} + \tau_{yy}\frac{\Delta y}{y_0} \tag{C.2.4}$$

where the triple prime indicates *per unit volume.* Once again, taking an instantaneous time derivative in the limit of infinitesimal Δx and Δy, one obtains an expression for the rate of work per unit volume.

$$\dot{W}''' = \tau_{xx}\dot{\varepsilon}_{xx} + \tau_{yy}\dot{\varepsilon}_{yy} \tag{C.2.5}$$

Noting the result of Eq. C.2.2, one may replace $\dot{\varepsilon}_{yy}$ by $-\dot{\varepsilon}_{xx}$ to find

$$\frac{\partial}{\partial t}\left(\frac{\partial W}{\partial V}\right) = \left(\tau_{xx} - \tau_{yy}\right)\dot{\varepsilon}_{xx} \tag{C.2.6}$$

where V denotes a unit volume.

An incremental work must be equal to the mechanical work acting on the material, $\partial W = P\partial V$ where P is pressure and V is volume, or alternatively $\partial W/\partial V = P$. Substituting this result into Eq. C.2.7, one obtains

$$\frac{dP}{dt} = \left(\tau_{xx} - \tau_{yy}\right)\dot{\varepsilon}_{xx} \tag{C.2.7}$$

The pressure term may be expanded by noting

$$\frac{dP}{dt} = \frac{dP}{dx}\frac{dx}{dt} = \frac{dP}{dx}u_x = \frac{dP}{dx}\frac{Q}{h_c w(x)} \tag{C.2.8}$$

Eq. C.2.8 may be separated and integrated from the appropriate limits of the contraction

$$Q\int_{P_u}^{P_c} dP = \int_0^{l_c}\left(\tau_{xx} - \tau_{yy}\right)\dot{\varepsilon}_{xx}h_c w(x)dx \tag{C.2.9}$$

Supposing $\tau_{xx} - \tau_{yy}$ and $\dot{\varepsilon}_{xx}$ are constant along the x-direction, solving for the integration, and substituting for the definition of extensional viscosity, $\eta_E = (\tau_{xx} - \tau_{yy})\dot{\varepsilon}_{xx}/$, one obtains

$$\eta_E = \frac{Q\Delta P}{V_c\dot{\varepsilon}_{xx}^2} \tag{C.2.10}$$

where V_c is the volume of the contraction and is equal to $V_c = kd\ln[(l_c + s)/s]$.

The normal stress difference, $N_1 = \tau_{xx} - \tau_{yy}$, is therefore

$$N_1 = \eta_E\dot{\varepsilon}_{xx} \tag{C.2.11}$$

Appendix D

Relating Optical Anisotropy to Material Stresses

D.1 The Stress Tensor and Relevant Equations

For a material element in a Cartesian coordinate system, as shown in Figure D.1.1, a stress tensor may be defined to capture both the directionality and magnitude of all deviatoric stresses acting on that element. For a generic coordinate system, defined here as the xy-frame, all components of the stress tensor, τ_{ij}, are defined such that that component acts along $\hat{j}$ on a surface whose outward facing unit normal vector is $\hat{i}$, where $\hat{i}$ and $\hat{j}$ are the unit vectors of the i-axis and j-axis, respectively. Since the measurement of birefringence typically employs a line-of-sight technique, with the assumption that the direction of light propagation is coincident with the z-axis in Figure D.1.1, our attention is restricted only to the xy-plane. This restriction follows the assumption that a lightwave will only sample material properties in the plane which is orthogonal to its direction of propagation, as outlined in Fuller (1995). Accordingly, the relevant stress tensor in the xy-frame for consideration is Eq. D.1.1.

$$\mathbf{T} = \begin{bmatrix} \tau_{xx} & \tau_{yx} \\ \tau_{xy} & \tau_{yy} \end{bmatrix} \tag{D.1.1}$$

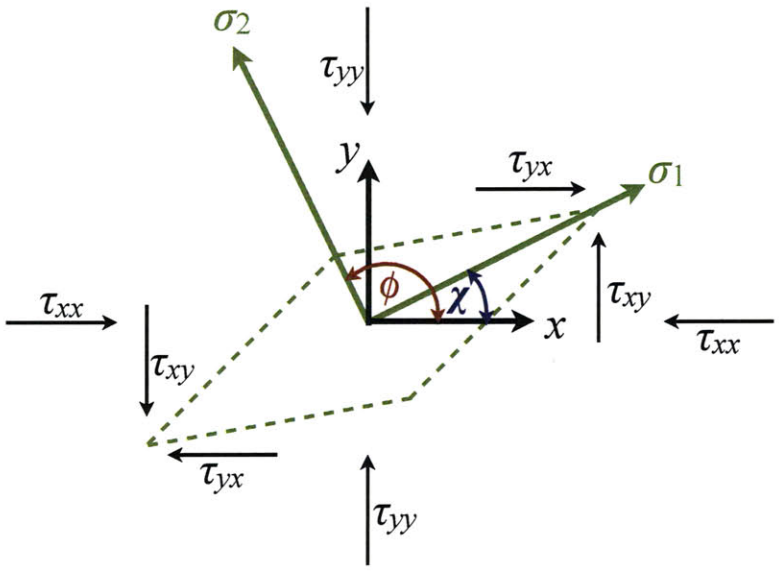

Figure D.1.1: Stresses acting on a deforming material element denoted by the dashed lines.

This stress tensor is necessarily symmetric, and so it should be noted that $\tau_{yx} = \tau_{xy}$.

D.1.1 Relating the xy Stress Tensor to the Principal Stress Tensor

Calculation of the Principal Stresses

The stress tensor in the xy-frame, may be decomposed into the matrix product of its eigenbasis, $\mathbf{E}$, eigenvalues, $\mathbf{\Sigma}$, and the transpose of its eigenbasis, $\mathbf{E^t}$, such that $\mathbf{T} = \mathbf{E} \cdot \mathbf{\Sigma} \cdot \mathbf{E^t}$. This matrix product takes the form of Eq. D.1.2.

$$\begin{bmatrix} \tau_{xx} & \tau_{yx} \\ \tau_{xy} & \tau_{yy} \end{bmatrix} = \begin{bmatrix} \cos\chi & -\sin\chi \\ \sin\chi & \cos\chi \end{bmatrix} \begin{bmatrix} \sigma_1 & \\ & \sigma_2 \end{bmatrix} \begin{bmatrix} \cos\chi & \sin\chi \\ -\sin\chi & \cos\chi \end{bmatrix} \tag{D.1.2}$$

Here, the two columns of $\mathbf{E}$ are the eigenvectors of the stress tensor $\mathbf{T}$, corresponding, respectively, to the two eigenvalues of the stress tensor $\mathbf{T}$, σ_1 and σ_2. Just as the xy-coordinate system is composed of two mutually orthogonal vectors, so too are

the eigenvectors of $\mathbf{T}$ mutually orthogonal. Thus the eigenvectors constitute another coordinate system, unique to the material element, with its own stress tensor $\mathbf{\Sigma}$. This coordinate system is known as the principal frame, since there are no off-diagonal stresses acting on the material in this reference frame. Indeed, only the diagonal components, σ_1 and σ_2, of the principal stress tensor, $\mathbf{\Sigma}$, may be non-zero. These components are known as principal stresses.

Keeping in mind that $\tau_{yx} = \tau_{xy}$, one may solve for the eignevalues of $\mathbf{T}$, in order to relate the deviatoric stresses in $\mathbf{T}$ to the principal stresses via the relations in Eq. D.1.3.

$$\begin{aligned} \sigma_1 &= \tfrac{1}{2}\left(\tau_{xx} + \tau_{yy} + \sqrt{(\tau_{xx} - \tau_{yy})^2 + 4\tau_{xy}^2}\right) \\ \sigma_2 &= \tfrac{1}{2}\left(\tau_{xx} + \tau_{yy} - \sqrt{(\tau_{xx} - \tau_{yy})^2 + 4\tau_{xy}^2}\right) \end{aligned} \tag{D.1.3}$$

These two stresses are the maximum and minimum stresses in a material, as noted in Parnes (2001). It should be noted here that it is common practice to consider the first normal stress difference, N_1, such that $N_1 \equiv \tau_{xx} - \tau_{yy}$, and the principal stress difference, $\Delta\sigma$, such that $\Delta\sigma \equiv \sigma_1 - \sigma_2$. The principal stress difference may be related to the stresses in the xy-frame via Eq. D.1.4. It is also apparent from Eq. D.1.3 and Eq. D.1.4 that for all physically meaningful values of τ_{xx}, τ_{yy} and τ_{xy}, σ_1 will always be greater than σ_2, thus $\Delta\sigma > 0$.

$$\Delta\sigma \equiv \sigma_1 - \sigma_2 = \sqrt{N_1^2 + 4\tau_{xy}^2} \tag{D.1.4}$$

Calculation of the Azimuthal Angle

The orientation of the principal coordinate system with respect to the xy-frame may be defined by the angles χ and ϕ, which are themselves related since $\phi \equiv \chi + \pi/2$, as seen in Figure D.1.1. These angles are commonly called azimuthal angles or extinction angles. In this case, the angle χ has been defined as the angle between the x-axis and the first eigenvector, $\mathbf{e_1}$, of $\mathbf{T}$, corresponding to the eigenvalue σ_1, while ϕ is necessarily the angle between the x-axis and the second eigenvector, $\mathbf{e_2}$, of $\mathbf{T}$, corresponding to

the eigenvalue σ_2. With these definitions in mind, we can write the eigenbasis, $\mathbf{E}$ of $\mathbf{T}$ as:

$$\mathbf{E} = \begin{bmatrix} | & | \\ \mathbf{e_1} & \mathbf{e_2} \\ | & | \end{bmatrix} = \begin{bmatrix} \cos\chi & -\sin\chi \\ \sin\chi & \cos\chi \end{bmatrix} = \begin{bmatrix} \cos\chi & \cos\phi \\ \sin\chi & \sin\phi \end{bmatrix} \tag{D.1.5}$$

Accordingly, χ relates the x-axis to the 1-axis of the principal frame (*i.e.* the σ_1-axis and the n_1-axis of the refractive index tensor). Furthermore, in order to fully specify the orientation of the principal axes with respect to the xy-frame, it is necessary to determine χ or ϕ within a range of 180^o, though this range may not necessarily vary between 0^o and 180^o. As the principal stress tensors, $\mathbf{\Sigma}$, is necessarily symmetric, it is evident that any relation specifying χ or ϕ within a range greater than 180^o would be redundant.

The deviatoric stresses of $\mathbf{T}$ and the principal stresses can be related to χ by completing the matrix product $\mathbf{T} = \mathbf{E} \cdot \mathbf{\Sigma} \cdot \mathbf{E^t}$, as shown in the right hand side of Eq. D.1.6.

$$\begin{bmatrix} \tau_{xx} & \tau_{yx} \\ \tau_{xy} & \tau_{yy} \end{bmatrix} = \begin{bmatrix} \sigma_1\cos^2\chi + \sigma_2\sin^2\chi & \Big(\sigma_1 - \sigma_2\Big)\cos\chi\sin\chi \\ \Big(\sigma_1 - \sigma_2\Big)\cos\chi\sin\chi & \sigma_2\cos^2\chi + \sigma_1\sin^2\chi \end{bmatrix} \tag{D.1.6}$$

Equating components of the tensors, one finds:

$$\begin{aligned} N_1 &= \Big(\sigma_1 - \sigma_2\Big)\Big(\cos^2\chi - \sin^2\chi\Big) = \Big(\sigma_1 - \sigma_2\Big)\cos 2\chi \\ \tau_{xy} &= \Big(\sigma_1 - \sigma_2\Big)\cos\chi\sin\chi = \Big(\sigma_1 - \sigma_2\Big)\Big(\tfrac{1}{2}\sin 2\chi\Big) \end{aligned} \tag{D.1.7}$$

A rearrangement of Eq. D.1.7 yields:

$$\Delta\sigma = \frac{N_1}{\cos 2\chi} \qquad \& \qquad \Delta\sigma = \frac{2\tau_{xy}}{\sin 2\chi} \tag{D.1.8}$$

Finally, an explicit equation relating χ to $\Delta\sigma$, N_1 and τ_{xy} may be written in three

ways:

$$\chi = \frac{1}{2}\arccos\left(\frac{N_1}{\Delta\sigma}\right) = \frac{1}{2}\arccos\left(\frac{N_1}{\sqrt{N_1^2 + 4\tau_{xy}^2}}\right) \tag{D.1.9}$$

$$\chi = \frac{1}{2}\arcsin\left(\frac{2\tau_{xy}}{\Delta\sigma}\right) = \frac{1}{2}\arcsin\left(\frac{2\tau_{xy}}{\sqrt{N_1^2 + 4\tau_{xy}^2}}\right) \tag{D.1.10}$$

$$\chi = \frac{1}{2}\arctan\left(\frac{2\tau_{xy}}{N_1}\right) \tag{D.1.11}$$

These equations for χ cannot themselves fully specify the orientation of the 1-axis of the principal frame. The equations are inadequate, because all of their solutions are restricted to a range of 90^o: a restriction which violates the requirement that the azimuthal angle be specified within a range of 180^o. Furthermore, Eq. D.1.9, D.1.10 and D.1.11 may yield different values depending on the signs of N_1 and τ_{xy}. It is therefore necessary to construct a logical framework to determine unambiguously the orientation angle of the 1-axis of the principal frame with respect to the x-axis, given the deformations and stresses of the material under consideration.

For a generic deformation, each component of the deformation rate tensor may be defined by Eq. D.1.12, such that the deforming material moves along $\hat{j}$ and deforms along $\hat{i}$. Thus the sign of $\dot{\gamma}_{ij}$ gives an indication of the molecular alignment.

$$\dot{\gamma}_{ij} = \frac{1}{2}\left(\frac{\partial V_i}{\partial x_j} + \frac{\partial V_j}{\partial x_i}\right) \tag{D.1.12}$$

For any non-zero value of $\dot{\gamma}_{ij}$ $(i \neq j)$, there will exist a shear stress, τ_{ij}, which acts to align the deforming material. Evidently $\dot{\gamma}_{ij} = \dot{\gamma}_{ji}$, and thus $\tau_{ij} = \tau_{ji}$, so the shear stresses acting on a deforming material will act to align it equally along $\hat{i}$ and $\hat{j}$. Therefore, on net, shear stresses act to orient a deforming material at $\pm 45^o$ relative to the i and j axes, depending on the sign of the stress. For polymeric and micellar solutions, shear flows typically induce normal forces, which themselves act to align the deforming material in the manner discussed in Larson (1998).[1] For a simple shear

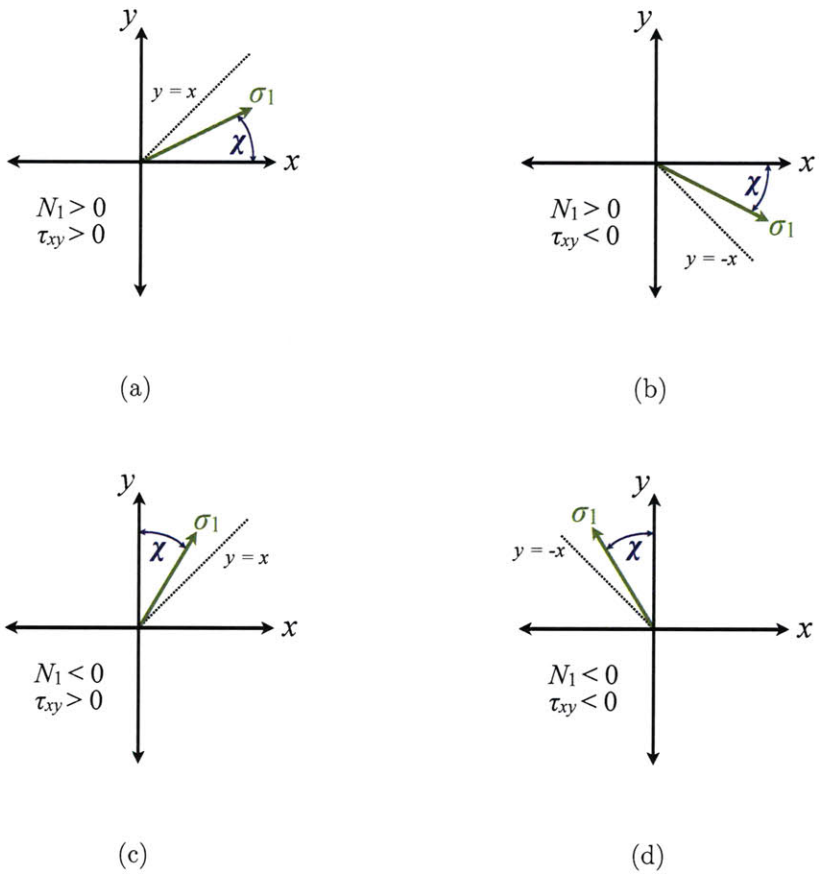

Figure D.1.2: Representative orientation angle of the 1-axis of the principal frame depending on the signs of N_1 and τ_{xy}.

flow, with velocity in the i-direction and velocity gradient in the j-direction, such that $\dot{\gamma}_{ij} = \partial V_i / \partial x_j$, the first normal stress difference $N_1 \equiv \tau_{ii} - \tau_{jj}$ is generally positive for polymeric and micellar solutions. In this case, a positive value of N_1 suggests a higher degree of molecular orientation in the i-direction than in the j-direction. Thus, normal stresses act to align a material along the i and j axes.

Since the first normal stress difference has been defined $N_1 \equiv \tau_{xx} - \tau_{yy}$, a positive value of N_1 indicates a higher degree of molecular orientation in the x-direction than in the y-direction. As such, for positive N_1 the 1-axis of the principal frame is oriented closer to the x-axis than to the y-axis (i.e. $-45^o \leq \chi \leq 45^o$). For the case when $N_1 >$

[1]See Larson (1998), Section 3.4.1 "The Polymer Stress and Birefringence Tensors."

0 and $\tau_{xy} > 0$, the shear stresses act to align the molecule along the $y = x$ line, so we would expect the 1-axis to lie in the first quadrant such that $0^o \leq \chi \leq 45^o$, illustrated in Figure D.1.2 (a). Conversely, if $N_1 > 0$, but $\tau_{xy} < 0$, the shear stresses act to align the molecule along the $y = -x$ line, so we would expect the 1-axis to lie in the fourth quadrant such that -45° $\leq \chi \leq 0^o$, illustrated in Figure D.1.2 (b). In these two cases, Eq. D.1.10 and D.1.11 may be shown to correctly identify the orientation of the 1-axis, while Eq. D.1.9 fails to predict the correct sign of the angle in both cases.

For the case of negative N_1, there is a higher degree of molecular orientation in the y-direction than in the x-direction. Thus when $N_1 < 0$ and $\tau_{xy} > 0$, again the shear stresses act to align the molecule along the $y = x$ line, so we would expect the 1-axis to lie in the first quadrant and closer to the y-axis such that $45^o \leq \chi \leq 90^o$, illustrated in Figure D.1.2 (c). Finally, if $N_1 < 0$, and $\tau_{xy} < 0$, the shear stresses act to align the molecule along the $y = -x$ line, so we would expect the 1-axis to lie in the second quadrant such that $90^o \leq \chi \leq 135^o$, illustrated in Figure D.1.2 (d).

In order to determine the correct mathematical expressions for χ for the case when $N_1 < 0$, it is helpful to consider rotating the xy-frame by a counterclockwise quarter turn such that N_1 in this rotated frame is again positive. In this new coordinate system, the stress tensor is $\mathbf{T_{90^o}}$, where the subscript denotes that its reference frame has been rotated by 90^o with respect to the xy-frame, such that $\mathbf{T_{90^o}} = \mathbf{R(90^o)^t} \cdot \mathbf{T} \cdot \mathbf{R(90^o)}$, where $\mathbf{R}(\theta)$ is the 2D rotation matrix and $\mathbf{T}$ is the stress tensor in the xy-frame.[2] Accordingly, one finds:

$$\mathbf{T_{90^o}} = \begin{bmatrix} \tau_{yy} & -\tau_{yx} \\ -\tau_{xy} & \tau_{xx} \end{bmatrix} \tag{D.1.13}$$

The proper equations to relate the orientation of the 1-axis to the x-axis must take into account the translation by 90^o and the change in the sign of the shear stresses incurred when rotating the coordinate system by 90^o.

[2] $\mathbf{R}(\theta) = \begin{bmatrix} \cos\theta & -\sin\theta \\ \sin\theta & \cos\theta \end{bmatrix}$

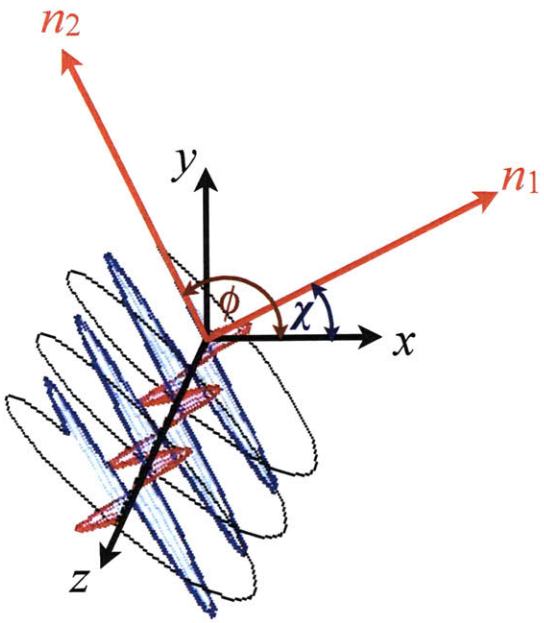

Figure D.2.1: Polarized lightwave propagating through an optically anisotropic sample.

Finally, the expressions that unambiguously define χ may be constructed by the following equations:

$$\chi = \begin{cases} \frac{1}{2}\arcsin\left(\frac{2\tau_{xy}}{\sqrt{N_1^2+4\tau_{xy}^2}}\right) & \text{for } N_1 \geq 0 \\ \frac{\pi}{2} - \frac{1}{2}\arcsin\left(\frac{2\tau_{xy}}{\sqrt{N_1^2+4\tau_{xy}^2}}\right) & \text{for } N_1 < 0 \end{cases} \tag{D.1.14}$$

Thus, we have in principle now derived an equation to relate the principal stress difference to the deviatoric stresses in the xy-frame, namely Eq. D.1.4 and a conditional equation to determine unambiguously the orientation of the principal axes relative to the xy-axes, namely Eq. D.1.14.

D.2 Optical Anisotropy and the Stress Optical Rule

For the optically anisotropic medium shown in Figure D.2.1, a refractive index tensor, $\mathbf{N}$ may be defined in a manner similar to that for the stress tensor, such that

$$\mathbf{N} = \begin{bmatrix} n_{xx} & n_{yx} \\ n_{xy} & n_{yy} \end{bmatrix} \tag{D.2.1}$$

As mentioned before, in the case of birefringence measurements, our attention is restricted exclusively to the xy-plane. Furthermore, this tensor, $\mathbf{N}$ is necessarily symmetric and may be decomposed into the matrix product of its eigenbasis, $\mathbf{E}$, eigenvalues, $\mathbf{n}$, and the transpose of its eigenbasis, $\mathbf{E^t}$, such that $\mathbf{T} = \mathbf{E} \cdot \mathbf{n} \cdot \mathbf{E^t}$. This matrix product takes the form of Eq. D.2.2.

$$\begin{bmatrix} n_{xx} & n_{yx} \\ n_{xy} & n_{yy} \end{bmatrix} = \begin{bmatrix} \cos\chi & -\sin\chi \\ \sin\chi & \cos\chi \end{bmatrix} \begin{bmatrix} n_1 & \\ & n_2 \end{bmatrix} \begin{bmatrix} \cos\chi & \sin\chi \\ -\sin\chi & \cos\chi \end{bmatrix} \tag{D.2.2}$$

Here n_1 and n_2 are the eigenvalues of the refractive index tensor. These refractive indices are commonly known as the ordinary and extraordinary refractive indices of a material. It is also no coincidence that the eignenbasis of the refractive index tensor is identical to the eigenbasis of the stress tensor. Indeed this analogy is the cornerstone of the Stress Optical Rule (SOR), which provides the link between stress in a material and its optical anisotropy. SOR states that the principal normal stress difference, $\Delta\sigma$, is linearly proportional to the difference between the ordinary and extraordinary refractive indices, $\Delta n \equiv n_1 - n_2$. The coefficient of proportionality is the stress optical coefficient, C, which depends on temperature and other material properties. Hence the Stress Optical Rule is

$$\Delta n = C\Delta\sigma \tag{D.2.3}$$

D.2.1 Relating Optical Anisotropy to Retardance

Retardance is a measure of the phase angle shift between two lightwaves, having entered an optically anisotropic medium in phase with each other, after the waves

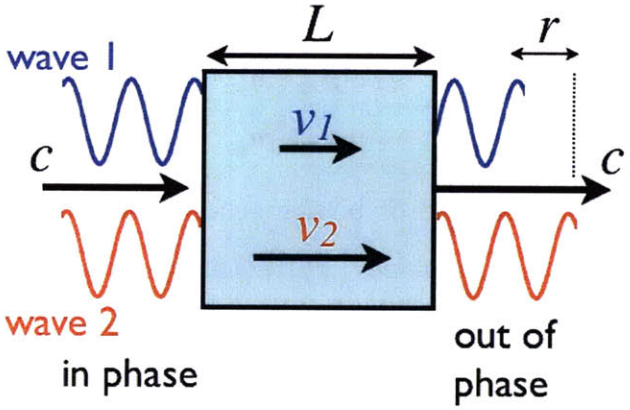

Figure D.2.2: Two lightwaves, initially in phase, traveling from left to right through a birefringent sample.

have emerged from the sample. Thus retardance is a measure of the amount by which one lightwave is slowed down, or retarded, relative to another wave, upon exiting a birefringent medium. Retardance, δ, may have units of radians, or units of length, in which case it is denoted with r. For a lightwave with wavelength, λ, dimensional retardance can be related to the dimensionless retardance via:

$$\frac{r}{\lambda} = \frac{\delta}{2\pi} \tag{D.2.4}$$

For a sample of thickness L, whose optical anisotropy is uniform in the direction of light propagation and which has ordinary and extraordinary refractive indices, n_1 and n_2, respectively, we may also write:

$$\Delta n = \frac{r}{L} = \frac{\lambda}{L}\frac{\delta}{2\pi} \tag{D.2.5}$$

The derivation of Eq. D.2.5 may be found in Fuller (1995), but a different derivation is also delivered here. In Figure D.2.2 there are two lightwaves traveling through a sample of thickness L, with speeds, v_1 and v_2. The light speed in the ambient medium is c. The time spent by wave 1 in the sample, t_1, and the time spent by wave 2 in the sample, t_2, are:

$$t_1 = \frac{L}{v_1} \qquad \& \qquad t_2 = \frac{L}{v_2} \tag{D.2.6}$$

Once both waves have reemerged from sample, wave 2 leads wave 1 by distance r, which is equal to the extra time spent by wave 2 in the sample (t_1-t_2) times the light speed in ambient medium (c), thus:

$$r = (t_1 - t_2)c = \left(\frac{L}{v_1} - \frac{L}{v_2}\right) c = \left(\frac{c}{v_1} - \frac{c}{v_2}\right) L = (n_1 - n_2)L = \Delta n L \tag{D.2.7}$$

which may be rearranged to yield Eq. D.2.5. It is with this equation that optical anisotropy may be related to the quantity that is measured by the ABRIO system.

Appendix E

The ABRIO System for Rheometry

E.1 Material Stress and ABRIO Measurements

For a particular data point, the ABRIO system reports a measured retrdance and azimuthal angle. One may relate the measured retardance to material stresses by combining Eq. D.1.4, D.2.3 and D.2.5, to obtain

$$r = LC\sqrt{N_1^2 + 4\tau_{xy}^2} \tag{E.1.1}$$

Relating χ and ϕ to material stresses requires some consideration, however. ABRIO reports the angle of the slow optical axis as the azimuthal angle. The slow optical axis has a larger refractive index, since refractive index is inversely proportional to the velocity of light in that medium. Therefore to determine if ABRIO will report ϕ or χ, one must consider the sign of the stress optical coefficient, C. Recall that we already proved that $\Delta\sigma$ is necessarily positive in Appendix D. Thus if C is positive, then Δn is positive, and so n_1 is greater than n_2, and accordingly the σ_1-axis corresponds to the slow axis, so ABRIO will report χ. Conversely, if C is negative, then Δn is negative, thus n_1 is less than n_2, and accordingly the σ_2-axis corresponds to the slow axis, so ABRIO will report ϕ.

Thus, to relate the azimuthal angle, Θ, measured by ABRIO to material stresses,

the following conditional equation may be used:

$$\Theta = \begin{cases} \chi & \text{for } C \geq 0 \\ \phi = \chi + \frac{\pi}{2} & \text{for } C < 0 \end{cases} \tag{E.1.2}$$

where χ has been defined by Eq. D.1.14.

E.2 Making the Birefringence Measurements

Birefringence measurements are typically made by observing the change in the state of polarization of a light wave after it emerges from a birefringent sample, as we have described in Appendix D. This measurement technique is known as a line-of-sight technique, since what is measured results from the birefringence of the sample integrated along the entire sample in the direction of light propagation. Measurements performed in this way may yield considerable error in relating the measured optical anisotropy to the stress in a material, if the optical anisotropy of the material varies significantly in the direction of light propagation.

E.2.1 Key Assumptions

In order to relate correctly the measurements of optical anisotropy to the stress in a flowing polymeric or micellar solution, one typically must make the following assumptions:

1) *Sample homogeneity in the direction of light propagation*: Experimental realization of this assumption is necessary to validly apply Eq. D.2.7. For polymeric and micellar solutions flowing in a channel, this assumption is an idealization, because a flow confined in such a geometry cannot be truly two dimensional, but it must be three dimensional, being affected by all of the channel walls. The inaccuracy of this assumption, however, may be lessened greatly through the utilization of channels with large aspect ratios. The flow in a channel whose dimension parallel to the direction

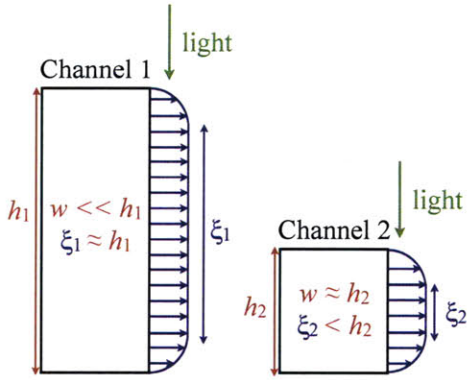

Figure E.2.1: Two rectangular channels of the same width into the page, w, and differing heights, h_1 & h_2. Birefringence measurements are made with light propagating in the direction parallel to the heights of the channel. The flow in Channel 1, with its high aspect ratio, is ideal for birefringence measurements, since the portion of the flow which is homogeneous, ξ_1, is comparable to the the height of the channel, h_1. The flow in Channel 2 is less suited to birefringence measurements, because the portion of the flow which is homogeneous, ξ_2, is small compared to the the height of the channel, h_2.

of light propagation is much greater than its other dimension normal to this direction will be homogenous along much the the channel height. This point is illustrated in Figure E.2.1. As the aspect ratio of the channel becomes very large, the ratio of thickness of the region of homogenous flow to the height of channel approaches unity and Eq. D.2.7 validly describes the relation between optical anistropy and retardance.

2) *Perfectly columnated light*: For high resolution birefringence measurements it necessary that the light beam have as small a diameter as possible and that is remain columnated as it travels through the sample. If these conditions are not met, then the light wave may sample varying optical anisotropy as it propagates through the medium, thus the signal will lose some fidelity.

3) *Light directed perfectly perpendicular to plane of interest*: If the light beam does not impinge upon the sample while propagating in the direction along which the flow in the channel is homogeneous, the applicability of Eq. D.2.7 may be compromised.

4) *Minimal parasitic birefringence*: Any component in the optical path of the light beam may have some amount of birefringence. It is necessary to account for the birefringence of the components other than the sample of interest in order to measure correctly the actual birefringence of the sample.

Exporting the Results

ABRIO stores image files as .pli files in the directory of the selected user session. Each pixel in the image has an associated retardance and azimuthal angle value, which the ABRIO software can readily display. If the user desires to analyze the data in another program (*e.g.* MATLAB), however, it is necessary to convert the .pli file to another file type. This conversion can be accomplished with the PliReadRetFile.m file and PliReaderMex.dll scripts, which have been provided by CRi, Inc. to the McKinley Group.

E.2.2 Restrictions on Sample Dimensions

In the case of the ABRIO system, for which birefringence measurements are made on a microscope, the light impinging on the sample is not perfectly columnated but rather is a cone of illumination, as seen in Figure E.2.2 (a), whose angle depends on the aperture of the light condenser of the microscope. For the light condenser of the Nikon TU-2000 microscope, this angle can be varied between 1^o and about 6.4^o. This cone shape is a slight non-ideality in measurements of birefringence.

Nevertheless, for very thin samples, it is still possible to obtain birefringence measurements whose accuracy may not be significantly compromised by the use of an illumination cone. Consider the sample of height, a, width, b, apect ratio, $\alpha^* = \frac{a}{b}$, being impinged on by a light beam with angle of incidence in the air, θ_{air} and angle of incidence in the sample, θ_{sample}, in Figure E.2.2 (b). Ideally, $\theta_{air} = \theta_{sample} = 0^o$, upholding assumption 3), but even if $\theta_{air} \neq 0^0$ it may still be reasonable to neglect

this non-ideality. To determine the amount by which the measured birefringence may be blurred, due to a non-zero θ_{air}, consider the distance, s, parallel to the width of the channel, that a light wave will travel in the most extreme case. According to Snell's Law of refraction:

$$n_{air}\sin(\theta_{air}) = n_{sample}\sin(\theta_{sample}) \tag{E.2.1}$$

where n_{air} and n_{sample} are the refractive indices of the air and the sample, respectively. For our purposes, $n_{air} = 1.0$ and $n_{sample} = 1.35$, being a typical value for polymeric and micellar solutions. A rearrangement of Eq. E.2.1 and a simple geometric argument will show that:

$$\frac{s}{b} = \alpha^* \tan\left[\sin^{-1}\left(\frac{n_{air}}{n_{sample}}\sin(\theta_{air})\right)\right] \tag{E.2.2}$$

The largest angle of incidence for the collection of light beams impinging on the sample will be the angle of the cone of illumination, which ranges between 1^o and 6.4^o. From Eq. E.2.2, we find that for $\theta_{air} = 1^o$, $\frac{s}{b} = 0.013\alpha^*$ and for $\theta_{air} = 6.4^o$, $\frac{s}{b} = 0.083\alpha^*$. Thus in the most extreme case, when the aperture of the light condenser is fully open, and for $\alpha^* = 10$, which is ideal for upholding assumption 1), a light beam may traverse over 80% of the channel width. Such a large percentage effectively prohibits the making of birefringence measurements on high aspect ratio geometries with high spatial resolution.

We now see that it is effectively impossible to uphold assumptions 1), 2) and 3) simultaneously with the ABRIO system, but depending on the goals of the experimentalist, such restrictions may not be totally inhibitive. For the straight channel used in this study, $\theta \approx 2^o$, $\alpha^* \approx 7.7$, so in the worst case a light wave traversed 20% of the channel width. In the example of flow in the microscale hyperbolic contraction used here, the height of the channel is 35 μm, while its smallest width at the exit of the contraction is also 50 μm. Thus the largest aspect ratio along the entire length of the contraction is only equal to $\alpha^* = 0.7$. So even for fully open light condenser

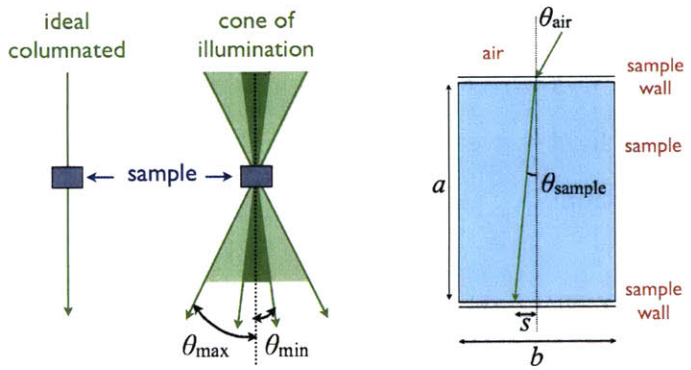

Figure E.2.2: (a) Ideal columnated light beam impinging on a sample, and, in the case of a setup on a microscope, a cone of illumination impinging on a birefringent sample for varying aperture of the light condenser. (b) Effective sampling distance, b, of a light beam propagating through a birefringent medium of thickness a.

$\theta_{air} = 6.4^o$, in the worst case, a light wave would travel across around 6% of the contraction width.

Example of the Influence of the Aperture on Birefringence Measurements

Here, the observed effect on birefringence measurements of changing the aperture of the light condenser is illustrated. The 100:60 mM CPyCl:NaSal system was pumped through a straight rectangular glass duct of height, $H = 970$ μm, and width, $W = 125$ μm. In Figure E.2.3, are shown the pseudocolor maps of retardance for this solution at two different flow rates and with the aperture of the light condenser fully and minimally opened. Additionally the average retardance profiles along the width of the channel are plotted in Figure E.2.4. The region of highest stress and thus birefringence is confined to a narrow section near the walls. It is evident that the measurement taken with the aperture minimally open, when the incident light was most column-like, yielded retardance profiles with higher values near the walls. These results confirmed that a light beam with a smaller angle of incidence samples a narrow region of roughly constant birefringence over a greater distance of propagation than

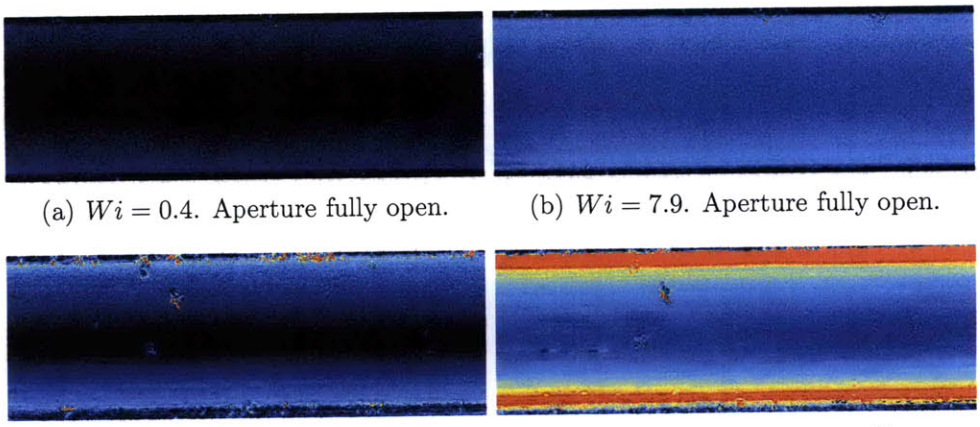

(a) $Wi = 0.4$. Aperture fully open.

(b) $Wi = 7.9$. Aperture fully open.

(c) $Wi = 0.4$. Aperture minimally open.

(d) $Wi = 7.9$. Aperture minimally open.

Figure E.2.3: Pseudocolor maps of retardance of a 100:60 mM CPyCl:NaSal solution flowing in a straight rectangular glass channel. 0 to 0.11 radian (0 to 10 nm) pseudocolor retardance scale.

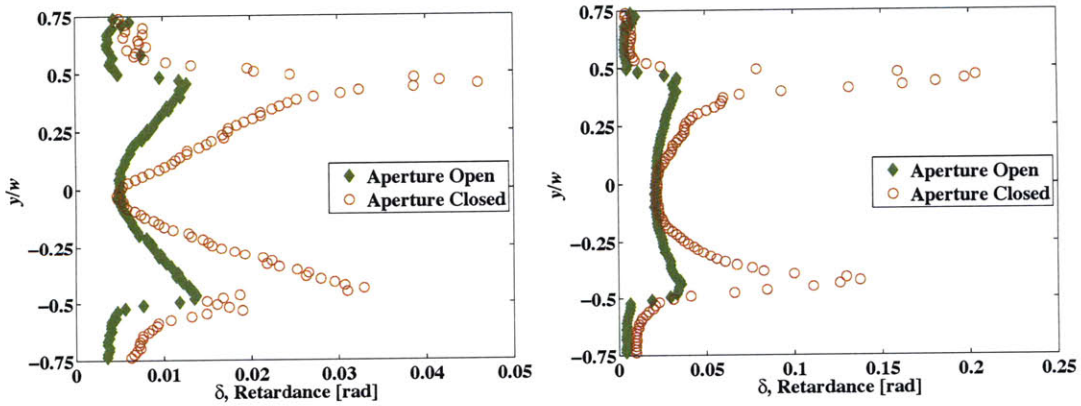

(a) $Wi = 0.4$

(b) $Wi = 7.9$

Figure E.2.4: Retardance profiles measured by ABRIO of a solution of 100:60 mM CPyCl:NaSal flowing in a rectangular microchannel of height, $H = 970$ μm, and width, $W = 125$ μm, for fully open and minimally open light condenser. Background taken with walls and stationary, unstressed fluid sample in view.

a light beam with a larger angle of incidence. From Eq. E.2.2, it is clear that, even for minimal aperture, blurring of the signal will occur. It is evident in Figure E.2.4 that a smaller aperture yield less blurring in the signal, however.

E.3 McKinley Group Contact at CRi, Inc.

As of the writing of this work, Leo Mirkin, *LMirkin@cri-inc.com*, and Cathy Boutin, *CBoutin@cri-inc.com*, were CRi, Inc. contacts for the McKinley Group.

Appendix F

Procedures

F.1 Straight Aluminum Channel

In this section a step-by-step procedure outlining the manufacture of the straight aluminum microchannel is presented.

1) Prepare sides of aluminum block to have the desired roughness, by either sanding or machining. The blocks should be at least 1.5 cm longer than the desired length of the microchannel.
2) Obtain a metal shim with the desired thickness for the spacing between the two channel walls.
3) Position the shim between the two blocks on a level surface. Make sure the shim is held tightly by the blocks to ensure that the thickness of the channel will not vary much along its length. Apply as even a distribution of weight on the two blocks to make certain that they are as flat as possible. Double check that the ends are all flush with the level surface, it is possible for epoxy to seep underneath the blocks and cause them to be glued together unevenly.
4) Place small drops of glue (epoxy) at both ends of the blocks to hold them together.
5) Once the glue has set, remove the shim and check that the spacing between the

blocks is as desired under a microscope.

6) If the spacing is not adequate, break the epoxy bond and remove the epoxy and repeat the above process. Use of ethanol is best for removing the epoxy because this technique does not alter the surface features of the aluminum sidewalls. Another approach is to sand off the epoxy, but this method can alter the sidewalls.

7) If the spacing is as desired, obtain a microscope cover slip longer than the desired length of the channel. The cover slip should be roughly 8 to 10 times the width of the slit to minimize the chance of trapping air bubbles when adhering it to the metal. Break the cover slip to obtain this width, if necessary.

8) Mix up a two part epoxy and spread a very thin layer with a razor on the bottom surface of the two blocks near the slit. Make sure the layer is thin and it stops very near the slit (< 1 mm away).

9) Place the broken cover slip onto of the slit and press down to spread the epoxy. Ensure good wetting so that there are no points where a test fluid in the channel could escape during an experiment.

10) Allow the epoxy to cure for the prescribed time.

11) Obtain a second shorter cover slip, and break it along its length so that it is roughly 8 to 10 times the width of the slit.

12) Spread a thin layer of epoxy as before on the top surface of the blocks.

13) Place the broken cover slip onto of the slit and press down to spread the epoxy. This shorter cover slip should be centered above the longer coverslip, so that at least 5 mm of the longer cover slip overhangs each end.

14) Once the epoxy has cured, ensure that both ends of the channel have been blocked with epoxy and attach the two syringe tips that will be used to connect to the syringe pump.

F.2 Photolithography

In this section a step-by-step procedure outlining the manufacture of the SU-8 molds is presented. This process always occurred in the Class 100 clean room in the microtechnologies lab (MTL) at MIT.

Checklist

- wafers
- tweezers
- MTL card
- procedure
- transparency/mask
- timer(s)
- pen
- safety goggles
- Ziploc for SU-8 masters

Materials

- SU-8 2050 - Permanent Epoxy Photoresist (Micro Chem, microchem.com)
- BC 7.5 - Barrier Coat (Shin Etsu MicroSi, microsi.com)
- CEM 388SS - Contrast Enhancer (Shin Etsu MicroSi, microsi.com)
- acetone
- methanol
- isopropanol

- PM acetate

Preparation

1) Clean all tools with ethanol and then dry them with compressed air.

2) Cut pieces of aluminum foil for use in the oven and in the hood near the hot plates.

3) Clean the shinny side of silicon wafer cleaning (hold with tweasers).

a) Rinse with acetone in the hood above the sink.

b) Rinse with methanol.

c) Rinse with isopropanol.

d) Dry with compressed air.

e) Place the wafer on a piece of aluminum foil in the oven (130 °C) for at least 10 minutes to allow it to dry (20-30 minutes is ideal).

4) While the wafer is in the oven:

a) Check that the hot plates are level.

b) Set the two plate temperatures (one to 65 °C and the other to 95 °C).

Turn on $\Longrightarrow$ Push set button $\Longrightarrow$ "Plate Temperature" $\Longrightarrow$ Enter temperature $\Longrightarrow$ "Enter"

c) Refill solvent bottles if necessary.

d) Obtain SU-8 2050 from flammables cabinet, avoid shaking it to prevent bubble formation.

Spin Coating

1) Remove wafer and place it on aluminum foil near hot plates and the spin coater.

2) Go to the computer to log in:

Coral $\Longrightarrow$ MTL $\Longrightarrow$ EML $\Longrightarrow$ Photo EML $\Longrightarrow$ Select item $\Longrightarrow$ Equipment Actions $\Longrightarrow$ Engage $\Longrightarrow$ Enter values $\Longrightarrow$ Save

3) Select the correct plate for the spin coating and attach it to the spin coater.

4) Align the wafer so that it is concentric with the plate, shinny side facing up.

5) Practice the spinning ramp sequence if necessary.

6) Pour approximately 1 mL SU-8 2050/inch of diameter on the wafer, avoid bubble formation.

7) During the spinning ramp hold a Q-tip near the edge of the chip to catch the SU-8 2050 that flies off, when the ship is spun at 3000 rpm hold the Q-tip so that it just touched the edge of the spinning wafer. It is vital that the Q-tip be held to the edge of the spinning wafer at the very end of the spinning sequence. If the Q-tip is removed too early, the SU-8 will form a small bump at the edge of the wafer, which will prevent good contact between the wafer and the mask during the exposure step.

8) Allow the wafer to sit for 20 minutes.

9) Move the chip to the 65 ^{o}C hot plate for 3 minutes, make sure it is resting level.

10) Quickly move the chip to the 95 ^{o}C hot plate for 7 minutes, make sure it is resting level.

11) Quickly move the chip to the 65 ^{o}C hot plate for 4 minutes, make sure it is resting level.

12) Allow the wafer to sit for 3 minutes at room temperature.

13) While the chip cools:

a) Clean a 50 mL beaker with actone and dry it with compressed air.

b) Obtain the barrier coat BC 7.5 from the flammables cabinet.

c) Fill the 50 mL beaker with about 10 mL of BC 7.5.

14) Move the wafer to the spin coater and center it on the plate.

15) Pour BC 7.5 from the beaker onto the wafer, cover as much of the chip as possible.

16) Follow the ramp sequence.

17) Allow the chip to rest for 5 minutes.

18) While the chip is resting:

a) Clean the beaker that held the BC 7.5 with water, then acetone and dry it with compressed air and place it on the drying rack.

b) Obtain a new 50 mL beaker and clean it with actone and dry it with compressed air.

c) Obtain CEM bottle from flammables cabinet.

d) Fill the 50 mL beaker with about 10 mL of CEM.

19) Move the wafer to the spin coater and center it on the plate.

20) Pour CEM from the beaker onto the wafer, cover as much of the chip as possible.

21) Follow the ramp sequence.

22) Remove the wafer from the spin coater and allow it to rest for 20 minutes.

23) While the chip is resting:

a) Log off the spin coater on the computer.

b) Clean the beaker that held CEM with water, then acetone and dry it with compressed air and place it on the drying rack.

Photoresist

1) Clean the mask, especially the dark side, which is the less shinny side (it will be the side in contact with the wafer), with acetone and then use compressed air to dry it (any excess dirt or drops can be removed with a Q-tip doused in acetone).

2) Dry the mask in the oven (130 °C).

3) Log on to the microscope.

4) Make sure the Power button is on, set dial on photolithography microscope to 0400m, standing for 4 minutes, keep the Soft Contact button off.

5) Place the wafer (conditioned side up) on the pad to the left of the microscope stage.

6) Place the mask on the vacuum pad, with the dark side looking away from the vacuum pad.

7) Turn on the Vacuum Mask button and check that there is a vacuum.

8) Position the vacuum pad into the slots on the microscope stand and tighten the knobs to keep it in place.

9) Check where the mask is positioned relative to the wafer and adjust accordingly. If this is one of your first times doing this, at this point you should call a more experienced FAB user (Kurt) to check over your set up.

10) The Separation Lever should be fully open (*i.e.* positioned away from the user).

11) There should also be a small piece to prevent the lever from opening beyond 180^o.

12) Move the contact lever to the left of the stage and be sure that the mask touches the wafer when the lever is oriented 135^o away from horizontal when it was initially pointing toward the front of the microscope, adjust the knob at the front of the microscope if it does not.

13) Between 135^o and 180^o there should be slightly increasing resistance to opening the lever and, when fully open, the lever should remain at 180^o, without wanting to move back, if this occurs adjust the knob at the front of the microscope.

14) When ready to expose the wafer, press the Exposure button.

15) When the exposure is complete, lower the contact lever.

16) Remove the vacuum pad and the mask and turn off the vacuum.

17) Remove the wafer and wash it with deionized water at low pressure until the wafer becomes shinny again (45-60 seconds).

18) Dry the wafer with compressed air at low pressure.

Finishing Steps

1) Place the wafer on the 65 ^{o}C hot plate for 3 minutes, make sure it is resting level.

2) Log off the microscope.

3) Quickly move the chip to the 95 ^{o}C hot plate for 5 minutes, make sure it is resting level.

4) Quickly move the chip to the 65 ^{o}C hot plate for 3 minutes, make sure it is resting level.

5) Log on to the spinning coater.

6) Place the wafer on the spinning plate and spin the wafer at 300 rpm.

7) Rinse the wafer with PM acetone applying low pressure to prevent crack formation for 60-90 seconds.

8) Rinse the wafer with isopropanol.

9) Ramp up the spinner speed until the chip is dried.

10) Place the wafer on a kimwipe.

11) Log off the spinning coater.

12) Clean tweezer and any other equipment needing cleaning.

13) Inspect the chips quality on the microscope near the flammables cabinet, using the pinkish light filter.

F.3 Making PDMS Channel

In this section a step-by-step procedure outlining the manufacture of the PDMS microchannels used in this study is presented.

Checklist

- SU8 Master
- chlorotrimethylsilane
- PDMS
- glass slides
- plastic pipette
- knife
- needle to punch entry holes in PDMS
- scotch tape
- marker
- legend to masks

1) Check mask for non-uniformities in SU8 (rainbow effect, white parts) and put in a plastic dish lined with aluminum foil. Cover with a lid.
2) Take mask to a fume hood and add one or two drops of chlorotrimethylsilane into the dish and wait for it to vaporize enough (approximately 30 minuts). Thie step changes the surface properties of the master and allows the PDMS to detach more easily from the SU8, avoiding damage to the master.
3) Put 5:1 PDMS resin:hardener into beaker (5-10 g in total is typical). If the mask is new, it must be fully covered, requiring around 50 g total.

4) Weigh beaker with holding beaker and put them into the centrifuge, adjusting for the correct weight.

5) Spin for 1 minute of mixing with 2 minutes for settling.

6) Pour the PDMS mixture on to the master and put the dish under vacuum for 15 minutes.

7) Mix up a second PDMS mixture, with a different ratio of around 10:1. The different ratio gives better bonding between the channel and the coated cover slip.

8) Clean a cover slip with compressed air or nitrogen. Place this cleaned cover slip in the spin coater and pour on a sufficient amount of the PDMS mixture made in the previous step.

9) Spin the cover slip at around 2200 rpm for 1 minute. Check that there are no non-uniformities in the PDMS layer.

10) Place the cover slips into a separate Petri dish and put this under vacuum also.

11) Cure de-gassed cover slips and channels for 30 minutes at 80 °C.

12) While the channels are curing, prepare labels for all of the channels, which are to be replicated.

13) Remove the channels from the oven and cut out appropriate channels. Punch out holes in the channels for the metal tubes using the sharp syringe tips. Do this quickly while the PDMS is still fresh.

14) Place the channels on the coated cover slips and cure over night.

Bibliography

Anna, S. L., & McKinley, G. H. 2001. Elasto-capillary thinning and breakup of model elastic liquids. *Journal of Rheology*, **45**(1), 115–138.

Becu, L., Manneville, S., & Colin, A. 2004. Spatiotemporal dynamics of wormlike micelles under shear. *Physical Review Letters*, **93**(1).

Berret, J-F. 2006. Rheology of Wormlike Micelles: Equilibrium Properties and Shear Banding Transitions. *Pages 667–720 of:* Weiss, R. G., & Terech, P. (eds), *Molecular Gels*. Springer Netherlands.

Berret, J. F., Roux, D. C., & Porte, G. 1994. Isotropic-to-Nematic Transition in Wormlike Micelles under Shear. *Journal De Physique II*, **4**(8), 1261–1279.

Berret, J. F., Porte, G., & Decruppe, J. P. 1997. Inhomogeneous shear rows of wormlike micelles: A master dynamic phase diagram. *Physical Review E*, **55**(2), 1668–1676.

Berret, J. F., Lerouge, S., & Decruppe, J. P. 2002. Kinetics of the shear-thickening transition observed in dilute surfactant solutions and investigated by flow birefringence. *Langmuir*, **18**(20), 7279–7286.

Bhardwaj, A., Miller, E., & Rothstein, J. P. 2007. Filament stretching and capillary breakup extensional rheometry measurements of viscoelastic wormlike micelle solutions. *Journal of Rheology*, **51**(4), 693–719.

Bird, R. Byron, Armstrong, Robert C., & Hassager, Ole. 1987. *Dynamics of Polymeric Liquids.* 2nd edn. Vol. 1. New York, NY: John Wiley & Sons, Inc.

Buckingham, E. 1914. On physically similar systems: illustrations of the use of dimensional equations. *Physical Review*, **4**(4), 345.

Cates, M. E. 1987. Reptation of Living Polymers - Dynamics of Entangled Polymers in the Presence of Reversible Chain-Scission Reactions. *Macromolecules*, **20**(9), 2289–2296.

Cates, M. E. 1990. Nonlinear Viscoelasticity of Wormlike Micelles (and Other Reversibly Breakable Polymers). *Journal of Physical Chemistry*, **94**(1), 371–375.

Cates, M. E., & Candau, S. J. 1990. Statics and Dynamics of Worm-Like Surfactant Micelles. *Journal of Physics-Condensed Matter*, **2**(33), 6869–6892.

Cates, M. E., & Fielding, S. M. 2006. Rheology of Giant Micelles. *Advances in Physics*, **55**(7-8), 799–879.

Chen, C. M., & Warr, G. G. 1997. Light scattering from wormlike micelles in an elongational field. *Langmuir*, **13**(6), 1374–1376.

Chen, S., & Rothstein, J. P. 2004. Flow of a wormlike micelle solution past a falling sphere. *Journal of Non-Newtonian Fluid Mechanics*, **116**(2-3), 205–234.

Cromer, M., Cook, L. P., & McKinley, G. H. 2009. Extensional flow of wormlike micellar solutions. *Chemical Engineering Science*, **64**(22), 4588–4596.

de Gennes, Pierre-Gilles. 1979. *Scaling Concepts in Polymer Physics.* Cornell University Press.

Dealy, J. M., & Wissbrun, K. F. 1990. *Melt Rheology and Its Role in Plastics Processing: Theory and Applications.* Van Nostrand Reinhold.

Decruppe, J. P., & Ponton, A. 2003. Flow birefringence, stress optical rule and rheology of four micellar solutions with the same low shear viscosity. *European Physical Journal E*, **10**(3), 201–207.

Decruppe, J. P., Cappelaere, E., & Cressely, R. 1997. Optical and rheological properties of a semi-diluted equimolar solution of cetyltrimethylammonium bromide and potassium bromide. *Journal De Physique II*, **7**(2), 257–270.

Decruppe, J. P., Lerouge, S., & Berret, J. F. 2001. Insight in shear banding under transient flow. *Physical Review E*, **6302**(2).

Degre, G., Joseph, P., Tabeling, P., Lerouge, S., Cloitre, M., & Ajdari, A. 2006. Rheology of complex fluids by particle image velocimetry in microchannels. *Applied Physics Letters*, **89**(2).

Doi, M., & Edwards, S. F. 1986. *The Theory of Polymer Dynamics.* Oxford University Press.

Einstein, Albert. 1906. *Investigations on the Theory of Brownian Movement.* Dover Publications, Inc.

Entov, V. M., & Hinch, E. J. 1997. Effect of a spectrum of relaxation times on the capillary thinning of a filament of elastic liquid. *Journal of Non-Newtonian Fluid Mechanics*, **72**(1), 31–53.

Fardin, M. A., Lasne, B., Cardoso, O., Gregoire, G., Argentina, M., Decruppe, J. P., & Lerouge, S. 2009. Taylor-like Vortices in Shear-Banding Flow of Giant Micelles. *Physical Review Letters*, **103**(2).

Feigl, K., Tanner, F., Edwards, B. J., & Collier, J. R. 2003. A numerical study of the measurement of elongational viscosity of polymeric fluids in a semihyperbolically converging die. *Journal of Non-Newtonian Fluid Mechanics*, **115**(2-3), 191–215.

Fielding, S. M. 2007. Complex dynamics of shear banded flows. *Soft Matter*, **3**(10), 1262–1279.

Fielding, S. M., & Olmsted, P. D. 2006. Nonlinear dynamics of an interface between shear bands. *Physical Review Letters*, **96**(10).

Fielding, S. M., & Wilson, H. J. 2010. Shear banding and interfacial instability in planar Poiseuille flow. *Journal of Non-Newtonian Fluid Mechanics*, **165**(5-6), 196–202.

Fischer, E., & Callaghan, P. T. 2000. Is a birefringence band a shear band? *Europhysics Letters*, **50**(6), 803–809.

Fischer, E., & Callaghan, P. T. 2001. Shear banding and the isotropic-to-nematic transition in wormlike micelles. *Physical Review E*, **6401**(1).

Fuller, Gerald G. 1995. *Optical Rheometry of Complex Fluids.* Oxford University Press.

Granek, R., & Cates, M. E. 1992. Stress-Relaxation in Living Polymers - Results from a Poisson Renewal Model. *Journal of Chemical Physics*, **96**(6), 4758–4767.

Groisman, A., & Quake, S. R. 2004. A microfluidic rectifier: Anisotropic flow resistance at low Reynolds numbers. *Physical Review Letters*, **92**(9), –.

Groisman, A., & Steinberg, V. 2000. Elastic turbulence in a polymer solution flow. *Nature*, **405**(6782), 53–55.

Guillot, P., Panizza, P., Salmon, J. B., Joanicot, M., Colin, A., Bruneau, C. H., & Colin, T. 2006. Viscosimeter on a microfluidic chip. *Langmuir*, **22**(14), 6438–6445.

Helgeson, M. E., Reichert, M. D., Hu, Y. T., & Wagner, N. J. 2009a. Relating shear banding, structure, and phase behavior in wormlike micellar solutions. *Soft Matter*, **5**(20), 3858–3869.

Helgeson, M. E., Vasquez, P. A., Kaler, E. W., & Wagner, N. J. 2009b. Rheology and spatially resolved structure of cetyltrimethylammonium bromide wormlike micelles through the shear banding transition. *Journal of Rheology*, **53**(3), 727–756.

Hu, Y. T., & Lips, A. 2005. Kinetics and mechanism of shear banding in an entangled micellar solution. *Journal of Rheology*, **49**(5), 1001–1027.

Hu, Y. T., Boltenhagen, P., & Pine, D. J. 1998. Shear thickening in low-concentration solutions of wormlike micelles. I. Direct visualization of transient behavior and phase transitions. *Journal of Rheology*, **42**(5), 1185–1208.

Hu, Y. T., Palla, C., & Lips, A. 2008. Comparison between shear banding and shear thinning in entangled micellar solutions. *Journal of Rheology*, **52**(2), 379–400.

Hutton, J. F. 1963. Fracture of Liquids in Shear. *Nature*, **200**(490), 646–648.

Israelachvili, Jacob. 2007. *Intermolecular & Surface Forces.* 2nd edn. Academic Press.

IUPAC. 1997. *Compendium of Chemical Terminology.* 2nd edn. Blackwell Scientific Publications.

James, D. F. 1991. Flow in a Converging Channel at Moderate Reynolds-Numbers. *AIChE Journal*, **37**(1), 59–64.

Johnson, M., & Segalman, D. 1977. A model for viscoelastic fluid behavior which allows non-affine deformation. *Journal of Non-Newtonian Fluid Mechanics*, **2**, 255–270.

Kang, K., Lee, L. J., & Koelling, K. W. 2005. High shear microfluidics and its application in rheological measurement. *Experiments in Fluids*, **38**(2), 222–232.

Kang, K., Koelling, K. W., & Lee, L. J. 2006. Microdevice end pressure evaluations with Bagley correction. *Microfluidics and Nanofluidics*, **2**(3), 223–235.

Kefi, S., Lee, J., Pope, T. L., Sullivan, P., Nelson, E., & Hernandez, A. N. 2005. Expanding Applications of Viscoelastic Surfactant Solutions. *Oilfield review*, **Winter 2004/2005**, 10–623.

Kim, N. J., Pipe, C. J., Ahn, K. H., Lee, S. J., & McKinley, G. H. 2010. Capillary breakup extensional rheometry of a wormlike micellar solution. *Korea-Australia Rheology Journal*, **22**(1), 31–41.

Larson, R. G. 2000. Fluid dynamics - Turbulence without inertia. *Nature*, **405**(6782), 27–28.

Larson, Ronald G. 1998. *The Structure and Rheology of Complex Fluids.* Oxford University Press.

Lee, C. S., Tripp, B. C., & Magda, J. J. 1992. Does N_1 or N_2 Control the Onset of Edge Fracture. *Rheologica Acta*, **31**(3), 306–308.

Lee, J. Y., Fuller, G. G., Hudson, N. E., & Yuan, X. F. 2005. Investigation of shear-banding structure in wormlike micellar solution by point-wise flow-induced birefringence measurements. *Journal of Rheology*, **49**(2), 537–550.

Lerouge, S., & Berret, J-F. 2009. Shear-induced transitions and instabilities in surfactant wormlike micelles. *ArXiv e-prints.*

Lerouge, S., Decruppe, J. P., & Berret, J. F. 2000. Correlations between rheological and optical properties of a micellar solution under shear banding flow. *Langmuir*, **16**(16), 6464–6474.

Lerouge, S., Decruppe, J. P., & Olmsted, P. D. 2004. Birefringence Banding in a Micellar Solution or the Complexity of Heterogeneous Flows. *Langmuir*, **20**(26), 11355–11365.

Lerouge, S., Fardin, M. A., Argentina, M., Gregoire, G., & Cardoso, O. 2008. Interface dynamics in shear-banding flow of giant micelles. *Soft Matter*, **4**(9), 1808–1819.

Lu, C. Y. D., Olmsted, P. D., & Ball, R. C. 2000. Effects of nonlocal stress on the determination of shear banding flow. *Physical Review Letters*, **84**(4), 642–645.

Macosko, C. W. 1994. *Rheology: Principles, Measurements, and Applications.* Wiley-VCH.

Masselon, C., Salmon, J. B., & Colin, A. 2008. Nonlocal effects in flows of wormlike micellar solutions. *Physical Review Letters*, **1**(3).

McKinley, G. H. 2005. Visco-Elasto-Capillary Thinning and Break-Up of Complex Fluids. *Annual Rheology Reviews, 2005.*

McKinley, G. H., Pakdel, P., & Öztekin, A. 1996. Rheological and geometric scaling of purely elastic flow instabilities. *Journal of Non-Newtonian Fluid Mechanics*, **67**, 19–47.

Meinhart, C. D., Wereley, S. T., & Gray, M. H. B. 2000. Volume illumination for two-dimensional particle image velocimetry. *Measurement Science & Technology*, **11**(6), 809–814.

Miller, E., & Rothstein, J. P. 2007. Transient evolution of shear-banding wormlike micellar solutions. *Journal of Non-Newtonian Fluid Mechanics*, **143**(1), 22–37.

Morozov, A. N., & van Saarloos, W. 2007. An introductory essay on subcritical instabilities and the transition to turbulence in visco-elastic parallel shear flows. *Physics Reports-Review Section of Physics Letters*, **447**(3-6), 112–143.

Nghe, P., Degre, G., Tabeling, P., & Ajdari, A. 2008. High shear rheology of shear banding fluids in microchannels. *Applied Physics Letters*, **93**(20).

Nghe, P., Fielding, S. M., Tabeling, P., & Ajdari, A. 2009. Microchannel flow of a shear-banding fluid: enhanced confinement effect and interfacial instability. *Unpublised.*

Oliveira, M. S. N., Alves, M. A., Pinho, F. T., & McKinley, G. H. 2007. Viscous flow through microfabricated hyperbolic contractions. *Experiments in Fluids*, **43**(2-3), 437–451.

Olmsted, P. D. 2008. Perspectives on shear banding in complex fluids. *Rheologica Acta*, **47**(3), 283–300.

Olmsted, P. D., Radulescu, O., & Lu, C. Y. D. 2000. Johnson-Segalman model with a diffusion term in cylindrical Couette flow. *Journal of Rheology*, **44**(2), 257–275.

Papageorgiou, D. T. 1995. On the Breakup of Viscous-Liquid Threads. *Physics of Fluids*, **7**(7), 1529–1544.

Parnes, Raymond. 2001. *Solid Mechanics in Engineering.* John Wiley & Sons, Ltd.

Pathak, J. A., & Hudson, S. D. 2006. Rheo-optics of equilibrium polymer solutions: Wormlike micelles in elongational flow in a microfluidic cross-slot. *Macromolecules*, **39**(25), 8782–8792.

Pipe, C. J., & McKinley, G. H. 2008. A microuidic extensional viscosity indexer. *Unpublished preprint.*

Pipe, C. J., Majmudar, T. S., & McKinley, G. H. 2008. High Shear Rate Viscometry. *Rheologica Acta*, **47**(5-6), 621–642.

Prud'homme, R. K., & Warr, G. G. 1994. Elongational Flow of Solutions of Rodlike Micelles. *Langmuir*, **10**(10), 3419–3426.

Raffel, M., Willert, C., & Kompenhans, J. 1998. *Particle Image Velocimetry.* Springer-Verlag.

Rehage, H., & Hoffmann, H. 1982. Shear Induced Phase-Transitions in Highly Dilute Aqueous Detergent Solutions. *Rheologica Acta*, **21**(4-5), 561–563.

Rehage, H., & Hoffmann, H. 1991. Viscoelastic Surfactant Solutions - Model Systems for Rheological Research. *Molecular Physics*, **74**(5), 933–973.

Rodd, L. E., Scott, T. P., Boger, D. V., Cooper-White, J. J., & McKinley, G. H. 2005. The inertio-elastic planar entry flow of low-viscosity elastic fluids in micro-fabricated geometries. *Journal of Non-Newtonian Fluid Mechanics*, **129**(1), 1–22.

Rodd, L. E., Cooper-White, J. J., Boger, D. V., & McKinley, G. H. 2007. Role of the elasticity number in the entry flow of dilute polymer solutions in micro-fabricated contraction geometries. *Journal of Non-Newtonian Fluid Mechanics*, **143**(2-3), 170–191.

Rothstein, J. P. 2003. Transient extensional rheology of wormlike micelle solutions. *Journal of Rheology*, **47**(5), 1227–1247.

Rothstein, J.P. 2009. Strong flows of viscoelastic wormlike micelle solutions. *Rheology Reviews.*

Salmon, J. B., Colin, A., & Manneville, S. 2003. Velocity Profiles in Shear-Banding Wormlike Micelles. *Physical Review Letters*, **90**(22).

Scott, T. P. 2004. *Contraction/Expansion Flow of Dilute Elastic Solutions in Microchannels.* Master of Science, Massachusetts Institute of Technology.

Shikata, T., Hirata, H., & Kotaka, T. 1987. Micelle Formation of Detergent Molecules in Aqueous-Media - Viscoelastic Properties of Aqueous Cetyltrimethylammonium Bromide Solutions. *Langmuir*, **3**(6), 1081–1086.

Shikata, T., Dahman, S. J., & Pearson, D. S. 1994. Rheooptical Behavior of Wormlike Micelles. *Langmuir*, **10**(10), 3470–3476.

Shribak, M., & Oldenbourg, R. 2003. Techniques for fast and sensitive measurements of two-dimensional birefringence distributions. *Applied Optics*, **42**(16), 3009–3017.

Soulages, J., Oliveira, M. S. N., Sousa, P. C., Alves, M. A., & McKinley, G. H. 2009. Investigating the stability of viscoelastic stagnation flows in T-shaped microchannels. *Journal of Non-Newtonian Fluid Mechanics*, **163**(1-3), 9–24.

Tanner, R. I., & Keentok, M. 1983. Shear Fracture in Cone Plate Rheometry. *Journal of Rheology*, **27**(1), 47–57.

Trouton, F. T. 1906. On the coefficient of viscous traction and its relation to that of viscosity. *Proceedings of the Royal Society of London Series A-Containing Papers of a Mathematical and Physical Character*, **77**(519), 426–440.

Turner, M. S., & Cates, M. E. 1991. Linear Viscoelasticity of Living Polymers - a Quantitative Probe of Chemical Relaxation-Times. *Langmuir*, **7**(8), 1590–1594.

Turner, M. S., & Cates, M. E. 1992. Linear Viscoelasticity of Wormlike Micelles - a Comparison of Micellar Reaction-Kinetics. *Journal De Physique II*, **2**(3), 503–519.

Turner, M. S., Marques, C., & Cates, M. E. 1993. Dynamics of Wormlike Micelles - the Bond-Interchange Reaction Scheme. *Langmuir*, **9**(3), 695–701.

Vasquez, P. A., McKinley, G. H., & Cook, L. P. 2007. A network scission model for wormlike micellar solutions - I. Model formulation and viscometric flow predictions. *Journal of Non-Newtonian Fluid Mechanics*, **144**(2-3), 122–139.

Wang, J., James, D. F., & Park, C. B. 2010. Planar extensional flow resistance of a foaming plastic. *Journal of Rheology*, **54**(1), 95–116.

White, F. M. 2003. *Viscous Fluid Flow*. 3rd edn. McGraw-Hill.

Wunderlich, I., Hoffmann, H., & Rehage, H. 1987. Flow birefringence and rheological measurements on shear induced micellar structures. *Rheologica Acta*, **26**, 532–542.

Xia, Y. N., & Whitesides, G. M. 1998. Soft Lithography. *Annual Review of Materials Science*, **28**, 153–184.

Yesilata, B., Clasen, C., & McKinley, G. H. 2006. Nonlinear Shear and Extensional Flow Dynamics of Wormlike Surfactant Solutions. *Journal of Non-Newtonian Fluid Mechanics*, 73–90.

Zhou, L., Vasquez, P. A., Cook, L. P., & McKinley, G. H. 2008. Modeling the inhomogeneous response and formation of shear bands in steady and transient flows of entangled liquids. *Journal of Rheology*, **52**(2), 591–623.